Turbulence in stably stratified boundary layers

by

Amir Atoufi

A thesis
presented to the University of Waterloo
in fulfillment of the
thesis requirement for the degree of
Doctor of Philosophy
in
Systems Design Engineering

Waterloo, Ontario, Canada, 2020

Examining Committee Membership

The following served on the Examining Committee for this thesis. The decision of the Examining Committee is by majority vote.

External Examiner:	James J. Riley Professor, Dept. of Mechanical Engineering, University of Washington
Supervisor(s):	Michael L. Waite Associate Professor, Dept. of Applied Mathematics, University of Waterloo K. Andrea Scott Associate Professor, Dept. of Systems Design Engineering, University of Waterloo
Internal Members:	Paul Fieguth Professor, Dept. of Systems Design Engineering, University of Waterloo Jean-Pierre Hickey Assistant Professor, Dept. of Mechanical Engineering, University of Waterloo
Internal-External Member:	Kevin Lamb Professor, Dept. of Applied Mathematics, University of Waterloo

Author's declaration

This thesis consists of material all of which I authored or co-authored: see Statement of Contributions included in the thesis. This is a true copy of the thesis, including any required final revisions, as accepted by my examiners.

I understand that my thesis may be made electronically available to the public.

Statement of Contribution

Chapter 3 is based on a paper entitled "Wall turbulence response to surface cooling and formation of strongly stable stratified boundary layers" published in *Physics of Fluids* [7]. Chapter 4 is based on a paper entitled "Characteristics of quasistationary near-wall turbulence subjected to strong stable stratification in open-channel flows" published in *Physical Review Fluids* [8]. Chapter 5 is based on of a paper entitled "Kinetic energy cascade in stably stratified open-channel flows" which is under review for publication in *Journal of Fluid Mechanics* [9].

These papers present part of the research activities that I have performed in my PhD studies. The published and submitted papers are co-authored with my supervisors, K. Andrea Scott and Michael L. Waite, who played a normal supervisory role in the research and made some editing works on the manuscript text.

Abstract

In this thesis, turbulence dynamics for a stably stratified boundary layer is studied. The processes by which stable boundary layers are formed through strong surface cooling imposed on neutrally stratified wall-bounded turbulence is explored first using high-resolution direct numerical simulation at a moderate Reynolds number. The adjustment of the flow to the imposed strong surface cooling is investigated.

Secondly, characteristics of near-wall turbulence at quasi-stationarity under strong wall cooling are studied. It is shown that if turbulence reaches quasi-stationarity, the characteristics of quasi-stationary near-wall turbulence, even with the strongest wall cooling rate, are generally similar to the weakly stratified case. The effects of strong stable stratification on the characteristics of near-wall turbulence are transient.

It is shown that among mechanisms that contribute to the budget of turbulent kinetic energy, transfer and pressure-work are more dependent on the stratification if turbulence reaches quasi-stationarity. Buoyancy destruction has a considerable effect on the evolution of turbulence producing eddies but not on production itself at stationarity. Relevant length scales are also discussed in detail.

In summary, it is found that the behaviour of near-wall turbulence at quasi-stationarity is approximately similar to weakly stratified cases, regardless of the choice of upper boundary condition.

Finally, the kinetic energy cascade in a stably stratified boundary layer is investigated. A mathematical framework to incorporate vertical scales into the conventional kinetic energy spectrum and its budget is introduced.

It is shown that energetic streamwise scales (λ_x) become larger with increasing vertical scale. For the strongest stratification, for which the turbulence becomes intermittent, the energetic streamwise scales are suppressed, and energy density resides in λ_x of the size of the domain. It is shown that in the unstratified case, vertical scales of the size comparable to the height of the logarithmic layer connect viscous regions to the outer layer. By contrast, in stratified cases, such a connection is not observed.

Acknowledgements

I would like to thank my supervisors, Michael Waite and Andrea Scott, for their constant supports throughout my PhD journey. I would always be deeply grateful to my supervisors for teaching me many lessons, encouraging supervision, patience, and helpful guidance over the last four years.

I would also like to thank my committee members for their insightful comments on this thesis. I am grateful to Dr. Ping He from the University of Michigan, who provided valuable guidance during the code development stage.

I'd like to thank Professor Fazle Hussain from Texas Tech University who taught me alot and I had a chance to meet and attend in his group meetings toward the end of my PhD.

I would like to thank my office mates and friends in the SYDE department, Nazanin Asadi, Keyvan Kasiri , Mohsen Ghanbari, Graham Stonebridge, and Yukun Zhao, Mehdi Shamsi, Saeed Taleghani, Stephon Nicholas Marshal, Anmol Sharan Nagi, and Armina Soleymani. I'd like to thank my MME friends Mehdi Ashrafi Zadeh, Hamid Daryan. I'd like to particularly thank my friend Hamid for being always open to discussions about different aspects of vortex dynamics and turbulence. I'd like to thanks former and current AMATH fluids lab members David Deepwell, Bejamin Storer, and Kwan Lai.

Finally, I would like to thank my family for their love, support, and patience.

Dedication

This thesis is dedicated to my love, best friend, and wife, Delara.

Table of Contents

List of Figures

List of Tables

Chapter 1

Introduction

Turbulence is one of the most challenging areas of fluid dynamics with a vast range of occurrence from astrophysical and geophysical flows to industrial, medical and biomedical applications. Flows in solar flares and the large-scale circulation of the earth's atmosphere are turbulent [28]. On much smaller scales, reactive flow in the combustion chamber of a jet engine, flow behind an airplane wing, and multiphase flow in sea-bed oil and gas pipelines are all turbulent.

Two main approaches are usually considered for analyzing turbulent flows: experiment and numerical simulations. In addition, field observations are another main technique to study atmospheric and oceanic turbulence. Each of these approaches has advantages and disadvantages. Experimental measurements are a reliable technique for studying turbulence, although the experimental setup is expensive and is typically limited to laboratory-scale testing. However, obtaining experimental data is difficult for some situations, for example in flow measurements around turbine blades inside a combustion chamber of a gas turbine engine. On the other hand, numerical simulation of turbulent flows, which is the focus of this thesis, provides an opportunity when there are limited experimental data available or too many tests are needed to choose optimized design parameters. Nonetheless, challenges include careful consideration of the grid resolution and the choice of proper physical model depending on the desired accuracy and available computational resources.

Direct numerical simulation (DNS) is the most accurate numerical approach to tackle turbulence and is aimed at resolving all scales from the largest to smallest eddies in a given flow configuration. Thus, no turbulence parameterization is required for DNS. Of course, DNS requires substantial computational resources increasing approximately in a cubic power of Reynolds number [112]. Large eddy simulation (LES) is an alternative

approach which only resolves the most energetic, large scale eddies and approximate the actions of the small eddies [143, 112]. Turbulence plays a central role in the dynamics of stratified atmospheric boundary layers (ABL), e.g in the dispersion of air pollutant and cloud formation. However, stable stratification, in which heavier air lies under lighter air, significantly affects turbulence and may lead to co-existence of turbulence and internal waves [4], or horizontal intermittency [46]. The mechanism for the interaction of turbulent and other motions in the very stable boundary layer is not yet well understood [94]. The stably stratified regime can occur by radiative cooling of the surface. The regime transition from neutral to stable stratification starts in late afternoon and continues overnight. Because of the complexity of this regime, it is challenging to represent in numerical weather prediction models [125].

The goal of this research is to develop a deeper understanding of turbulence dynamics in a strongly stable ABL. This thesis is organized as follows. The rest of Chapter 1 gives an introduction to the thesis topic including background material. Chapter 2 presents details of numerical methods. Chapter 3 focuses on regime transition from the neutral to strongly stable case. Chapter 4 addresses turbulence characteristics at stationarity. Chapter 5 addresses the kinetic energy cascade in stably stratified boundary layers where effects of horizontal and vertical scales on turbulence dynamics are addressed. Chapter 6 consists of concluding remarks and areas of future work.

1.1 Background

The present section is devoted to an introduction of the background materials that will be used throughout this thesis. In the first subsection, we describe the mathematical framework of stratified flow in the ABL. In the next section, a brief introduction to scales and the energy cascade in turbulent flows is presented. Then, stratified turbulence and wall-bounded turbulence are concisely reviewed. Finally, the turbulence simulation approach is introduced.

1.1.1 Mathematical modelling of stratified turbulence in ABL

It is common practice in the study of the ABL to separate thermodynamic variables into a fluctuating part and a motionless basic state. The motivation is that the decrease of pressure and temperature changes in the lower part of atmosphere is governed mostly through the ideal gas relation for air where pressure and density are in hydrostatic balance

[125, 143]. Assuming a motionless base state, denoted with a subscript zero, we can write the ideal gas law for a dry atmosphere as [143]

$$p_0(z) = \rho_0(z) R_d T_0(z), \tag{1.1}$$

where R_d is the gas constant for dry air. We represent all thermodynamic variables as the sum of the background state variables plus small deviations from hydrostatic background state, denoted with primes, about the background state [143]:

$$\begin{aligned} \rho'(x,y,z,t) &= \rho(x,y,z,t) - \rho_0(z), \\ p'(x,y,z,t) &= p(x,y,z,t) - p_0(z), \\ T'(x,y,z,t) &= T(x,y,z,t) - T_0(z), \end{aligned} \tag{1.2}$$

where p, ρ, T are pressure, density and temperature respectively and $\rho'/\rho_0 \ll 1, p'/p_0 \ll 1, T'/T_0 \ll 1$. Furthermore, temperature and density deviations are related through the linearized ideal gas law relation (motivated by the assumption of low-compressibility effects in the flow) [143]

$$\rho' = -\frac{\rho_0}{T_0} T'. \tag{1.3}$$

In the study of the ABL, normally potential temperature θ is used to evaluate the thermal stability of stratified boundary layer. It is defined as the temperature that a parcel of air at height z would have after it traveled isentropically to the surface and is given by [143]:

$$\theta(x,y,z,t) = T(x,y,z,t) \left(\frac{p_0(0)}{p(x,y,z,t)} \right)^{\frac{R_d}{c_p}}. \tag{1.4}$$

where c_p is the heat capacity at constant pressure. Potential temperature determines whether the atmospheric stratification is stable, neutral, or unstable based on whether $\partial\theta/\partial z$ is positive, zero, or negative, respectively [81]. The linearized relationship between base states and the deviations for temperature and potential temperature is given by

$$\theta_0(z) = T_0(z) \left(\frac{p_0(0)}{p_0(z)} \right)^{\frac{R_d}{c_p}}, \ \theta'(x,y,z,t) = T'(x,y,z,t) \left(\frac{p_0(0)}{p_0(z)} \right)^{\frac{R_d}{c_p}}. \tag{1.5}$$

The general equations governing stratified flows stem from conservation laws of mass, momentum, and energy which are well-known as the continuity, Navier-Stokes, and energy equations. In most cases, environmental flows are considered as low-speed flows in which the velocity of fluid flow is much smaller than the local speed of sound [5] allowing the use of

the Oberbeck-Boussinesq approximation. This approximation is known to be appropriate for stratified water and the shallow ABL and is a simplification of the Navier-Stokes equations for the situations in which the fluid flow is mechanically incompressible but buoyancy effects are important [114]. Essentially this assumption only considers density perturbations due to the temperature variations and neglects the effect of pressure fluctuations, e.g. acoustic waves. The criteria for the validity of Oberbeck-Boussinesq approximation are as follow [122, 132]:

- Velocity scale of the flow is much less than the speed of sound at the considered atmospheric conditions.
- Flow is confined to a layer with a depth much smaller than atmospheric scale height (roughly equal to 10 km).
- Oscillations are low frequency (compared to acoustic frequencies).

The Oberbeck-Boussinesq approximation allows us to remove the effects of sound waves and to utilize the linearized relation between density and temperature deviations by neglecting the effect of pressure dependence in ideal gas relation. Thus, temperature becomes an active scalar such that momentum and energy equations couples only due to gravity and not thermodynamics interconnection between pressure and temperature.

In this thesis a Cartesian frame of reference is used having the z (or x_3) axis aligned vertically upward and the x, y (or x_1, x_2) axes contained in the horizontal plane. The velocity components will be u, v, w (or u_1, u_2, u_3) respectively along x, y, z. Here our focus is to study stratified turbulence in the dry ABL and thus, the Oberbeck-Boussinesq form of the continuity, momentum, and energy equations set reads as [143]:

$$\frac{\partial u_i}{\partial x_i} = 0, \tag{1.6}$$

$$\frac{\partial u_i}{\partial t} + u_j \frac{\partial u_i}{\partial x_j} = -\frac{1}{\rho_0}\frac{\partial p'}{\partial x_i} + \frac{g}{\theta_0}\theta' \delta_{3i} + \nu \frac{\partial^2 u_i}{\partial x_j \partial x_j}, \tag{1.7}$$

$$\frac{\partial \theta}{\partial t} + u_j \frac{\partial \theta}{\partial x_j} = \alpha \frac{\partial^2 \theta}{\partial x_j \partial x_j}, \tag{1.8}$$

where g is the gravitational acceleration, ν is the kinematic viscosity, and the tensors δ_{ij} is Kronecker delta, $\alpha = \kappa/\rho c_p$ is thermal diffusivity, κ is thermal conductivity coefficient, and again c_p is fluid heat capacity at constant pressure. In the above equations the effect of earth's rotation and atmospheric radiation has been neglected. We have considered a

general form of the base state as a function of height so far. However, for a shallow ABL the θ_0 does not vary significantly. Hence, assuming a constant background state is a valid approximation for a shallow ABL [5, 143] which is the focus of this research. Thus, constant background state versus height for density, temperature, and potential temperature is assumed. Equations (1.6-1.8) are nonlinear and have to be solved numerically.

Chaos and Turbulence

Chaos is often known as a nonperiodic and long-term behavior in the deterministic nonlinear dynamical systems with sensitivity to small changes in initial condition [124]. For example Lorenz system [90] which is an idealized model for atmospheric circulation [124] shows chaotic behavior and strong sensitivity to small changes in initial condition. Turbulence is a chaotic state in the flow which shows sensitivity which changes in both initial and boundary conditions. The sensitivity of such dependency upon theses changes depend on non-dimensional parameters and also type of the flow.

1.1.2 Different scales and energy cascade in a turbulent flow

In 1922, L.F. Richardson stated: *"One gets a similar impression when making a drawing of a rising cumulus from a fixed point; the details change before the sketch can be completed. We realize that big whirls have little whirls that feed on their velocity, and little whirls have lesser whirls and so on to viscosity- in the molecular sense"* [116]. This poetic expression describes one of the cornerstones of the theory of turbulence, called the energy cascade. The energy cascade can be understood as follows. The large eddies break up since they are unstable, transferring their energy to slightly smaller eddies through vortex stretching. These smaller eddies experience a similar break-up process and pass down their energy to yet smaller eddies. This cascade of energy, in which energy is transferred to sequentially smaller and smaller eddies, continues until the Reynolds number is small enough for eddy motions to be stable, and molecular viscosity can dissipate the kinetic energy efficiently [112]. An important implication of the energy cascade mechanism is that it dynamically couples all the eddies, from largest to smallest, in a turbulent flow [143]. The largest eddies transfer their energy to the smaller eddies on the time scale similar to their turnover time l/u, where u, l represent the typical velocity and length scale of these largest structures. The average dissipation rate of energy per unit of mass in which energy is passed down the to the slightly smaller scales can be approximated by [28],

$$\epsilon \sim \frac{\text{Kinetic energy per unit mass of the largest eddies}}{\text{Largest eddies turn over time}} \sim \frac{u^2}{l/u} = \frac{u^3}{l}. \tag{1.9}$$

The rate of dissipation of energy at the smallest scales is $\epsilon = 2\nu\langle s_{ij}s_{ij}\rangle$, where s_{ij} is the strain rate [112] and $\langle\rangle$ denotes an ensemble average [10]. Now, let η, u_η, and τ_η be the length, velocity and time scale of the smallest eddies, so,

$$\epsilon \sim \nu\frac{u_\eta^2}{\eta^2}. \tag{1.10}$$

For a statistically steady condition and for homogeneous turbulence the rate of extraction of energy from the largest eddies (or energy-containing eddies) should match exactly the dissipation rate of energy at the smallest scales. Otherwise, an accumulation of energy would be expected in the intermediate scales which is not consistent with the concept of energy cascade [28]. Since the Reynolds number based on velocity and length scales of the small eddies is order unity,

$$\frac{u_\eta\eta}{\nu} \sim 1 \Longrightarrow u_\eta \sim \frac{\nu}{\eta}. \tag{1.11}$$

Using (1.10,1.11) this implies,

$$\eta = (\frac{\nu^3}{\epsilon})^{\frac{1}{4}},\ u_\eta = (\nu\epsilon)^{\frac{1}{4}},\ \tau_\eta = \frac{\eta}{u_\eta} = (\frac{\nu}{\epsilon})^{\frac{1}{2}}. \tag{1.12}$$

These are known as Kolmogorov's length, velocity and time scales of the smallest (or dissipative) eddies. Following the classical theory of homogeneous isotropic turbulence, only large scales are affected by the external agitation or forcing applied on the system boundaries. The process of transferring energy across different scales is accompanied by a loss of the information regarding directionality in energy transfer [10]. For incompressible turbulence, the pressure field increases the tendency of eliminating directional preferences in the energy flux from large to small scales through inter-component transfer of turbulent kinetic energy [143]. Therefore for statistically steady turbulence, it is expected that when moving to smaller scales the turbulence will become increasingly isotropic and independent of large eddies. Hence, for the smallest eddies, turbulence has universal behavior, which is called universal equilibrium. Using Kolmogorov's first similarity hypothesis [78], for locally isotropic turbulence at sufficiently high Reynolds number, the statistical characteristics of the small-scale eddies obeys a universal form that is uniquely determined by ν and ϵ. Thus, as shown in (1.12) Kolmogorov's scales represent the smallest scales in statistically stationary turbulence at high Reynolds number, independent of flow field configuration, initial and boundary conditions.

The energy cascade process can be explained using the kinetic energy spectrum $E(k)$ where k is the magnitude of the wavenumber vector. A schematic of the kinetic energy

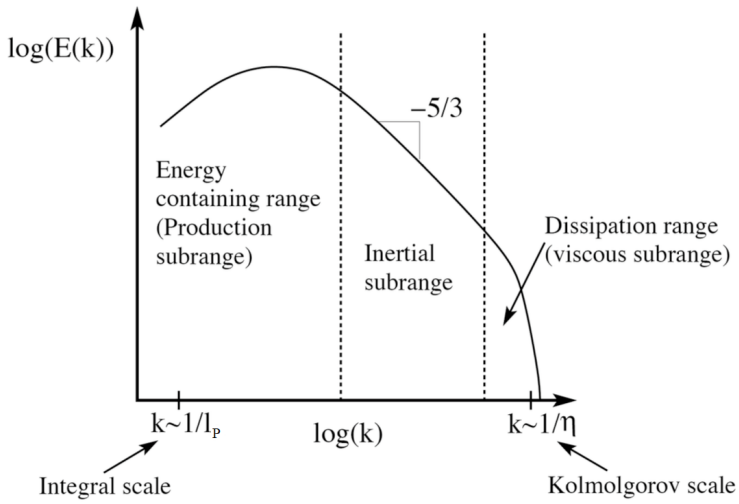

Figure 1.1: Schematic of the kinetic energy spectrum mentioning different subranges in the energy cascade process in isotropic turbulence

spectrum is illustrated in figure 1.1. The spectrum for the full range of wavenumbers consists of at least three regions also known as subranges; the energy containing range in which energy is extracted from large scales, the inertial subrange in which energy is transfer from larger to smaller scales, and the dissipation range in which energy is dissipated to heat by the smallest scales. Following a dimensional analysis, the energy spectrum in the inertial subrange can be estimated as follows [143]:

$$E(k) \sim \epsilon^{2/3} k^{-5/3}. \tag{1.13}$$

However, as it will be briefly discussed in the next section, stratification may affect this spectrum at scales larger than Ozmidov scales.

1.1.3 Stratified turbulence

In this section, the effect of stable stratification on turbulence is briefly reviewed. Our review in this section only homogeneous turbulence subjected to stable stratification is considered.

Scales and dimensionless groups

In a stratified flow, the buoyancy frequency or Brunt-Väisällä frequency, N, defined via [26]

$$N^2 = \frac{g}{\theta_0}\frac{\partial \theta}{\partial z}, \tag{1.14}$$

measures the period of small oscillation of vertical displacements. The displaced fluid particle will accelerate back toward or accelerate away from its origin depending on the sign of N^2. If $N^2 > 0$, the fluid particle pulls back to the origin and becomes dynamically stable. If $N^2 < 0$, the displaced fluid particle moves away from the origin and thus becomes unstable. If $N^2 = 0$ fluid particle remains neutral with respect to any displacement [81]. The dimensionless Froude number is defined as:

$$Fr = \frac{u_r}{N\ l_r}, \tag{1.15}$$

where u_r and l_r are reference velocity and length scale, respectively. Fr represents the ratio of inertial forces to buoyancy forces, with small Fr corresponding to strong stratification. In other words, the Froude number represents the ratio of buoyancy time scale $1/N$ to the typical eddy turnover time l_r/u_r.

In stratified turbulence, it is also possible to define a vertical or horizontal Froude number based on whether a vertical or horizontal length scales is used in the definition of Froude number. The vertical Froude number is defined as $Fr_v = u_r/Nl_z$ where l_z denotes a vertical length scale, and the horizontal Froude number is $Fr_h = u_r/Nl_h$ where l_h denotes a horizontal length scale, based on the intrinsic length scales of the flow in the vertical and horizontal directions [85].

From (1.9) we know that the characteristic length scale of the problem is the integral scale $l_r = u_r^3/\epsilon$. It is common to define a characteristic length scale for stratification as l_O which is obtained by defining a turbulent velocity $(\epsilon L_O)^{1/3}$ such that the associated Froude number $(\epsilon L_O)^{1/3}/Nl_O = 1$. This relation yields [85],

$$l_O = \left(\frac{\epsilon}{N^3}\right)^{\frac{1}{2}}. \tag{1.16}$$

This scale is known as Ozmidov scale [93, 118], and corresponds to a balance between inertial and buoyant effects. Using (1.9) and (1.15-1.16) one obtains the relation

$$Fr = \left(\frac{l_O}{l_r}\right)^{2/3}, \tag{1.17}$$

which shows that stratification has a negligible effect on turbulence if $l_r \ll l_O$, and becomes dynamically important when the size of the eddies are of the order of or larger than the Ozmidov scale. At low Froude number where $l_r \gg l_O$, stratification effects becomes dominant since as scales become larger than l_O, the local Froude number decreases, and the effects of buoyancy increase [118]. It can be be further expected that stable stratification will limit the amplitude of vertical fluctuations of fluid particles approximately at a scale around the Ozimodov scale [85].

The primary interest of this thesis is in strongly stable stratified turbulence in which the buoyancy force is as strong as inertia ($Fr \lesssim O(1)$). In the real ABL we also assume that $Re \gg 1$ providing wide scale separation, so that there is a wide range of scales. Thus, according to discussion above, the buoyancy force becomes relatively weaker as we move from large to small scales, so at scales around l_O there is a transition from strongly stratified turbulence to more isotropic turbulence, in which the buoyancy force is relatively weak. This mechanism of the transition is still poorly understood [75]. So typically we have two sets of dynamics coexisting in such flows in the absence of inhomogeneity: the large scales are strongly stratified while the small scales are more like conventional Kolmogorov turbulence [75, 26].

There are two other dimensionless numbers that are widely used in stratified turbulence, the buoyancy Reynolds number (Re_b) and Richardson number (Ri). The buoyancy Reynolds number is defined as follow [26]

$$Re_b = \frac{\epsilon}{\nu N^2} \sim \frac{u_r^3/l_h}{\nu N^2} \sim \frac{u_r l_h}{\nu} \frac{u_r^2}{N^2 l_h^2} = Re\ Fr_h^2, \tag{1.18}$$

where $Re = u_r l_h/\nu$ denotes Reynolds number. In (1.18) the dissipation is assumed to be proportional to kinetic energy flux such that $\epsilon \sim u_r^3/l_h$ (Taylor's hypothesis). Using horizontal components of the vorticity equation in a stratified fluid, the viscous and vortex stretching terms can be related as [26]

$$\frac{\omega_j \partial_j u_h}{\nu \partial_{jj} \omega_h} \sim \frac{\omega_z \partial_z u_h}{\nu \partial_{zz} \omega_h} \sim \frac{\frac{u_r}{l_h}\frac{u_r}{l_z}}{\nu \frac{\frac{u_r}{l_z}}{l_z^2}} \sim \frac{u_r l_h}{\nu} \cdot \frac{l_z^2}{l_h^2}, \tag{1.19}$$

where ω_h and u_h refer to horizontal components of vorticity and velocity, respectively. The ∂_j refers to derivative with respect to x_j. Since, the frequency of vertical motions for a stratified fluid is proportional to N, a typical vertical scales can be obtained as $l_z \sim u_r/N$ [141]. In other words, the vertical Froude number is $Fr_v = u_r/N l_z \sim 1$. Thus the horizontal Froude number for a stratified flow can be rewritten based on ratio of vertical to

horizontal scales as $Fr_h = l_z/l_h$ [26]. Therefore Re_b in stratified flow refers to the ratio of the vortex stretching mechanism and vortex diffusion mechanism (damping by viscosity) in the horizontal planes. In stably stratified turbulence, $Re_b \gg 1$ results in the dominance of vortex stretching and survival of turbulence as a result of sustained energy injection into different scales by vortex stretching. In strongly stable stratified flow, we expect the vertical motion to be suppressed and $Fr_h \ll 1$ [75, 26].

1.1.4 Wall-bounded turbulent flows

ABL turbulence can be studied in the more general framework of wall-bounded turbulent flows. Understanding the physical mechanisms in those type of flows would help us to better conceive of how turbulence in the real ABL behaves. Wall-bounded turbulence is a turbulent flow that is formed next to a boundary, at which the velocity must be equal to the velocity of the boundary.

In the following subsections, we provide a brief introduction of the energy cascade mechanism, scaling, and flow structures in typical wall-bounded turbulence such as pipe, channel flow or spatially developing boundary layer (e.g., zero pressure gradient flat plate boundary layer). For now, we do not include the impact of stratification. Stratified wall-bounded flows have been the subject of far fewer studies.

Scaling laws in boundary layers

In a boundary layer, because of the presence of a surface and no-slip boundary condition, there is a layer near the wall in which viscosity is important, and the typical length scale is ν/u_τ, where u_τ is friction velocity which is defined as,

$$\tau_w = \rho_0 u_\tau^2 = \mu \frac{\partial \overline{u}}{\partial z}\Big|_w, \tag{1.20}$$

where $\mu = \rho_0 \nu$, μ is the dynamic viscosity and $\overline{u}$ is horizontal mean velocity profile. The subscript w refers to the location of wall in the vertical direction (e.g. at $z = 0$). Hence, we have two distinct regions based on distance from the wall: the inner region in which viscosity is important, the outer region where the effect of viscosity is insignificant, and a overlap region connecting the inner and outer region. In this study we consider the overlap region as part of a larger inner region. The inner region is relatively thin and, when $z \gg \nu/u_\tau$, viscous effects can be neglected and the typical length scale δ is of the size of boundary layer thickness or channel half height [59, 25]. Two dimensionless scaling

quantities, which are called wall units and are frequently used in wall-bounded flows, are defined as [59, 25]:

$$z^+ = \frac{z u_\tau}{\nu}, \quad u^+ = \frac{\overline{u}}{u_\tau}. \tag{1.21}$$

With these parameters, one can obtain universal profiles for mean velocity at a certain distance from the wall [59]. Typically, the inner and outer regions are divided into four layers [25, 112],

- viscous sublayer: $z^+ < 5$; $u^+ = z^+$
- buffer layer: $5 < z^+ < 30$; $u^+ = f_1(z^+)$
- logarithmic layer: $30 < z^+ < 0.15 Re_\tau$; $u^+ = \kappa^{-1} \ln z^+ + A$
- outer layer: $z^+ > 0.15 Re_\tau$; $(U_\infty - \overline{u})^+ = f_2(z/\delta)$

where U_∞ is the free stream velocity. In the viscous sublayer, the streamwise velocity profile exhibits linear variation with respect to z [112]. The first three layers forms the inner layer. The amount of turbulent production of turbulent kinetic energy is given by $P = \tau_{ij} \partial \overline{u}_i / \partial x_j$ with $\overline{u}_i$ as the mean velocity in ith direction and τ_{ij} is the component of the Reynolds stress (or turbulent shear stress) perpendicular to the i direction and parallel to j direction [112]. The buffer region is the viscous dominated region with the peak production of turbulence and also the peak streamwise turbulence intensity [25]. The logarithmic layer (overlap layer) is the common part of the inner and outer regions, and the outer layer is the outer most part of the boundary layer where viscosity has an insignificant role for the mean and turbulent quantities over which δ is the length scale of the eddies in that region [25].

Energy distribution

As discussed above, the velocity profile in wall-bounded turbulence is inhomogeneous as it varies between different layers based on distance from the wall. As opposed to homogeneous isotropic turbulence, in fully developed wall-turbulence in a channel flow with height of $2h$ or boundary layer of thickness δ, the size, shape, and orientation of eddies are dependant on location of eddies with respect to wall. The outer region (which is the core of the boundary layer) can be considered similar to homogeneous turbulence, with a cascade analogous to Kolmogorov cascade (see section 1.1.2) [68]. As we approach the wall, the size of large scales will be affected more and more by the presence of the wall so that they can fit in the

space available between their height and the wall [68]. In between the core region and the wall, there is an overlap region (logarithmic layer), where $z^+ \gg 1$ but $z/h \ll 1$ which may include some of the large scales. However, the wall put bounds on the size of largest scales (of size h) in this region and exclude these largest scales [68]. In this region turbulent shear stress is proportional to $\tau_{13} \approx u_\tau^2$ and the production of turbulent kinetic energy is approximately in equilibrium with local dissipation given by the Kolmogorov argument as $u_\tau^3/\kappa z$ such that [134, 112],

$$P = u_\tau^2 \frac{\partial \overline{u}}{\partial z} = \frac{u_\tau^3}{\kappa z}, \quad \Rightarrow u^+ = \frac{1}{\kappa} \ln z^+ + A, \tag{1.22}$$

where $\kappa \approx 0.4$ is the universal von Kármán constant. The integration constant A depends on the flow details near the wall and is not directly determined by the overlap region. Its value based on experiments for smooth walls is $A \approx 5.2$ [68].

In channel flow turbulence the energy generated in the viscous region near the wall at dissipative scales is transported across the logarithmic layer and to the large scale eddies in the outer region. This energy is dissipated in the outer region by the locally isotropic energy cascade [67, 68]. The energy-containing scales are small near the wall (as they are affected by viscosity) whereas energy-containing scales at outer region are large. Thus, in channel flow turbulence there is an inverse spatial cascade [67, 68] from small eddies near the wall to large eddies in the outer region.

The wall-distance dependence of energy containing eddies in the logarithmic layer implies that spectral density per unit streamwise wavenumber k_x of the energy-containing eddies for streamwise velocity should be proportional to [111]

$$E_{uu}(k_x) \sim u_\tau^2 \;\; k_x^{-1}, \tag{1.23}$$

where $\langle u_1' u_1' \rangle = \int_0^\infty E_{uu}(k_x)\, dk_x$. The spectrum is steepened to $-5/3$ slope from large to smaller scales (the Kolmogorov spectrum) for the inertial eddies in logarithmic region which is indeed confirmed by the spectrum from experimental data for the boundary layers [111, 104].

1.2 Direct numerical simulation

In direct numerical simulation, all scales from the largest to smallest eddies are resolved. The range of scales that needs to be resolved in a DNS can be estimated by considering

the ratio of the Kolmogorov scale and the size of the largest eddies, l:

$$\frac{\eta}{l} = \nu^{3/4}\epsilon^{-1/4}l^{-1} = Re^{-3/4}\frac{l\epsilon}{u_r^3}, \tag{1.24}$$

where $Re = u_r l/\nu$ with u_r as the velocity scale associated with the largest scale (of the size l) motions. In wall-bounded turbulence smallest scales are also dependant upon wall-normal distance. The last term is the dissipation normalized by the velocity and length scales of the largest eddies in the flow. The $l\epsilon/u_r^3$ term is independent of Reynolds number since dissipation is viscosity independent based on Kolmogorov's second similarity hypothesis [78, 10]. Thus, the number of grid points to be resolved in each direction in a DNS will scale with $N \approx l/\eta \sim O(Re^{3/4})$ leading to $N^3 \approx O(Re^{9/4})$ for three-dimensional simulation [112]. Therefore, increasing Reynolds number by a factor of 2 will approximately increase the required number of grid points for a DNS by a factor of 5. In addition, the time step decreases with the grid spacing which implies an extra limitation for a DNS. The total number of time steps is proportional to $M \approx O(Re^{3/4})$ [112]. Therefore, the total computational costs would be in order of $O(N^3M \approx Re^{9/4}Re^{3/4} = Re^3)$. This expense significantly constrains the use of DNS for practical problems since DNS can be done only at relatively small Reynolds numbers. The Reynolds number for typical engineering applications is on the order of $10^5 - 10^6$ and for typical geophysical application such as ABL is on the order of $10^8 - 10^9$ or even higher. These constraints makes DNS an impractical approach to tackle turbulence for real-world or laboratory scales applications and so it is considered mostly as a research tool [101].

As stated above, DNS is a powerful tool to study turbulence with high accuracy, but it is substantially expensive in terms of computations. However, increasing computing power in recent decades has motivated the use of DNS to investigate complex turbulent flows such as channel flow turbulence at Reynolds number close to wind tunnel experiments [84].

1.3 Motivation

Stable boundary layers (SBLs) have many environmental and industrial applications. Oceanic and nocturnal atmospheric boundary layers, and flow over sea ice are only a few examples of environmental flows that are often stably stratified. From the perspective of industrial applications, power output of a large wind farm is remarkably decreased in stable ABLs [1] and therefore such flow regimes are a key factor in designing individual wind turbines as well as in designing layout of wind farms [39, 127]. However, SBLs and turbulence in SBLs in particular, involves many challenging complexities such as turbulence collapse [46, 36, 7],

spatio-temporal intermittencies, turbulence recovery [7], and gravity wave breaking [94], which are far from being understood [106, 94]. Thus, our understanding of SBLs needs to be improved to improve our predictions from such flows. Unraveling turbulence dynamics in SBLs especially under strongly stable stratification regime is the main motivation for the current thesis. Improving our understanding of turbulence dynamics in a strongly stable boundary layer is a necessity to improve available turbulence models which are known to poorly perform in such a flow regime [94] and thus improving our prediction capabilities of flow behaviour at such stratification regime.

1.4 Objectives

This thesis aims to address the following research questions.

1.4.1 SBL formation from a neutral boundary layer

The first step in this investigation is to identify processes in which a SBL is formed from a neutrally stratified boundary layer and how turbulence is affected by such processes. In this step we aim to address following questions:

- How does a neutral boundary layer evolve into a SBL in the presence of surface cooling? In particular, how does wall turbulence respond to strong surface cooling?

1.4.2 Near-wall turbulence in a SBL

The purpose of this topic is to address the following question:

- What is the effect of thermal stratification on stationary turbulence dynamics including statistics, length scales, etc., particularly in the near-wall region where most turbulence production happens?

1.4.3 Turbulent kinetic energy cascade in a SBL

The inhomogeneity generated by the presence of the wall in boundary layer turbulence causes complexity in analysing kinetic energy cascade, which are mostly investigated based

on analysis of the spectra of velocity field in horizontal planes. Thus the effects of vertical scales on kinetic energy cascade in SBLs are still unknown. Since horizontal spectra are computed based on Fourier series for the velocity field, which relies on periodic boundary condition, an alternative approach is required to examine scale dependence of kinetic energy dynamics that includes the wall-normal direction. To analyze the effect of vertical scales one need to develop a mathematical framework to incorporate vertical scales in the kinetic energy spectra. Using the framework developed, the following questions were then addressed:

- What are the mechanisms that are involved in the kinetic energy cascade for SBLs?
- What is the scale dependence of such mechanisms?

The governing equations, numerical methods and methodology will be described in the next chapter followed by in-depth analysis of the above questions and concluding remarks.

Chapter 2

Methodology

2.1 Problem formulation

In this section, we describe the case study, present the governing equations, boundary conditions, and non-dimensionalized parameters, and outline the different layers of the stratified boundary layer.

2.1.1 Test case description

The motivation for the present work is to study turbulence in the near-ground (a first few hundred meters above the Earth's surface which is known as the surface layer) of a stably stratified dry ABL. To do so, an open channel flow configuration is considered, with an imposed cooling flux at the lower boundary and an adiabatic upper boundary. The geometry of the open channel is shown in Fig. 2.1. A uniform pressure gradient drives flow in the x direction, periodic boundary conditions are applied in both horizontal directions, while no-slip and no-stress surfaces are applied to the bottom and top boundaries, respectively. The y axis is the spanwise direction and the z axis is normal to the wall. The velocities in the x, y, and z directions are denoted by u, v, and w, and we let $(x_1, x_2, x_3) = (x, y, z)$ and $(u_1, u_2, u_3) = (u, v, w)$. The domain size in the x and y directions is L_x and L_y, respectively and the channel depth is h. The potential temperature field is denoted by θ and is defined as the fluctuation from background θ_0. We will drop the "potential" and simply call θ as temperature hereinafter. For simplicity, the free surface is assumed to be undeformed, an approximation applicable for low Froude number [80, 79, 83, 73] which is a common approach in studies of the idealized ABL [106, 46, 30].

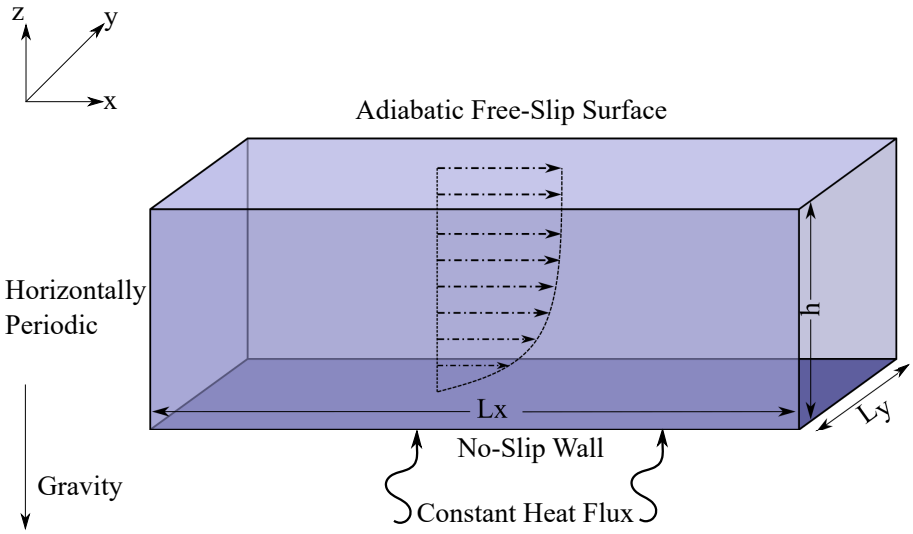

Figure 2.1: Stratified open channel configuration.

2.1.2 Governing equations and dimensionless parameters

The governing equations for this work are the Navier-Stokes equations under Oberbeck-Bousinesq approximation (OBA). The OBA equations can be normalized using the channel height h, a reference velocity u_0, and the value of the imposed bottom-surface temperature gradient F. With these choices, the dimensionless OBA equations can be written as [130, 58]

$$\frac{\partial u_i}{\partial x_i} = 0, \tag{2.1}$$

$$\frac{\partial u_i}{\partial t} + u_j \frac{\partial u_i}{\partial x_j} = -\frac{\partial p}{\partial x_i} + \frac{1}{Re}\frac{\partial^2 u_i}{\partial x_j \partial x_j} + Ri\ \theta\ \delta_{i3} + \delta_{i1}, \tag{2.2}$$

$$\frac{\partial \theta}{\partial t} + u_j \frac{\partial \theta}{\partial x_j} = \frac{1}{PrRe}\frac{\partial^2 \theta}{\partial x_j \partial x_j}, \tag{2.3}$$

where Re, Ri, and Pr are reference Reynolds, Richardson and Prandtl numbers. Here we assume constant background (reference) temperature θ_0 in hydrostatic balance with background pressure. The variable p is the pressure fluctuation from the background pressure and θ is the temperature fluctuation from θ_0. Density and temperature are related

through the linearized equation of state for an ideal gas (1.3). Wall scale non-dimensional parameters are defined as

$$Re_\tau = \frac{u_\tau h}{\nu}, \quad Ri_\tau = \frac{g}{\theta_0} F \frac{h^2}{u_\tau^2}, \tag{2.4}$$

where friction velocity $u_\tau = (\tau_w/\rho_0)^{\frac{1}{2}}$, ρ_0 is the reference density, and g is the gravitational acceleration. Here τ_w is the surface shear stress. The imposed uniform horizontal pressure gradient drives flow in the x direction and forces the mean flow to balance the mean wall shear stress (averaged over the horizontal plane) and maintain the flow from deceleration in the streamwise direction. Thus, the time dependant values of Ri_τ and Re_τ will converge to their corresponding reference values Ri and Re as the flow approaches stationarity.

The bulk Richardson and Reynolds numbers are defined by

$$Re_b = \frac{U_b h}{\nu}, \quad Ri_b = \frac{g}{\theta_0} F \frac{h^2}{U_b^2}, \tag{2.5}$$

where $U_b = \frac{1}{h}\int \overline{u}\, dz$ is the bulk velocity, and $\overline{(\ )}$ denotes averaging over horizontal planes at each z. Note that because the vertical gradient of temperature is specified at the lower surface, Ri_τ is the parameter that determines the cooling rate, and therefore the stratification regime. Bulk and friction Richardson number are related through $Ri_b = Ri_\tau u_\tau^2/U_b^2$.

The boundary conditions are:

$$z = 0: \qquad u = v = w = 0, \qquad \frac{\partial \theta}{\partial z} = 1, \tag{2.6}$$

$$z = h: \qquad \frac{\partial u}{\partial z} = \frac{\partial v}{\partial z} = w = \frac{\partial \theta}{\partial z} = 0. \tag{2.7}$$

The temperature boundary condition at the bottom boundary is Neumann with $\partial\theta/\partial z = 1$ to impose surface cooling and stable stratification as stated in (2.6) throughout this thesis. Two types of boundary conditions are considered for the temperature of the upper boundary: Neumann ($\partial\theta/\partial z = 0$) for the main simulations, where the upper boundary is adiabatic, and Dirichlet ($\theta = 0$) for additional cases that include heat entrainment at the upper boundary.

This choice of no heat flux at the upper boundary excludes heat diffusion, which represents entrainment from the free atmosphere and provides a framework to focus on the

effect of surface cooling alone on wall generated turbulence. Although this choice leads to a constant rate of change in mean temperature [130], it will be shown that the mean velocity, mean temperature gradient, and fluctuating quantities reach equilibrium after sufficient time.

Superscript $^+$ denotes non-dimensionalization by near wall scaling parameters (u_τ^0, ν) (e.g. $z^+ = zu_\tau^0/\nu$) and superscript ^{o} represents non-dimensionalization by outer layer scaling parameters (u_τ^0, h) (e.g. $t^o = tu_\tau^0/h$) where the u_τ^0 refers to the initial value of the friction velocity (i.e. friction velocity of neutral case).

2.2 Numerical approach

The numerical model used for this study is Hercules, which is a scalable open-source DNS solver that solves the OBA equations for a channel flow configuration [58]. Minor modifications to include different types of surface temperature boundary conditions have been implemented in the code. Hercules has been validated for a wide range of Reynolds and Richardson numbers in a previous study [58] for unstratified channel flow at $Re_\tau = 180,\ 395,\ 590$ and for a stratified channel flow at $Re_\tau = 180$ for Richardson numbers $Ri_\tau = 0,\ 18,\ 120,\ 480$. However, we also perform an additional verification of the flow solver for a case with $Re_\tau = 180$ and $Ri_\tau = 0$ as will be discussed later.

Details of the numerical approach will be presented shortly. In summary, the governing equations are discretized using the Fourier spectral method in the horizontal plane with periodic boundary conditions and a second-order central finite difference scheme in the vertical direction [51]. In horizontal directions we employ a uniform mesh, co-located variables and use the Fourier transform to calculate derivatives [129]. The two-thirds de-aliasing technique has been used to prevent aliasing error from energy transfer to unresolved wavenumbers [18]. In the wall-normal direction, the non-linear terms are treated in skew-symmetric form to reduce the amplitude of aliasing errors [13] for derivatives in the vertical direction. The mesh is Cartesian and non-uniform in the vertical direction. A vertically staggered grid is employed, in which the vertical velocity is located at cell faces and the horizontal velocity, pressure, and scalars are defined at cell centers. The staggering is done to remedy the problem of pressure-velocity decoupling and checkerboard oscillation of pressure [45]. Linear interpolation is used to map variables between the half-grid and full-grid (Fig. 2.3) point [51, 58]. Hyperbolic tangent stretching is used in the z-direction to condense grid points near the solid boundaries to resolve the near-wall

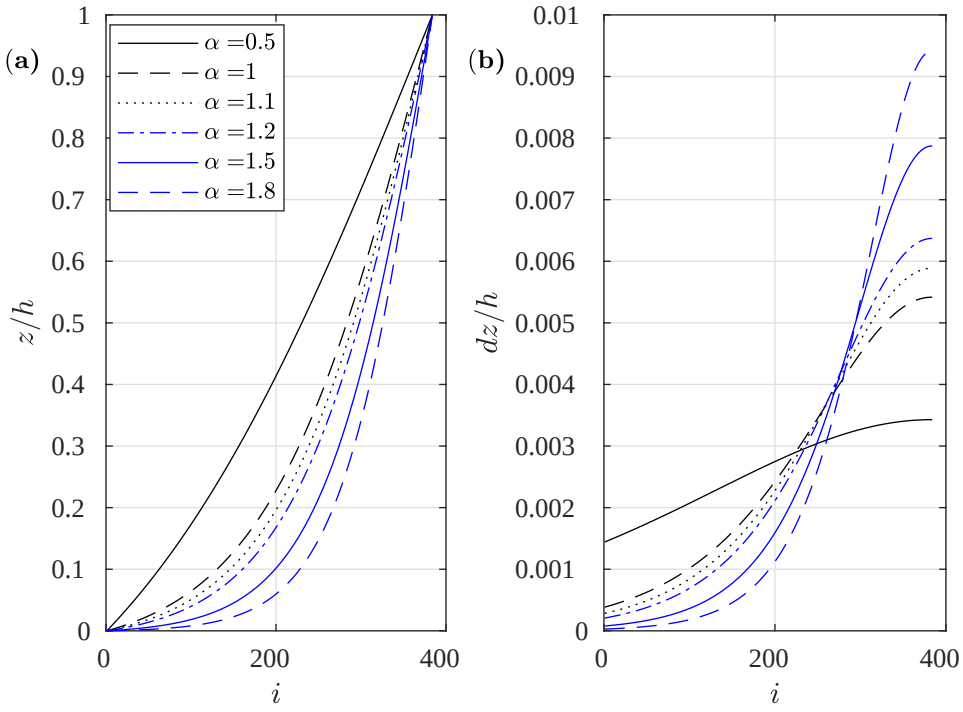

Figure 2.2: The profiles of (a) $z(i)$ and (b) $dz(i) = z(i+1) - z(i)$ for $N_z = 384$ and various values for α in (2.8) where i is refers to node number in the wall-normal direction.

small-scale structures, with level i at [51, 58]:

$$z_i = h - \frac{h}{\tanh(2\alpha)} \tanh\left(\frac{2\alpha}{1-N_z}(i-N_z)\right), \tag{2.8}$$

where $\alpha = 1.1$ is a parameter to control the stretching and N_z is the number of grid points in the vertical direction. The profiles of $z(i)$ and $dz(i) = z(i+1) - z(i)$ for $N_z = 384$ are shown in the Fig. 2.2 where i is the index referring to node number in the wall-normal direction. As it can be seen increasing α results in decrease in grid-spacing at the wall ($dz(1)$) and increase in grid-spacing near the channel top ($dz(nz)$).

2.2.1 Spatial discritization scheme

The Fourier series representation of a variable f is [51, 100]:

$$f(x,y,z,t) = \sum_{n_x=-\frac{N_x}{2}+1}^{N_x/2} \sum_{n_y=-\frac{N_y}{2}+1}^{N_y/2} \widehat{f}(k_x,k_y,z,t) e^{i(k_x x + k_y y)}, \tag{2.9}$$

where $k_x = 2\pi n_x/L_x$ and $k_y = 2\pi n_y/L_y$ are the wave numbers in the x- and y-directions respectively. The total numbers of grid points in the horizontal directions are denoted by N_x and N_y, respectively. The $\widehat{f}$ is the discrete Fourier transform (DFT) of f and derived as follows [100]:

$$\widehat{f}(k_x,k_y,z,t) = \frac{1}{N_x N_y} \sum_{m=1}^{N_x} \sum_{n=1}^{N_y} f(x,y,z,t) e^{-i(k_x x_m + k_y y_n)}, \tag{2.10}$$

where $x_m = (m-1)L_x/N_x$ and $y_n = (n-1)L_y/N_y$. To obtain discrete Fourier transforms the open-source FFTW software library (see www.fftw.org) are used which is one of the fastest discrete Fourier transform algorithms [49].

For the purpose of presenting how derivatives are numerically calculated using DFT we consider a 1D variable f. The Fourier transform of a discrete function f_j that is defined on the discrete points $j = 1 \dots N$ will be denoted by $\widehat{f}_k$ where the associated wavenumber are $k = -\frac{N}{2} + 1 \dots 0, \dots \frac{N}{2}$ for the case when total number of points (N) is even. Therefore, $\widehat{df/dx} = ik\widehat{f}_k$ and spatial derivative can be easily found by transforming $\widehat{df/dx}$ back to physical space. If f is real $\widehat{f}_k = \widehat{f}^*_{-k}$ where * denotes the complex conjugate. At the Nyquist wavenumber, $k = N/2$, the transformed function $\widehat{f}_{N/2}$ is real for a real function and when considering an odd derivatives of real functions the discrete Fourier transform cannot generate a real function back and thus the coefficient $\widehat{f}_{N/2}$ are set to zero [12]. Therefore, we only need to store $0, \dots, \frac{N}{2} - 1$.

Generally speaking and by neglecting inverse cascade, the nonlinear term in the governing equations transfers energy from low to high wavenumbers. Thus interaction of relatively large wavenumber modes through the nonlinear term may produce energy in wavenumbers larger than the Nyquist wavenumber [129, 12]. As it will be discussed shortly, such unresolved high wavenumber energy can project onto small wavenumber modes leading to an error known as the aliasing error that is often removed to avoid nonlinear instability [42]. This error is the result of the fact that the k Fourier mode and the $k + rN$ mode are equivalent where r is a positive or negative integer [129, 12]. Therefore, it is possible for

high wavenumbers (larger than Nyquist wavenumber) to inject energy to low wavenumber modes that is not physical and causes error in the numerical solution [129, 12]. The non-linear advection terms result in the convolution sum when using DFT. For example for a 1D variable f the DFT of nonlinear term f^2 can be written as,

$$\widehat{ff}(k) = \frac{1}{N}\sum_{m+n=k}\widehat{f}_m\widehat{f}_n = \frac{1}{N}\sum_{\substack{-\frac{N}{2}+1\leq m\leq\frac{N}{2},\\ -\frac{N}{2}+1\leq k-m\leq\frac{N}{2}}}\widehat{f}_m\widehat{f}_{k-m} + \frac{1}{N}\sum_{\substack{-\frac{N}{2}+1\leq m\leq\frac{N}{2},\\ k-m>\frac{N}{2}\text{ or }k-m<-\frac{N}{2}+1}}\widehat{f}_m\widehat{f}_{k-m}, \tag{2.11}$$

where in the second term, the Fourier mode with unresolved wave number $k-m > N/2$ for $k, m \in [-N/2+1, N/2]$ is aliased to the Fourier mode with wave number $k-m-N$. Similarly, the Fourier mode with unresolved wave number $k-m < -N/2+1$ is aliased to the Fourier mode with wave number $k-m+N$. Thus the aliased wavenumbers are $k-m\pm N$. The truncating modes with wavenumber larger than M (or zero padding) [18] is a convenient method for de-aliasing where $\widehat{f}_k = 0$ ($\forall\ |k| > M$) and M is to be found in order to vanish the second term in (2.11). If $|k-m\pm N| > M$, then $\widehat{f}_{k-m} = 0$ for these aliased wavenumbers and the second term in (2.11) vanishes. Since, the wavenumbers larger than M are truncated and $\widehat{f}_m = 0$ ($\forall\ |k| > M$) the second term automatically cancels for such m values and we only consider $m = \pm M$ as it's extremums. Now, by using $k = M$ and $m = -M$ the M is found such that $k-m-N \notin (-M, M)$ leading to $M+M-N \leq -M$ and $M \leq N/3$. Similarly, by using $k = -M$ and $m = M$ the M is found using $k-m+N$ modes such that $k-m+N \notin (-M, M)$ leading to $-M-M+N \geq M$ and $M \leq N/3$. Therefore $M = N/3$ is the maximum values that M can have to cancel aliasing error arising from a quadratic nonlinearity. Thus, by truncating 2/3 of the wavenumbers and keeping the 1/3 of wavenumbers the the second term in (2.11) is canceled out. This technique for dealiasing is often known is 2/3-rule. For de-aliasing, the 2/3-rule is used in this research [18]. In Hercules, all Fourier modes with wavenumbers k where $k > N/3$ are truncated [129].

In the wall normal direction a second order, finite-difference scheme is used and the non-linear terms are treated in skew-symmetric form to reduced amplitude of the aliasing errors [13] such as;

$$\frac{\partial(\varphi w)}{\partial z} = \frac{1}{2}\left(w\frac{\partial\varphi}{\partial z} + \varphi\frac{\partial w}{\partial z} + \frac{\partial(\varphi w)}{\partial z}\right), \tag{2.12}$$

where φ is an arbitrary flow variable such as u_i or θ.

For the vertical derivatives, the second-order central difference scheme is used, for example [58]:

$$\frac{\partial u_{(i,j,k)}}{\partial z} \approx \frac{u_{(i,j,k+\frac{1}{2})} - u_{(i,j,k-\frac{1}{2})}}{\Delta z(k)}, \tag{2.13}$$

$$\begin{aligned} \frac{\partial^2 u_{(i,j,k)}}{\partial z^2} = \frac{\partial}{\partial z}\left(\frac{\partial u_{(i,j,k)}}{\partial z}\right) &\approx \frac{\dfrac{\partial u_{(i,j,k+\frac{1}{2})}}{\partial z} - \dfrac{\partial u_{(i,j,k-\frac{1}{2})}}{\partial z}}{\Delta z(k)} \\ &= \frac{\dfrac{u_{(i,j,k+1)} - u_{(i,j,k)}}{\Delta z_t(k)} - \dfrac{u_{(i,j,k)} - u_{(i,j,k-1)}}{\Delta z_b(k)}}{\Delta z(k)}, \end{aligned} \tag{2.14}$$

where

$$\begin{aligned} \Delta z_t(k) &= \frac{\Delta z(k) + \Delta z(k+1)}{2}, \\ \Delta z_b(k) &= \frac{\Delta z(k) + \Delta z(k-1)}{2}. \end{aligned} \tag{2.15}$$

The velocity $u_{(i,j,k+\frac{1}{2})}$ and $u_{(i,j,k-\frac{1}{2})}$ can be obtained by linear interpolation in the z direction as

$$\begin{aligned} u_{(i,j,k+\frac{1}{2})} &= \frac{u_{(i,j,k+1)}\Delta z(k)}{\Delta z(k) + \Delta z(k+1)} + \frac{u_{(i,j,k)}\Delta z(k+1)}{\Delta z(k) + \Delta z(k+1)} \\ &= u_{(i,j,k+1)} l_t(k) + u_{(i,j,k)}(1 - l_t(k)), \end{aligned} \tag{2.16}$$

where

$$l_t(k) = \frac{\Delta z(k)}{\Delta z(k) + \Delta z(k+1)}. \tag{2.17}$$

The $\Delta z(k)$ and $\Delta z(k+1)$ are linear weights to interpolate $u_{(i,j,k)}$ and $u_{(i,j,k+1)}$ onto $u_{(i,j,k+\frac{1}{2})}$. For example if $\Delta z(k) \ll \Delta z(k+1)$, then $u_{(i,j,k+\frac{1}{2})} = u_{(i,j,k)}$, using (2.16). If $\Delta z(k+1) \ll \Delta z(k)$, then $u_{(i,j,k+\frac{1}{2})} = u_{(i,j,k+1)}$. Similarly

$$\begin{aligned} u_{(i,j,k-\frac{1}{2})} &= \frac{u_{(i,j,k-1)}\Delta z(k)}{\Delta z(k) + \Delta z(k+1)} + \frac{u_{(i,j,k)}\Delta z(k-1)}{\Delta z(k) + \Delta z(k+1)} \\ &= u_{(i,j,k-1)} l_b(k) + u_{(i,j,k)}(1 - l_b(k)), \end{aligned} \tag{2.18}$$

where

$$l_b(k) = \frac{\Delta z(k)}{\Delta z(k) + \Delta z(k-1)}. \tag{2.19}$$

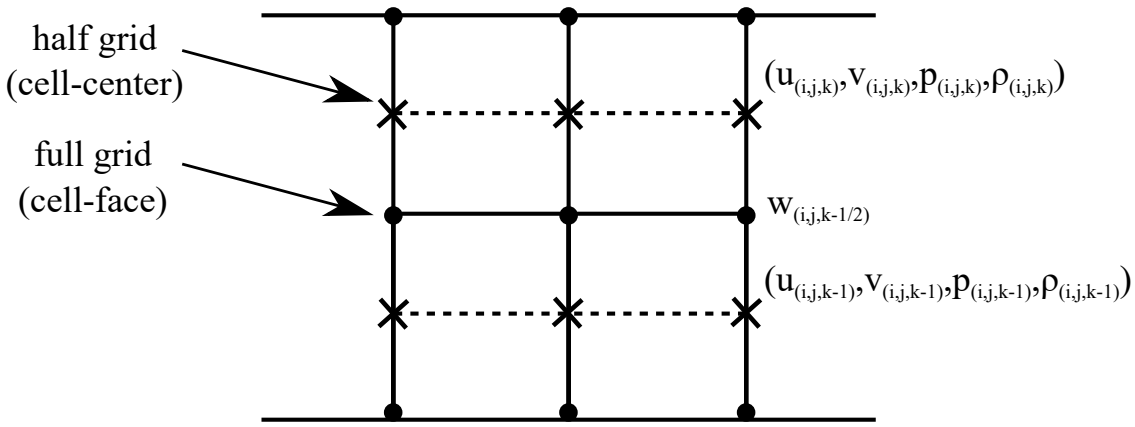

Figure 2.3: Staggered grid configuration in wall-normal direction).

2.2.2 Time advancement method

The time stepping method is based on the fractional-step [76] and the explicit third-order Runge-Kutta (RKW3) methods combined with the implicit Crank-Nicolson scheme [109]. The Crank-Nicolson scheme is used for discretization of the diffusive terms and RKW3 is used for the convective terms [58]. The Crank-Nicolson scheme is unconditionally stable for a pure diffusion problem [100]. In boundary layer flows, the minimum grid spacing is typically in the wall-normal direction and occurs close to the wall. The minimum grid spacing near the wall motivates use of Crank-Nicolson method for the diffusion terms since purely explicit scheme requires very small time steps to have numerically stable solutions. The Runge-Kutta method uses substeps to improve the accuracy of the scheme [109, 12]. The low-storage Runge-Kutta-Wray algorithm is used for memory consideration [109, 12]. This algorithm for the ordinary differential equation $dy/dt = f(y,t)$ can be written [109, 12] as:

$$k_1 = f(y_n, t_n), \tag{2.20}$$

$$k_2 = f(y_n + \beta_1 h k_1, t_n + \alpha_1 h), \tag{2.21}$$

$$k_3 = f(y_n + \beta_2 h k_1 + \beta_3 h k_2, t_n + \alpha_2 h), \tag{2.22}$$

$$y_{n+1} = y_n + h(\gamma_1 k_1 + \gamma_2 k_2 + \gamma_3 k_3), \tag{2.23}$$

where

$$\beta_1 = 8/15,\ \beta_2 = 1/4,\ \beta_3 = 5/12,$$
$$\alpha_1 = 8/15,\ \alpha_2 = 2/3,$$

$$\gamma_1 = 1/4,\ \gamma_2 = 0,\ \gamma_3 = 3/4.$$

There are only two storage variables required in the computation associated with each substeps [109].

To ensure a divergence-free velocity field, as required by mass conservation under the OBA, the fractional step method is used. First, at each RKW3 substep ($j = 1, 2, 3$), time-marching gives an intermediate velocity field ${u_i^*}^j$ that is not necessarily divergence free. Then the fractional step method uses a second step by computing the pressure gradient that is required to force the velocity to be divergence free. If the corrected velocity field at time step j is denoted by ${u_i}^j$ [129, 76]:

$${u_i}^j = {u_i^*}^j - h_j \frac{\partial \phi}{\partial x_i}, \tag{2.24}$$

where $\phi = p^{j+1} - p^j$ is the adjustment of pressure between successive RKW3 substeps and h_j is computed based on to the time step and for the RKW3 scheme is [129, 12]:

$$h_1 = \frac{8}{15}\Delta t,\ h_2 = \frac{2}{15}\Delta t,\ h_3 = \frac{5}{15}\Delta t. \tag{2.25}$$

Taking the divergence of (2.24) leads to a Poisson equation for ϕ which involves only the known ${u_i^*}^j$ since ${u_i}^j$ is defined to be divergence free [129]. Thus by,

$$\nabla^2 \phi = \frac{1}{h_j} \nabla \cdot {u_i^*}^j, \tag{2.26}$$

we can obtain the pressure adjustment ϕ and substitute the result back into (2.24) to obtain corrected velocity ${u_i}^j$ [129, 12].

2.2.3 Two-dimensional domain decomposition

In this research, a two dimensional (2D) pencil domain decomposition method is used for parallel computation on distributed-memory systems [58]. In the previous generation of parallel computation of stratified wall-bounded turbulent flows only 1D domain decomposition was typically used [129, 51]. The 1D domain decomposition restricts possible usage of available cluster computers and shows poor parallel scaling behavior for more than few hundred CPUs. Compared to the 1D domain decomposition, the 2D decomposition configuration significantly increases the number of CPUs that a simulation can utilize, which

then can enable us to perform petascale DNS. After domain decomposition, all governing equation can be solved on the decomposed domain and there is no need to change the programming logic and numerical algorithm. However, domain interfaces need communication which is done by the MPI routines.

Implementation of the 2D decomposition in the solver is shown by a simplified example in Fig. 2.4. In this example the computational domain is divided into $12 \times 12 \times 8$ cells (black thin lines) in the x, y, and z directions, respectively. The domain is then decomposed into 4 rows and 3 columns of pencils (Prow = 4, Pcol = 3; red thick lines), so that each MPI processors works on one pencil in parallel to the other processors [58]. The data transfer is a crucial step for parallel communication and in many parallelized spectral methods, the data transposition is implemented through the MPI_ALLTOALL function. This function imposes a significant computational expense. In this function, each processor is exchanging data to and from all other processors. Therefore, this operation can cause considerable communication delay. It would be best to minimize usage of this function for a more parallel computations.

For each RK substep a total of 12 transpositions are needed. In a 3D field communication between each processors can be complicated. However, several high-performance data transposition libraries are available, e.g. P3DFFT [110] and 2DECOMP& FFT [86]. In Hercules, the 2D transposition is performed using the 2DECOMP& FFT library v1.5.847 and the FFT is conducted with the FFTW library v3.3.4.

Initially, the domain is decomposed based on the Z pencil arrangement as shown in Fig. 2.4(c). Parallel communication is required for calculating the spatial derivatives in the convective, viscous, pressure terms, etc. Also, for the solution of the velocity, temperature, and pressure equations which involve a tridiagonal system of equations [58] requires performing the 2D Fast Fourier Transform (FFT). Standard MPI blocking communication is used in the horizontal direction between each pencil in all required communications among processors. In order to perform 2D FFT on horizontal planes, the Z pencil arrangement is transposed to Y pencil arrangement (Fig. 2.4b) and 1D FFT is carried out along the y direction. Then, the Y pencil arrangement is further transposed to the X pencil arrangement (Fig. 2.4a) and another 1D FFT is performed along the x direction to obtain the 2D FFT coefficients. Finally, the calculated 2D FFT coefficients in the X pencil is transposed back to the Z pencil. Once the 2D FFT coefficients are known, by using Thomas algorithm in the Z pencil arrangement, solution of the linear system of equation resulting from second-order finite difference discritization can be found and no extra parallel communication is needed [58].

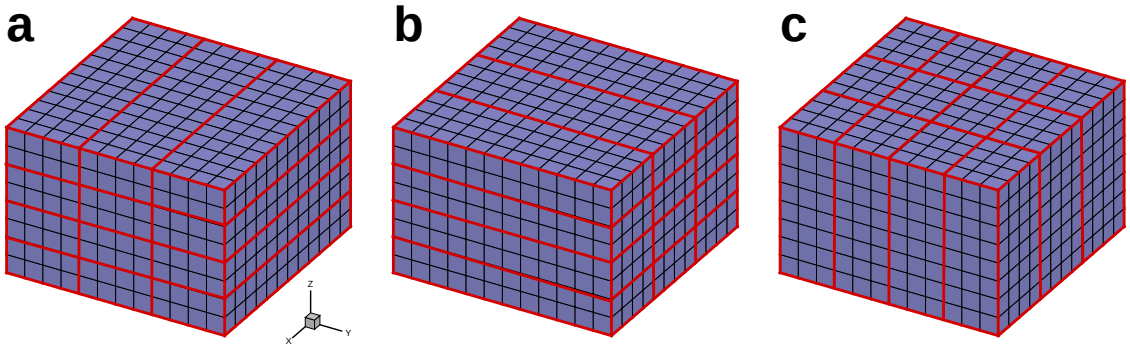

Figure 2.4: 2D pencil decomposition for the computational domain and transposition among different pencils. (a), (b), and (c) respectively represents for the X, Y, and Z pencil arrangements. Here the computational domain is decomposed into 12 $\times$12 $\times$8 cells (black thin lines) in the x,y, and z directions, respectively. This decomposition involves 4 rows and 3 columns ($\mathrm{P_{row}} = 4$, $\mathrm{P}_{row} = 3$; red thick lines) in the Z pencil arrangement for parallel computations. The Z pencil arrangement is further transposed to the Y or X pencil for parallel communication [58] .

2.2.4 Parallel efficiency

Parallel efficiency, or the scalability, is essential for large-scale DNS or fine-grid large eddy simulation. The parallel efficiency of Hercules has been tested on the Graham SHARCNET high-performance computing (HPC) platform. Parallel performance of Hercules is examined for two different grid resolutions. First, strong scalability of the solver has been tested. The strong scalability is defined as the variation of simulation speed (elapsed time per step) when increasing the CPU cores for a fixed grid size. A perfect strong scalability refers to the situation over which the speed increases by a factor of two if the CPU cores are doubled. He [58] tested scalability of Hercules for a petascale DNS up to 32000 cores and 34.4 billion grid points and showed excellent scaling [58]. Here, in order to re-examining the scaling of Hercules on our available cluster, two stably stratified open-channel flow cases, with the grid points being 4 and 134 million, are simulated using various numbers of processors. The parallel efficiency for strong scalability is calculated as $E_1 = \frac{P_0}{P}\frac{T_0}{T}$ [58]. Here P and T are the number of cores and the elapsed time per step,respectively. The subscript 0 denotes the case using the smallest number of cores. He [58] reported a minimum efficiency of 78% among different clusters. We observed 50% as lowest value for the efficiency. The possible reason for this is that we used a much lower number of grid points

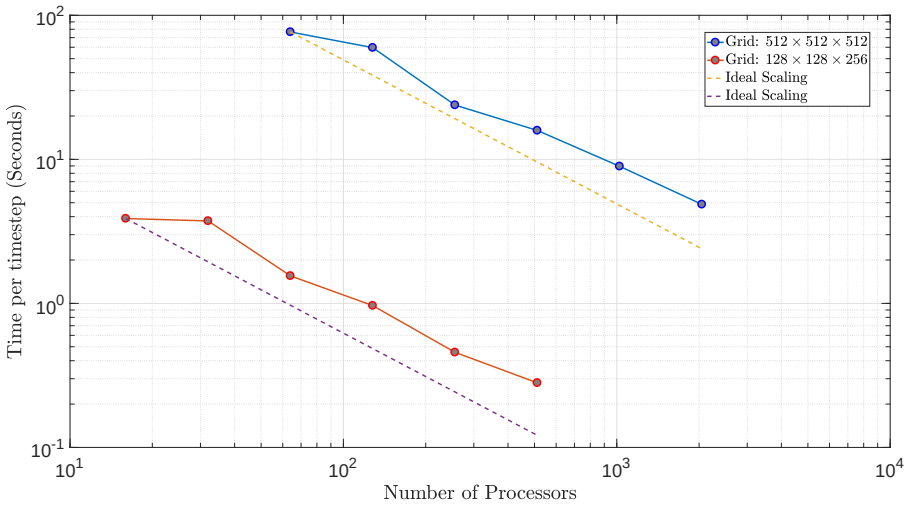

Figure 2.5: Parallel scalability analysis for the current DNS solver on Graham. Platform: Graham-SHARCNET. CPU: Intel E5-2683 v4 (Broadwell) with 2.1 GHz; Interconnection: EDR + FDR Infiniband. Compiler: Intel-Fortran v16.0.4; MPI library: openmpi v2.1.1.

in our test and the efficiency of Hercules is improved by using more grid-points. Also, the network topology of SHARCNET system is probably different compared to the cluster in which He obtained his parallel efficiency results. In addition to the strong scalability, the speed up is shown in Fig. 2.5. The speed up is defined as the variation of simulation speed when increasing the number of CPUs. It can be seen that by increasing the number of cores, the elapsed time per step decreases. Overall, we observe quite reasonable parallel performance of the Hercules on our available HPC cluster.

2.2.5 Verification of numerical solver

Although Hercules has been verified in previous studies [58] based on first and second order statistics, here, we perform another verification based on analysis of the spectra to ascertain that spectra are not affected by dissipation caused by the finite difference discretization scheme employed in the vertical direction. To do so we compare the kinetic energy spectrum to that from the closed-channel simulation of Moser *et. al* [102], which utilizes the Chebyshev spectral method in the wall-normal direction. The friction Reynolds number is $Re_\tau = 180$, and the computational domain is of size $Lx/h = 4\pi$ and $Ly/h = 4\pi/3$ as a benchmark. This comparison is shown in Fig. 2.6 for both streamwise and spanwise

wavenumbers. As can be seen, the results of the current numerical method agree well with the data of MKM.

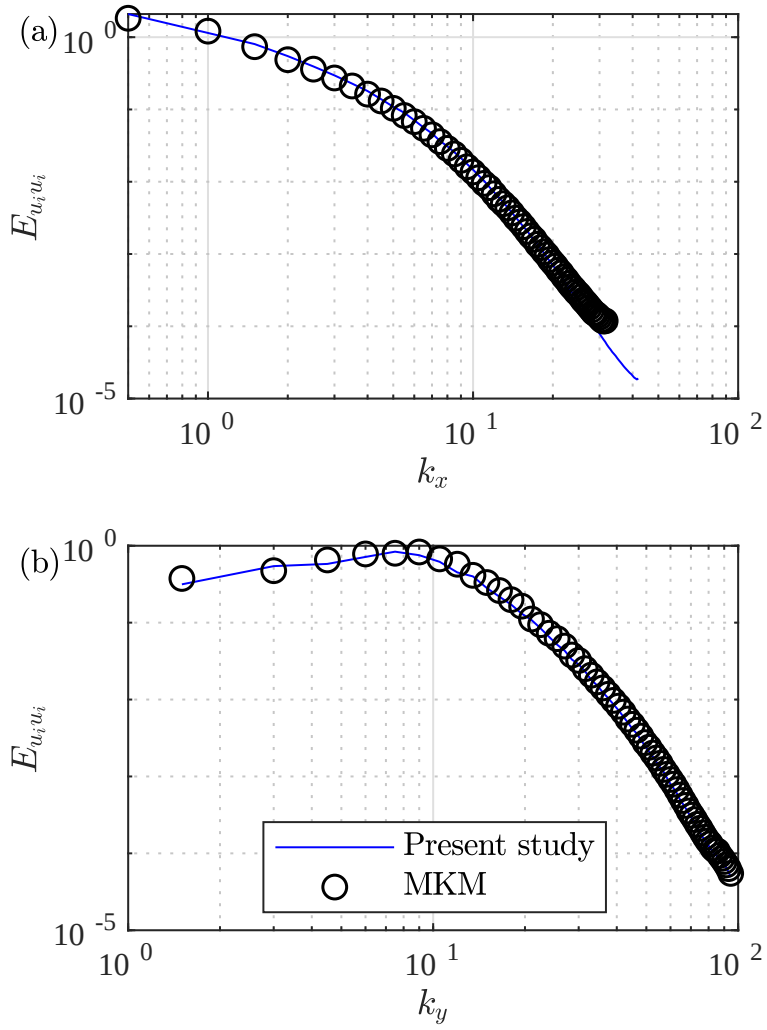

Figure 2.6: Comparison of energy spectra using numerical method of current work with MKM at $z^+ = 10.41$ of (a) $E_{u_iu_i}(k_x)$ and (b) $E_{u_iu_i}(k_y)$. Channel flow data of MKM has been extracted from https://turbulence.oden.utexas.edu/data/MKM/chan180/.

Chapter 3

Transient dynamics

In this chapter wall turbulence response to surface cooling is investigated. The processes in which a stably stratified boundary layer is formed from a neutral wall-bounded flow are also explored. This chapter is based on Ref. [7].

3.1 Introduction

Turbulence plays a central role in the dynamics of the atmospheric boundary layer (ABL), e.g. in the mixing of heat and water vapor, dispersion of air pollutants, and cloud formation. However, stable stratification, in which heavier air lies under lighter air, significantly affects boundary layer turbulence [125, 143, 94, 145]. Strongly stable stratification may lead to co-existence of turbulence and internal waves [4, 94, 74], horizontal intermittency, [46] or oblique laminar-turbulent patterns [16]. These features of the strongly stable regime demand extra consideration and add additional challenges for numerical simulations (e.g microfronts [94] and potential collapse of turbulence [145]). Because of the complexity of the stably stratified regime, it presents a challenge for parameterization of boundary layer mixing in weather forecasting models [125].

The stably stratified boundary layer (SBL) can form by radiative cooling of the surface (e.g. nocturnal ABL) or by advection of warm air over cold surfaces (e.g. ABL over sea ice). From an environmental perspective, the SBL can lead to a decrease in the dispersion of air pollutants or an accumulation of aerosols (e.g. black carbon [115]) in near-surface regions [35, 87]. The SBL can also adversely impact the local ecology in the by rapid depletion of nutrients due to the decrease in surface layer mixing in the ocean [22, 2]. From the

perspective of wind energy, stable stratification can cause a significant reduction in the total power output of large wind farms [1].

In the SBL, the dynamics of turbulence and the energy cascade are controlled by the simultaneous effects of stable stratification and the solid boundary. For stable stratification, energy is transferred from large anisotropic eddies to smaller and more isotropic eddies. In particular, for scales above the Ozmidov scale, anisotropy is characterized by thin pancake vortices, layers of strong shear, and gravity waves; below the Ozmidov scale, there is a transition to more isotropic three-dimensional turbulence [117, 88, 82]. The presence of the wall, on the other hand, creates another source of anisotropy by which the size of the energy-containing eddies increases when moving away from the wall. This causes an inverse spatial cascade in the near-wall region where energy and momentum are transferred from smaller eddies to larger eddies aloft [67, 70].

The SBL has been the subject of numerous studies by numerical simulations and atmospheric measurements and observations [94]. However, the interplay of the solid boundary and stratified turbulence, particularly for strong stratification, has been less studied [145]. Some of the outcomes of these studies of stably stratified wall-bounded turbulence (mostly from numerical simulations of closed or open channel flow) are briefly reviewed here.

SBL flows can be classified into "buoyancy affected", "buoyancy controlled", or "buoyancy dominated" based on Richardson and Reynolds number [52]. SBL turbulence is sustained for weak stratification or high Reynolds number (buoyancy affected flows) [52, 4, 130, 106, 50, 46]. Nevertheless, stratification substantially affects turbulence in the outer layer while the near-wall region and the logarithmic layer remain almost unaffected [130, 50]. For moderate stratification (buoyancy controlled flows), symmetry around the center of the closed channel is broken [52]. However, symmetry is eventually restored through a transition process by eddies crossing over the channel center [52]. Open channel flows at moderate stratification have lower turbulent mass flux, lower density gradient, and higher values for the ratio of potential energy to vertical turbulent kinetic energy [130] compared to the weak stratification regime.

For strong stratification or low Reynolds number (buoyancy dominated flows), the turbulence production mechanism is significantly suppressed by stratification, leading to decoupling of the inner and outer layers [52] or formation of large laminar patches in the near-wall region [46, 50, 16, 58] (depending on stratification level) where strongly stable stratification damps the intensity of near-wall streaks [4, 50] generated from global modes [50]. The damping of these modes eventually leads to vanishing of turbulent momentum and buoyancy fluxes in the core of the channel due to the disappearance of large-scale streaks in near-wall region [50]. The dominance of internal gravity waves in the central

region has also been observed for buoyancy dominated flows in closed channel simulations [4, 50, 74].

Although flow characteristics are fundamentally different for each of these three stratification regimes, they have some common basic features. For example, increasing stratification leads to an increase in the mean streamwise velocity, decrease in the skin friction coefficient, decrease in vertical velocity fluctuations, and decrease in tangential Reynolds stress [51, 4, 130, 106, 46, 50, 58].

In the buoyancy dominated SBL, the ratio of the Monin-Obhukov (MO) length to the channel height is often used to indicate whether turbulence will survive or collapse [106, 46]. The MO scale L_{MO} is defined as [46]

$$\frac{L_{MO}}{h} = -\frac{u_\tau^3/(\kappa h)}{(g/\theta_0)\overline{\theta w}|_s}, \tag{3.1}$$

where u_τ is the friction velocity based on the wall shear stress, $\kappa \approx 0.41$ is the von Kármán constant, h is a reference length scale (channel height for open channel flow configuration and channel half height for closed channel), and $\overline{\theta w}|_s$ is the vertical temperature flux at the bottom surface, where the overbar denotes a horizontal average. Essentially, L_{MO} is the height at which the temperature flux at the bottom surface is of the same order as the turbulent energy production in the log-law region, where stratification effects are assumed to be small [46].

Nieuwstadt [106] performed pioneering direct numerical simulations (DNS) of a turbulent open channel flow with a uniformly cooled bottom surface and fixed-temperature upper surface and introduced h/L_{MO} as a stability parameter. He reported that turbulence survives only for $h/L_{MO} < 1.25$, for which most locations in the channel satisfy $Ri_g^h < 0.25$, where the gradient Richardson number $Ri_g^h = N^2/S^2$ is the squared ratio between the buoyancy frequency N and mean shear S averaged over horizontal planes. He showed that turbulence decays for larger values of h/L_{MO}. Similar criteria have been found for turbulence collapse at higher Reynolds numbers and larger computational domain sizes [32].

Flores and Riley [46] performed DNS of a case similar to Nieuwstadt [106] at higher Reynolds and Richardson numbers as an idealized model for the nocturnal atmospheric surface layer. They found that surface cooling causes the turbulence statistics near the ground to adjust on a time scale on the order of L_{MO}/u_τ. They found that turbulence is sustained for relatively weak cooling, but when the Monin-Obukhov Reynolds number $Re_{L_{MO}} = L_{MO}u_\tau/\nu$ falls below around 100, turbulence collapses [46]. Here ν is the kinematic viscosity. This criterion implies that the logarithmic layer is not large enough to

accommodate a buffer region beneath when $Re_{L_{MO}} \lesssim 100$ since the height of buffer region is about 100 ν/u_τ[46]. A similar study [48] related turbulence collapse as a local process, regardless of the outer region dynamics. To reach that conclusion, they simulated a capped Ekman layer, which has a different outer flow and found similar criteria [48].

Donda *et. al* [36, 37] also performed DNS of a open channel flow with setup similar to the work of Nieuwstadt [106] and showed that recovery of turbulence would occur if perturbations of finite amplitude are imposed on the laminarized state after sufficient time. They argued that in the SBL, the available momentum in the bulk of the flow impose a maximum possible downward heat flux, which they called the maximum sustainable heat flux (MSHF). This limit is due to the fact that the time scale of boundary layer diffusion is much smaller than the time scale for flow acceleration [29] and therefore the available momentum for downward heat transport is limited in the case of strong surface cooling [29]. For surface cooling rates larger than MSHF, efficient vertical heat transport hinders and eventually causes turbulence to be suppressed fully by the intensive density stratification.

The focus of these previous studies has been the stationary SBL when turbulence is strong enough to survive surface cooling [52, 4, 130, 50], and/or the determination of conditions for turbulence collapse [106, 46, 32, 36, 37, 48]. Another question that has been less discussed in the literature is how a neutrally stratified boundary layer transforms to a SBL through surface cooling. This question is of particular relevance to the formation of a nocturnal ABL. Answering this question can improve our understanding of 1) the process under which turbulence collapses for strongly stable stratification, and 2) the mechanism by which turbulence may or may not recover from such collapse. Addressing these questions is the central focus of this paper.

In this chapter, we aim to study how a neutral boundary layer evolves into a SBL in the presence of surface cooling. In particular, we investigate how wall turbulence responds to strong surface cooling, how patchiness appears through adjustment of wall turbulence to strong stratification, and how turbulence may recover from such patchy states. We also consider the properties of the patchy state, when it is present, and how wall-bounded turbulence is laminarized for very strong stratification.

This chapter starts with a general statement of the problem in Sec. 2.1 where the mathematical formulation, governing equations, dimensionless parameters, and boundary conditions are introduced. The computational approach, simulation parameters, and properties of the database generated in this investigation are discussed in Sec. 2.2. In Sec. 3.3, simulation results are presented. First, we describe the feedback process over which the flow responds to strong surface cooling. Then possible feedback mechanisms that may be responsible for flow adjustment are considered. The chapter ends with concluding remarks

in Sec. 3.4.

3.2 Overview of simulations

In this study, we considered one neutral and five stratified simulations with Ri up to 2800. A summary table of the simulations is presented in Table 3.1. Case C1 refers to the neutral case in which temperature is a passive scalar and buoyancy frequency

$$N^2(z) = \frac{g}{\theta_0}\frac{\partial \overline{\theta}}{\partial z} \tag{3.2}$$

is zero everywhere. Fields from the stationary state of the neutral case are used to initialize other simulations. The Prandtl number (Pr) is set to unity in all cases.

Simulations are performed on a computational domain $L_x/h = 2\pi$, $L_y/h = \pi$ with resolution $N_x \times N_y \times N_z = 768 \times 768 \times 384$ for a moderate Reynolds number $Re = 560$ which correspond to wall unit grid spacings $\Delta x^+ = 4.6$, $\Delta y^+ = 2.3$, and $\Delta z^+ \in [0.08 - 3.3]$. The Δy^+ is smaller than Δx^+ since, as it will be explained later, the energetic spanwise scales are typically smaller than energetic streamwise scales. The domain size and physical parameters are comparable to the case S00-S12 in Flores and Riley [46] but approximately three times higher spatial resolution in the horizontal directions and two times in the vertical direction is used to analyze small scale features of strongly stable wall turbulence. This resolution is comparable to the work of Vreman and Kuerten [139] which used high resolution to study statistics of velocity derivatives. The time step is equal to $\Delta t = 0.0002$ in C1 and C2 and $\Delta t = 0.00015$ for the other cases. Fields are output with interval t_s, where $t_s u_\tau/h \approx [0.02 - 0.1]$. This output frequency corresponds to $t_s \approx [1 - 8]t_\eta$ where t_η is Kolmogorov timescale[112] obtained using minimum values of the domain averaged viscous dissipation throughout simulation time history.

Although the size of the computational domain considered here is small, it is large enough to contain the widest flow structure associated with at least one ejection and corresponding sweep, and therefore it allows maintenance of "healthy" turbulence in the sense of producing correct mean flow behavior and one-point statistics when compared to simulations with larger domains [47, 91]. In addition, it has recently been shown that for channel flow simulations with passive heat transfer, this domain size accurately predicts the evolution of turbulent heat flux and RMS values of fluctuating temperature [89]. To show the adequacy of the domain size, we computed the two-point correlation of the velocity

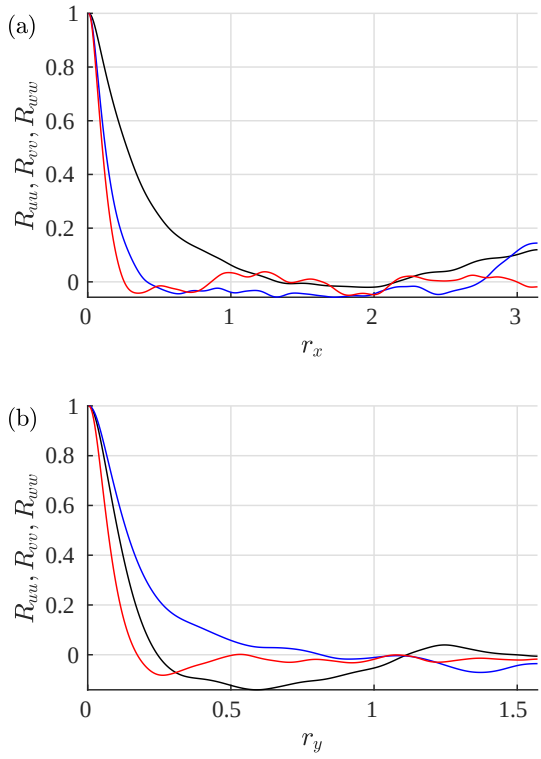

Figure 3.1: Two point correlation in outer layer where $z^+ = 420$ at $t^o = 57.98$ for C5: (a) correlation in streamwise direction, (b) correlation in spanwise direction. r_x and r_y are separations in x and y direction, respectively. Black, blue, and red lines refer to $R_{u'}$, R_{vv}, and R_{ww}, respectively.

fluctuations. The normalized correlations are defined as

$$R_{ij} = \frac{\overline{u'_i(\mathbf{x},t)u'_j(\mathbf{x}+\mathbf{x}',t)}}{\overline{u'_i(\mathbf{x},t)^2}^{\frac{1}{2}}\overline{u'_j(\mathbf{x}',t)^2}^{\frac{1}{2}}}, \tag{3.3}$$

and are plotted in Fig. 3.2. The employed computational domain size considered here provides more than 90% reduction in normalized correlation in the streamwise direction for separation $r_x \gtrsim 1$ for largest outer layer streamwise structures at $z^+ = 420$ (Fig. 3.2a). Velocity fluctuations become nearly uncorrelated for spanwise separation $r_y \gtrsim 1$ as shown in Fig. 3.2b). These correlation analyses shows the sufficiency of the considered computational domain for the purpose of current study. The same domain size has been used for similar Reynolds and Richardson numbers in Flores and Riley [46].

Table 3.1: Main simulations parameters. In the last column, t_f is the final time of the simulation. Re and Ri are reference values for friction Reynolds (Re_τ) and Richardson numbers (Ri_τ).

Case	Re	Ri	h/L_{MO}	$t_f u_\tau^0/h$
C1	560	0	0	53.2
C2	560	560	0.41	48.5
C3	560	697	0.51	47.7
C4	560	833	0.61	55.19
C5	560	1120	0.82	62.6
C6	560	2800	2.05	30.9

3.3 Results

3.3.1 Overview

In this section, we first categorize the different phases of the wall turbulence response to surface cooling. Then, we further classify stratification regimes based on differences in the feedback process for different cooling rates. It will be shown that there is a critical cooling rate at which turbulence becomes patchy, and beyond which there is total suppression of turbulence. The mechanism for these feedback processes is also discussed.

Figure 3.2(a-d) shows time series of friction and bulk Reynolds and Richardson numbers. Figure 3.2(e-f) shows time series of domain integrated K and k, where $K = \overline{u_i u_i}/2$ is mean kinetic energy (MKE) and $k = \overline{u_i' u_i'}/2$ is turbulent kinetic energy (TKE). Prime denotes fluctuation from horizontal average. After stratification is introduced at $t^o = 0$, the friction velocity initially decreases, which leads to reduced wall shear stress. This reduction of shear stress with increasing stratification is consistent with field observations of stably stratified ABLs [24, 120] and laboratory experiments of SBLs [142]. Consequently, the bulk velocity and bulk Reynolds number increase due to flow acceleration. The evolution of the friction Reynolds number exhibits three different phases: turbulence decay, turbulence recovery, and a quasi-stationary state. The evolution of domain integrated TKE also shows similar trend (Fig. 3.2f).

Turbulence decay starts from the introduction of stratification at $t^o = 0$ and lasts up to $t^o \approx 4 - 6$ in all cases, where TKE reaches its minimum through the cooling process. The recovery phase starts at the time associated with the TKE minimum. The duration of the recovery phase depends on Ri, where higher Ri requires more time for recovery. For example, while for case C2 the recovery phase continues up to $t^o \approx 20$, for C5 it lasts

until $t^o \approx 45$. This difference is consistent with the time scale of the flow adjustment L_{MO}/u_τ as suggested in Flores and Riley [46]. However, the recovery phase is different for the lower Ri_τ cases (C2 and C3) compared to the higher Ri_τ cases (C4, C5). In the former cases recovery involves a monotonic increase in TKE to a quasi-stationary state, while in the latter case there is an overshoot of TKE before the turbulence approaches quasi-stationarity.

Similar to the plots of Re_τ in Fig. 3.2(b), for C2 and C3, k in Fig. 3.2(f) decays and then recovers until it reaches quasi-stationarity, while K monotonically increases until becoming quasi-steady as shown in Fig. 3.2(e). By contrast, in C4 and C5, K increases initially, reaches a maximum and then decreases to a quasi-stationary state, while k decays until $t \approx 4$ and then recovers and reaches a maximum at $t^o \approx 21$ for case C4 and $t^o \approx 24$ for case C5. After this time, the bulk flow decelerates and k reaches quasi-equilibrium. While the minimum k in the decay phase decreases with increasing stratification, the k maxima in the recovery phase for cases C4 and C5 cases increases with stratification.

Time evolution of the friction and bulk Richardson numbers are shown in Fig. 3.2 (c-d). The Ri_b and Ri_τ are inversely proportional to the bulk and wall scale kinetic energy. These plots show a trend opposite to Re_b, Re_τ suggesting that Ri_b, Ri_τ correlates to the conversion of kinetic energy to potential energy in mean and fluctuating fields, respectively.

The most stratified case C6 in Fig. 3.2 shows laminarization, as indicated by the sudden drop in Re_τ, until $t^o \approx 10$ (as will be shown further below). We did not continue this case to achieve quasi-stationarity.

These results support earlier studies [106, 46, 32] that have used h/L_{MO} to categorize the dependence of SBL turbulence on cooling rate. For $h/L_{MO} < 0.6$ (cases C2 and C3), turbulence is affected by stratification but continuously exists, similar to weakly stratified cases as in earlier works [52, 130]. For $h/L_{MO} \geq 0.6$ (cases C4, C5), in the recovery state, TKE achieves a larger peak than in the neutral case. For $h/L_{MO} \gtrsim 1$ (case C6), the energy-containing modes are strongly affected by stable stratification and laminarization is the dominant feature of the decay phase. However, there is uncertainty in the literature about exact criteria for turbulence collapse for stably stratified wall-bounded turbulence. The $h/L_{MO} > 1.2$ criterion was reported [106, 32] in earlier studies for turbulence collapse. Nevertheless, this criteria might be affected by Reynolds number [32, 46], computational domain size [50], and also initial conditions [46, 36, 37].

The main focus of the present chapter is case C5. However, we partly discuss other cases and in particular C6. The C2-C4 simulations are mainly presented to exhibit the overall effects of weaker stratification (compared to C5 and C6) on different phases of the cooling process.

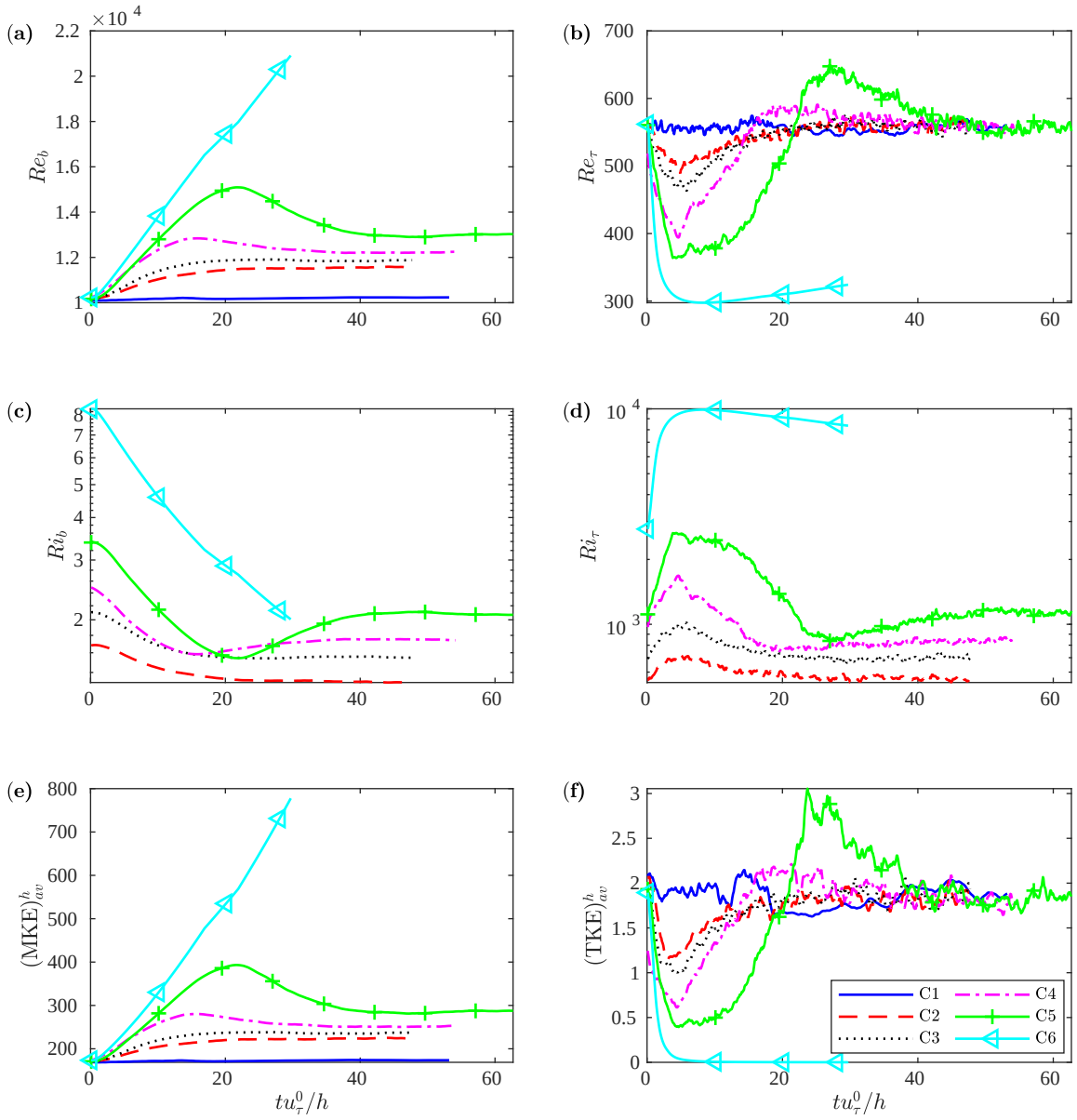

Figure 3.2: Time series of (a) bulk Reynolds number, (b) friction Reynolds number, (c) bulk Richardson number, and (d) friction Richardson number, (e) domain integrated MKE, and (f) domain integrated TKE.

3.3.2 Identifying inner and outer regions

To study the response of wall turbulence to surface cooling in the decay and recovery phases, we now identify how different layers (viscous sublayer, buffer layer, logarithmic, and outer layer) respond to different cooling rates.

In C5, because of the initially strong suppression of TKE, the wall-normal distances over which these layers are defined can be different from the neutral case. To see this discrepancy, consider Fig. 3.3, where u^+ are shown at different times during the surface cooling process for case C5. It is clear that the decay phase changes the viscous sublayer, such that parabolic behavior of this layer extends up to $z^+ = 15$ and the buffer layer shrinks. However, log-linear behavior up to $30 \lesssim z^+ \lesssim 100$ is still observed, but with different constants in the log-linear profile at different times. By using mixing length theory and linear variability of length scales with respect to z within the logarithmic layer [68], the turbulence production in the logarithmic region is closely related to the slope of the log-linear profile. However, while the slope is not significantly different at different times in Fig. 3.3, the constant in the log-linear profiles varies substantially, suggesting that this coefficient is set by the details of other layers and not the logarithmic layer itself. Changes of slope of the log-linear profile between two successive times are smaller than changes of the additive constant of the log-linear profile between two successive times. The slope increases monotonically while the additive constant undergoes sharp changes. The mean velocity profile in the viscous sublayer and buffer layer at $t^o = 23.7$ are similar at $t^o = 42$, but the outer layer behavior is different. This difference in outer layer behavior suggests that the additive constant in the log-linear profile is set by the details of outer layer, similar to unstratified logarithmic layer [68].

To avoid the complication of the evolution of the viscous and buffer layers as the surface cools, we focus on the inner layer, where $z^+ \leq 100$, and outer layer, where $z^+ > 100$. This criterion separates the inner and outer regions at all times in Fig. 3.3 and is also valid for cases C2-C4 (not shown). With this splitting, we can analyze the differences in how the inner and outer regions respond to surface cooling.

3.3.3 Inner and outer layer response to surface cooling

Figure 3.4 shows the integrated TKE rate of change over the inner and outer layers scaled with their initial values in each of those layers for the decay and recovery phases. In this figure, $\langle \mathrm{d}k_{av}/\mathrm{d}t \rangle$ is the average TKE rate of change, where $\langle\ \ \rangle$ means time average of the quantity over the desired period. The subscript av refers to layer over which integration of TKE is performed (i.e. inner or outer).

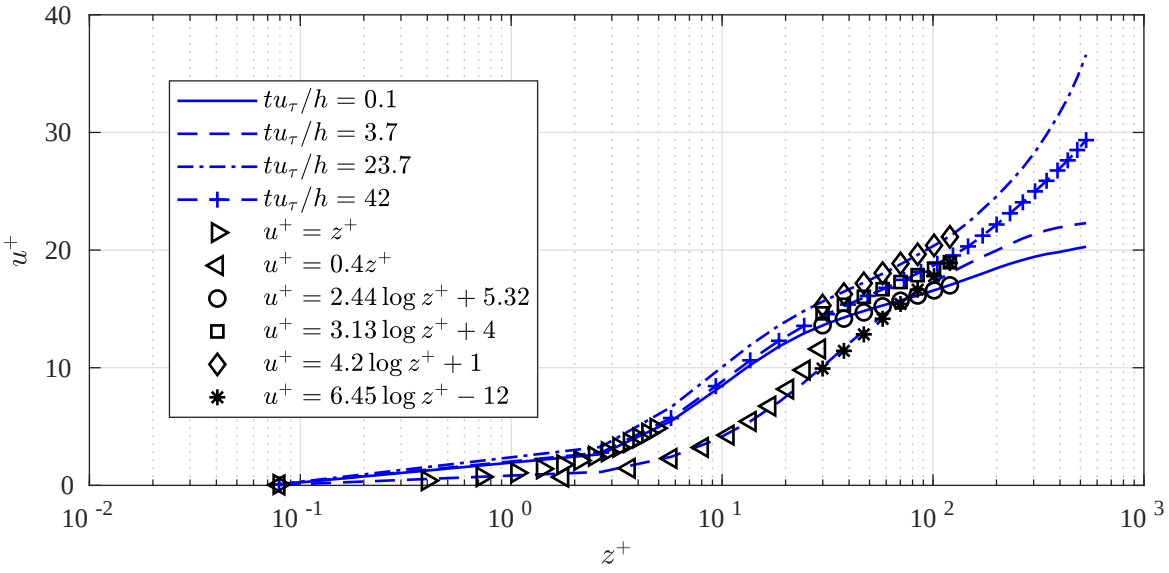

Figure 3.3: Mean velocity profiles for case C5 at early time $t^o = 0.1$ (solid), time of maximum decay $t^o = 3.7$ (dashed), end of recovery $t^o = 23.7$ (dash-dot), and stationarity $t^o = 42$ (dash-cross sign).

In the decay phase (Fig. 3.4a), it can be seen that for C4 and C5, the outer layer has the largest decay rate. Except in C2, as stratification increases, the difference between the decay rate in the inner and outer layers becomes larger. Indeed, for C5, the inner layer has the largest decay rate, suggesting a possible collapse of near-wall turbulence. We will show later that for this case, near wall turbulence does collapses temporarily and the flow becomes patchy. In the recovery phase for C5 (Fig. 3.4b), the outer layer has the largest recovery rate but the difference between recovery rates of the inner and outer layers increases with increasing Ri_τ, suggesting that there is a time delay between the recovery of the inner and outer layers. Generally, the decay rate is faster than the recovery rate for the cases considered here.

3.3.4 Feedback process in C5 and C6

Turbulence in cases C2-C4 is continuously sustained. However, in C5 it becomes patchy soon after the beginning of surface cooling. As shown in Fig. 3.5, this patchy turbulence exists for about 10 eddy turnover times ($t^o \approx 10$) in the recovery phase until turbulence is eventually fully revived. Our main interest in this chapter is to study features of the

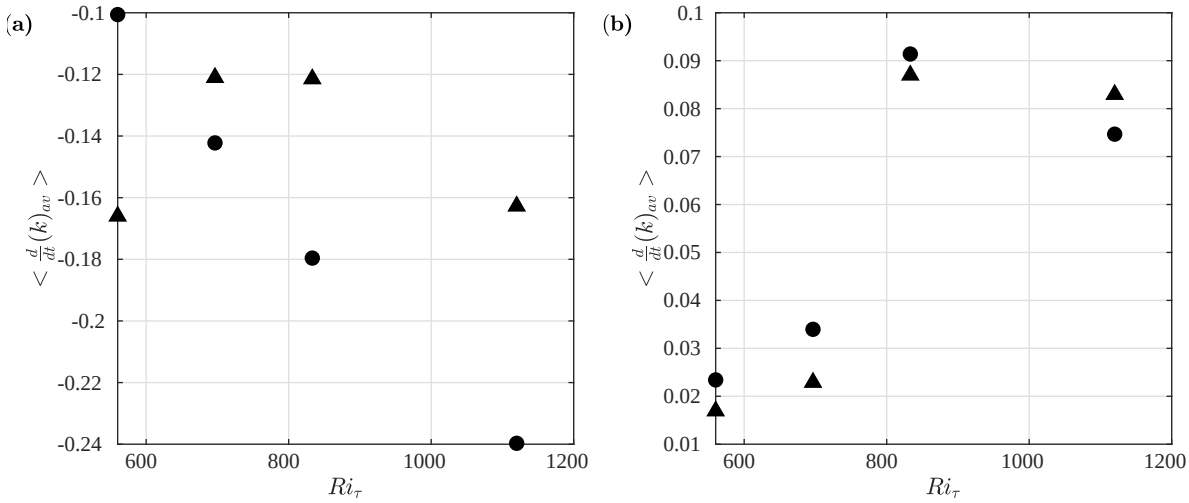

Figure 3.4: Time-averaged decay rate of scaled (with respect to its initial value for each layer and each Ri_τ) integrated TKE in the inner (circles) and outer (triangles) layers, averaged over the (a) decay and (b) recovery phase. The $Ri_\tau = 560$, 697, 833, and 1120 in these plots refer to C2, C3, C4, and C5 cases, respectively.

turbulence in the strongly stratified case C5. We present a detailed look at this case in this section. For comparison, we also consider the most strongly stratified case C6.

Horizontal snapshots of the streamwise velocity fluctuations for case C5 are shown at four vertical levels in Fig. 3.5 for different times during the cooling process. Shortly after the start of surface cooling at $t^o \approx 0.1$, near-wall streaks spread over the full horizontal plane, (Fig. 3.5a-c). Moving upward from the inner to outer layer, the streamwise aligned structures become more isotropic as shown in Fig. 3.5(d). During the decay phase, turbulence decays in all layers and, as shown in Fig. 3.5(e-g) at $t^o = 3.7$, the structures in the inner layer, and in particular near-wall streaks, disappear in some regions. Interestingly, laminar-turbulence coexistence is observed in Fig. 3.5 (e-g,i-k,m-o), with a turbulent strip of spanwise width $\lambda_y \approx 1.5h$ in the viscous sublayer and buffer layer. Turbulence is suppressed outside the strip. The turbulent strip becomes narrower in the early part of recovery at $t^o = 8.7, 14$ (Fig. 3.5i-j,m-n), decreasing to $\lambda_y \approx h$. Meanwhile, the fluctuations within the turbulent strip become stronger (e.g. streak velocities become stronger in Fig. 3.5(i,m) compared to Fig. 3.5(e)). The logarithmic layer also follows the trend of the near-wall regions as it becomes patchy. However, it has a wider turbulent strip.

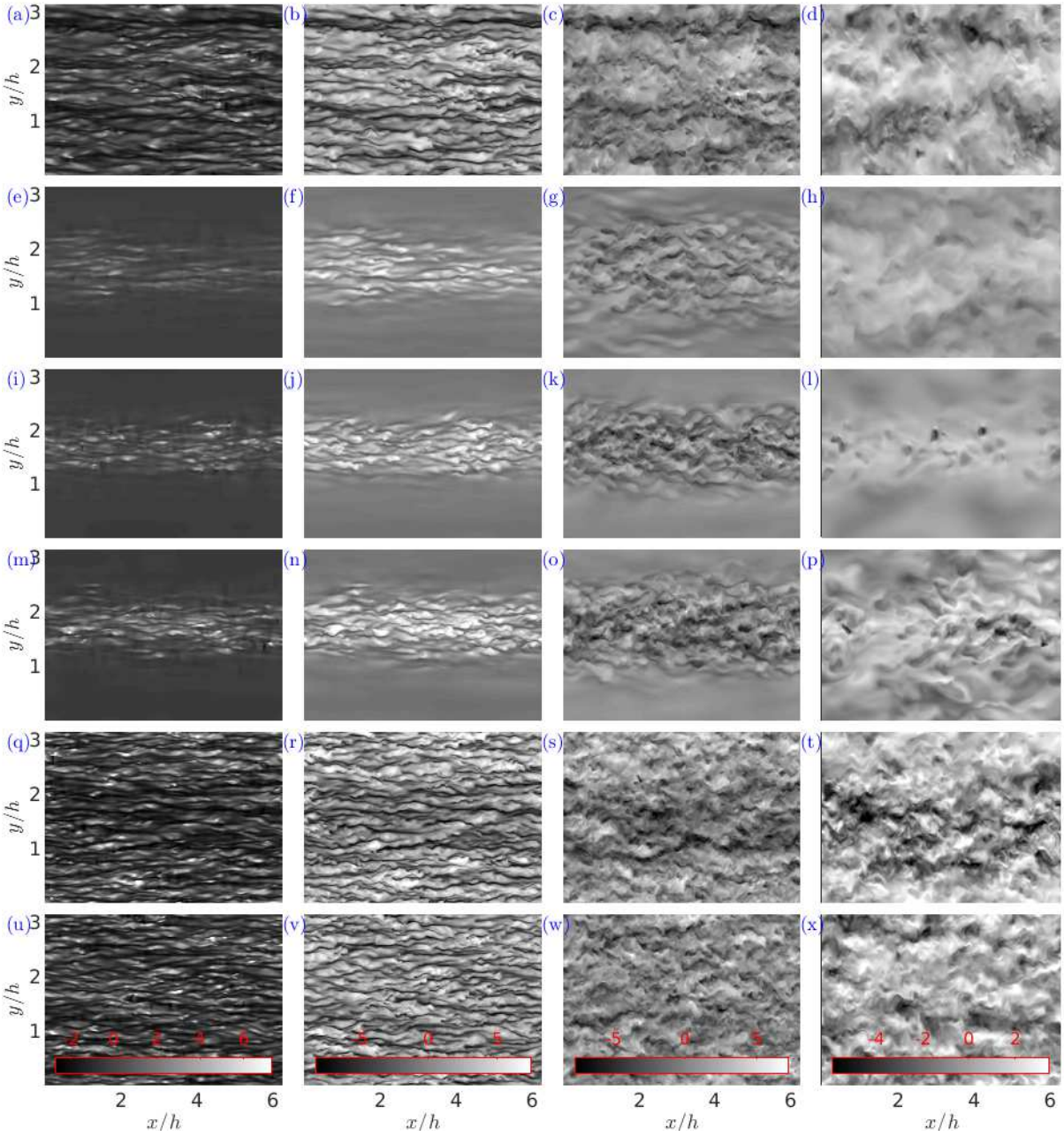
(a)
(b)
(c)
(d)
(e)
(f)
(g)
(h)
(i)
(j)
(k)
(l)
(m)
(n)
(o)
(p)
(q)
(r)
(s)
(t)
(u)
(v)
(w)
(x)
y/h
x/h
1
2
3
4
6
-2
0
2
-5
5
-4

Figure 3.5: Fluctuating streamwise velocity u'^+ at different layers and different times for C5. Each column shows a different level; from left to right, these are $z^+ = 3.5$, 15 , 70, and 300. Each row shows a different time; from top to bottom, these are $t^o = 0.1$, 3.7, 8.7, 14.7, 23.7, and 29.7. Colorbars on each layer are based on u'^+ for different layers at $t^o = 0.1$. These colorbars are shown on the bottom inside of the last row in panels (u-x). As cooling progresses it can be seen turbulence evolves into a patchy state where an active region is located next to a quiet region. The sequence of inner layer partial collapse followed by outer layer patchiness is also observed.

As cooling of the surface continues, the patchiness eventually extends to the outer region at $t^o = 14.7$ as in Fig. 3.5(p), which strongly supports the necessity of inner layer production in sustaining outer layer turbulence. However, patchiness in the outer layer disappears after a few eddy turn over times as shown in Fig. 3.5(x).

During the recovery in Fig. 3.5 (i-t), inner layer TKE builds up, although some patchiness still exists. The inner layer structures are fully recovered by $t^o = 23.7$. It will be discussed below that the quiet regions in the neighborhood of the turbulent strip in Fig. 3.5, which are often referred to as a laminar region [46, 16], actually appear to consist of layered turbulence with flat structures.

Profiles of k at different times in the cooling process are shown in Fig. 3.6. The decay, recovery, and approach to quasi-equilibrium can be seen in this plot. At early times $t^o \lesssim 3.7$, the TKE maximum shifts upward to $z^+ \approx 30$ as a result of the shrinking buffer layer and boundary layer growth, as shown by the mean velocity and temperature gradients in Fig. 3.7. At later times, the maximum TKE occurs around $z^+ = 15$, suggesting that the buffer layer is rebuilding. During the recovery phase, when TKE in the buffer layer starts to recover, TKE in the outer layer with $z^+ \gtrsim 300$ is still decreasing. This sequencing strongly suggests that there is a delayed recovery in the outer layer, which uses energy that has been produced earlier in the buffer layer during the decay phase. This delay in recovery is consistent with the discussion given in Sec. 3.3.3.

The boundary layer thickness starts growing during the decay phase and it continues growing until $t^o \approx 13$ in the recovery phase as shown in Fig. 3.7. Mean shear at the wall and in the region $z^+ \lesssim 20$ is built up during the recovery phase. Therefore, this region may be responsible for turbulence production when sufficiently large tangential Reynolds stress is available. Both mean shear and mean temperature gradient acquire quasi-equilibrium at $t^o \approx 42$.

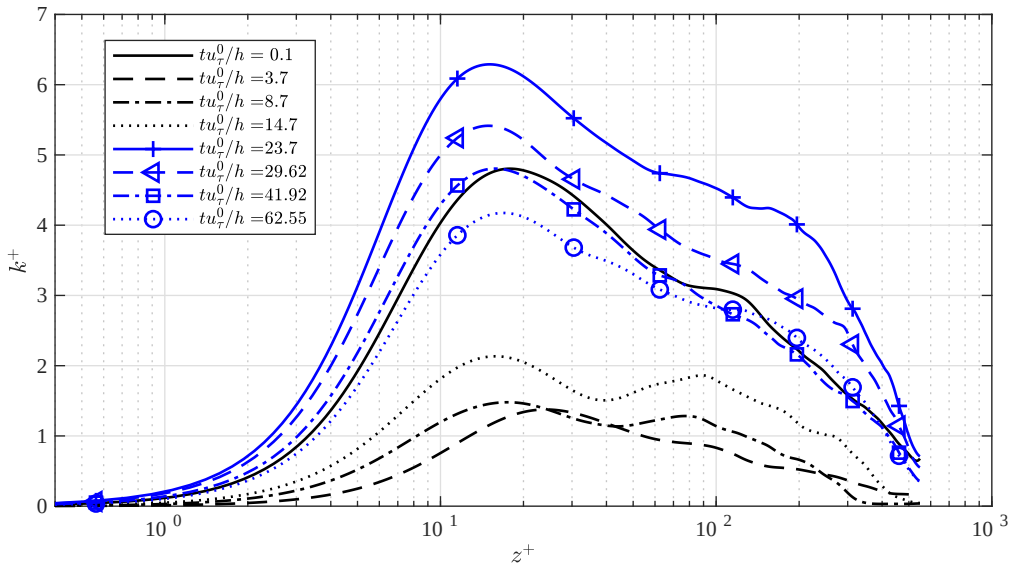

Figure 3.6: Instantaneous TKE for C5 at different times. Solid black line is for $t^o = 0.1$, dashed black line for $t^o = 3.7$, solid blue line is for $t^o = 14.7$, dashed blue line for $t^o = 23.7$, green line is for $t^o = 29.7$ and red is for $t^o = 41.9$.

Profiles of the different contributions to the TKE budget are presented in Fig. 3.8 (see Appendix A.1). Except for the viscous sublayer, where viscous diffusion has large values, the main balance in the TKE budget at all times is between production and dissipation. The peak of buoyancy destruction at $z^+ \approx 100$ is an order of magnitude smaller than the peak of production and dissipation. In the lower part of the viscous sublayer, the wall impermeability prevents turbulent production when $z^+ \lesssim 2$ at all times. Except for early times when peak production shifts upward as a result of boundary layer growth, dissipation dominates the inner layer outside of the buffer layer $5 \lesssim z^+ \lesssim 30$, where production has larger values. Above $z^+ \approx 100$, production and dissipation are balanced. Production and dissipation are weakened during the decay phase $0.1 \lesssim t^o \lesssim 3.7$, suggesting that the appearance of the patches results from a lack of production rather than an excess in dissipation. The impact of lack of production in turbulence collapse is also supported by experimental studies of SBLs [142].

Furthermore, tangential Reynolds stresses are suppressed in the decay phase (Fig. 3.9a) as a result of the damping effect of stable stratification, which leads to damping of vertical velocity fluctuations. Therefore, ejection and sweep events are hindered. This interruption in momentum transfer can also be seen in T^+, Fig. 3.8(d), where upward TKE transfer

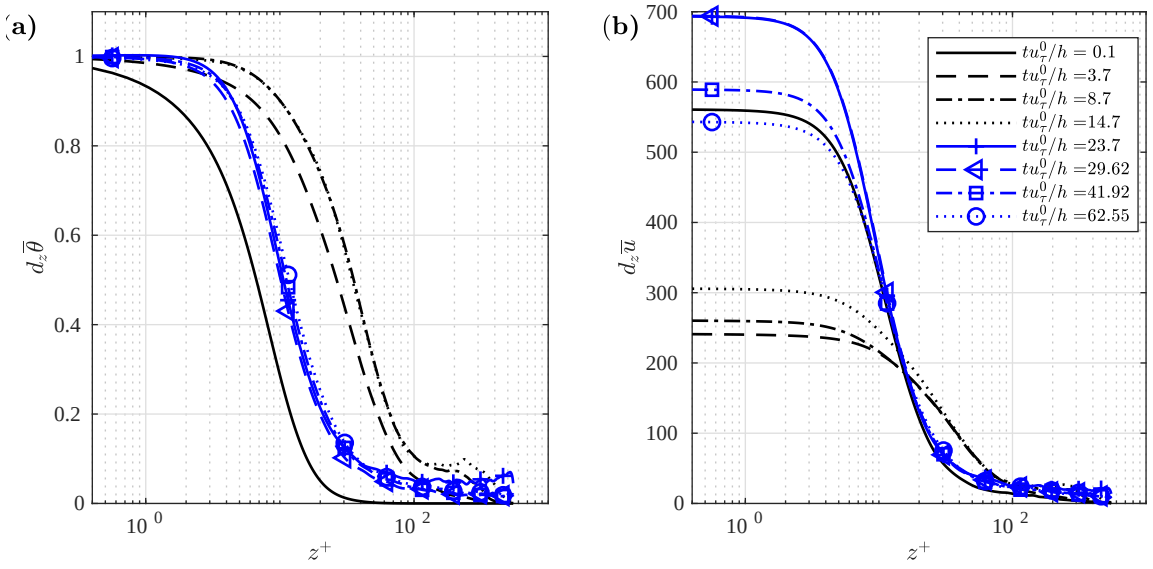

Figure 3.7: (a) Instantaneous mean temperature (b) and velocity gradient for C5 at different times. Solid black line is for $t^o = 0.1$, dashed black line for $t^o = 3.7$, solid blue line is for $t^o = 14.7$, dashed blue line for $t^o = 23.7$, green line is for $t^o = 29.7$ and red is for $t^o = 41.9$.

is almost fully suppressed and downward TKE transfer is significantly reduced. This is expected since once fluid in the near-wall region becomes heavier as a result of surface cooling, more energy is required for vertical motions. The buoyancy frequency has larger values as we approach the wall due to the thermal boundary condition (Fig. 3.7), and therefore fluid closer to the wall feels a stronger restoring force. Pressure-work has its largest value in lower part of viscous sublayer at all times.

Figure 3.10 shows streamwise velocity fluctuations for case C6. This figure reveals that for the strongest surface cooling, while turbulence in the inner region is damped in Fig. 3.10(e-g,i-k), the outer layer (Fig. 3.10h,l) still has active turbulence (although the intensity of the fluctuations is strongly reduced). The surviving streaks at time $t^o = 3.7$ in the buffer region (Fig. 3.10f) are of size $\lambda_x \approx L_x$, suggesting they are associated with the largest modes that the computational domain can handle. Structures similar to the streaks in buffer region (with higher intensity) exist in the logarithmic layer for this time. The buffer and logarithmic layers also shows analogous large scale features [64, 63]. In this case, the near wall streak intensities are an order of magnitude smaller than those in case C5 at the same time. The inner and outer layers are almost decoupled. The diffusive nature of the inner region for case C6 is also clear. Continuing surface cooling leads to complete removal of quasi-streamwise structures and continuous decrease of intensity of fluctuations. By time $t^o = 14$, outer layer turbulence is also damped.

3.3.5 Feedback mechanism in C5 and C6

In this section, we discuss possible mechanisms that may explain the response of the flow to the surface cooling described in the previous section. We first visualize the change in flow structures with cooling. We use the Q-criterion, which is the second invariant of the velocity gradient tensor, which is defined as[62],

$$Q = -\frac{1}{2}\frac{\partial u_i}{\partial x_j}\frac{\partial u_j}{\partial x_i}. \tag{3.4}$$

Figure 3.11 shows Q at $t^o = 0.1$. At this early time, turbulence spans whole cross-section and the near wall region ($z^+ \leq 30$) is dominated by quasi-streamwise vortical structures. Lifted-up vorticies from these quasi-streamwise vortical structures are also present and are surrounded by other incoherent structures aloft. These near-wall structures contribute to sweep and ejection events associated with pulling high-momentum fluid from upper levels and pushing low-momentum fluid to upper levels, creating velocity streaks and maintaining

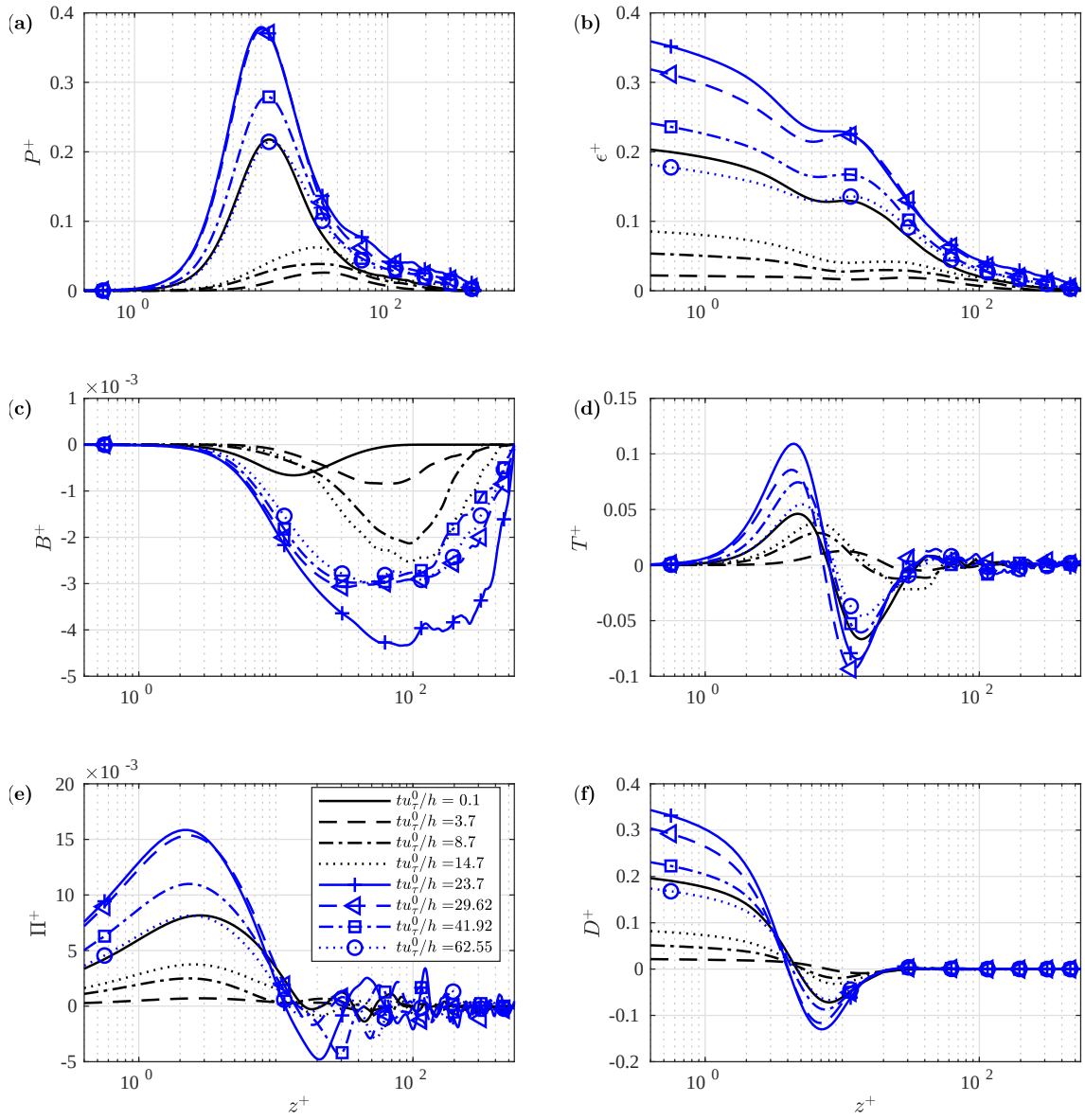

Figure 3.8: Different contributions to the evolution of TKE for C5 at different times: (a) production, (b) dissipation, (c) Buoyancy destruction, (d) turbulent transport, (e) pressure-work, and (f) viscous diffusion. Solid black line is for $t^o = 0.1$, dashed black line for $t^o = 3.7$, solid blue line is for $t^o = 14.7$, dashed blue line for $t^o = 23.7$, green line is for $t^o = 29.7$ and red is for $t^o = 41.9$.

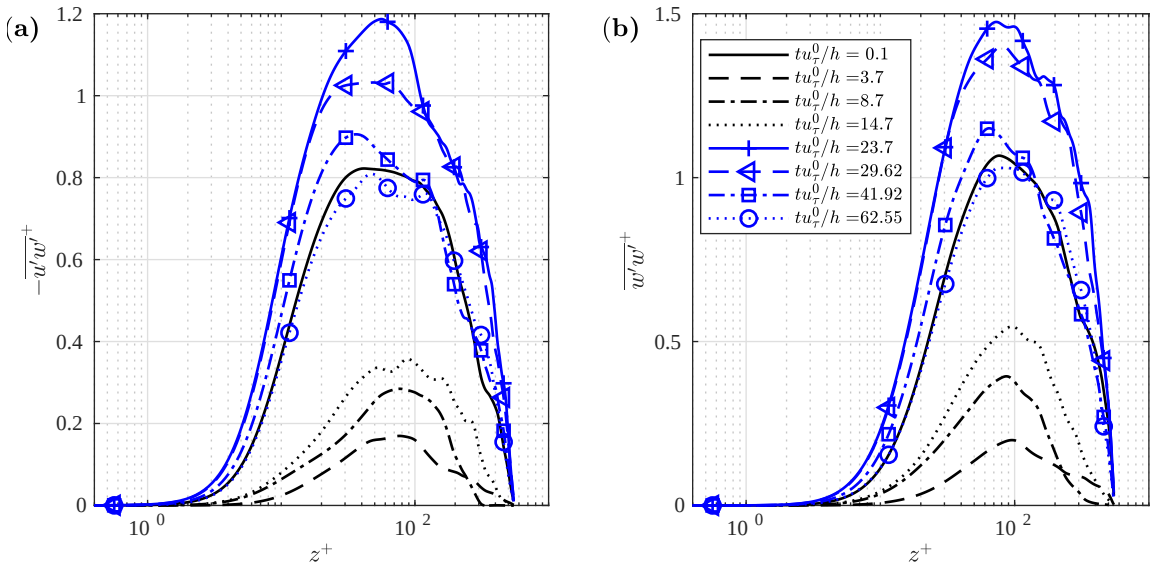

Figure 3.9: Instantaneous (a) $-\overline{u'w'}$ and (b) $\overline{w'w'}$ for C5 at different times. Black lines correspond to decay phase.Solid black line is for $t^o = 0.1$, dashed black line for $t^o = 3.7$, solid blue line is for $t^o = 14.7$, dashed blue line for $t^o = 23.7$, green line is for $t^o = 29.7$ and red is for $t^o = 41.9$.

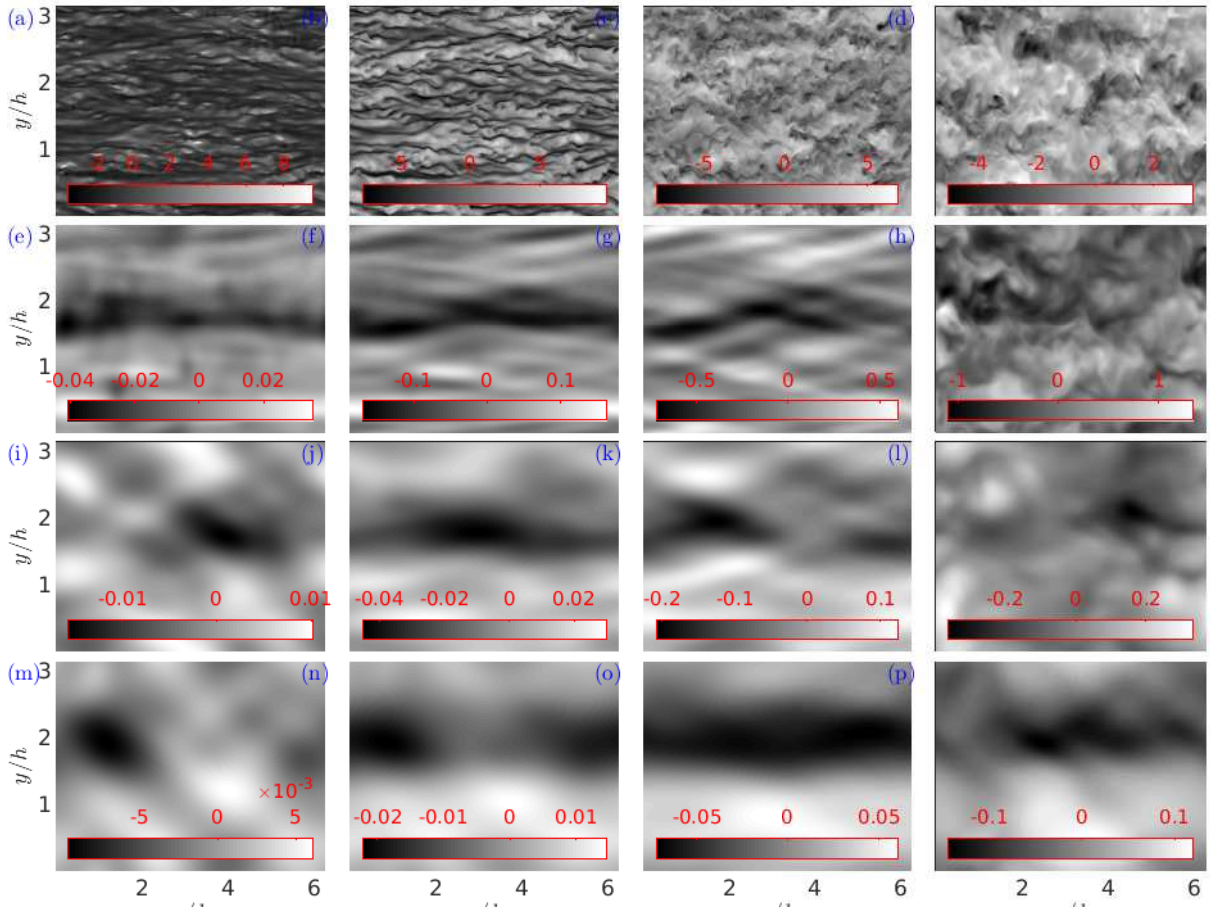

Figure 3.10: Fluctuation streamwise velocity u'^{+} at different layers and different times for C6. Each column shows a different level; from left to right, these are $z^{+} = 3.5$, 15 , 70, and 420. Each row shows a different time; from top to bottom, these are $t^{o} = 0.1$, 3.7, 8.7, 14.7. Colorbars on each layer are are shown on the bottom inside of each layer. As cooling progresses turbulence in the near-wall region collapses and the outer layer turbulence collapses subsequently.

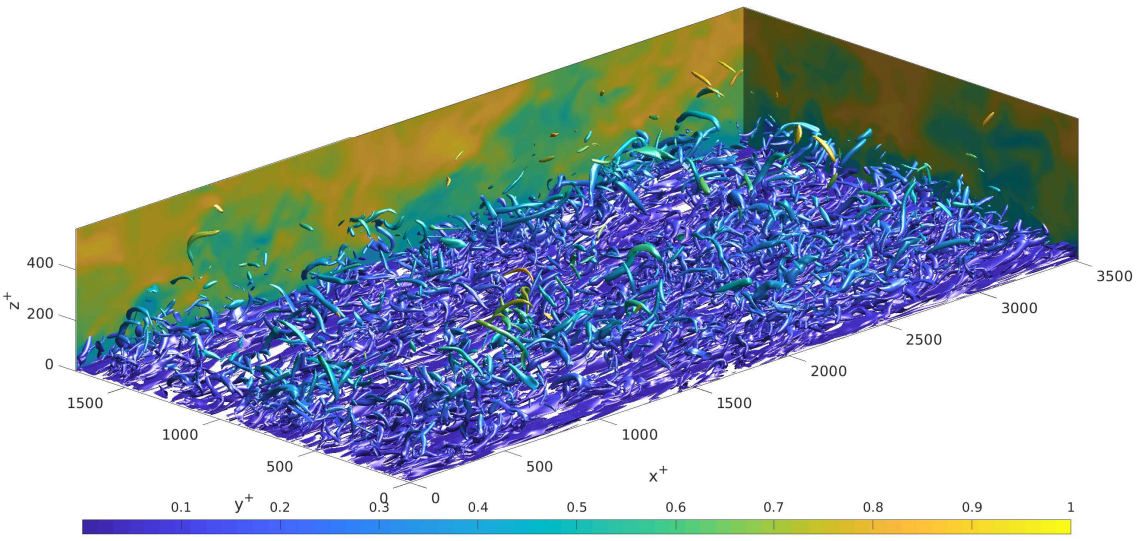

Figure 3.11: Visualization of instantaneous scaled Q'^{+} at time $t^o = 0.1$ as an indication of vortical structures for case C5 colored by distance from the wall. Cross-sectional slices are total kinetic energy in streamwise and spanwise planes. Both Q'^{+} and total kinetic energy are scaled with their maximum values. Isosurfaces of scaled Q'^{+} are plotted at the level of 0.01. Colorbar is based on values of scaled total kinetic energy.

turbulence. However, as shown in Figs. 3.5 and 3.10 stable stratification can change the organization, population, and intensity of these structures.

Figure 3.12 shows Q at a later time $t^o = 11$, in the early stage of the recovery phase. Contour plots of the total kinetic energy are also included to indicate energy transfer. The modulation of vortical structures caused by stable stratification is clear. The quasi-streamwise vortical structures are absent in the regions outside of the turbulent strip, which we refer to as quiet zones. Turbulence is concentrated in the strip, which comprises numerous quasi-streamwise vortices and hairpin like structures [38, 43]. However, the quantity of lifted and detached vorticies is considerably lower in comparison with $t^o = 0.1$, even in the turbulent strip which can explain the reduction in turbulence production from its initial value. This modulation can also be seen in the contour plots of the total kinetic energy in Fig. 3.12, where vertical transport of lower to higher momentum from the inner to outer layer is significantly altered. Boundary layer growth up to $z^+ \approx 300$ can be seen from these contour plots along with shear instabilities at the top of the boundary layer.

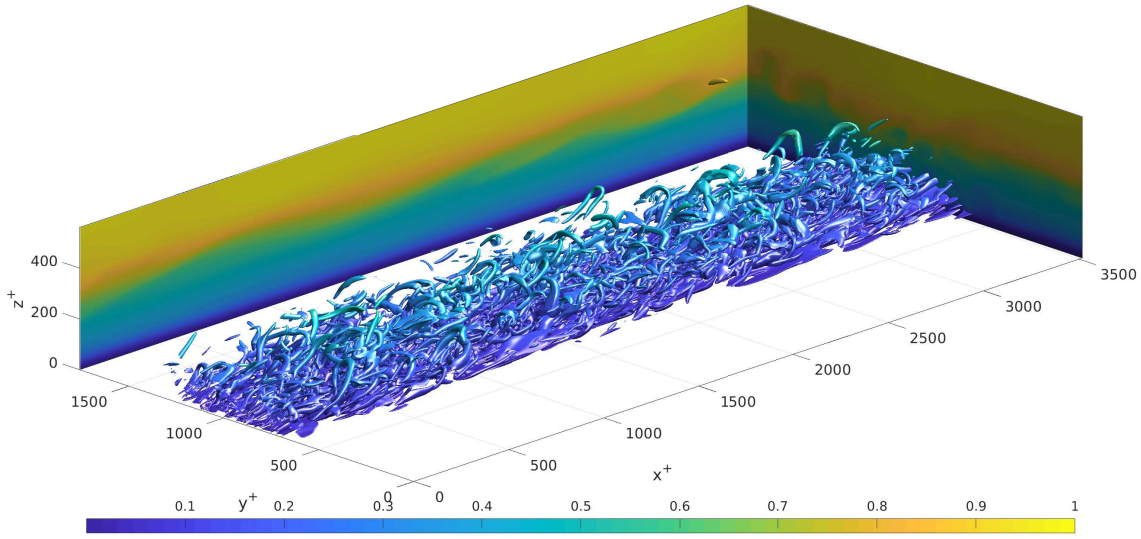

Figure 3.12: Visualization of instantaneous scaled Q'^{+} criterion at time $t^{o} = 11$ as an indication vortical structures for case C5 colored by distance from the wall. Cross-sectional slice plots are total kinetic energy in streamwise and spanwise planes. Both Q'^{+} and total kinetic energy are scaled with their maximum values. Isosurfaces of scaled Q'^{+} are plotted at the level of 0.01. Colorbar is based on values of scaled total kinetic energy.

An important question is how turbulence recovers from the patchy state in C5. Different scenarios may be considered for this recovery: it could be due to spread of the turbulent strip in the spanwise direction as a result of the built-up of shear and tangential Reynolds stress as the front of the turbulent strip destabilizes the neighboring quiet region [126] leading to spreading of turbulence in the spanwise direction, and/or it could be excitation from large scale eddies aloft that can trigger transition and cause recovery. Hairpin-like vortices [3] are observed in Fig. 3.12 at $y^+ \gtrsim 1500$ in the near-wall region for $x^+ \gtrsim 2000$ and $x^+ \approx 3500$. This hairpin vortex is 200 wall units in the spanwise direction away from the turbulent strip, which is consistent with the scenario based on excitation from the boundary layer top. On the other hand, if the recovery is independent of fluctuations at the boundary layer top, then turbulence in the quiet region should be recovered in the absence of those fluctuations.

To test this hypothesis, we perform two experiments in which we remove the fluctuations at certain heights from the right-hand side of the governing equation by replacing the terms in Eq. 2.2-2.3, with their horizontal average. The fluctuations are removed above $z^+ = 200$ in the first experiment and $z^+ = 300$ in the second. Both experiments are initialized using fields from C5 at time $tu_\tau/h = 3.7$ associated with maximum decay. Time series of domain integrated MKE and TKE are shown in Fig. 3.13 for these two experiments. These plots reveal that while MKE is essentially the same in both experiments, the presence of fluctuations at $z^+ \gtrsim 300$ is important for recovery from a localized patch such as a turbulent strip. This finding supports the hypothesis that recovery in the quiet regions is triggered by large structures in the outer layer rather than spreading of the strip.

Thus the recovery process in C5 can be understood as follows: Once turbulence reaches maximum decay in the inner layer, energy-containing eddies in the outer layer still use TKE that has been produced in the buffer region at previous times (which had higher TKE) due to delay in the decay of the inner and outer layer. These outer layer eddies can control decay of inner layer TKE from further fall-off through interaction of inner and outer layers where large scale eddies of the size of $\lambda_z^+ \approx 300$ ($\gtrsim h/2$) in the outer layer can penetrate down close to the wall and stir the flow (in the sense of Townsend's wall attached eddies hypothesis [134]).

Active eddies in the turbulent strip in the buffer layer will continuously maintain turbulence in the log and outer layers. However, since these eddies lose a significant portion of their TKE during the decay phase, the outer layer will not be maintained sufficiently and will experience decay at a later time.

Excitation of inner layer turbulence by outer layer sweepening in the decay phase helps to reinvigorate the regeneration cycle of near-wall turbulence [57]. Then, streaks in the

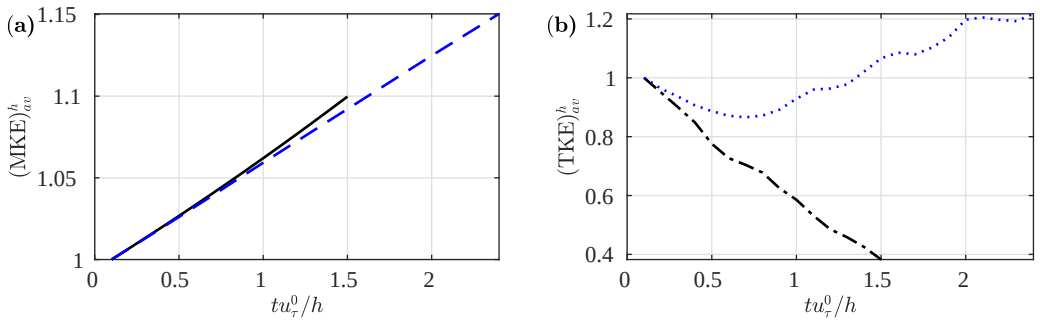

Figure 3.13: Time series of (a) domain averaged MKE and (b) domain averaged TKE for C5 experiments where fluctuations are removed above $z^+ = 200$ (blue lines) and $z^+ = 300$ (red lines). MKE and TKE have been scaled by their initial values. Time zero here corresponds to $tu_\tau/h = 3.7$ in Fig. 3.2.

viscous sublayer and buffer layer reappear, reactivating ejection and sweep events in quiet regions near the wall. Eventually, turbulence spans the whole channel width and fully recovers. While TKE is building up in the inner layer, a smaller amount of production from the inner layer is needed for outer layer recovery, and therefore the outer layer recovers faster due to fact that the effect of viscosity is less significant there.

The most stratified case C6 is different. Figure 3.14 shows Q for C6 at a later time $t^o = 23.7$. It can be seen that the cooling process leads to a collapse of the vertical scale in the vortical structures in the inner region, and leads to the formation of quasi-flat structures. The flat structures are also observed in the outer layer. As shown in Fig. 3.10, elongated streamwise structures are replaced by these flat pancake-like structures.

In the stably stratified ABL, intermittencies such as local patches of turbulence also exist under strongly stable stratification [94]. A similar recovery process to what we have discussed in this section has also been suggested in field studies of the stable ABL. These studies suggest that the patchiness in strongly stable ABLs could be interrupted through the intrusion of shear instabilities from the boundary layer aloft into the stable surface layer [23, 121].

3.3.6 Nature of quiet zones in C5

In this section, we consider the characteristics of quiet regions adjacent to the turbulent strip that appear during the cooling process in C5. To do so we investigate the spectra of the streamwise velocity fluctuations.

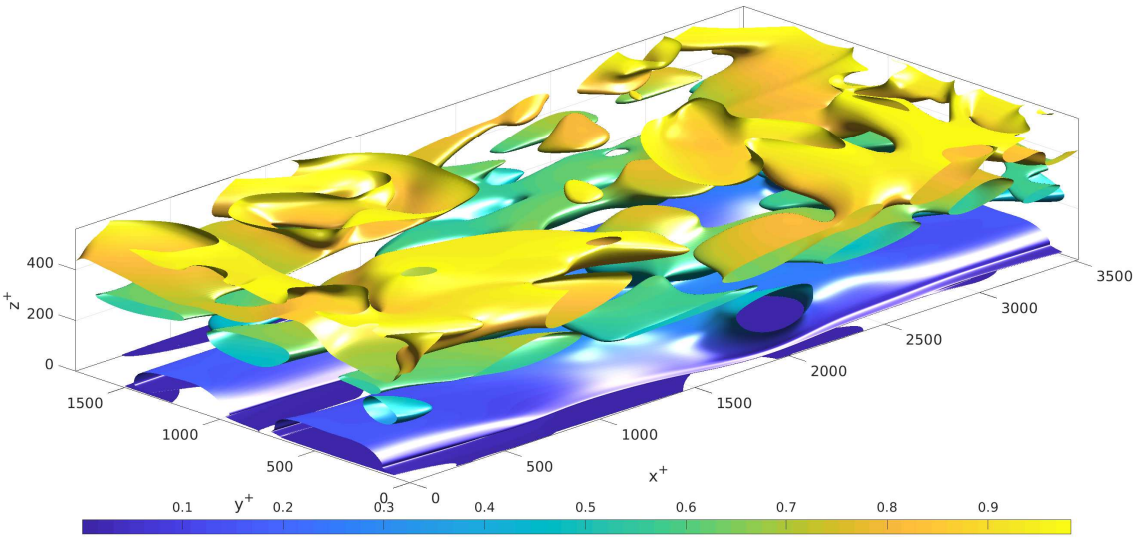

Figure 3.14: Visualization of instantaneous Q'^{+} criterion at time $t^o = 23.7$ as an indication vortical structures for case C6 colored by distance from the wall. The Q'^{+} is scaled with their maximum values. Isosurfaces of scaled Q'^{+} are plotted at the level of 0.01. Colorbar is based on distance from the wall.

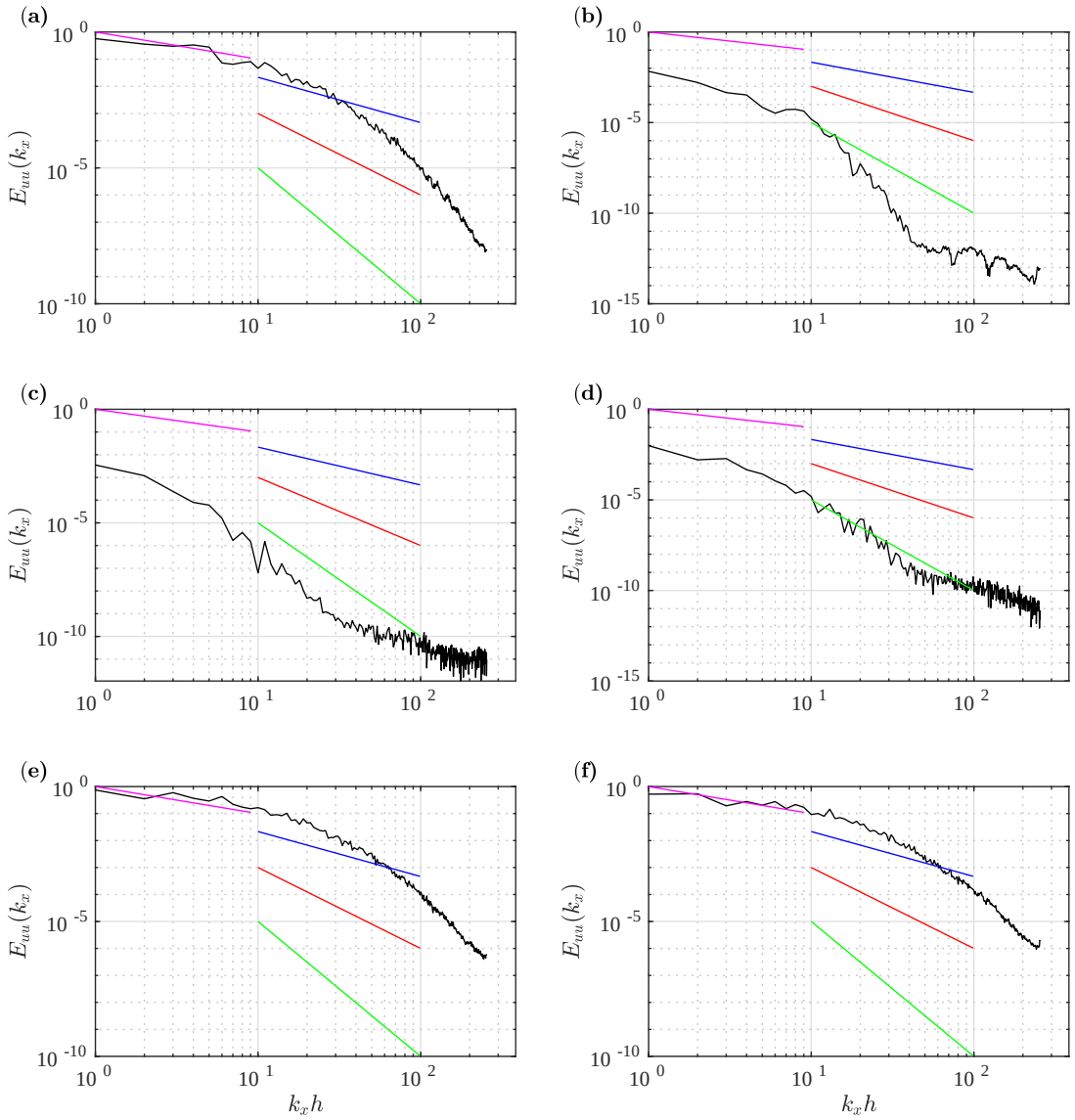

Figure 3.15: Longitudinal spectra of streamwise kinetic energy $E_{uu}(k_x)$ at $z^+ = 15$ at different times in a sub-box corresponding to a quiet region at maximum decay, which is $5\pi/6 \leq y/h \leq \pi$. Times correspond to (a) $t^o = 0.1$,(b) $t^o = 3.7$, (c) $t^o = 8.7$, (d) $t^o = 14$, (e) $t^o = 23.7$, and (f) $t^o = 32.9$, respectively. Magenta, blue, red, and green lines have slopes of -1, -5/3, -3, and -5, respectively.

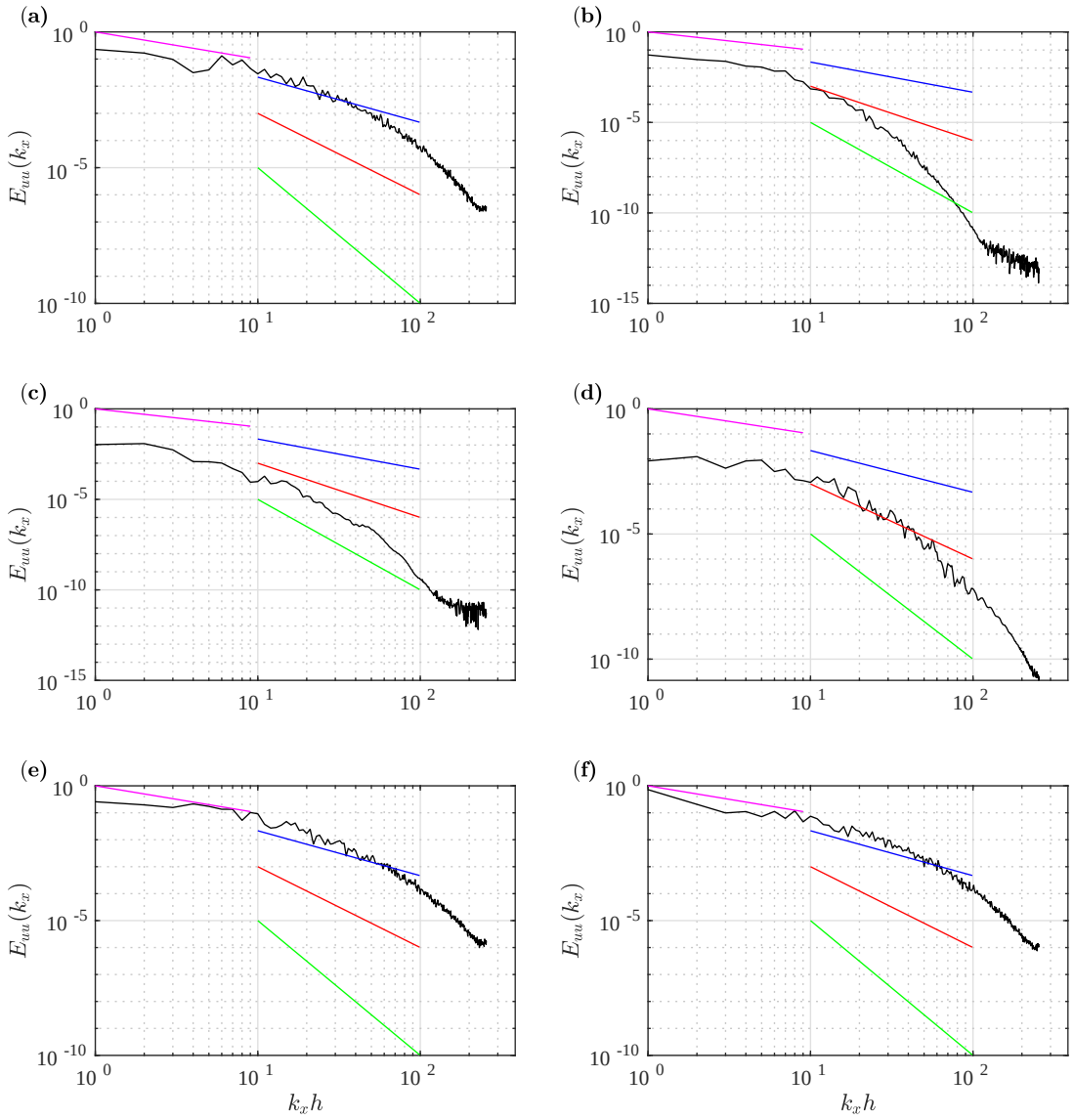

Figure 3.16: Same as Fig. 3.15 but for $z^+ = 70$.

The one-dimensional longitudinal spectra of streamwise velocity, averaged over y at $z^+ = 15$, are shown in Fig. 3.15. Spectra are averaged in y over regions that become quiet during the decay and recovery phase. As expected, initially, the spectrum shows an approximate $k_x^{-5/3}$ behavior over $10 \lesssim k_x h \lesssim 100$, where k_x is the streamwise wave number. During decay as shown in Fig. 3.15(b), the spectrum become steeper over these wave numbers as turbulence is suppressed. The slope of the spectrum increases in the recovery phase as shown in Fig. 3.15 (c,d). However, for about 5 eddy turnover times the slope of the spectrum is approximately -5 as shown in Fig. 3.15 (c,d), similar to viscously coupled stratified turbulence [141, 140]. In the logarithmic region, the steepening of the spectrum is weaker compared to the near-wall region and the slope of spectra becomes approximately -3 as shown in Fig. 3.16(a-f). The smallest wavenumbers present k_x^{-1} behavior initially (Figs. 3.15a and 3.16a), and once turbulence is recovered (Figs. 3.15e-f and 3.16e-f).

The behavior of the spectra suggests that the quiet regions may consist of viscously layered pancake vortices, where vertical fluctuations are strongly suppressed by stable stratification and the vertical scale of the eddies is set by viscosity [26, 140]. In this regime, the Ozmidov scale is smaller than the Kolmogorov scale, where the Ozmidov scale is defined as $L_o = (\epsilon/N^3)^{1/2}$. The buoyancy Reynolds number, which is related to the ratio of Ozmidov to Kolmogorov scales, is defined as [34],

$$Re_B = \left(\frac{L_o}{\eta}\right)^{3/4} = \frac{\epsilon}{\nu N^2}, \tag{3.5}$$

where $\eta = (\nu^3/\epsilon)^{1/4}$ is the Kolmogorov scale. Re_B can be used to detect regions of viscously coupled pancake vortices: regions where $Re_B \ll 1$ correspond to viscously layered vorticies, and regions where $Re_B \gg 1$ contain overturning and small scale vortices. Plots of horizontally-averaged Re_B in the quiet regions and the turbulent strip are shown in Fig. 3.17. At $tu_\tau/h = 0.1$, these two regions have the same Re_B due to spanwise homogeneity of the turbulence at this time. For both of these regions, $Re_B > 1$ where $z^+ > 10$. At later times, until turbulence is fully recovered, Re_B in the quiet region is smaller than Re_B in active region. During the decay phase as shown in Fig. 3.17(b), Re_B in both regions is reduced. In the turbulent strip, $Re_B < 1$ for up to $z^+ \approx 60$ while in the quiet region, $Re_B \ll 1$ even up to $z^+ \approx 200$. The steepening of the spectrum corresponds to a reduction in Re_B. When the slope of $E_{uu}(k_x)$ is close to -5 in the quiet region during recovery (Fig. 3.15c-d), Re_B in the same region is $O(10^{-4})$, which is two orders of magnitude smaller than Re_B in turbulent strip. Once turbulence is fully recovered, Re_B for these two regions become similar again.

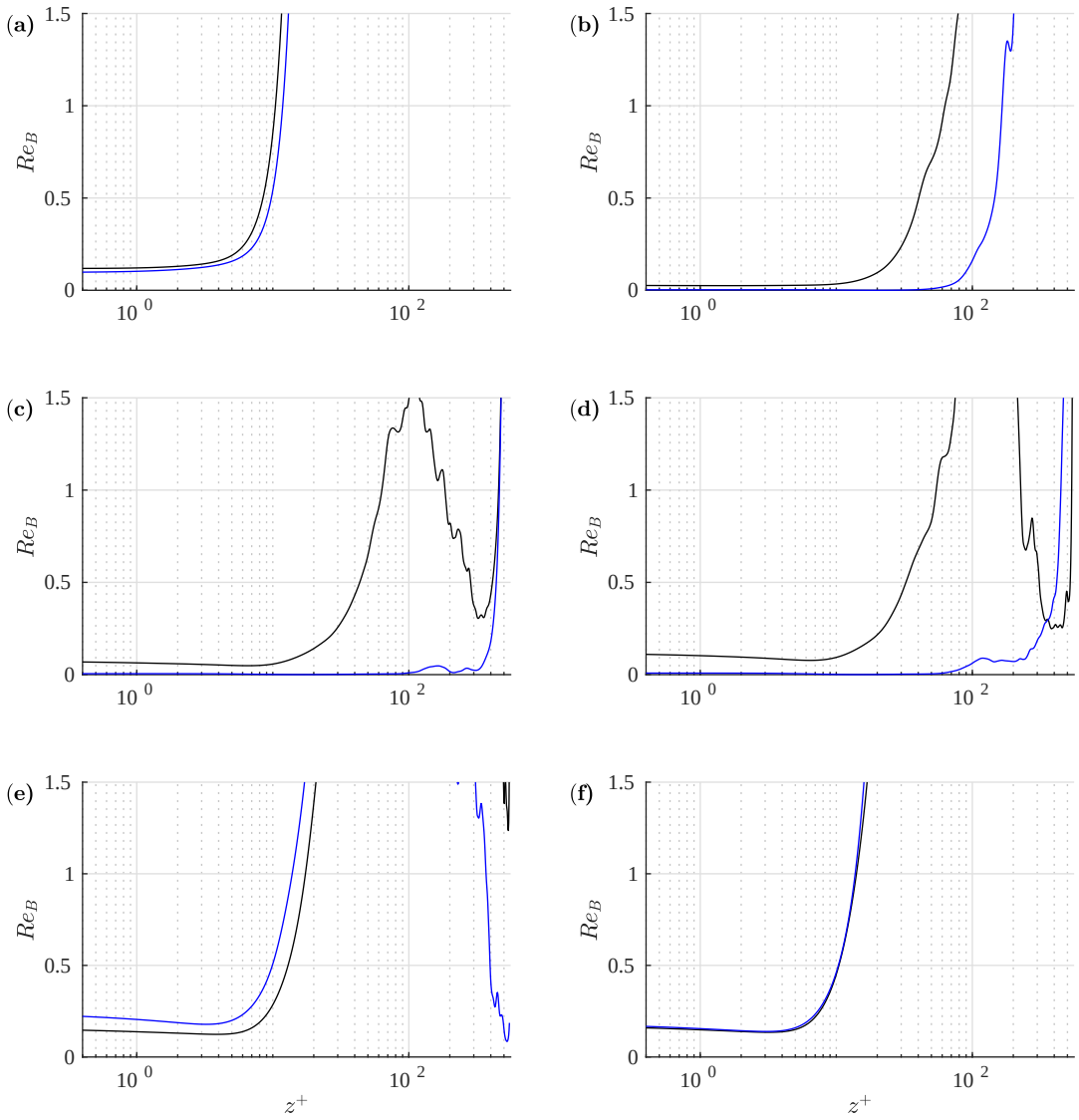

Figure 3.17: Buoyancy Reynolds number computed in quiet region (blue lines) where $5\pi/6 \leq y/h \leq \pi$ and active regions (black lines) $\pi/3 \leq y/h \leq 2\pi/3$. Times correspond to (a) $t^o = 0.1$,(b) $t^o = 3.7$, (c) $t^o = 8.7$, (d) $t^o = 14$, (e) $t^o = 23.7$, and (f) $t^o = 32.9$, respectively.

3.3.7 Effect of upper thermal boundary condition

The results shown thus far were obtained using a neutral boundary condition for heat transfer from the upper boundary of the SBL. If heat entrainment from the upper boundary is permitted, it may affect the decay and recovery of turbulence, since heating the SBL from the top leads to the formation of a capping inversion [36, 31].

In Flores and Riley [46], a Dirichlet boundary condition for temperature was used at the upper boundary. In their $Ri = 1120$ simulation initialized from a neutral case, only the experiment perturbed with 5 percent higher-than-average TKE in the outer region could recover. Here, we observed that C5 can recover from partial collapse without perturbations to the initial condition. This suggest the SBL upper boundary condition can play an important role when strong cooling from the bottom surface is imposed. To investigate this, we carried out another simulation with initial condition and parameters identical to C5, but with a Dirichlet boundary condition ($\theta = 0$) at the upper boundary (case C5D). In Fig. 3.18(a), a time series of the domain-integrated TKE for this case is shown and compared to that from C5. Although heat entrainment from the upper boundary leads to a decrease in decay rate up to $t^o = tu_\tau^0/h \approx 4$, the time of recovery in C5, the C5D case continues decaying after this time. This finding strongly suggests that the impact of the upper boundary condition on outer layer dynamics influences recovery, since (as shown earlier) recovery in C5 is strongly linked with outer layer large-scale structures. It should be pointed out that in C5D, turbulence become patchy as well shortly after introducing stratification. Nevertheless, by $t^o \approx 6.8$ near-wall streaks disappear in C5D as decay continues. For example, the value of TKE at $z^+ = 15$ becomes almost two orders of magnitude smaller than in C5 at same time, as shown in Fig. 3.18(b). The shift in TKE for C5D toward higher z^+ is likely a result of laminarization, where wall shear is strongly reduced and the boundary layer cannot accommodate a buffer layer. In laminarization of the boundary layer, the buffer layer is not capable of sufficient turbulence production to overcome dissipation caused by viscosity. Thus, the energetic eddies are located farther from the wall since viscous dissipation is reduced moving from the wall towards the channel center.

3.4 Conclusion

In this chapter, the response of wall turbulence to strong surface cooling was studied using high-resolution DNS. It was shown that the cooling process can be divided into different phases depending on the cooling rate. Turbulence first undergoes decay regardless of the

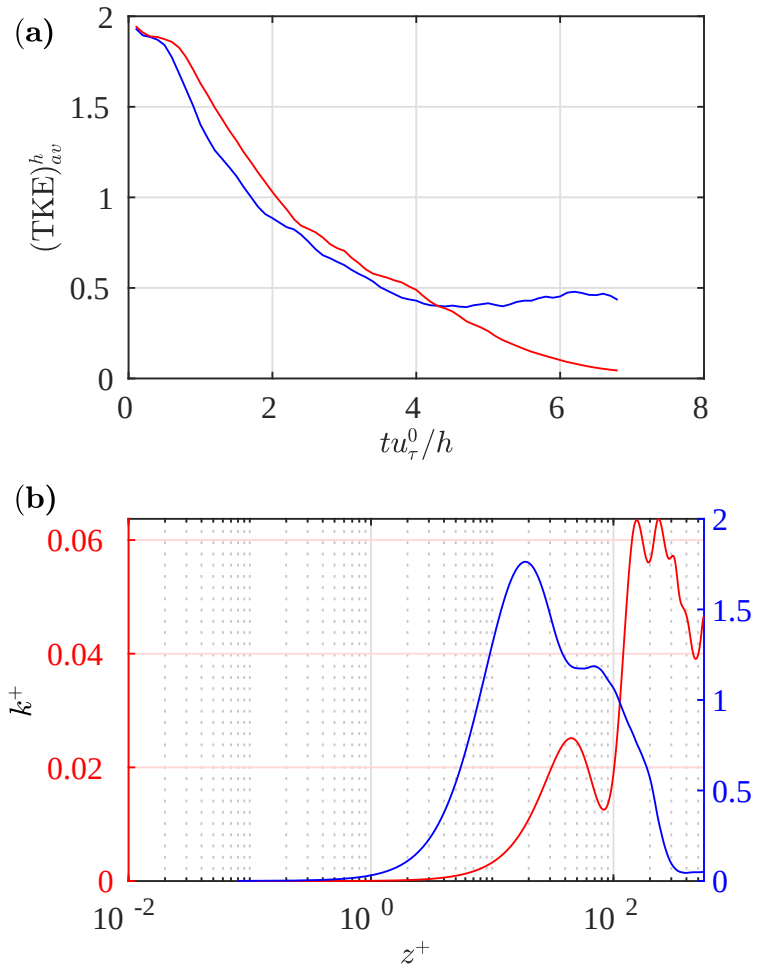

Figure 3.18: Effects of the upper boundary condition on (a) domain integrated TKE and (b) TKE profile at $t^o(= tu^0_\tau/h) = 6.8$ for C5 (blue) and an analogous simulation (C5D) with Dirichlet boundary conditions at the upper boundary (red, with $\theta = 0$ at $z = h$).

imposed cooling rate. However, recovery largely depends on the cooling rate. For a weaker cooling rate, turbulence is ubiquitous at all vertical levels, consistent with previous studies [52, 130]. In this situation, TKE recovers to a level comparable to the neutral case. For stronger cooling rates, TKE reaches values during recovery that are higher than those in the neutral case. In these strongly stratified cases, turbulence may collapse partially with the SBL turbulence becoming patchy, or turbulence may collapse totally.

For patchy turbulence ($Ri = 1120$), it was shown that during decay, the viscous sublayer grows to $z^+ \approx 15$ and the buffer region shrinks as the boundary layer grows. However, logarithmic behavior is observed up to $z^+ \approx 100$ at all times, with slope and additive constants that depend on time.

For $Ri = 1120$ (case C5), a thorough analysis of the TKE budget confirms that the dominant balance is between production and dissipation at all times. It was shown the appearance of patchiness is due to a significant reduction in turbulent production (due to direct impact of stable stratification on tangential Reynolds stress), and not excess dissipation. This reduction in production is then linked to a decrease in the population and intensity of quasi-streamwise vortical structures. During decay and part of the recovery phase, a quiet region appears in the near-wall region with width between $[1 - 1.5]h$.

It was shown that the quiet regions outside of the turbulent strip actually resemble viscously layered stratified turbulence, with layered vortices, suppressed vertical momentum flux, and $Re_B \ll 1$. In these regions, longitudinal spectra of streamwise velocity shows k_x^{-5} behavior in the buffer layer and k_x^{-3} in the logarithmic layer.

In the most stratified case with $Ri = 2800$ (case C6), the inner layer turbulence is completely suppressed and the outer layer turbulence decays subsequently, leading to the formation of flat structures in the near-wall region and pancake-like vortices in the outer layer.

The recovery of turbulence in C5 is discussed in detail. One might say for this Richardson number ($Ri = 1120$) the autonomous cycle of near-wall turbulence, where turbulence in the near-wall region can autonomously sustain itself without intervention of eddies from the core region[72], is partially or totally hindered in the decay phase by the action of strongly stable stratification. In C5, however, the outer layer large scales of size $\lambda_z^+ \gtrsim 300$ have enough intensity to excite the partially damped turbulence in the inner layer, which can restart the inner layer regeneration cycle [57, 72]. In C6 ($Ri = 2800$) this autonomous cycle of near-wall turbulence is suppressed completely as near-wall streaks are damped soon after starting the cooling process.

The effect of higher Reynolds number, Richardson numbers, and larger domain size on the characteristics of the patchy state, the evolution of TKE and vorticity, and possible

turbulence recovery will be the subject of future work. These simulations can improve our understanding of the more realistic SBL, in particular once turbulence becomes intermittent for strongly stable stratification. Moreover, in future work, it could be interesting to explore non-OBA effects on strongly-stable stratified wall-bounded flow by solving the Navier-Stokes equations under the low Mach number approximation [53].

Chapter 4

Quasi-stationary dynamics

In this chapter characteristics of wall turbulence subjected to stable stratification at times from starting surface cooling (quasi-stationary state) are investigated. This chapter is based on Ref. [8].

4.1 Introduction

Turbulence in the stably stratified ABL involves complexities such as spatio-temporal intermittency [7, 58, 94, 145, 46, 50], microfronts [94, 95], and gravity wave breaking [94], which are not yet completely understood. These complexities can be studied by simulating stably-stratified wall-bounded shear-flow (e.g. stratified channel flows) as an idealized model for the stable atmospheric boundary layer.

For such idealized models, wall-modelled LES studies of the ABL in rotating reference frames [61] have shown that an increase in stable stratification leads to stronger vertical gradients of the mean temperature, a decrease in vertical turbulent momentum flux, an increase in vertical turbulent temperature flux, and a ABL that is typically shallower [61, 142]. The integral length scale and turbulence production decrease as stratification increases [61].

The effects of stratification on the budget of turbulent kinetic energy (TKE) have been studied for quasi-stationary turbulence with LES [52, 4, 130] and non-stationary turbulence with direct numerical simulations (DNS) [48, 7]. Furthermore, the recent experimental study of Williams *et. al* [142] of stably stratified turbulence over a flat plate has shown that increasing stratification is associated with strong reductions in tangential Reynolds

stress, leading to the collapse of turbulence production by mean shear. The motions that contribute to negative Reynolds stress and positive turbulence production due to mean shear (Q2 and Q4 events [25, 3]) are most affected by stratification. The ejections (Q2) are damped and sweeps (Q4) are not significantly affected by stable stratification. The motions that contribute to positive tangential Reynolds stress and negative production ($Q1$ and $Q3$ events) are less affected.

Taylor *et. al* [130] performed an LES study of open channel flow at friction Reynolds number $Re = 400$ with imposed negative density gradient at the top and zero density gradient at the bottom for relatively weak stratification up to friction Richardson number $Ri = 500$ and Prandtl number $Pr = 5$. The velocity fluctuations in the inner layer of the bottom boundary layer are not significantly influenced by stratification in their results. This minimal dependence of near-wall velocity fluctuations on stratification raises a question regarding the location of the imposed density gradient. If the density gradient (source of strongly stable stratification) were placed on the bottom wall, which is where the turbulence is generated by shear, would the turbulence be more affected by the stratification? Here, we address this question for open channel flow at quasi-stationarity, which was also the state investigated in Taylor *et. al* [130]. While there are a number of relatively recent DNS studies that have also addressed this question, these studies used either a closed channel [50, 58] or an open channel with fixed top temperature [46, 36, 37, 48]. From the perspective of a nocturnal ABL, an open channel is the more relevant idealized case. In the latter studies, stratification is imposed on both the bottom wall and the upper boundary. However, these latter studies did not discuss characteristics of the strongly stable regime. By strongly stable, we mean stratification that is strong enough to cause intermittency or full collapse and relaminarization of fully developed turbulence shortly after stratification is introduced; this perspective is motivated by earlier experimental [108, 142] and numerical studies [46, 50, 58].

In the case of strong stable stratification, an important question is how strongly stratified turbulence that recovers from possible collapse compares to weakly or neutrally stratified wall-bounded turbulence.

Apart from bottom cooling, heat entrainment from the upper boundary layer for strong stable stratification can significantly affect boundary layer dynamics as a result of the strong capping inversion [31, 143, 37, 36] that develops in the lower part of the boundary layer beneath [7]. In the real nocturnal ABL the capping inversion controls the boundary layer height [31]. It is therefore also important to address the impact of heat entrainment from the upper boundary on the characteristics of wall-bounded turbulence.

Here, we mainly examine the quasi-stationary state, which may nevertheless inform

our perception of evolving stable boundary layers, which are usually complicated by the dependence of the turbulence statistics upon time. The main themes of the present work are as follows: 1) characterizing first and second-order statistics and relevant length scales of wall-generated turbulence under strong stable stratification at a quasi-stationarity state with a focus on the near-wall region where turbulence has been shown to be largely affected by buoyancy earlier in the surface cooling process [7], 2) investigating the impact of a capping inversion, and 3) analyzing sensitivity to the choice of computational domain size. The rest of the chapter is divided into three sections. In Sec. 4.2, the governing equations are presented and the numerical approach is briefly discussed. The results are shown in Sec. 4.3. The notion of "strong stable" stratification is first discussed in the context of the current study in Sec. 4.3.1. We then study the effect of stratification on the first and second-order statistics and TKE in Sec. 4.3.3. Then, mixing and stratification effects are diagnosed using non-dimensional numbers in Sec. 4.3.4. The TKE budget is presented and discussed in Sec. 4.3.5. Kinetic energy redistribution is addressed in Sec. 4.3.6. After studying the TKE budget, turbulence production is explored in Sec. 4.3.7. Typical length scales for stratified wall-bounded turbulence are introduced and investigated in Sec. 4.3.8 and in Sec. 4.3.9. Higher-order statistics are examined in Sec. 4.3.10. The results section concludes by reviewing the sensitivity of some of the diagnostics to heat entrainment from the upper boundary in Sec. 4.3.11 and computational domain size in Sec. 4.3.12. The chapter ends with conclusions in Sec. 4.5.

4.2 Governing equations and methodology

In this work, the non-dimensional Navier-Stokes equations under the Oberbeck-Boussinesq approximation (OBA) are used.

Five main high-resolution simulations (C1-C5) with $Re = 560$ are performed in this study, as presented in Table 4.1. For these simulations the domain size is $L_x = 2\pi$, $L_y = \pi$, and $h = 1$ and grid spacings based on wall units are $\Delta x^+ = 4.6$, $\Delta y^+ = 2.3$ in the horizontal directions, and $\Delta z^+ \in [0.08 - 3.3]$ in the vertical. Plus unit are scaled by Reynolds number, e.g. $\Delta z^+ = \Delta z\ Re$. Simulations include one unstratified case (C1) and four stratified cases (C2-C5), with Ri ranging from 0 to 1120. The time step is $\Delta t = 0.0002$ in C1 and C2 and $\Delta t = 0.00015$ for C3-C5. The stratified cases C2-C5 are initialized from an output of the neutral case C1 within the quasi-stationarity state. The unstratified case is run for a total of 53 outer layer time units $t^d = t/t^o$, where $t^o = h/u_\tau$ is in order of the time scales of the outer layer eddies and u_τ is the friction velocity based on the value of the mean shear at the wall and h is the channel height. After initialization, cases C2, C3, C4, and C5 are run

for 49, 48, 55, and 62 outer layer unit times, respectively.

The temporal evolution of TKE $k = \overline{u_i' u_i'}/2$, where $u_i' = u_i - \overline{u}_i$ and mean kinetic energy (MKE) $K = \overline{u}_i \overline{u}_i/2$ integrated over the domain are shown in Fig. 4.1 for C1-C5. Overbar denotes averaging over horizontal directions and time throughout this chapter (except for explicitly stated quantities that are time dependant, for which overbar denotes horizontal averaging only). It can be seen that, during the last 12 time units, a quasi-stationary state is reached for the cases considered here. Therefore the reported quantities in this study are averaged over the last 12 time units. Moreover, as shown in Fig. 4.1, the stratified cases take more time to reach quasi-stationarity due to the increase of flow time scales caused by stable stratification [7].

Note that the qualifier "quasi" is used since the domain-averaged temperature decreases due to the boundary conditions [130] (pure cooling) for C2-C5 and does not reach stationarity. Nevertheless, this decrease does not affect the buoyancy frequency, mean velocities, and fluctuating fields, which all appear stationary as shown in Fig. 4.1 [7].

Additional simulations are performed to investigate the effect of very strong stratification (C6), computational domain size (C5DC, L5D) and the upper thermal boundary condition (C2D, C5D). Turbulence in case C6 collapses and does not recover (Fig. 4.1), which shows that Ri in C5 is approximately the maximum at which near wall turbulence may recover to quasi-stationarity. This case is run for 30 outer layer unit times. For C5DC and L5D $\Delta x^+ = 9.2$, $\Delta y^+ = 4.6$, and $\Delta z^+ \in [0.32 - 6.3]$. For cases C2D, C5D, and C6, the same grid spacings as in C1-C5 are used. For C2D, C5D, and C6, the time step is $\Delta t = 0.00015$, while $\Delta t = 0.0003$ is used for C5DC and L5D. The case C5DC is initialized by sampling the output of C5D at the time TKE become quasi-stationary on a grid that is two times coarser in each direction. Using the output of C5DC at quasi-stationarity, case L5D is initialized by periodically extending the output of C5DC by 8 times in the streamwise direction and 6 times in the spanwise direction. The BC column in Table I refers to the choice of upper thermal boundary condition where N refers to Neumann ($\partial\theta/\partial z = 0$) and D refers to Dirichlet ($\theta = 0$). The latter leads to entrainment of heat from the upper boundary.

The h/L_{MO} in Table 4.1 refers to the ratio of Monin-Obukhov scale to channel height, where the MO scale L_{MO} is (in terms of dimensionless quantities)

$$\frac{L_{MO}}{h} = \frac{RePr}{\kappa Ri}, \tag{4.1}$$

and $\kappa \approx 0.41$ is the von Kármán constant. More details for simulations C1-C5 are given in chapter 3 and also in Atoufi *et. al* [7]. All parameters and diagnostic quantities are dimensionless.

Table 4.1: Parameters of simulations

Case	Re	Ri	h/L_{MO}	L_x/h	L_y/h	t_f	BC	N_x	N_y	N_z
C1	560	0	0	2π	π	53.2	N/N	768	768	384
C2	560	560	0.41	2π	π	48.5	N/N	768	768	384
C3	560	697	0.51	2π	π	47.7	N/N	768	768	384
C4	560	833	0.61	2π	π	55.19	N/N	768	768	384
C5	560	1120	0.82	2π	π	62.6	N/N	768	768	384
C6	560	2800	2.05	2π	π	30.9	N/N	768	768	384
C2D	560	560	0.41	2π	π	40	N/D	768	768	384
C5D	560	1120	0.82	2π	π	60	N/D	768	768	384
C5DC	560	1120	0.82	2π	π	140.8	N/D	384	384	192
L5D	560	1120	0.82	8π	6π	70.9	N/D	1536	2304	192

4.3 Results

4.3.1 Strength of Stratification

Before we discuss the results, let us clarify what we mean by "strong stable stratification" within the context of the current study, as we often use this terminology. The classification of stable stratification regimes in this work, as a result of wall cooling, is determined by the transient state. The time evolution of cases C1-C6 in Fig. 4.1 show that distinct phases exist in the cooling process, which we discuss in detail in chapter 3 and [7]. These cases undergo an initial decay that lasts for 4-6 (outer layer eddy) turnover times, where the longest decay phase corresponds to the strongest stable case, C6, considered here. The next phase is recovery, when turbulence recovers from the initial decay caused by the stable stratification. The recovery phase is generally longer than the decay phase, and simulations with higher Ri take longer to recover from the initial decay. For instance, the recovery phase for C5 is $4 \lesssim tu_\tau^0/h \lesssim 45$, which highlights the significance of stable stratification in increasing the time scale of the energy-containing eddies during the decay phase.

The recovery of the more strongly stratified cases C4 and C5 behave differently when compared to the more weakly stratified cases C1-C3, which suggests that C4 and C5 are in a different stable stratification regime. In these two cases, the domain integrated MKE and TKE (Fig. 4.1) show an overshoot in the recovery phase of the cooling process, which is different from C2 and C3 where quasi-stationarity is asymptotically approached without such overshoots. Moreover, for C4 and C5, the initial decay of TKE (Fig. 4.1b) is larger than C2 and C3. In particular, in C5, the effect of stratification is strong enough to cause

partial collapse of turbulence for almost 20 turnover times. Due to these differences, we mark stratification regime for C4 and C5 as strongly stable. In C6, stratification is so strong that the flow does not recover to a turbulent state and fully collapses.

The Ri for C5 and C6 lie in the region of strongly-stratified turbulence in the $(Re - Ri)$ space diagram for stably stratified wall-bounded flows given by Zonta and Soldati [145] based on previous DNS studies. The impact of this strong stratification on flow structures in the inner-region is visualized in Fig. 4.2. For weak stratification (C2) turbulence covers the entire domain (Fig. 4.2a). As Ri increases (C5), the flow become patchy (Fig. 4.2b). In C6, turbulence fully collapses and flow at all heights [7] consists of layered horizontal vortices with small intensities (Fig. 4.2c).

Flores and Riley [46] also simulated open-channel flow with the same parameters and bottom boundary condition as in C5 and used a Dirichlet boundary condition at top. They found the stratification in this case to be strong enough to cause intermittency. However, and as we will show in this study, despite the fact that the impact of stratification on the flow is strong in the decay and recovery phase, when quasi-stationarity is reached, the impact of stratification is weak.

The friction coefficient is defined as the ratio of the wall shear stress to the kinetic energy of the bulk flow and is expressed as [130]

$$C_f = \frac{2\tau_w}{\rho u_b^2} = \frac{2u_\tau^2}{u_b^2}, \tag{4.2}$$

where $u_b = \frac{1}{h}\int_0^h \overline{u}\ \mathrm{d}z$ is the bulk flow velocity and overbar refers to averaging over the horizontal plane. Time series of the friction coefficient are shown in Fig. 4.1(d). The friction coefficient monotonically decreases with increasing surface cooling rate (increasing Ri), consistent with other studies of stably stratified boundary layers [142, 130, 4]. Similar to TKE, C_f also undergoes a rapid decay followed by recovery to a quasi-stationary value for each case. The C_f values for C6 also shows drastic decrease and no signs of recovery consistent will full collapse of turbulence across whole boundary layer.

4.3.2 Overall effects of stratification

4.3.3 First- and second-order statistics

In this section, we focus on the overall effect of stratification on characteristics of the quasi-stationary state for simulations C1-C5. The mean velocity profile is shown in Fig. 4.3a.

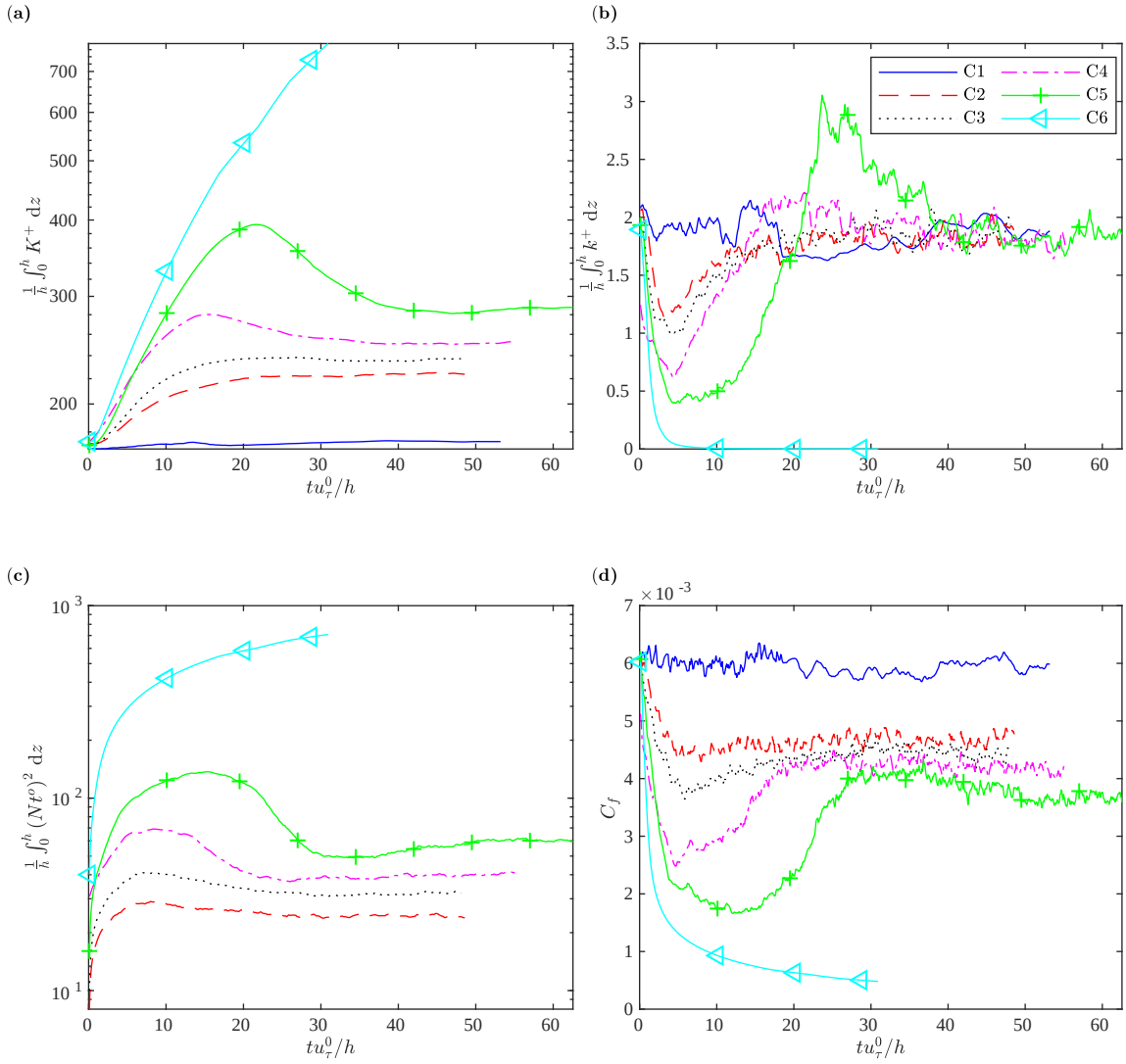

Figure 4.1: Time series of (a) domain integrated MKE, (b) domain integrated TKE, (c) domain-integrated buoyancy frequency, and (d) friction coefficient for C1-C6.

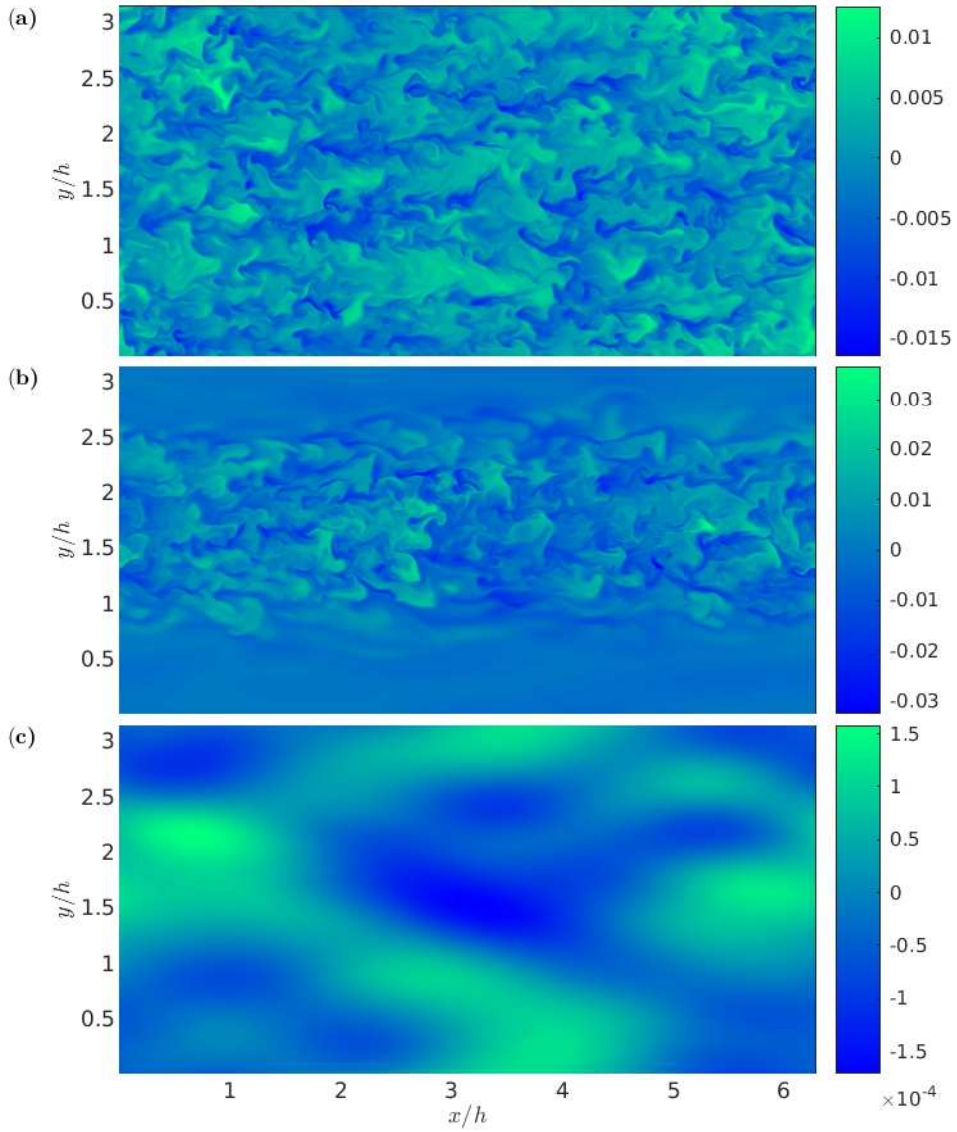

Figure 4.2: Instantaneous snapshot of fluctuating temperature at $tu_\tau^0/h = 14.7$ (time associated with turbulence recovery in C5) in $z^+ = 70$, for (a) C2 , (b) C5, and (c) C6.

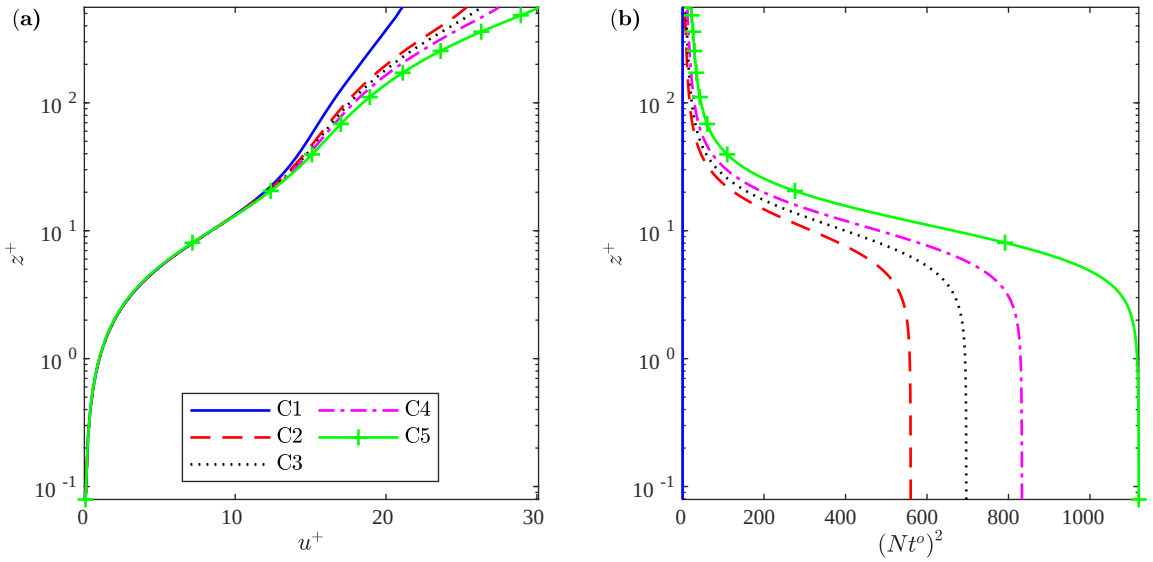

Figure 4.3: Horizontally averaged profiles of (a) streamwise velocity and (b) buoyancy frequency.

Increasing stratification (i.e. by increasing the bottom wall cooling flux by increasing Ri) increases the mean velocity above the buffer layer at $z^+ \gtrsim 30$; as will be shown below, this is a result of flow acceleration due to the decrease in wall shear stress (Fig. 4.7a). All cases exhibit log-linear behaviour of mean velocity for $30 \lesssim z^+ \lesssim 100$ with a monotonic increase of the slope of the log-linear profile as Ri increases. The mean velocity up to the end of the buffer region ($z^+ \lesssim 30$) is almost independent of stratification.

Profiles of the buoyancy frequency N^2, where

$$N^2 = Ri \, \frac{\partial \overline{\theta}}{\partial z}, \tag{4.3}$$

are shown in Fig. 4.3(b). In contrast to the mean velocity profiles, the effect of the cooling flux on the mean temperature gradient is greatest near the lower boundary. As expected, increasing Ri results in monotonic enhancement of N^2 near the wall, which becomes weaker moving upward. However, the dependence of N^2 upon Ri is much less pronounced above $z^+ = 100$. Therefore, for C2-C5, the buoyancy restoring force, which increases with Ri, is strongest at lower boundary and becomes weakest at the upper boundary.

One-point statistics of velocity fluctuations are shown in Fig. 4.4, and TKE is shown in Fig. 4.5. Generally, and similar to studies of weakly stratified cases [130], all cases show

similar profiles in the inner layer for $z \lesssim 0.2$ ($z^+ \leq 100$) and slightly different trends in the outer layer $z \gtrsim 0.2$ ($z^+ > 100$). For example, $\overline{u'^2}$ and $\overline{v'^2}$ above $z > 0.6$ decrease slightly as Ri increases. The decrease in $\overline{w'^2}$ with increasing stratification is consistent across the channel height.

The dominant contribution to TKE for $z \lesssim 0.1$ comes from $\overline{u'^2}$. Specifically, almost 85% of the TKE peak in the near-wall region comes from the streamwise velocity fluctuations. The maximum of this streamwise fraction of the TKE in the buffer region is reduced as stratification increases (zoomed-in box in Fig. 4.4a). However, above $z \approx 0.2$ the $\overline{u'^2}$ contribution is reduced to about 50% where the $\overline{v'^2}$ and $\overline{w'^2}$ contributions increase and reach about 30% and 20% of total TKE respectively up to $z \approx 0.9$.

Although the mean velocity profiles show clear differences, even in the buffer layer (Fig. 4.3a), the maxima of the velocity fluctuations with stratification are within 10% of those from the neutral case. The result here are consistent with the study of Taylor *et. al* [130] although we have used different boundary conditions by imposing the source of stable stratification on the bottom wall where turbulence is generated.

This degree of similarity between velocity fluctuations for different stratifications, even in the most strongly stable quasi-stationary case C5, for which turbulence partially collapsed at an earlier stage of the cooling process [7], strongly supports the idea that the destruction of TKE by stable stratification is a transient process as also discussed in Donda *et. al* [36, 37]. If turbulence passes the decay and recovery phases [7], the quasi-stationary characteristics of near-wall turbulence are generally similar to the weakly stratified case. This transient effect will be further discussed when the budget of TKE and tangential Reynolds stresses are introduced.

It is worth discussing some of the differences between cases C1-C5 and those in Donda *et. al* [36, 37]. For C1-C5 there is no heat flux from the upper boundary and the lower boundary is continuously cooled. Thus the maximum sustainable heat flux (MSHF) [36], which is an upper limit for effective heat transfer across the channel height to balance wall cooling, is zero in C1-C5. In Donda *et. al* [36, 37] it is hypothesized that a stably stratified wall-bounded flow with heat entrainment from the upper boundary has a non-zero MSHF beyond which turbulence collapses. As mentioned earlier, turbulence recovers from partial collapse in C5 [7]. Interestingly, turbulence recovers for other more strongly stratified cases with $Ri \lesssim 2000$, $h/L_{MO} < 1.4$ if properly initialized but not for $h/L_{MO} \gtrsim 1.5$ (not shown here). Therefore, in C2-C5, the flow is limited by a minimum shear capacity (MSC) as discussed in van Hooijdonk *et. al* [137] (and not a MSHF), below which turbulence production cannot be maintained and starts to collapse. This difference suggests investigating turbulence collapse based on shear production as a more reliable approach.

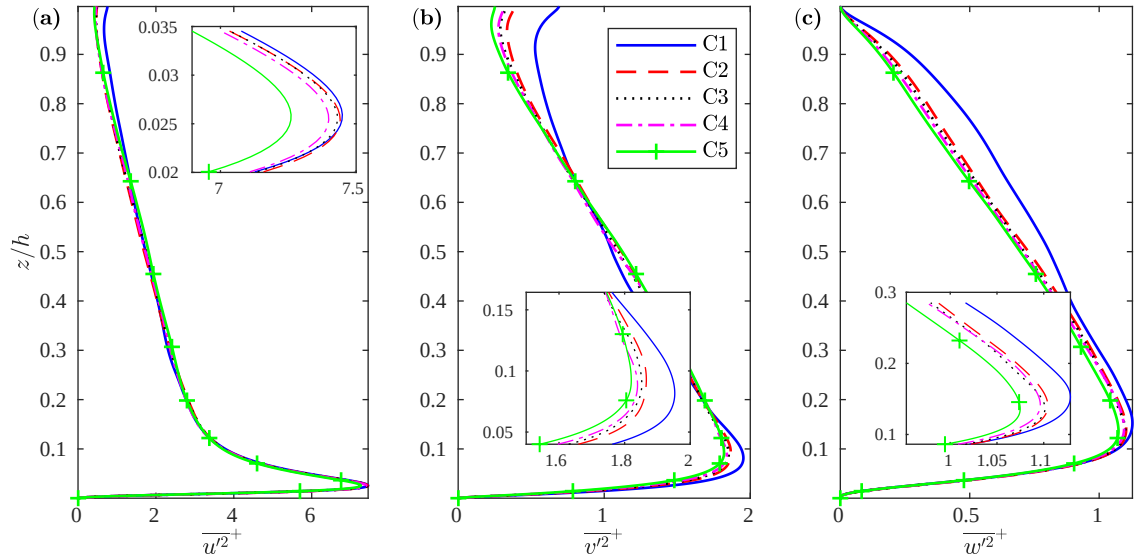

Figure 4.4: Second order moment of fluctuations of (a) streamwise velocity ($\overline{u'^2}$), (b) spanwise velocity ($\overline{v'^2}$), and (c) vertical velocity ($\overline{w'^2}$).

Moreover, compared to the work of Taylor and coworkers (Fig. 8 in Taylor *et. al* [130] and Fig. 4.4 here), after reaching quasi-stationarity the velocity fluctuations in the inner layer are not significantly sensitive to the location of the imposed stable stratification. Similar results are obtained whether it is imposed at the bottom wall where turbulence is being generated, or at the upper boundary where there is no source of turbulence production. This similarity among velocity statistics regardless of the choice where stable stratification introduced is due to the fact that shear dominates over buoyancy in the quasi-stationary state, as will be shown in Sec. 4.3.4.

Profiles of mean and root-mean-square (RMS) temperature are shown in Fig. 4.6. It is clear that increasing stratification results in more stable boundary layers. Temperature fluctuations are relatively small everywhere, with somewhat higher values as Ri increases. The effect of Ri become more clear in the outer layer as shown in Fig. 4.6b where wall-generated shear becomes less dominant.

The tangential Reynolds stress is shown Fig. 4.7(a). Stratification leads to a monotonic decrease of $-\overline{u'w'}$ at all heights. This decrease in $-\overline{u'w'}$ with increasing Ri explains the flow acceleration by stratification in Fig. 4.3a. Turbulent heat fluxes are shown in Fig. 4.7(b-c). The streamwise turbulent heat flux is an order of magnitude larger than the vertical heat flux. The larger values of streamwise turbulent heat flux are due to the fact

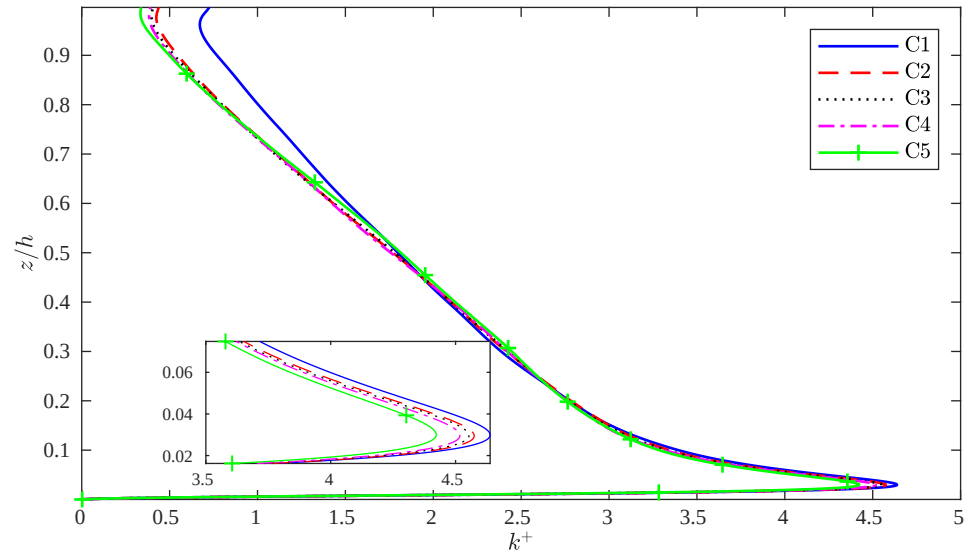

Figure 4.5: Turbulent kinetic energy profile.

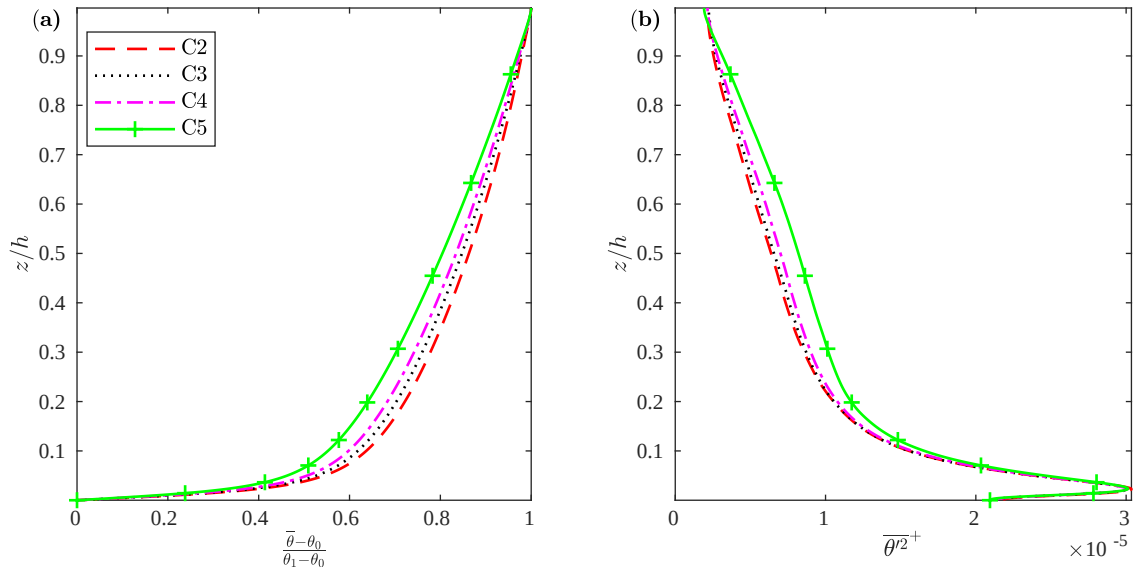

Figure 4.6: First and second order statistics for temperature field. (a) Mean, and (b) root-mean-square. The θ_0 and θ_1 in (a) are values of mean temperature at bottom ($z/h = 0$) and top boundary ($z/h = 1$), respectively.

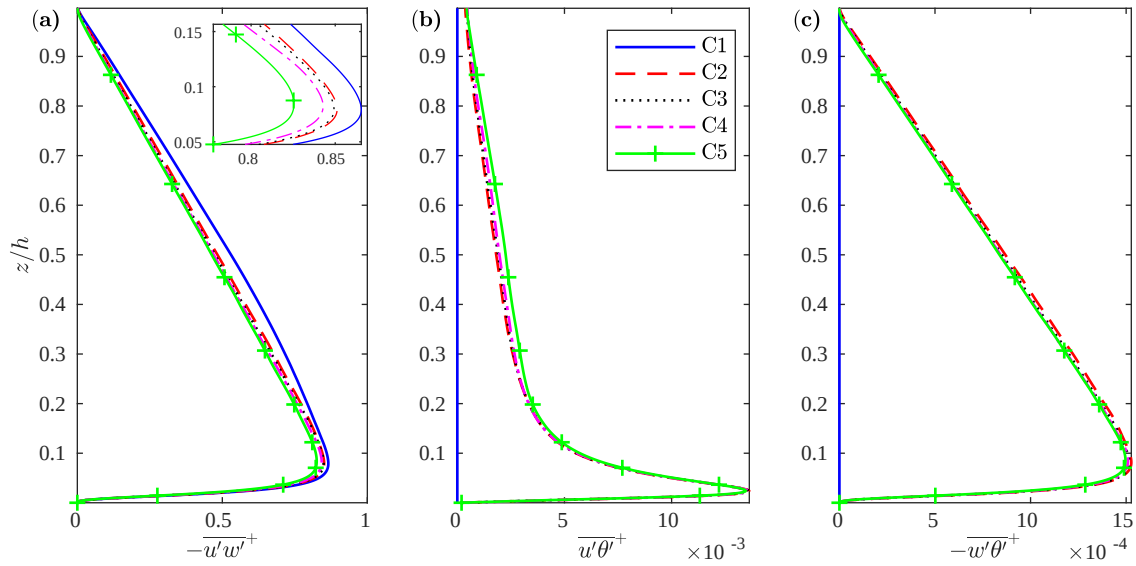

Figure 4.7: Second order moment of (a) streamwise-vertical velocity fluctuations, (b) streamwise velocity-temperature fluctuations, (c) vertical velocity-temperature fluctuations.

that streamwise velocity fluctuations are largest compared to the wall-normal and spanwise counterparts. Profiles of $\overline{u'\theta'}$ and $-\overline{w'\theta'}$ closely follow the profiles of $\overline{u'^2}$ and $\overline{w'^2}$ in Fig. 4.4(a,c) by a factor of $O(10^{-3})$ signifying small values for θ' correlating with u' and w'. Additionally, Fig. 4.4(a,c) and Fig. 4.7(b,c) together show that the normalized correlation between fluctuating streamwise velocity and temperature $R_{u\theta} = \overline{u'\theta'}/(\sqrt{\overline{u'^2}}\sqrt{\overline{\theta'^2}})$ is larger than the normalized correlation between fluctuating wall-normal velocity and temperature $R_{w\theta} = \overline{-w'\theta'}/(\sqrt{\overline{w'^2}}\sqrt{\overline{\theta'^2}})$. The larger normalized correlation between u' and θ' suggests that the effect of buoyancy is more pronounced in the evolution of the quantities that directly depend on $\overline{u'\theta'}$ (e.g. evolution of turbulence production) rather than $\overline{w'\theta'}$ (e.g. evolution of the variance of vertical velocity fluctuations).

Statistical signature of the turbulence at stationarity for the tangential Reynolds stress in C5 is shown in Fig. 4.8. The error bars show the standard deviation of $-\overline{u'w'}$ at each height in the entire time-averaging intervals and signifies the statistical variation of the $-\overline{u'w'}$ at different times. The maximum values for the standard deviation of the $-\overline{u'w'}$ over the time-averaging interval and across channel is 0.02 and shows fluctuation around the time-averaged profiles are small.

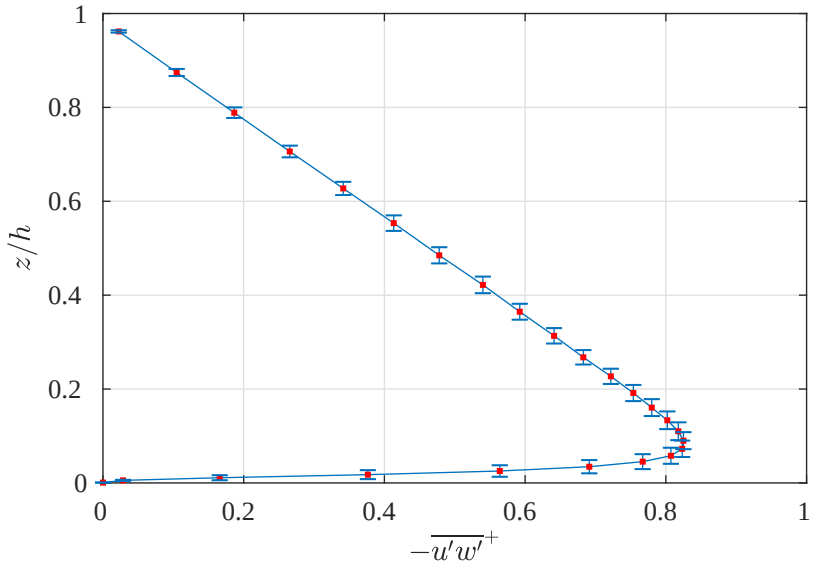

Figure 4.8: Error bar plot of $-\overline{u'w'}$ for C5 at stationarity. The error bars plotted based on standard deviation of the instantaneous tangential Reynolds stress over the averaging time interval.

4.3.4 Buoyancy Reynolds number and gradient and flux Richardson numbers

In this section, we aim to further explore the nature of stable stratification caused by wall cooling in C2-C5. To do so, we relate stratification effects to the mean shear and turbulence dissipation, which control the characteristics of the turbulence and thus momentum mixing. To reach this goal we use three different non-dimensional parameters by which stratification can be quantified: the buoyancy Reynolds number Re_b, gradient Richardson number (Ri_g) and flux Richardson number (Ri_f).

The buoyancy Reynolds number is defined as [34]

$$Re_b = Re\frac{\epsilon}{N^2}, \tag{4.4}$$

where horizontally and temporally averaged values are used for the kinetic energy dissipation ϵ and buoyancy frequency. Re_b is related to the ratio of the Ozmidov to Kolmogorov scales (both will be defined in Sec. 4.3.8), and quantifies the range of small scales that are not affected by stratification [85, 26]. Regions with $Re_b \gg 1$ include overturning, enhanced mixing, and more isotropic small-scale turbulence. Vertical profiles of Re_b are

shown in Fig. 4.9(a). Even in C5, the minimum value of Re_b is much larger than unity at all heights, showing that there are inertial range eddies that are not significantly affected by stratification [26], similar to a weakly stratified case. Therefore, features of near-wall turbulence are far from the viscously coupled stratified turbulence (VCST) regime with $Re_b < 1$ [7, 140, 141]. By contrast, at early times in C5, during the decay and early stages of the recovery phase, VCST was the dominant feature of the near-wall region, which had $Re_b < 1$ [7] (and also in chapter 3).

The gradient Richardson number is defined as [106, 50]

$$Ri_g = \frac{N^2}{S^2}, \tag{4.5}$$

where $S = \partial\overline{u}/\partial z$. The gradient Richardson number shows regions of the flow where either buoyancy or shear dominates. In shear-dominated regions, turbulence is enhanced and mixing becomes stronger. Only the regions above $z \approx 0.9$ satisfy the criteria $Ri_g > 0.25$ [106] and mean shear dominates everywhere else for all cases, as shown in Fig. 4.9(b). Therefore, it is expected that near-wall turbulence in the stratified cases is similar to that in the neutral case since Ri_g is relatively small for all stratifications. The small values for Ri_g near the wall are due to the fact that mean shear near the wall is very large and almost independent of stratification (Fig. 4.3a) in the quasi-stationary state. Therefore, Ri_g becomes very small near the wall $z < 0.1$ with only a small dependence on stratification.

The flux Richardson number is defined as [130]

$$Ri_f = \frac{-B}{-B + \epsilon}, \tag{4.6}$$

where horizontally and temporally averaged values are used for the viscous dissipation (ϵ) and buoyancy destruction (B) (these quantities will be defined and described in more detail below). Effectively Ri_f is the ratio between buoyancy destruction B and TKE production P, where the balance $P \sim -B-\epsilon$ is used to have meaningful values where P is small within the logarithmic and outer layer regions. Therefore Ri_f measures the work that is needed to overcome the destroying effect of stable stratification that may lead to reduction in momentum mixing [130]. The Ri_f in Fig. 4.9(c) increases with increasing stratification at all heights. Also, Ri_f increases when moving away from the wall until $z \approx 0.8$. Therefore, with increasing height, more work is needed to overcome the destroying effect of buoyancy until $z \lesssim 0.8$, showing that the outer layer is mostly affected by stratification. Mean shear production dominates buoyancy in the near-wall region and the effects of stable stratification become minimal where $z \lesssim 0.2$. Above $z \approx 0.8$, Ri_f becomes smaller due to the impermeable free-slip-wall at the upper boundary.

Now let us return to the discussion of strong stable stratification prior to quasi-stationarity. To complement our qualitative observation of collapse and recovery at early times [7] (Fig. 4.2, and chapter 3) we now quantify strong stable stratification with the gradient Richardson number, which gives a local measure of stratification strength. Profiles of Ri_g at different times in the inner region are shown in Fig. 4.10. It is important to note that although the quasi-stationary value of Ri_g in the inner layer ($z \lesssim 0.2$) are less than 0.1 for C2-C5 (Fig. 4.9b), Ri_g acquires higher values in this region at earlier times of surface cooling process (Fig. 4.10). The values of Ri_g (Fig. 4.10d) in the inner region for C5 reaches 0.2, which is close to the threshold of 0.25 [99, 60] for the stability of stratified shear flow. This is in agreement with the appearance of intermittency in this region at early times. In C6, Ri_g reaches 0.25 at early times (Fig. 4.10e) and turbulence in the near-wall region completely collapses (Fig. 4.1). The inner-region collapse of turbulence leads to full collapse of outer layer turbulence at subsequent times.

Due to the fact that turbulence in C6 fully collapses, leading to completely different boundary layer structures (e.g layered vortices as shown in Atoufi *et. al* [7] and chapter 3), quasi-stationarity is not reached for this case. Thus for the moderate Reynolds number considered here, the strongest surface cooling rate (set by Ri) which may be imposed on a neutral open-channel flow while allowing for the recovery of fully developed turbulence must be between C5 and C6, i.e. Ri between 1120 and 2800. The relatively high values for Ri_g in the inner region in C5 confirms the presence of strong stable stratification in this case earlier in the cooling process.

4.3.5 TKE budget

In this section, we aim to investigate the mechanisms that contribute to the TKE budget for quasi-stationary stably-stratified wall-bounded turbulence. The different terms in the TKE budget are defined in Appendix A and shown in Fig. 4.11: production P, dissipation ϵ, buoyancy destruction B, turbulent transport T, viscous diffusion D, and pressure work Π. It is noteworthy that buoyancy flux as sometimes used in the literature (e.g. Huang and Bou Zeid [61]) differs in sign from B. For clarity only cases C1, C3, and C5 are shown, and we focus on inner-layer balances where $z^+ \leq 100$. Although the major balance is between production and dissipation, stratification affects these two mechanisms only slightly. Overall, the behaviour is different from the transient case, where stratification has a significant impact on the evolution of TKE [7] (and also in chapter 3).

In general, the effects of stratification are more prominent going from the neutral case C1 to C2. For C2-C5, all of terms that contribute to the budget of TKE become close

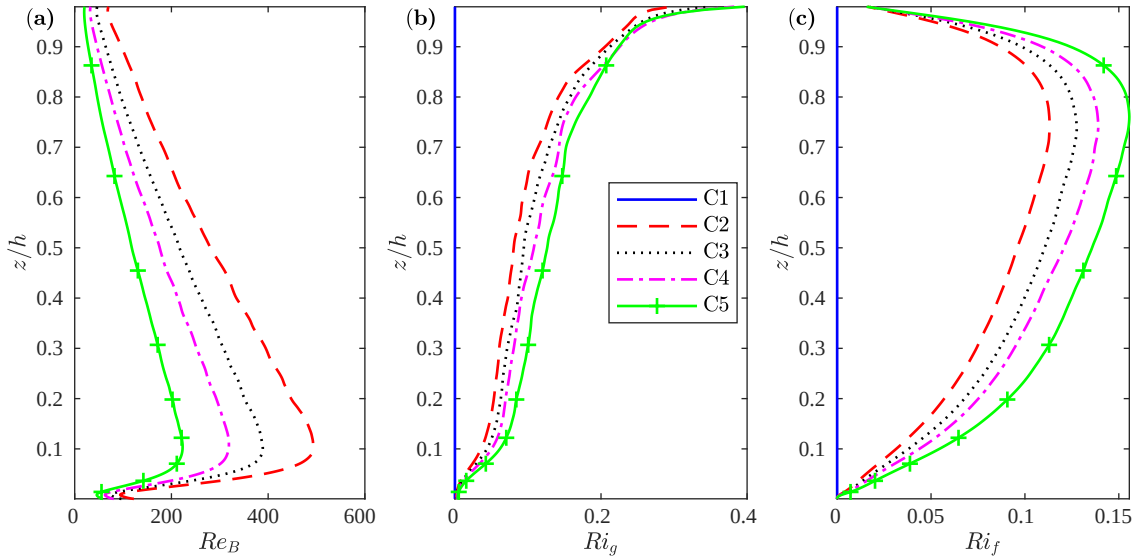

Figure 4.9: Vertical profiles of (a) buoyancy Reynolds number, (b) gradient Richardson number, and (c) flux Richardson number.

together even when Ri increases by a factor of two from C2 to C5, which causes partial collapse before turbulence reaches stationarity [7]. Production and dissipation vary only slightly with stratification. Turbulence production in the inner layer decreases with increasing Ri for $z^+ \gtrsim 20$ and increases with increasing Ri for $z^+ \lesssim 20$. (Fig. 4.11a). Except in the viscous sublayer (VSL) where $z^+ \lesssim 5$, dissipation decreases with increasing Ri. Stratification has a more significant effect on the smaller terms B, T, and Π. The buoyancy destruction B is an order of magnitude smaller than production and dissipation, which indicates that buoyancy destruction has a small impact on TKE exchange. The turbulent transport T is approximately equal to the transport of $\overline{u'^2}$ ($T \approx T_{11}$, see Appendix A.2). Interestingly, in the upper VSL, T decreases as Ri increases. Its magnitude also decreases in the buffer layer as Ri increases. As will be shown in Sec. 4.3.10, this change of T with stratification is consistent with weakening ejection and intensifying sweep events as Ri increases.

The pressure-work term Π [131, 28] describes the work that is associated with the pressure field that can modify the kinetic energy of fluid elements. In the VSL, viscosity plays a significant role and the kinetic energy is not sufficient to initiate lift-up of the fluid elements. The pressure-work Π (along with D) can amplify kinetic energy of fluid elements to be sufficiently large for lift-up and escape from such a highly viscous region as the VSL. The largest values for Π are limited to the VSL, where Π decreases as Ri increases. This

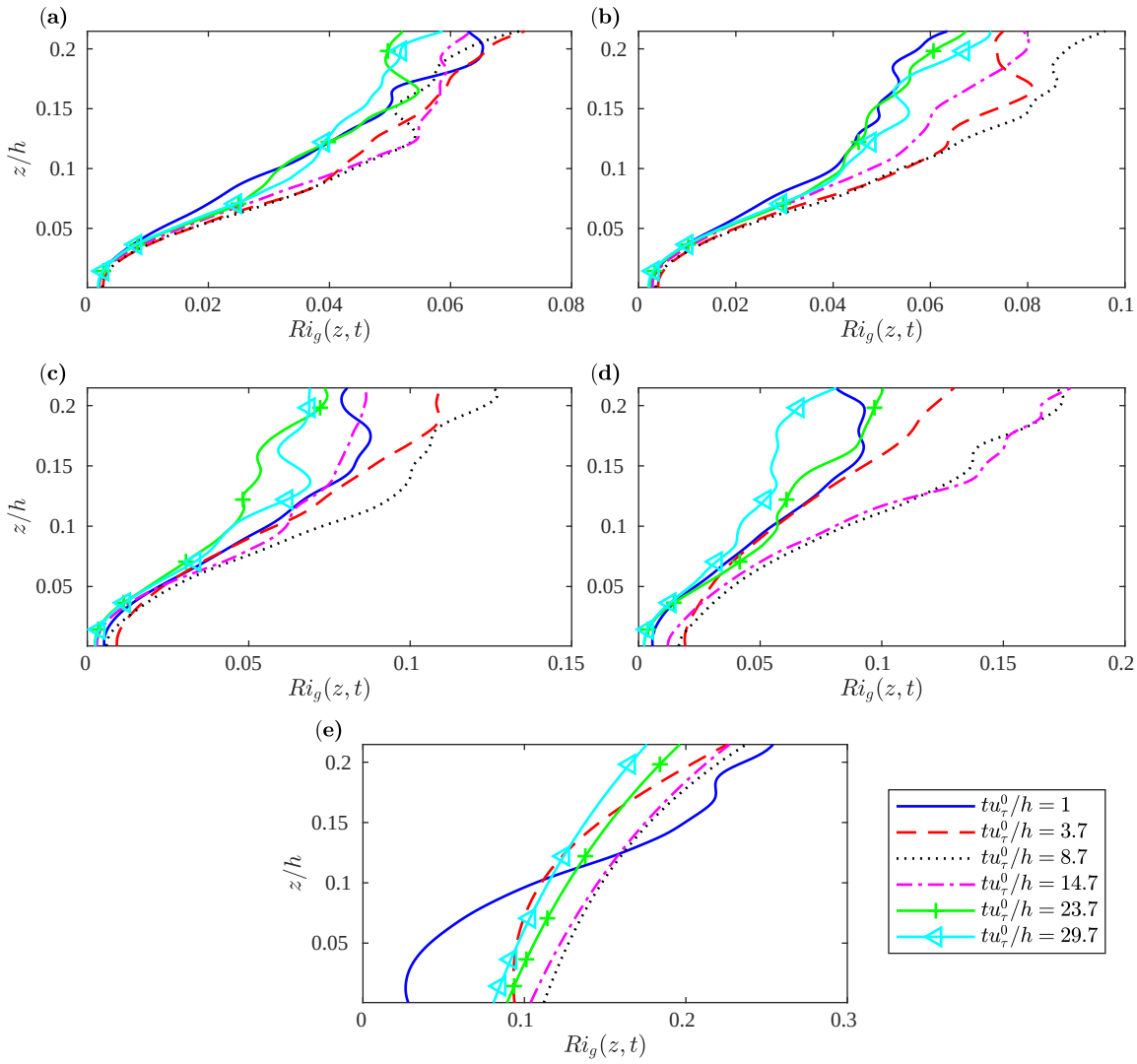

Figure 4.10: Changes of gradient Richardson number over inner region at different times for (a) C2, (b) C3, (c) C4, (d) C5, and (e) C6. The u_τ^0 refers to friction velocity of neutral case. The outer layer part is not shown for clarity since Ri_g obtains large values in this region during the decay phase and early recovery phase of the cooling process.

decrease in Π with increasing stratification signifies that the ability of fluid elements to lift-up from the lower part of the VSL is reduced as Ri increases.

In the VSL, viscous diffusion and pressure-work are energy sources. The net effect of these two TKE sources, along with dissipation, are transferred upward to the buffer layer by T. In the lowest part of the VSL $z^+ \leq 1$, where velocity fluctuations are small, D and ϵ balance each other. Thus, Π is the key mechanism in this part of the VSL to perform the work that is needed to transport fluid elements to the upper VSL where velocity fluctuations become stronger and T plays a more dominant role transferring TKE.

4.3.6 Inter-component energy redistribution

So far, we have explored the behaviour of the components of the velocity fluctuations and the TKE budget. An important question is how TKE is being distributed among horizontal and vertical components of velocity fluctuations. To analyze inter-component energy transfer at different vertical levels, the diagonal components of Φ_{ij} (Appendix A.2) are examined. The Φ_{ij} is defined as,

$$\Phi_{\mathrm{ij}} = \overline{\left(p' \frac{\partial u_i'}{\partial x_j} + p' \frac{\partial u_j'}{\partial x_i} \right)}, \tag{4.7}$$

and refers to pressure-strain mechanism leading to cross-component redistribution of velocity fluctuations. These terms can be used because continuity implies that the pressure-strain mechanism does not contribute to the budget of TKE and acts to redistribute among different portion of TKE.

Inter-component energy redistribution Φ_{ii} (no summation over i) is shown in Fig. 4.12. Overall, the dependence of the components of Φ_{ii} on z^+ is the same with stratification as without. In the lower part of the VSL $z^+ \lesssim 3$, Φ_{33} is a sink in the budget of $\overline{w'^2}$, and Φ_{11}, Φ_{22} are sources for $\overline{u'^2}$ and $\overline{v'^2}$ ($\Phi_{11}, \Phi_{22} > 0$). However, in that region Φ_{11} is small and TKE is transferred mostly from $\overline{w'^2}$ to $\overline{v'^2}$, showing that flow structures are becoming mostly lifted up. This flow of energy between fluctuating components may be due to vertical excitation of spanwise vortex rolls as in the early stage of hairpin vortex formation [17, 59]. In the upper VSL ($3 \lesssim z^+ \lesssim 5$), TKE is extracted from $\overline{w'^2}$ and $\overline{u'^2}$ and distributed into $\overline{v'^2}$, which suggests lifting up of the legs of quasi-streamwise hairpin vortex [3, 25]. These vortical structures become more streamwise aligned moving upward into the buffer layer as Φ_{11} becomes increasingly negative while Φ_{22} and Φ_{33} become more positive.

In the lower buffer layer where $5 \lesssim z^+ \lesssim 10$, Φ_{11} becomes a considerable sink in the budget of $\overline{u'^2}$ showing that flow structures become dominantly streamwise aligned

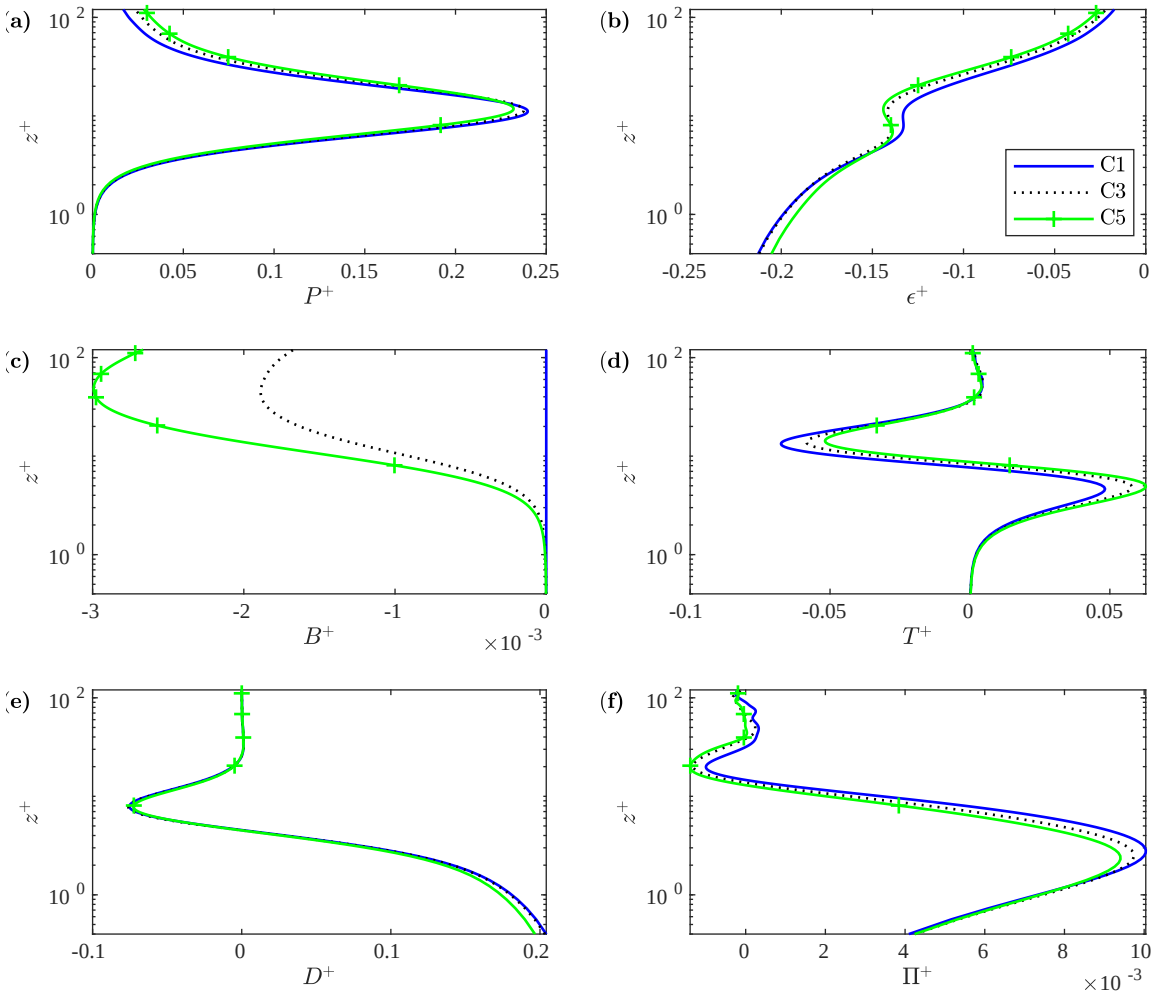

Figure 4.11: Different contributions to the budget of TKE: (a) production, (b) dissipation, (c) buoyancy destruction, (d) turbulent transport, (e) pressure-work, and (f) viscous diffusion. Each term is scaled by Re which is equivalent to conventional near-wall scaling by friction velocity u_τ and viscosity ν as ν/u_τ^2.

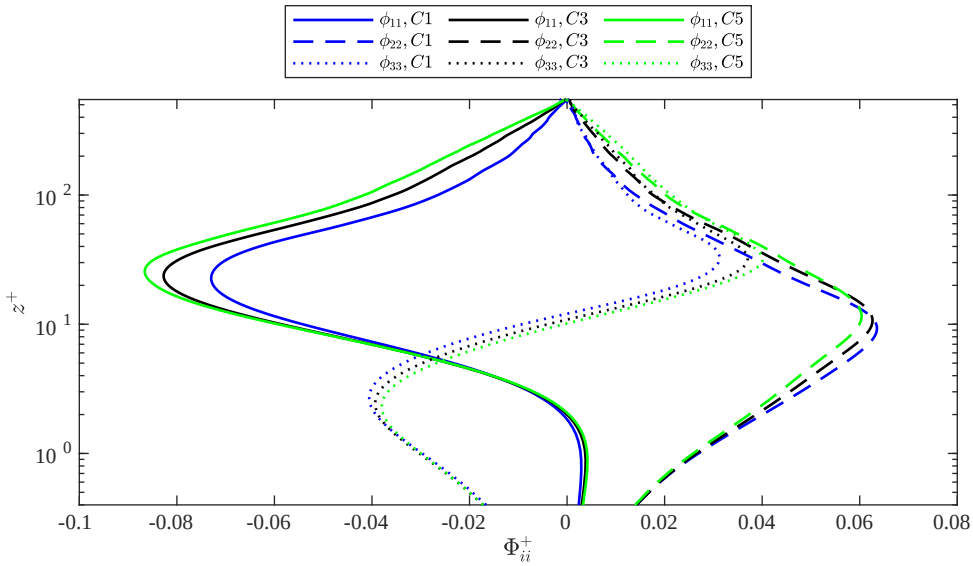

Figure 4.12: Inter-component energy redistribution.

(e.g. formation of streaks from legs of hairpin vortices). TKE still redistributes from $\overline{u'^2}$ and $\overline{w'^2}$ to $\overline{v'^2}$, but the rate of energy distribution from $\overline{u'^2}$ intensifies compared to the upper VSL. From $z^+ \gtrsim 10$, TKE redistributes from $\overline{u'^2}$ to $\overline{v'^2}$ and $\overline{w'^2}$. Above the buffer region where $z^+ \gtrsim 30$, TKE is almost equally distributed from $\overline{u'^2}$ to $\overline{w'^2}$ and to $\overline{v'^2}$. In these inter-component TKE redistributions above the VSL, the magnitude of Φ_{11} and Φ_{33} increase as Ri increases.

The change in Φ_{11} with stratification for $z^+ \gtrsim 10$ is more pronounced than that of Φ_{22} and Φ_{33}. This suggests stratification is in favor of straightening of tilted streamwise structures, as the decrease in Φ_{11} leads to decrease in Φ_{22} and Φ_{33}.

4.3.7 Budget of tangential Reynolds stress

In Sec. 4.3.5, we explored the budget of TKE at equilibrium. While production was influenced by stratification, the influence was less than expected. In this section, we aim to achieve a better understanding of why this is the case. To do so, we examine the budget of the tangential Reynolds stress, because of the key role that it plays in turbulence production.

The different contributions to the budget of $\overline{u'w'}$ are production (P_{13}), dissipation (ϵ_{13}), buoyancy destruction (B_{13}), turbulent transport (T_{13}), viscous diffusion (T_{13}), pressure-

transport Π_{13}, and pressure-strain (Φ_{13}); these terms are defined in Appendix A.2 and profiles are shown in Fig. 4.13. Similar to the TKE budget, we focus on inner layer balances. Interestingly for $\overline{u'w'}$, production P_{13} (Fig. 4.13a) and the buoyancy term B_{13} (Fig. 4.13c) are the same order of magnitude, showing that stratification has a more important effect on the budget of $\overline{u'w'}$ than the TKE budget. The maximum of P_{13} is in the buffer layer and is an order of magnitude larger than the dissipation ϵ_{13}. Another significant contribution to the budget of $\overline{u'w'}$ within the buffer layer comes from Φ_{13}.

Transfer of $\overline{u'w'}$ in part of the buffer layer where $5 \lesssim z^+ \lesssim 20$ corresponds to a sign change in T_{13} (Fig. 4.13d), which shows a transfer of tangential Reynolds stress from the wall to the upper boundary layer (ejection) for $z^+ \lesssim 10$ and from the upper boundary layer toward the wall (sweep) for $10 \lesssim z^+ \lesssim 50$. In both the VSL and the buffer layer, T_{13} shows a significant decrease from C1 to C2. B_{13} increases with stratification while ϵ_{13} and D_{13} are not very sensitive to stratification. The effect of stratification on Π_{13} is largest in the VSL. Above the VSL, stratification does not significantly affect these mechanisms within the inner layer. The magnitude of Φ_{13} in the VSL is increased with increasing Ri. Very close to the wall where $z^+ < 1$, Φ_{13} and Π_{13} balance each other and ϵ_{13} is balanced by D_{13}. The maximum of B_{13} occurs at $z^+ \approx 15$. The neighbourhood of this location is associated with suppression of ejection and sweeping of tangential Reynolds stress as shown in Fig. 4.13(d).

The importance of buoyancy on the budget of the tangential Reynolds stress highlights the significance of stratification on the evolution of turbulence producing eddies. Thus it is expected that turbulence collapses at early stages of strong surface cooling when the time scale of turbulence producing eddies is larger than the time scale of buoyancy destruction through boundary layer growth [7]. As a result, they cannot adjust accordingly and the boundary layer cannot accommodate a buffer region [46] with net positive production.

Although we mainly discuss the quasi-stationary state, the hierarchy of the different terms in the Reynolds stress budget is independent of whether the transient or quasi-stationary state is considered. Hence, another motivation for the examination of the budget of $\overline{u'w'}$ is to have a clearer understanding of the mechanisms that most significantly contribute to the transiently evolving turbulence-producing eddies seen in an earlier study for the same configuration [7]. The significance of buoyancy on the evolution of turbulence production rather than buoyancy destruction of TKE has been found in other flow configurations. Recently, Shah and Bouzeid [119] showed that for an evolving Ekman boundary layer under stable stratification, turbulence decay is controlled by the decrease in TKE production and not buoyancy destruction.

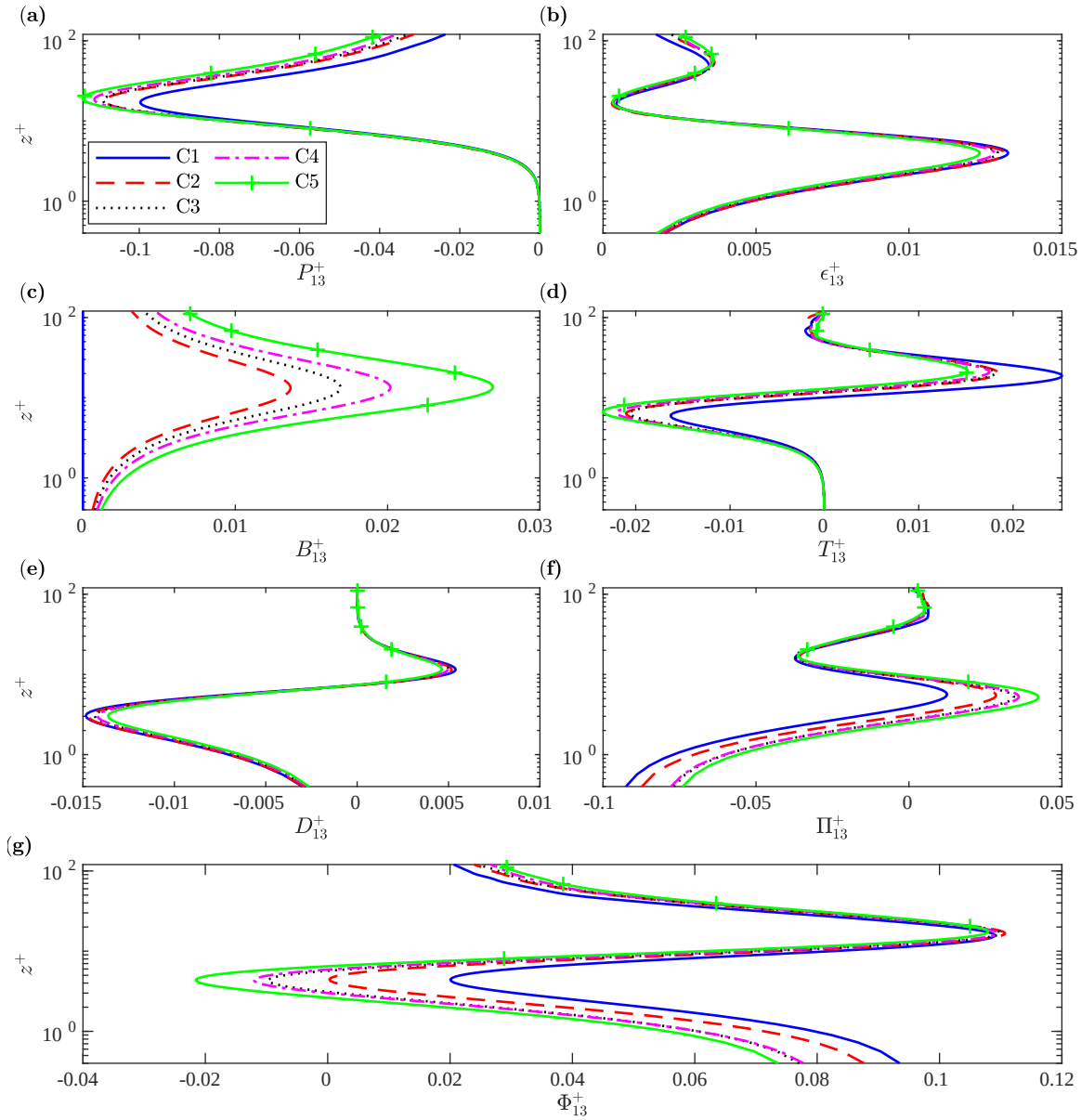

Figure 4.13: Different contribution to the budget of $\overline{u'w'}$: (a) production, (b) dissipation, (c) buoyancy destruction, (d) transfer, (e) viscous diffusion (f) pressure transport, and (g) pressure-strain.

4.3.8 Length scales

Although relevant length scales for homogeneous stratified turbulence [117] and unstratified wall-bounded shear flows [70] have been studied independently in numerous studies [26, 25], far fewer studies have looked at length scales for stratified wall-bounded shear flows [130]. In this section, we examine various length scales, and also check the basic requirement for the grid scales to be smaller than that of the smallest dissipative eddies. Meeting this requirement implies we are accurately resolving the interaction of scales at all levels. Vertical grid-spacing is denoted by Δz and is a function of height due to grid-stretching.

We begin by looking at the Kolmogorov length scale due to its fundamental importance as the typical length scale of small, dissipative eddies in a turbulent flow. The Kolmogorov length scale is defined as

$$\eta = (Re^3\epsilon)^{-1/4}. \tag{4.8}$$

It has recently been suggested that the Kolmogorov scale is not necessarily the smallest dissipative scale, particularly in regions of the flow that contain strong velocity gradients [40]. Since dissipation is governed by velocity gradients, it is useful to define scales that are derived based on statistics of velocity derivatives. Fine-scale structures in the velocity field are defined as [139]

$$\lambda_i^{u_i} = \left(\frac{\overline{\left(\frac{\partial u_i'}{\partial x_i}\right)^2}}{\overline{\left(\frac{\partial^2 u_i'}{\partial x_i^2}\right)^2}} \right)^{1/2}, \tag{4.9}$$

where the summation convention is not used. With this definition, $\lambda_i^{u_i}$ is the scale of momentum-carrying structures that are fine enough to capture both dissipation and diffusion process (u_i-structures hereinafter). The consideration of diffusion becomes important in the lower VSL where viscous dissipation and diffusion have similar values. In particular for $w-$structures, wall impermeability imposes very small values for wall normal velocity in the lower VSL and having the correct turbulent diffusion becomes very important.

Shear generated by the presence of the wall plays a key role in maintaining turbulence production for wall-bounded turbulence. If l_C is the length scale of the eddies that have time scales comparable to inverse mean shear $1/S$, then their velocity is of order $u_{l_C} \approx (\epsilon l_C)^{1/3}$ [70] using the inertial-range approximation. Therefore, from $l_C/u_{l_C} = 1/S$, the

Corrsin length scale is defined as [70]

$$l_C = \left(\frac{\epsilon}{S^3}\right)^{1/2}. \tag{4.10}$$

The Corrsin scale is typically used in shear flows [70].

In stratified turbulent flows it is common to define a characteristic scale of stratification, which we will denote as l_O, for which there is a balance between inertial and buoyant effects [26]. This scale is called the Ozmidov scale and is defined as,

$$l_O = \left(\frac{\epsilon}{N^3}\right)^{1/2}. \tag{4.11}$$

Analogous to the Corrsin scale, l_O is the scale at which the eddy time scale is similar to N. Therefore, stratification has a negligible effect on turbulence for scales much smaller than l_O, and the effect of stratification becomes dynamically important when the eddy size is similar to or greater than the Ozmidov scale.

All the length scales that have been discussed so far depend on velocity fluctuations and are therefore inherently linked to the kinetic energy of the flow. It is also important to identify scales that primarily involve potential energy. If we assume a fluid particles passes a vertical distance l_E until it pulls back by buoyancy restoring force, then using the transport equation for temperature variances yields [52]

$$\frac{\overline{\theta'^2}}{\partial t} = -\overline{\theta' w'}\frac{\partial \overline{\theta}}{\partial z} + ... \tag{4.12}$$

For an eddy of size l_E and time scale of τ_E by using mixing length theory one can relate turbulent heat flux and temperature gradient based on eddy thermal diffusivity coefficient κ_t as $\overline{\theta' w'} = -\kappa_t \partial\overline{\theta}/\partial z$ where $\kappa_t \sim \tau_E (l_E/\tau_E)^2$. Using Eq. 4.12, $\overline{\theta'^2}/\tau_E \sim (\partial\overline{\theta}/\partial z)^2 l_E^2/\tau_E$. The potential energy is proportional to $\overline{\theta'^2}$ and kinetic energy for eddies of size l_E is proportional to $(l_E/\tau_E)^2$. The Ellison scale l_E is a distance that a fluid particle can travel before all of its kinetic energy transfers to potential energy and pull back toward equilibrium position [44, 97]. Therefore, the Ellison scale is an overturning scale and it is defined as [44, 33, 130, 97]

$$l_E = \frac{\sqrt{\overline{\theta'^2}}}{\overline{\frac{\partial \overline{\theta}}{\partial z}}}. \tag{4.13}$$

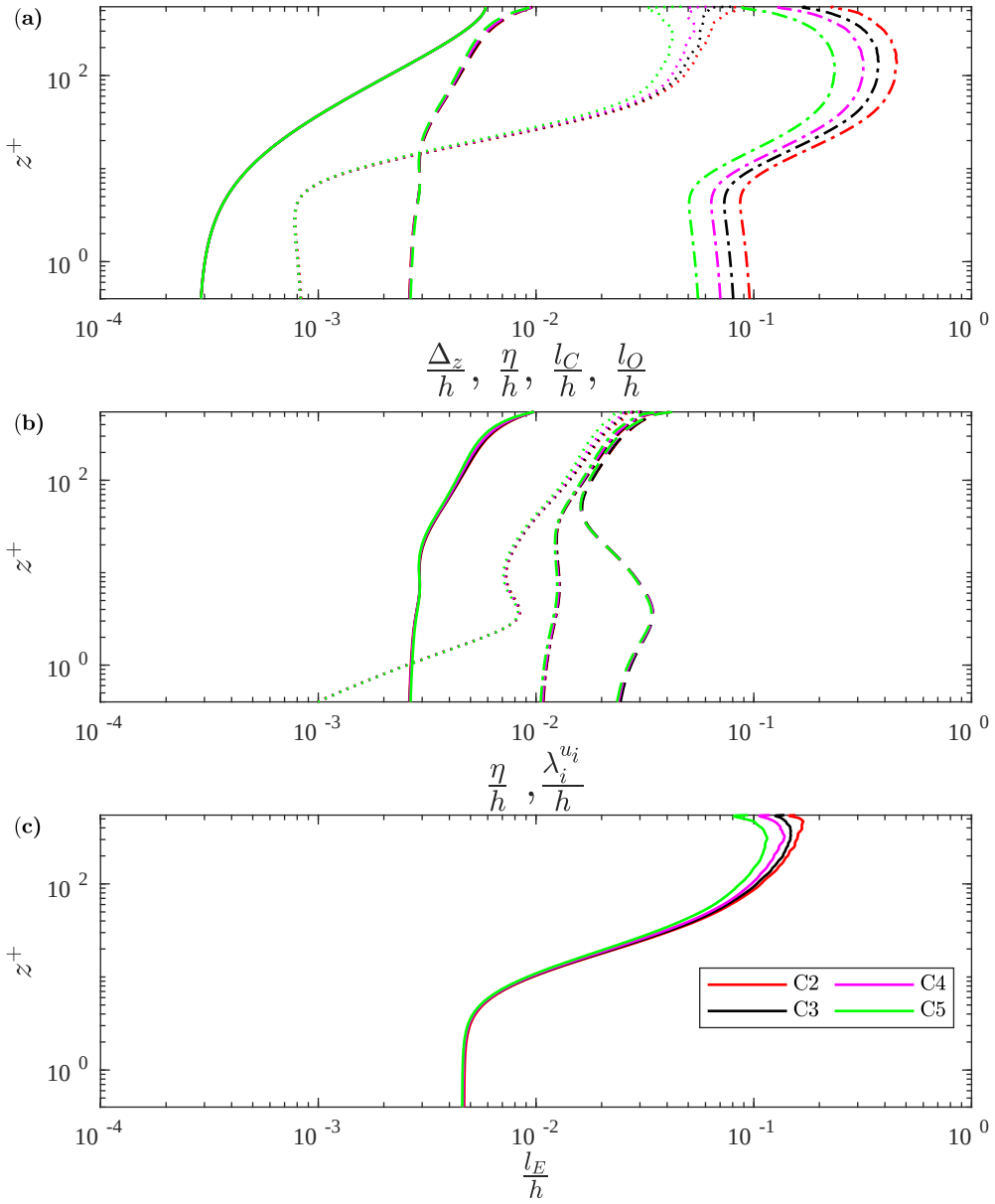

Figure 4.14: Length scales as a function of wall normal distance. (a) grid (solid lines), Kolmogorov (dashed lines), Corrsin (dotted lines), and Ozmidov scales (dash-dotted lines). (b) Kolmogorov scales (solid lines), fine scales of w-structures (dotted lines), v-structures (dash-dotted lines), and u-structures (dashed lines). (c) Ellison scales.

Figure 4.14 shows these length scales as functions of height from the wall. In Fig 4.14(a) we can see first of all that η and l_C are smaller than the Ozmidov scale. The Kolmogorov scale shows little dependence on stratification, while the Corrsin scale does show some dependence on stratification in the outer region above $z^+ \approx 100$, where l_C decreases as Ri increases. This is particularly interesting because they are still smaller than the Ozmidov scale. Note also that the Corrsin scale is smaller than the Kolmogorov scale below $z^+ \approx 10$ in Fig 4.14(a), implying that all scales are affected by strong near-wall shear. Both the Kolmogorov and Corrsin scales are indeed larger than the grid scale, indicating that the flow is well resolved.

Fine scales of w-structures (λ_z^w), shown in Fig. 4.14(b), are smaller than η in the lower VSL where $z^+ \lesssim 1$ as a result of wall-impermeability leading to small vertical velocity. Moreover, the limiting behaviour of the velocity fluctuations [112, 41] leads to a linear profile for λ_z^w close to the wall [139]. The λ_x^u, λ_y^v, and λ_z^w fine scales of velocity structures are smaller than the Ozmidov scale and are not sensitive to stratification at all vertical levels, as shown in Fig 4.14(b). As expected, the outer layer values of λ_x^u, λ_y^v, and λ_z^w are similar, indicating that small scales in that region are close to isotropic. Fine structures of u are larger than the other components and fine structures of w are the smallest.

Fig. 4.14(c) shows the Ellison scale, which does not exhibit a dependence on Ri in the near-wall region. However, l_E is sensitive to stratification in the outer layer, although it is smaller than l_O.

4.3.9 Kinetic energy spectra and horizontal scales

To address vertical dependence of the horizontal length scales that may contribute to the kinetic energy cascade we look at premultiplied streamwise and spanwise energy spectra as a function of height. The pre-multiplied energy spectra are defined as

$$\phi_E^x(k_x, z) = \frac{k_x}{2} \sum_{k_y} k_y \widehat{u}_i \widehat{u}_i^*, \tag{4.14}$$

$$\phi_E^y(k_y, z) = \frac{k_y}{2} \sum_{k_x} k_x \widehat{u}_i \widehat{u}_i^*, \tag{4.15}$$

where $\widehat{(\,)}$ refers to Fourier transform, $*$ represents complex conjugate and k_x and k_y are wavenumbers in streamwise and spanwise directions. Premultipied spectra are frequently shown [50, 69, 70] because of their relationship with kinetic energy. For example, spanwise averaged kinetic energy corresponds to $\int E \, \mathrm{d}k_x = \int \phi_E^x \, \mathrm{d}(\log k_x) = \int \phi_E^x \mathrm{d}(\log \lambda_x)$ where

$E = \sum_{k_y} \widehat{u}_i \widehat{u}_i^*/2$ and $\lambda_x = 2\pi/k_x$ is the wavelength in the streamwise direction. A similar expression is valid for the streamwise averaged kinetic energy. Thus, on a logarithmic wavelength axis, ϕ_E^x and ϕ_E^y visualize spectral energy densities [50] for streamwise and spanwise wavelengths, respectively.

The premultiplied spectra are shown in Fig 4.15. For clarity, only spectra for cases C1 and C5 are shown. It can be seen that the energetic scales in the buffer layer in the spanwise direction are smaller than those in the buffer layer in the streamwise direction. For example, the contours containing 90% of the spectral energy density are centered at $\lambda_y \approx 100$ and $\lambda_x \approx 800$ for spanwise and streamwise scales, respectively. The λ_x and λ_y corresponding to each contour line at all levels become slightly smaller with increasing stratification. The inclination of spectral energy density contours with height (dashed-dotted line in Fig 4.15(a)) for the spanwise scales is more pronounced in comparison to the streamwise scales (Fig 4.15(b)). This difference suggests that widening of spanwise scales with respect to height occurs at a larger rate compared to elongating of streamwise scales. Large outer-layer spanwise scales with $\lambda_y \gtrsim L_y$ ($\lambda_y^+ \gtrsim 1760$) contain only $\lesssim 10\%$ of spectral energy density as shown in Fig 4.15(a). However, they penetrate down to the VSL. Large outer-layer streamwise scales with $\lambda_x \gtrsim L_x$ contain $\gtrsim 40\%$ of the spectral energy density, as shown in Fig 4.15(b). However, they do not contribute significantly to statistics as shown below, probably due to the paucity of those scales [91]. Large outer-layer streamwise structures of the size $\lambda_x \gtrsim L_x$ ($\lambda_y^+ \gtrsim 3520$) contain $\lesssim 10\%$ of the spectral energy density and have also their roots in the VSL.

For the neutral case, spanwise length scales increase monotonically with height and contour lines of spectral energy density show a relatively symmetric shape around the reference line $\lambda_y \propto z$. Interestingly, for strongly stable stratification, this symmetry of the spectral energy density around the line $\lambda_y \propto z$ is broken for spanwise scales (in Fig. 4.15a) while the shape of spectral energy density for streamwise scales is approximately preserved (Fig. 4.15b). Thus, distribution of kinetic energy among different λ_x scales does not change significantly with stratification at all heights. In C5, the change of λ_y with height that contribute between 30% and 70% of the ϕ_E^y is smaller in comparison to the scales that contribute more than 70% of ϕ_E^y. For scales that contain less than 30% of ϕ_E^y in C5, the increase with height is smaller compared to scales that contain a similar portion of ϕ_E^y in C1. Thus, stratification causes asymmetry in distribution of kinetic energy among different λ_y scales with respect to height.

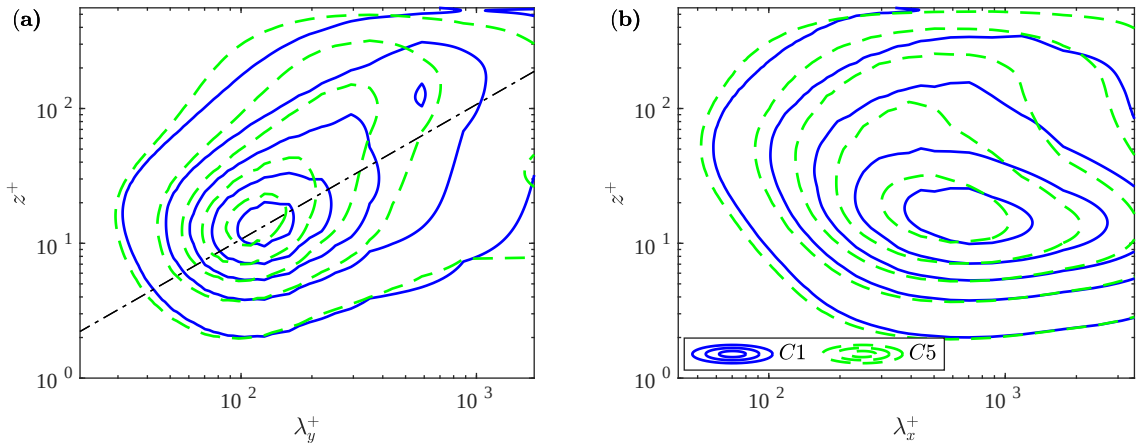

Figure 4.15: Spectral energy density (a) ϕ_E^y and (b) ϕ_E^x. Blue and green lines correspond to C1 and C5 respectively. Contours are plotted at the level of 0.1, 0.3, 0.5, 0.7, and 0.9 of maximum values of the corresponding spectrum. The slope of the black diagonal dash-dotted line is 1 in (a) where $z = \frac{60}{Re}\lambda_y$.

4.3.10 Higher-order statistics

Higher-order statistics can provide additional insight into our understanding of the distribution of TKE. For example, third-order moments of velocity fluctuations can provide insight into energy transfer and fourth-order moments can accentuate activities of less energetic scales. We scale $\overline{u'^2}$ and $\overline{u'^4}$ by their maximum so that both have values between zero and one. Then, below the log-region where the flow is energetic these profiles look similar. However, above that region where the flow is less energetic, the difference between these scaled profiles become more prominent (not shown).

Plots of $\overline{u'^3}$ with respect $\overline{u'^2}$ and $\overline{u'^4}$ are presented in Fig. 4.16. Third order moments of u' and w' are correlated with the transfer of $\overline{u'^2}$ and $\overline{w'^2}$ (T_{ij} term in Appendix A.2). By looking at Fig. 4.16(c,d) one can say is that $\overline{u'^2}$ and $\overline{u'^4}$ are strongly correlated (a similar relationship is seen for $\overline{w'^2}$ and $\overline{w'^4}$). Similar results have been found in LES simulations of atmospheric boundary layers [113]. From the modeling perspective, this strong correlation between second and fourth order statistics suggest that fourth and second order statistics are functionally related. The Fig. 4.16(c,d) further suggest that a linear model that relates fourth order moments and second order moments can be used to represent effects of fourth order moments. This results supports quasi-normal approximation [128, 138, 113] which can be used in model development [144, 138].

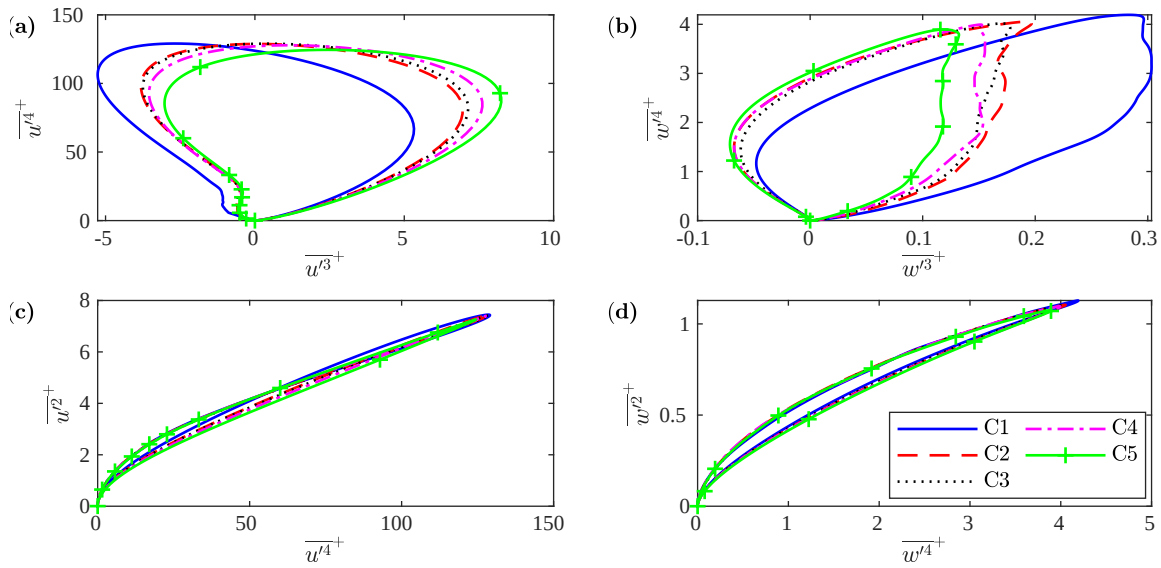

Figure 4.16: Profiles of (a) third-order versus fourth-order moments of streamwise velocity fluctuations, (b) third-order versus fourth-order moments of vertical velocity fluctuations, (c) fourth-order versus second-order moments of streamwise velocity fluctuations, and (d) fourth-order versus second-order moments of vertical velocity fluctuations.

Also, strong positive fluctuations in $\overline{u'^3}$ are enhanced as stratification increases, while strong negative ones are weakened. Therefore, stratification is in favor (in a quasi-stationary sense) of intensifying high-speed streaks and weakening low-speed streaks (Fig. 4.16a). Positive streamwise velocity fluctuations can be seen (Fig. 4.17) to increase in the upper VSL as Ri increases whereas negative streamwise velocity fluctuations in the buffer layer decrease. For $\overline{w'^3}$, the positive vertical velocity fluctuations are strongly weakened and the magnitude of the negative vertical velocity fluctuations are slightly increased, in particular in the log region.

This behaviour of third-order velocity statistics can be summarized in terms of a Q2 (ejection) and Q4 (sweep) map. As shown in Fig. 4.17c, ejection events (Q2) are hindered as Ri increases and sweeping events (Q4) are less affected compared to the neutral case, consistent with earlier studies [130, 142]. The larger effect of stratification on ejection events is due to the fact that these events are strongest close to the wall where N^2 is largest. Therefore, buoyancy restoring force has more effect on these events rather than sweeping events, which are initiated further from the wall with a smaller N^2 [130, 142].

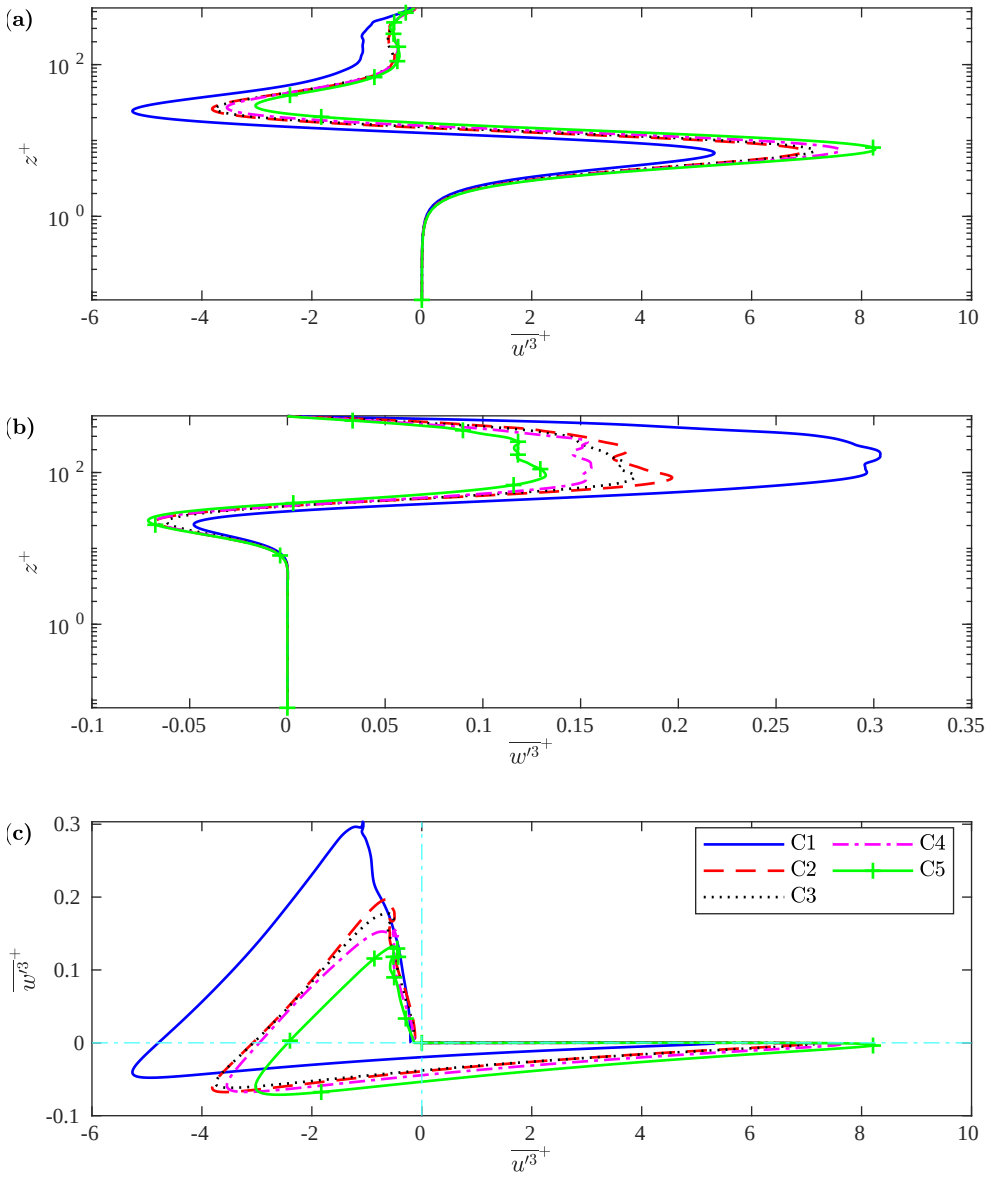

Figure 4.17: Vertical profile of (a) third-order moment of streamwise velocity fluctuations and (b) third-order moment of vertical velocity fluctuations, and (c) $\overline{w'^3}$ versus $\overline{u'^3}$ for analysis of quadrant events (Q1-Q4).

4.3.11 Effect of heat entrainment from upper boundary

For the stratified cases shown so far (C2-C5) we have neglected the effect of possible heat transfer from the upper boundary. In doing so, we have isolated near-wall turbulence from modulations caused by stable stratification (i.e. capping inversion) due to heat entrainment at the upper boundary. As discussed by Atoufi *et. al* [7] and in chapter 3, heat entrainment from the upper boundary results in weakening of the outer layer eddies, which can significantly affect the wall turbulence. These outer layer eddies play an important role in turbulence recovery for strong stable stratification. Removing them from the flow results in full collapse of turbulence during transient cooling [7] (and also in chapter 3), and intensifying their available TKE, even by 10%, can enable recovery from collapse [46].

In this section, we study the effect of the upper thermal boundary condition on statistics of the quasi-stationary state. To do so, we compare C2 and C5 with C2D and C5D. In C2 and C5 heat transfer from the upper boundary is not permitted. Cases C2D and C5D use Dirichlet upper boundary conditions and therefore allow entrainment of heat from the upper boundary. For C2D and C5D, simulations are initialized using fields from the quasi-stationary states from C2 and C5, respectively. As shown in Fig. 4.18(a) heat entrainment from the upper boundary results in trends for TKE that are similar to more weakly stratified cases (see Fig. 4.1b) when stratification is imposed only at the bottom wall such as C2 (see Atoufi *et. al* [7] and chapter 3 for the temporal evolution of C2-C5). In both C2D and C5D, turbulence first undergoes a decay until $t \approx 5$ and then starts recovering afterward. However, the overshoot of domain integrated TKE in C5 is not observed for C5D. An important point here is that turbulence can recover from initial decay with or without entrainment of heat from the upper boundary. To distinguish between these two situations, one can say that the former flow is limited to a maximum sustainable heat flux [36, 37] and the latter flow is limited to a minimum shear capacity to sustain turbulence [137] (see Sec. 4.3.3 for more detailed explanation).

The profile of TKE in Fig. 4.18(b) shows that the upper thermal boundary condition can modulate flow characteristics (e.g. TKE, mean shear, and N^2) for $z \gtrsim 0.3$ in the quasi-stationary state. Compared to C5, C5D has lower TKE for $z > 0.8$. Moreover, in C5D the flow acceleration due to reduced tangential Reynolds stress leads to larger streamwise velocity for $z > 0.3$ (Fig. 4.19a). The temporal evolution of domain integrated TKE suggests that entrainment of heat from the upper boundary also has a transient effect and if turbulence approaches a quasi-stationary state the TKE become close to the weakly stratified case. A strong capping inversion caused by heat entrainment from the upper boundary can be clearly seen in Fig. 4.19b, where for $z > 0.3$ buoyancy restoring force significantly increases. The effect of heat entrainment from the upper boundary is

significant on mean flow velocity and buoyancy frequency above the buffer layer. However, TKE for all stratified cases shows similar behaviour (Fig. 4.18b and also Fig. 19 in Taylor *et. al* [130]). This similarity strongly suggests that characteristics of stably-stratified wall-turbulence become similar to weakly stratified cases if quasi-stationarity is acquired. This similarity means that, regardless of the choice of the upper boundary condition, the TKE profile becomes roughly similar to weakly stratified cases.

4.3.12 Computational domain size effect

Results presented so far were obtained on a domain of medium size [69, 92] with $L_x = 2\pi$ and $L_y = \pi$. For the unstratified case, such a domain contains a few minimal flow units [71] including at least one ejection and one sweep [47]. Here we examine the effect of the computational domain on mean flow behaviour, second-order statistics, and energy spectra. In this section the results from a larger domain simulation L5D with $L_x = 8\pi$ and $L_y = 6\pi$ are compared to medium domain case C5DC, which both have the same grid resolution, which is lower than that of the main simulations C1-C5. Note that these simulations employ Dirichlet boundary conditions at the upper boundary and therefore have heat entrainment. The size of the larger domain was chosen based on the study of García-Villalba and del Álamo [50].

The mean flow velocity and temperature profiles for medium and large domain size simulations in Fig. 4.20 look quite similar. This is consistent with unstratified channel flow simulations [92]. The only slight differences between medium and large domains are observed for $z > 0.6$. Second-order statistics of velocity and temperature also have similar profiles for medium and large domain sizes, as seen in Fig. 4.21. The turbulent heat flux in the vertical direction shows slightly larger sensitivity to the choice of domain size.

The streamwise-averaged pre-multiplied kinetic energy spectrum for the smaller domain shows that it is already sufficient to represent the scales in the spanwise direction (Fig. 4.22a). The widest structures belong to the outer layer whereas the tallest structures are streaks that belong to the buffer layer, where $10 \lesssim z^+ \lesssim 20$. Streaks with size $\lambda_x \leq L_x$ in the buffer layer contain $\gtrsim 60\%$ of energy spectrum as shown in Fig. 4.22(b). As expected, spanwise length scales are typically smaller than streamwise length scales. Moreover, and consistent with earlier studies [91], the spectrum for the small domain closely follows that for the larger domain up to the cutoff wavelength that is set by the domain size in the streamwise direction. It is worth mentioning that the tall length scales in Fig. 4.22(b), with $\lambda_x \approx 25h$ and about 10% of the TKE, are likely attached inactive structures [133]. These structures enhance viscous dissipation as they are connected to the VSL [15]. These

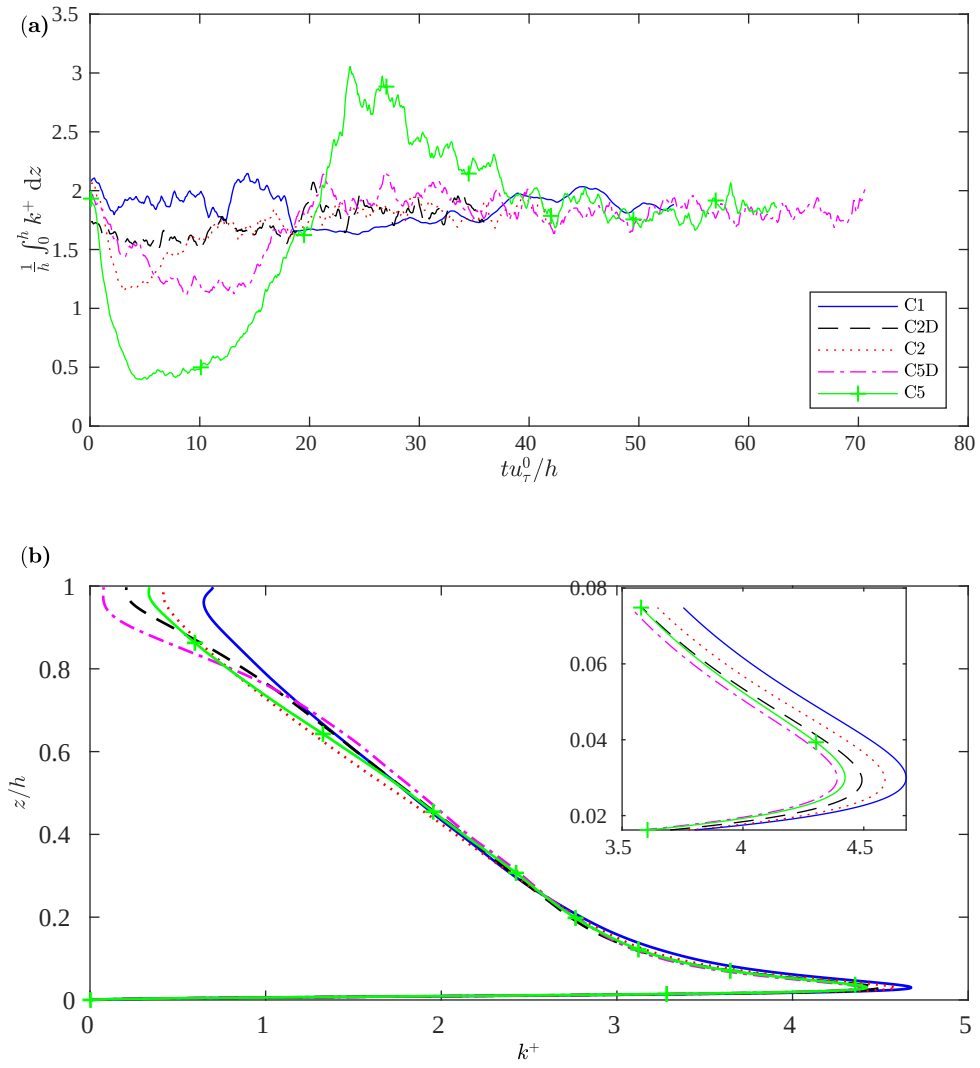

Figure 4.18: Effects of heat entrainment from the upper boundary on (a) domain-integrated TKE and (b) vertical profile of TKE.

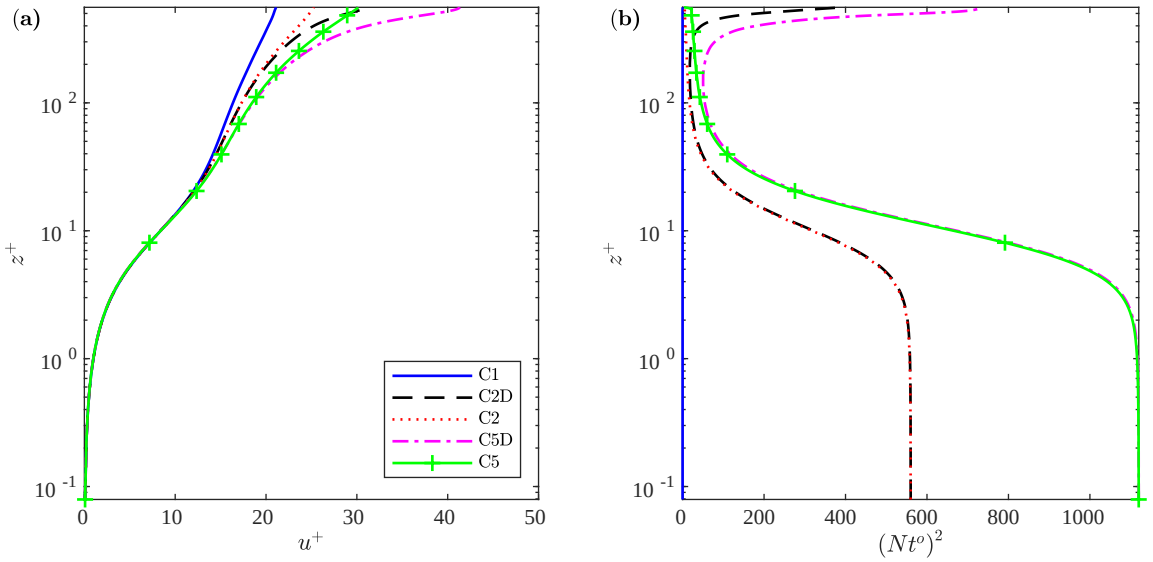

Figure 4.19: Effects of heat entrainment from upper boundary on (a) mean velocity profile and (b) buoyancy frequency.

inactive structures most likely contain swirling or meandering type of motions [133] which will not contribute to top-down transfer of tangential Reynolds stresses.

4.4 Discussion

4.4.1 Description of quasi-stationary state

We describe the state used for averaging statistics as quasi-stationary rather than stationary, due to the fact that the domain averaged temperature decays at a constant rate $\frac{1}{RePr}$, as shown in Taylor *et. al* [130]. Nevertheless, despite the steady cooling, the buoyancy frequency is stationary (Fig 4.1d). Indeed, by knowing this decay rate, one can use following change of variable for temperature

$$\Theta = \theta + \frac{t}{RePr} \tag{4.16}$$

in the energy equation (Eq. 2.3). Applying a horizontal average to the resulting equation, integrating over the channel height, and applying the boundary conditions used for C2-C6 (Neumann at the bottom and specified temperature at the top) yields, $\frac{1}{h}\frac{\partial}{\partial t}\int_0^h \overline{\Theta}\ \mathrm{d}z = 0$.

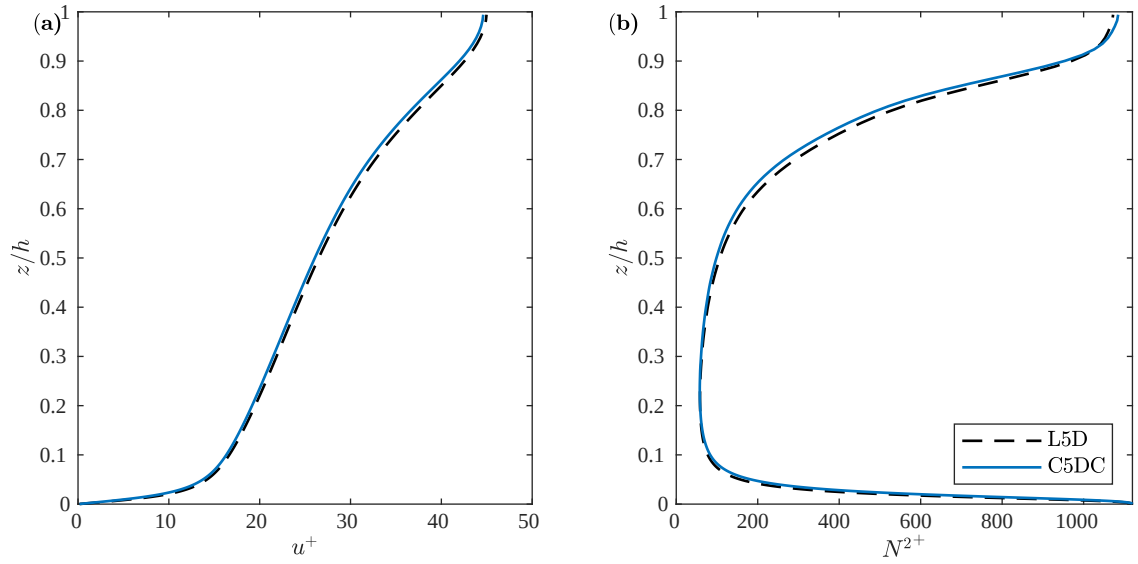

Figure 4.20: Computational domain size effect on (a) mean velocity profiles and (b) buoyancy frequency.

The vertical derivative of Θ is the same as θ, so they both give the same N^2. Since evolution equations for rms of temperature fluctuations $\overline{\theta'^2}$ [52], and temperature fluxes $\overline{u_i'\theta'}$ [52] are dependant on θ', $\partial\overline{\theta}/\partial z$ and not on $\overline{\theta}$ thus using Oberbeck-Boussinesq equations, turbulence characteristics that are addressed in this chapter are the same if either θ or Θ are used. Hence, temperature fluctuations, which alter momentum fluxes through the Reynolds stress equations (Appendix A.2), can approach stationarity regardless of the time dependence of θ. Therefore, since the buoyancy frequency and temperature fluctuations can acquire quasi-stationarity, the related turbulence statistics also approach stationarity. Nevertheless, we did consider an alternative configuration by which the bottom cooling is compensated for: in simulations C2D, C5D, C5DC, and L5D, we allow heat entrainment from the upper boundary, an approach previously used by Niewdsaut [106], Flores and Riley [46], and others. As can be seen in Fig. 4.18(a), with this boundary condition turbulence reaches a stationary state. As shown in Fig. 4.18 and Fig. 4.19, TKE and mean flow profiles for the cases with heat entrainment (C2D, C5D) are close to the corresponding cases without heat entrainment (C2,C5). These matches in profiles, in particular in near-wall region which is the focus of current work, proves quasi-stationarity for the cases where there is no heat entrainment from top boundary (C2, C5).

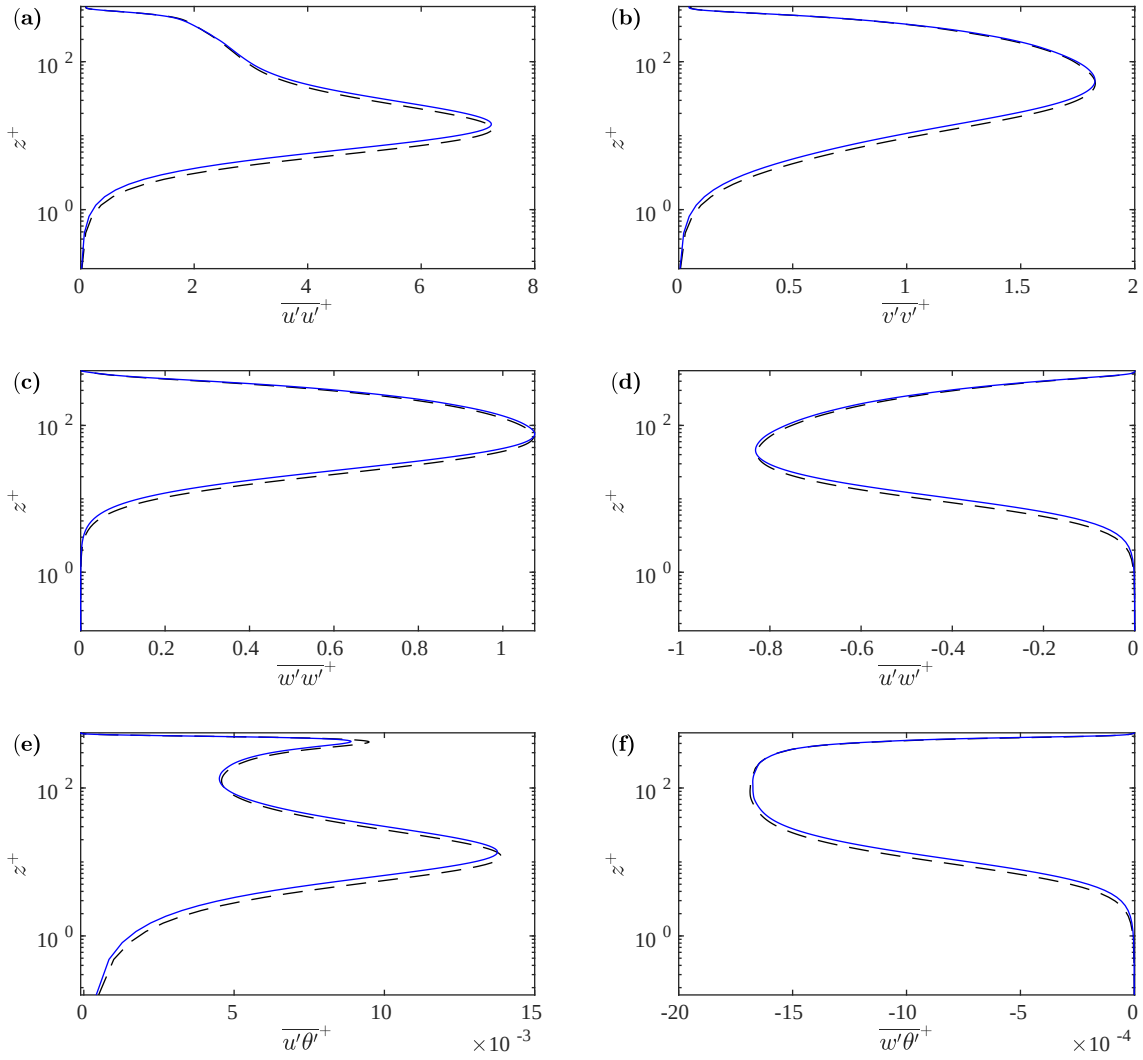

Figure 4.21: Computational domain size effect on (a) $\overline{u'^2}$, (b) $\overline{v'^2}$, (c) $\overline{w'^2}$, (d) $\overline{u'w'}$, (e) $\overline{u'\theta'}$, and (f) $\overline{w'\theta'}$. Line colors are similar to Fig. 4.20

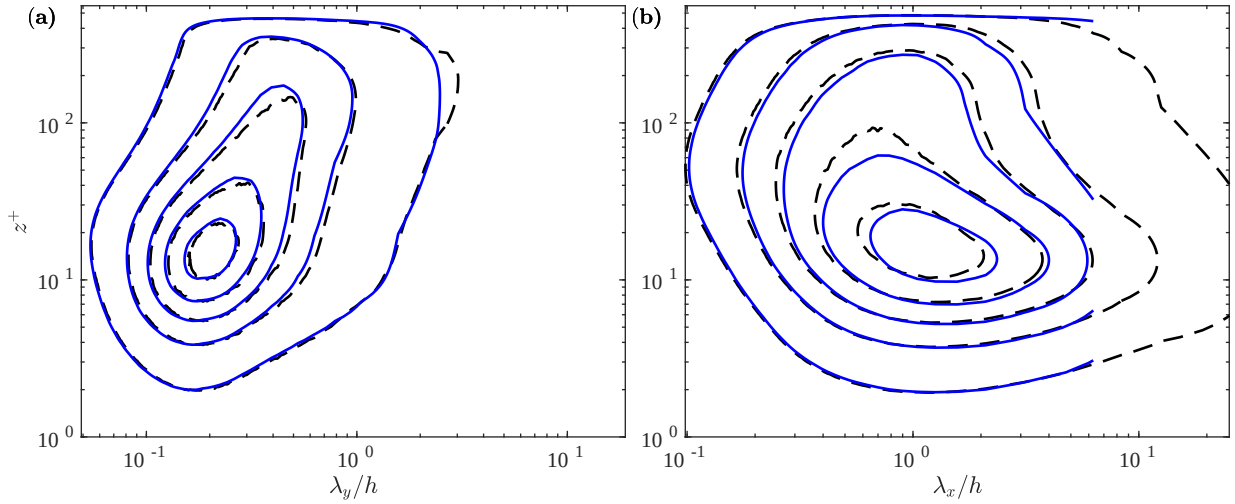

Figure 4.22: Computational domain size effect on (a) spanwise pre-multiplied energy spectrum and (b) streamwise pre-multiplied energy spectrum. Line colors are similar to Fig. 4.20. Contours are plotted at the level of (0.1, 0.3, 0.5, 0.7, 0.9) of maximum values of energy spectrum.

4.4.2 Sufficiency of samples

From Fig. 4.1, we can see that in the last $\Delta T = 12$ turnover times C1-C5 are at quasi-stationarity. To quantify this, consider a time interval $[t_f - \Delta T, t_f]$. The variation of N^2 with respect to the starting time of this interval, $t_s = t_f - \Delta T$, is less than 10% over almost $\Delta T = 20$, and less than 5% over the last $\Delta T = 12$.

In Fig. 4.23 below, profiles of mean flow velocity, normalized temperature, and TKE are shown using different sampling time intervals ΔT from output field at $= t_f$ for C3. This case is chosen because we have a longer period over which to sample. We change the sampling interval, $[t_f - \Delta T, t_f]$, by changing ΔT where t_f is the latest time of the saved output as reported in Table 4.1. It can be seen $\Delta T = 12$ appears to be sufficient for collecting first and second order statistics. $\Delta T = 30$ results in slightly higher TKE in the near-wall region but is overall very similar to the averages with smaller ΔT.

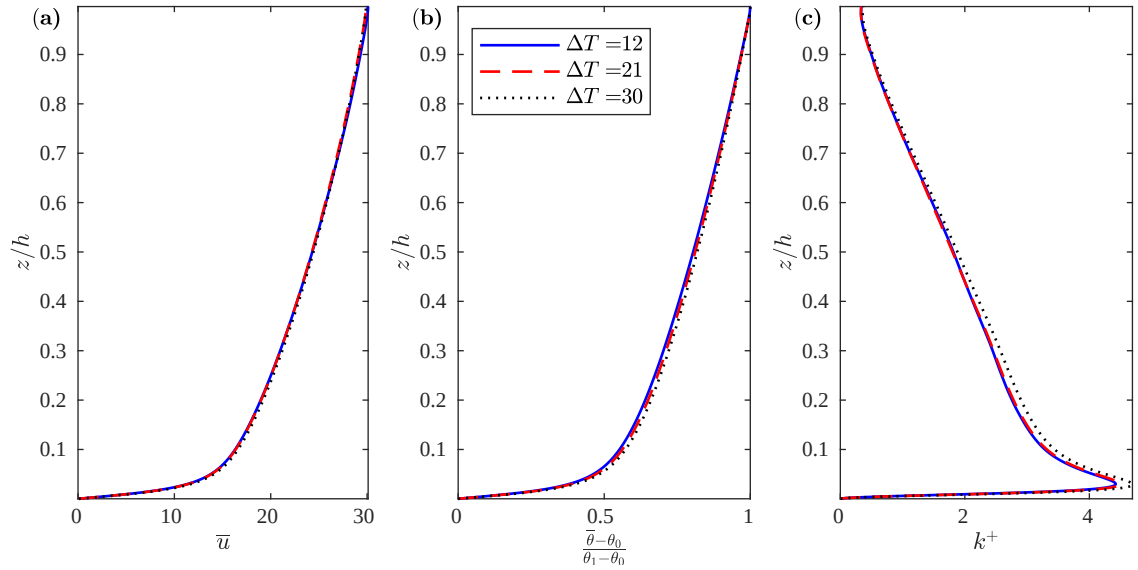

Figure 4.23: Sampling time interval (from latest saved output data of C3 (a) mean flow velocity, (b) normalized mean temperature, and (c) TKE.

4.5 Conclusion

In this chapter, near-wall turbulence under strong stable stratification has been studied using DNS. To address the effects of stable stratification on the characteristics of near-wall turbulence, five different high-resolution cases (C1-C5) are considered with different Richardson numbers ranging from the neutral to strongly stable stratified regime.

The configuration for cases C1-C5 was chosen similar to Atoufi *et. al* [7] and chapter 3 to analyze the response in the near-wall region due to stratification imposed by bottom wall cooling. Although this response was found to be significant in the transient case [7] (also in chapter 3), at quasi-stationarity the impact is much smaller. Nonetheless, in the near-wall region, where $z \lesssim 0.1$, stratification leads to a decrease in velocity variances, TKE, tangential Reynolds stress, and heat flux in the streamwise and wall-normal direction. Using analysis of higher-order statistics it was shown that the tendency of streamwise velocity fluctuations to acquire positive values is intensified as stratification increases.

Mean flow velocity above $z^+ \gtrsim 10$ is increased as Ri increases due to flow acceleration caused by a reduction in near-wall tangential Reynolds stress. The buoyancy restoring force is strongest at the wall and becomes weaker moving away from the wall. Increasing Ri intensifies this restoring force. However, the shear stress generated by the mean shear

dominates these buoyancy forces. By analyzing Re_b it was shown that for C2-C5, overturning and not layering of vortical structures is a dominant feature of eddy motions in the near-wall region if quasi-stationarity is reached. Up to $z \lesssim 0.8$, the flux Richardson number is reduced with increasing height and stratification.

Analysis of the TKE budget shows that production and dissipation are the dominant terms in balancing TKE above the VSL and buoyancy destruction does not significantly affect the TKE budget. It was shown that very near the wall where $z^+ \lesssim 1$, velocity fluctuations are small and pressure-work term plays an important role in transferring TKE to higher-momentum fluid farther away from the wall. To further explore the effects of stratification on turbulence production, we examined the budget of tangential Reynolds stress. By doing so, it was shown that buoyancy has a considerable effect on the budget of tangential Reynolds stress. Therefore, the appearance of patchy turbulence during the cooling process due to a lack of production (and not excessive dissipation [7]) is likely linked to the significance of buoyancy destruction on the evolution of tangential Reynolds stress.

By analyzing length scales, it was found that in the outer layer, $z^+ \gtrsim 100$, for each Ri: $l_O > l_E > l_C$. Each of these scales shows some sensitivity to stratification. It was shown that there are scales smaller than the Kolmogorov scale that may be important for wall-bounded stratified turbulence. Particularly in the VSL, the Corrsin scales are smaller than Kolmogorov scales. Very near the wall where $z^+ \lesssim 1$, λ_z^w structures are also smaller than Kolmogorov scales. In the VSL, $l_C < \lambda_z^w$ in general.

Analysis of inter-component energy transfer Φ_{ii} shows that energy extraction by $\overline{u'^2}$ is more sensitive to stable stratification than $\overline{v'^2}$ or $\overline{w'^2}$. Comparison of the various terms in Φ_{ii} suggests there are changes in the directivity (or preferred alignment angles) of the vortical structures in the near-wall region with stratification. This will be investigated in a future study.

Quasi-stationary wall turbulence under strong bottom cooling responds to the entrainment of heat from the upper boundary in a manner similar to weakly stratified turbulence with bottom cooling that has been initialized from the neutrally stratified case. However, in the quasi-stationary state, this entrainment of heat significantly affects the mean flow characteristics of the outer layer with minimal change on turbulence of the inner layer.

The effect of domain size on the results was also considered by running an additional simulation on a large domain. It was shown that mean velocity and buoyancy frequency can be accurately represented in the lower half of the channel using the smaller domain size. In the upper half, mean flow and buoyancy frequency slightly deviate from larger domain simulations. However, and consistent with studies of unstratified wall-bounded

turbulence [91], one-point second-order statistics are accurately represented on a domain size of $L_x = 2\pi$, $L_y = \pi$. Although the mechanisms that are involved in the balance of TKE have been discussed here, the cascade of kinetic energy in strongly stable stratified wall turbulence remains an open question that will be addressed in future work.

Chapter 5

Kinetic energy cascade

In this chapter the kinetic energy cascade and mechanisms that affect the kinetic energy among different scales for SBLs are studied. This chapter is based on Ref. [9].

5.1 Introduction

Due to its practical importance, the SBL has been extensively investigated via laboratory experiments [103, 6, 108, 135, 142], numerical studies [52, 4, 130, 106, 32, 50, 46, 61, 36, 37, 136, 48, 77, 7, 8], and field measurements [105, 120, 94, 95]. These studies showed that stable stratification (SS) reduces turbulent heat flux resulting in reduction of thermal mixing and momentum flux across the boundary layer leading to reduction of skin friction coefficient.

SBLs are often classified into three different stratification regimes: weak, moderate, and strong based on values of the Richardson number [52, 4, 120, 142] or the ratio between the boundary layer thickness h and the Monin-Obukhov scale, L_{MO} [107, 46, 8]. For $h/L_{MO} < 0.4$, which are weakly stratified cases, turbulence behaves similar to neutral cases [52, 4, 130]. For the moderate stratification range, with $0.4 \leq h/L_{MO} < 0.8$, features of the flow are controlled by buoyancy [52, 130]. Strongly stable boundary layers (SSBL), with $h/L_{MO} \geq 0.8$ [46, 50, 58, 7, 8] are dominated by the stabilizing effect of buoyancy through which turbulence becomes patchy or fully collapses, at least at early times. All these regimes involve simultaneous effects of buoyancy and the presence of the wall, each of which adds anisotropy to the kinetic energy cascade [143, 26, 28]. Due to the complex nature of SSBLs, the physics of this flow regime is not yet fully understood [106, 94]. The

SSBL may lead to the coexistence of patches of active turbulence next to layered vortices [7] or full relaminarization depending on the friction Reynolds and Richardson number [106, 46, 36, 37, 58, 7]. Recently, it is shown that the relaminarization could be transient, depending on how the flow is initialized [36, 37]. Artificial enhancement of turbulent kinetic energy (TKE) at a few turnover times before the full collapse of turbulence will cease the laminarization process [36, 37]. Furthermore, outer layer (OUL) structures play an important role in controlling dynamics of the SSBL where increasing their kinetic energy prevents full collapse of turbulence [46], and removing them prevents recovery from partial collapse [7].

The first phase of the wall turbulence response of a neutral boundary layer to the introduction of SS, whether by cooling from the bottom or heating from the top boundary, is decay [52, 46, 7]. This phase can be understood using Reynolds stress budget equations [6, 52, 7, 8]. The diagonal components of these equations explain the evolution of velocity variances. Due to the vertical orientation of the buoyancy force, the immediate effect of SS is to decrease vertical velocity fluctuations. Subsequently, tangential Reynolds stress along with production of vertical momentum flux of turbulence are suppressed [123, 6, 135, 142, 7, 8]. The effect of SS on the production of vertical momentum is shown to be more dominant compared to the effect of SS on tangential Reynolds stress (and thus the production of turbulent kinetic energy) [103, 6, 135, 119, 7]. The significance of SS in the evolution of turbulence producing structures embedded in the budget of vertical momentum flux over turbulence production itself shows that the impact of SS on near-wall turbulence is transient for those flows that are weakly stratified or strongly stratified but somehow recovered from partial or full collapse [8]. Thus, even for strong stratification, the near-wall cascade of TKE is expected to follow weakly stratified flows if turbulence is fully recovered. However, details of stratification effects on large outer scale motions are yet to be addressed.

A more comprehensive picture of SS effects can be gained by analyzing the spectral representation of velocity components [50, 48]. In the buffer layer (BFL) of closed-channel flows, while streamwise and spanwise scales for spanwise velocity are generally smaller in the presence of SS, the wall-normal component is less sensitive [50]. In the logarithmic layer (LGL), effects are more pronounced. Spectra of all velocity components reveal that energetic scales become smaller with increasing stratification [50]. In the OUL, the effects of strong stable stratification are stronger than in other layers, and spectra become different compared to those from a neutral case. In the OUL, the energy containing spanwise scales become larger as stratification increases as shown in Fig. 16 of [50].

In boundary layers, due to the inhomogeneity of the flow in the vertical direction the conventional representation of velocity components in Fourier space can inform us only

about horizontal scales. To better understand the kinetic energy cascade in an SBL, the role of vertical scales needs to be considered, which has not been addressed sufficiently in earlier studies. For homogeneous directions, by using Fourier transform, the standard energy spectrum provides a convenient definition of energy density (i.e. energy per wavenumber). For inhomogeneous directions there is no consensus in the literature on how to define energy density. One approach is to use the second order structure function [27, 21]. The second-order structure function can describe how kinetic energy is distributed among the hierarchy of eddies. The structure function provides information about the energy of eddies when their size is much smaller than the separation r. The eddies of size much greater than r make little contribution to the structure function at separation r. For eddies of size in between, the structure function mixes information from large and small scales [27]. The Ref. [27] proposed using the signature function, which can reproduce TKE when integrated over all separations and does not involve the Fourier transform. Thus the proposed definition can provide a picture of the energy spectrum in physical space. The authors then showed that (Fig. 1,2 of [27]) the proposed definition leads to accurate description of viscous effects on the energy cascade by comparing their result against the conventional energy spectrum for grid turbulence. Nonetheless, second-order structure functions and also signature functions are not kinetic energy, but it can be shown that the structure function is related to kinetic energy in the limit of large scales.

Another approach, first proposed by Ref. [54, 55], is to use the two-point correlation function. This idea is inspired by the observation that for isotropic turbulence one can write the energy of scales larger than a given scale, r, in terms of the two-point correlation function. Hamba [55] used this idea to develop the concept of the energy density (ED), which is the kinetic energy per unit length scale for inhomogeneous turbulence. To obtain a positive energy density for isotropic turbulence, [55] used the two-point correlation function filtered with a kernel function. By analyzing energy transfer for homogeneous and inhomogeneous directions within scale space, [55] showed that there is an energy cascade from large to small scales using the proposed formulation for energy density. Interestingly, an inverse energy cascade from large to very large scales in the near-wall region was shown to happen in the spanwise direction of scale space [55]. Moreover, the new formulation was shown to predict the scale dependence of the upward and downward flux of turbulence kinetic energy. These promising capabilities of the energy density formulation for inhomogeneous direction motivates the present study where we use it for SS open-channel flow in the vertical direction. The present work contributes to our understanding of the mechanisms involved in the energy cascade for SSBL. Characterizing scales that are dominant in the kinetic energy cascade is another critical theme which this chapter aims to address. To do so, kinetic energy density and its budget equation are investigated in wavenumber-scale

Abbreviation	Description
VSL	viscous sublayer
BFL	buffeer layer
LGL	logarithmic layer
OUL	outer layer
SBL	stably stratified boundary layer
SS	stable stratification
SSBL	strongly stable stratified boundary layer
TKE	Turbulent kinetic energy
OBA	Oberbeck-Boussinesq approximation

Table 5.1: List of abbreviations used in this chapter.

space. The energy density is constructed based on a modification of the conventional kinetic energy spectrum by vertical scales. To incorporate vertical scales, we use the filtering of the correlation function as proposed in Ref. [55]. We mainly analyze the scale dependence in the vertical through the use of a hierarchy of scales based on known channel flow physics. We also analyze and compare unstratified and strongly stably stratified cases, the latter of which is computationally challenging and physically less well-understood.

This chapter is organized as follows. The mathematical problem formulation is presented in section 5.2, including numerical methods and mathematical framework for energy density in spectral-scale space. The budget of energy density in spectral-scale space is introduced and discussed in 5.2.2. The details of the simulations carried out are introduced in section 5.3. Results are discussed in section 5.4. The different mechanisms that contribute to the energy cascade are addressed in the results section. This chapter will end in section 5.6, where concluding remarks are highlighted.

5.2 Mathematical formulation

In this chapter we adopt the non-dimensionalized Navier-Stokes equations under the Oberbeck-Boussinesq approximation (OBA) as given in (2.1-2.3).

The simulation test case considered for this work is an open-channel flow with constant cooling flux imposed at the bottom boundary and fixed temperature at the top boundary. No-slip and free-slip boundary conditions are respectively applied to velocity components at the bottom and top boundary. Boundary conditions on temperature are

cooling ($\partial\theta/\partial z = 1$) at the bottom and constant temperature ($\theta = 0$) at the top in the wall-normal direction. Periodic boundary conditions are used for all fields in the streamwise and spanwise directions.

This mathematical formulations and boundary conditions have been used in previous studies [106, 46, 36, 37]. This configuration is similar to the situation at sunset in the ABL, where the background virtual potential temperature is nearly constant in the first few hundreds of meters above ground [98] leading to $\theta = 0$ in Oberbeck-Boussinesq type models for dry air.

The governing equations are solved using a scalable solver called Hercules. The details of the numerical scheme have been presented in chapter 2 and previous studies [58, 7, 8].

5.2.1 Energy density in spectral-scale space

For horizontally homogeneous and stationary turbulence, the horizontal Fourier transform of the two-point velocity correlation can be written as

$$\widehat{Q_{ii}}^{*}(\mathbf{k}, \xi_z, z) = \left\langle \widehat{u_i'}(\mathbf{k}, z, t)\widehat{u_i'}^{*}(\mathbf{k}, z + \xi_z, t) \right\rangle, \tag{5.1}$$

where ξ_z is the vertical separation and $\mathbf{k} = (k_x, k_y)$ is the horizontal wave number vector. The $\langle . \rangle$ stands for time average. The $\widehat{u_i'}$ are the two dimensional Fourier transform of the velocity fluctuations about the horizontal average. The * represents complex conjugate.

For separations with $\xi_z = 0$, i.e. purely horizontal separations, the horizontal energy spectrum can be directly extracted from $\widehat{Q_{ii}}^{*}/2$. For the vertical direction, we adopt the formulation proposed in Ref. [55] to define energy density for turbulence with possible inhomogeneity. However, unlike [55, 56], we keep the Fourier approach in the horizontal while applying Hamba's (2018, 2019) [55, 56] approach in the vertical direction only. The resulting expression for energy density is derived in this section, based on the ideas in Ref. [54, 55, 56]. In what follows, we drop time dependence for simplicity. Moreover, we use the same notation as used in Ref. [55] for the energy, but here it is in horizontal Fourier space, whereas in Ref. [55], it is in physical space.

First, let $E_>(\mathbf{k}, r_z, z)$ be the kinetic energy associated with horizontal wave number $\mathbf{k}$ and vertical scales larger than a given vertical scale r_z. Then, the contribution to the kinetic energy from eddies of vertical length scales l_z slightly larger than r_z, i.e. with $r_z \leq l_z \leq r_z + dr_z$, is

$$E_>(\mathbf{k}, r_z, z) - E_>(\mathbf{k}, r_z + dr_z, z) \approx -(\partial E_>/\partial r_z)dr_z \tag{5.2}$$

for sufficiently small dr_z. Thus $\partial E_>/\partial r_z$ contains information about energy concentration around scales r_z. The next step is constructing $E_>$. Two constraints should be satisfied, although they might not lead to a unique expression. These constraints are extensions of the criteria given in Ref. [55], who gave them entirely in physical space, to horizontal spectral and vertical scale space (spectral-scale). These constraints are

$$\begin{aligned} &E_>(\mathbf{k}, r_z = 0, z) = \widehat{Q_{ii}}^*(\mathbf{k}, \xi_z = 0, z), \\ &\lim_{r_z \to \infty} E_>(\mathbf{k}, r_z, z) = 0. \end{aligned} \tag{5.3}$$

The first constraint is that $E_>(\mathbf{k}, 0, z)$ must recover the horizontal wavenumber kinetic energy spectrum at each z. The second constraint ensures boundedness for large r_z. From the first constraint $E_>(\mathbf{k}, r_z = 0, z)$ is positive semi-definite. The energy density is defined as

$$\mathrm{ED} = -\frac{\partial E_>}{\partial r_z}. \tag{5.4}$$

The $\widehat{Q_{ii}}^*$ satisfies the constraints mentioned above in case of homogeneity in all three dimensions. Thus $\widehat{Q_{ii}}^*$ might be considered as a possible choice for $E_>$. However, $\widehat{Q_{ii}}^*$ is not necessarily a decreasing function in wall-normal direction, and thus special treatment is considered to modify velocity correlations by which the constraints are satisfied.

By applying [55, 56] only for vertical scales, $E_>(\mathbf{k}, r_z, z)$ is the kinetic energy associated with horizontal wave number $\mathbf{k}$ and vertical scales larger than r_z. Thus, $E_>$ has a low-pass (compared to r_z) filter of velocity correlation in its definition. In what follows we adopt $\widehat{Q_{ii}}^*$ as a base function and we seek the class of filter kernels by which, when applied to $\widehat{Q}^*_{ii}$, give $E_>$ that satisfies the constraints. Following [55, 56], $E_>$ can be expressed as

$$E_>(\mathbf{k}, r_z, z) = \int_{-\infty}^{+\infty} G(\xi_z, r_z) \widehat{Q_{ii}}^*(\mathbf{k}, \xi_z, z)\, \mathrm{d}\xi_z, \tag{5.5}$$

where G is the filter kernel that needs to be specified. The first constraint for $E_>$ implies that

$$\int_{-\infty}^{+\infty} G(\xi_z, 0) \widehat{Q_{ii}}^*(\mathbf{k}, \xi_z, z)\, \mathrm{d}\xi_z = \widehat{Q_{ii}}^*(\mathbf{k}, 0, z). \tag{5.6}$$

The second constraint imposes that

$$\lim_{r_z \to \infty} \int_{-\infty}^{+\infty} G(\xi_z, r_z) \widehat{Q_{ii}}^*(\mathbf{k}, \xi_z, z)\, \mathrm{d}\xi_z = 0, \tag{5.7}$$

and thus $\lim_{r_z\to\infty} G(\xi_z, r_z) = 0$, which suggests $G \sim \frac{1}{r_z} f(\xi_z/r_z)$ where f is a similarity function which should remain bounded when r_z approaches infinity. By assuming $\widehat{Q_{ii}}^*$ is infinitely differentiable with respect to ξ_z, using Taylor series expansion around $\xi_z = 0$ (5.6) yields

$$\lim_{r_z\to 0} \int_{-\infty}^{+\infty} G(\xi_z, r_z)\ \mathrm{d}\xi_z = 1, \tag{5.8}$$
$$\lim_{r_z\to 0} \int_{-\infty}^{+\infty} \xi_z^n G(\xi_z, r_z)\ \mathrm{d}\xi_z = 0, \quad (n = 1, 2, ...),$$

as two plausible constraints for the filter kernel. These imply that G is a filter kernel of filter width r_z where the moments of order greater than one are all equal to zero. These criteria imply that for very small values of r_z, f should approaches zero at a rate much faster than the rate $1/r_z$ approaches infinity. Hence, a Gaussian form for f where $f(\xi_z/r_z) = \frac{1}{a}\exp\left(-(1/b)(\xi_z/r_z)^2\right)$ is one possible choice as employed in Ref. [55]. Using (5.8) leads to $a = \sqrt{2\pi}$, $b = 2$, and thus, the filter kernel could be expressed as

$$G(\xi_z, r_z) = \frac{1}{\sqrt{(2\pi)}r_z} \exp(-\frac{\xi_z^2}{2r_z^2}). \tag{5.9}$$

Therefore, for channel flow turbulence, energy density in spectral-scale space based on (5.4) can be defined as [55],

$$\mathrm{ED}(\mathbf{k}, z, r_z, t) = \int_{-\infty}^{+\infty} \widehat{Q_{ii}}^*(\mathbf{k}, \xi_z, z, t)\ G_D(\xi_z, r_z)\ \mathrm{d}\xi_z = G_D \circ \widehat{Q_{ii}}^*, \tag{5.10}$$

where

$$G_D(\xi_z, r_z) = -\frac{\partial G}{\partial r_z} = \frac{1}{\sqrt{2\pi}r_z^2}\left(1 - \frac{\xi_z^2}{r_z^2}\right)\exp\left(-\frac{\xi_z^2}{2r_z^2}\right), \tag{5.11}$$

and $\circ$ denotes integral operation as specified in (5.10).

On the one hand, computations that involve the two-point velocity correlation are generally expensive. Thus, carrying out energy density calculations in purely physical space is costly for analyzing simulations with a large computational domain or high Reynolds number. On the other hand, computation of Fourier modes required for spectral analysis are typically fast and can be efficiently extended for massively parallel calculations. The formulation for energy density discussed in this section provides a mathematical framework

to incorporate vertical scales in conventional horizontal spectral analysis. This approach can make the computational expense affordable for large domains and high Reynolds numbers. In addition, analyzing horizontal Fourier spectra has been an essential part of the numerous studies [69] of kinetic energy cascade in wall-bounded flows. It is convenient to use the same framework wherever it is possible (horizontal planes).

5.2.2 Energy density exchange in spectral-scale space

To derive an equation for the evolution of kinetic energy density in stably stratified boundary layers, we employ the governing equations of velocity fluctuations

$$\frac{\partial u_i'}{\partial x_i} = 0, \tag{5.12}$$

$$\frac{\partial u_i'}{\partial t} + \frac{\partial \overline{u_i} u_j'}{\partial x_j} + \frac{\partial u_i' \overline{u_j}}{\partial x_j} + \frac{\partial u_i' u_j'}{\partial x_j} = -\frac{\partial p'}{\partial x_i} + \frac{1}{Re}\frac{\partial^2 u_i'}{\partial x_j \partial x_j} + Ri\theta'\delta_{i3} + \frac{\partial \overline{u_i' u_j'}}{\partial x_j}, \tag{5.13}$$

where over bars refer to horizontal averaging and primes refers to fluctuations from horizontal averaging. We will use two independent coordinate systems, one of which is vertically shifted by ξ_z from the original coordinate x_i. So, the vertically shifted coordinate system has components $\eta_i = x_i + \xi_z \delta_{i3}$. Variables belonging to the shifted coordinate are denoted by $|_{\xi_z}$. For example, $\widehat{u_i'}^*|_{\xi_z}$ describes complex conjugate of Fourier transform of fluctuating velocity component on a domain that is vertically shifted by ξ_z. The governing equation of the rate of change of energy density is readily derived by adding $\widehat{u_i'}^*|_{\xi_z}\partial\widehat{u_i'}/\partial t$ and $\widehat{u_i'}\partial\widehat{u_i'|^*_{\xi_z}}/\partial t$. Then, the resulting expression is multiplied by the kernel function and integrated. The budget equation for energy density then reads as

$$\frac{\partial \mathrm{ED}}{\partial t} = \quad \frac{1}{2}\left(\mathrm{TR} + \mathrm{SP} + \mathrm{PW} + \mathrm{VD} + \mathrm{BD} + \mathrm{RS}\right), \tag{5.14}$$

where the terms on the right-hand side are: nonlinear transfer, shear production, pressure transport (work), viscous contribution, buoyancy, and Reynolds stress work.

The TR term is the nonlinear transfer of energy density, which is a convolution sum and therefore involves triad interactions among horizontal wavenumbers. For instance, the first part of the nonlinear term in the OBA equations (2.1-2.3) can be expanded as

$$\widehat{\frac{\partial u_i' u_j'}{\partial x_j}} = Ik_1\widehat{u_i' u_1'} + Ik_2\widehat{u_i' u_2'} + \frac{\partial \widehat{u_i' u_3'}}{\partial x_3}, \tag{5.15}$$

which involves two kinds of nonlinear interactions: in-plane triad interactions as in the first two terms and inter-plane interactions dictated by the last term [14]. The total nonlinear transfer term is a summation of these two mechanisms as

$$\mathrm{TR} = -\mathrm{TR}_i - \mathrm{TR}_o = -G_D \circ \left(\widehat{\frac{\partial u_i' u_j'}{\partial x_j}} \widehat{u_i'}^* |_{\xi_z} + \widehat{\frac{\partial u_i' |_{\xi_z} u_j'|_{\xi_z}}{\partial \eta_j}}^* \widehat{u_i'} \right), \tag{5.16}$$

and represents how TKE density is transferred and transported by nonlinear interactions between scales and throughout the channel. For a given set of horizontal wavelengths (λ_x, λ_y), vertical scale r_z, and height z, positive TR means ED is being transferred into that particular wavelength, vertical scale and height by nonlinear interactions and hence ED is increased. Similarly, negative TR means ED is being transferred out of that particular wavelength, vertical scale and height by nonlinear interactions and hence ED is decreased. The two contributions to TR are

$$\begin{aligned} \mathrm{TR}_i = \quad & G_D \circ \left\{ \left(Ik_1 \widehat{u_i' u_1'} + Ik_2 \widehat{u_i' u_2'} \right) \widehat{u_i'}^* |_{\xi_z} \right\} + \\ & G_D \circ \left\{ \left(-Ik_1 \widehat{u_i' |_{\xi_z} u_1'|_{\xi_z}}^* - Ik_2 \widehat{u_i' |_{\xi_z} u_2'|_{\xi_z}}^* \right) \widehat{u_i'} \right\}, \end{aligned} \tag{5.17}$$

which involves in-plane triad interaction as will be discussed shortly, and

$$\mathrm{TR}_o = G_D \circ \left(\widehat{\frac{\partial u_i' u_3'}{\partial x_3}} \widehat{u_i'}^* |_{\xi_z} + \widehat{\frac{\partial u_i' |_{\xi_z} u_3'|_{\xi_z}}{\partial \eta_3}}^* \widehat{u_i'} \right), \tag{5.18}$$

which includes inter-plane interactions [14]. TR_o refers to the rate at which ED varies due to vertical transport with wall-normal velocity in at least one of the pairs. At each vertical level, if this variation positively correlates with a corresponding fluctuating velocity component at a distance ξ_z aloft (or below), then energy density increases at that specific height.

The SP term represents production of kinetic energy density caused by mean shear. The SP reads as

$$\mathrm{SP} = -G_D \circ \left(\widehat{\frac{\partial \overline{u_i} u_j'}{\partial x_j}} \widehat{u_i'}^* |_{\xi_z} + \widehat{\frac{\partial \overline{u_i} |_{\xi_z} u_j'|_{\xi_z}}{\partial \eta_j}}^* \widehat{u_i'} \right), \tag{5.19}$$

and involves the contribution to mean shear production for both original and vertically shifted domains. In deriving this equation the fact that mean profiles and components of Reynolds stresses are only z dependent and come out of horizontal Fourier transform operations is used. In addition, the horizontally averaged vertical velocity profile is zero (i.e. $\overline{u_3} = 0$) which has been used accordingly.

The pressure transport term is given by

$$\mathrm{PW} = -G_D \circ \left(\widehat{\frac{\partial u_3'|_{\xi_z}}{\partial \eta_3}}^{*} \widehat{p'} + \widehat{\frac{\partial p'}{\partial x_3}} \widehat{u_3'}^{*}|_{\xi_z} + \widehat{\frac{\partial u_3'}{\partial x_3}} \widehat{p'|_{\xi_z}}^{*} + \widehat{\frac{\partial p'|_{\xi_z}}{\partial \eta_3}}^{*} \widehat{u_3'} \right), \tag{5.20}$$

and therefore is due to vertical variation of correlation between fluctuating pressure in original domain and fluctuating velocity of shifted domain and vice versa.

Similar to nonlinear transfer, the viscous term VD has in-plane and inter-plane contributions as [14]

$$\mathrm{VD} = \mathrm{VD}_i + \mathrm{VD}_o = \frac{1}{Re} G_D \circ \left(\widehat{u_i'}^{*}|_{\xi_z} \widehat{\frac{\partial^2 u_i'}{\partial x_j \partial x_j}} + \widehat{u_i'} \widehat{\frac{\partial^2 u_i'|_{\xi_z}}{\partial \eta_j \partial \eta_j}}^{*} \right), \tag{5.21}$$

where

$$\mathrm{VD}_i = -\frac{1}{Re} G_D \circ \left({k_1}^2 \widehat{u_i'} \widehat{u_i'}^{*}|_{\xi_z} + {k_2}^2 \widehat{u_i'} \widehat{u_i'}^{*}|_{\xi_z} \right), \tag{5.22}$$

is the horizontal gradient effect of viscosity and

$$\mathrm{VD}_o = \frac{1}{Re} G_D \circ \left(\widehat{u_i'}^{*}|_{\xi_z} \frac{\partial^2 \widehat{u_i'}}{\partial x_3^2} + \widehat{u_i'} \frac{\partial^2 \left(\widehat{u_i'}^{*}|_{\xi_z} \right)}{\partial \eta_3^2} \right), \tag{5.23}$$

is the vertical gradient effect of viscosity. The contribution due to buoyancy BD is given as

$$\mathrm{BD} = Ri G_D \circ \left(\widehat{\theta'} \widehat{u_3'}^{*}|_{\xi_z} + \widehat{\theta'|_{\xi_z}}^{*} \widehat{u_3'} \right), \tag{5.24}$$

which involves correlation between fluctuating vertical velocity and temperature among the original and vertically shifted domains. Finally the contribution of Reynolds stresses have the form

$$\mathrm{RS} = G_D \circ \left(\widehat{u_i'}^{*}|_{\xi_z} \widehat{\frac{\partial \overline{u_i' u_3'}}{\partial x_3}} + \widehat{u_i'} \widehat{\frac{\partial \overline{u_i'|_{\xi_z} u_3'|_{\xi_z}}}{\partial \eta_3}}^{*} \right) = 0. \tag{5.25}$$

The RS term arises from the fact that Reynolds stresses ($-\overline{u_i' u_j'}$) affect the dynamics of u_i' by $\partial\overline{u_i' u_j'}/\partial x_j$. However, terms in the integrand that involve derivatives with respect to x_3 and η_3 are horizontally uniform, and therefore do not have have contributions in spectral space other than the mean mode. These terms are multiplied by $\widehat{u_i'}$ and $\widehat{u_i'}^*|_{\xi_z}$ which do not have mean mode contribution, thus RS = 0.

It is worth mentioning that, apart from the sound mathematical foundation that is provided by the Fourier spectral representation of the flow field data to analyze the energy cascade in the horizontal, we chose Fourier spectral representation because of its computational efficiency as well. For example, applying the FFT to compute the in-plane energy spectrum is much faster than the calculation of the two-point velocity correlation in horizontal planes. However, even applying the scale-space formulation only in one direction, as we do here, is expensive and involves massive calculations in five dimensions at each analysis time: two for horizontal wave numbers k, one for the wall-normal direction z, one for the vertical separation ξ_z, and one for vertical length scales r_z. As a result, a moderate Reynolds number is considered to make computations tractable.

5.3 Simulations overview

To analyze the TKE cascade for an SBL, we considered three different simulations: an unstratified case L0, and two strongly stable stratified cases L1 and L2. Parameters for these test cases are summarized in Table 5.2. In all of these simulations a computational domain of size $L_x/h = 8\pi$, $L_y/h = 6\pi$, and $L_z/h = 1$ with h as the height of the open-channel is discretized using $N_x = 1536$, $N_y = 2304$, and $N_z = 192$ grid points. The friction Reynolds number is of a moderate value of $Re = 560$. The friction Richardson numbers considered in this work covers neutral stratification where $Ri = 0$ as well as strong stratification with $Ri = 1120$ for L1 and $Ri = 1680$ for L2. Prandtl number $Pr = 1$ for all cases. Grid resolution in the horizontal plane (in wall units, eg. $\Delta x^+ = \Delta x Re$) is $\Delta x^+ = 9.2$ and $\Delta y^+ = 4.6$. In the vertical direction, Δz^+ increases from 0.32 to 6.3 at the wall and top of the open-channel, respectively, as the grid is stretched in the wall-normal direction. The Reynolds number and grid resolutions in our simulations are comparable to case B5b in Ref. [50]. The t_{av} in the Table 5.2 refers to averaging time interval for collecting statistics in the stationary state. The time step is $\Delta t = 0.0003$ for L0 and L1 and $\Delta t = 0.0002$ for L2.

The $Ri = 1120$ and $Ri = 1680$ cases considered here correspond to $h/L_{MO} = 0.82$ and $h/L_{MO} = 1.23$. For values of $h/L_{MO} \lesssim 1$, near-wall turbulence is strongly affected by

stratification, although the turbulence may not collapse depending on the initial condition [7, 8]. In cases such as L2 where $h/L_{MO} > 1$, turbulence will collapse or undergo significant spatio-temporal intermittencies, as will be described later.

In the strongly stable stratification regime for open-channel flow, the evolution of TKE is extremely sensitive to the choice of the initial condition. In fact, the effect of stratification on the transient dynamic is so strong, only simulations with carefully designed initial conditions will manage to survive significant decay early in the cooling process and recover from laminarization. For example, initializing strongly stratified cases (L1, L2) with the unstratified case (L0) leads to laminarization without recovery.

The unstratified case, L0, is initialized from a neutrally stratified open-channel flow simulation that has reached a stationary state on a smaller domain, with $L_x = 2\pi$ and $L_y = \pi$ with the same grid resolution as L0. Then the initial condition for L0 is obtained by copying the smaller domain simulation 4 times in the streamwise direction and 6 times in the spanwise direction. This systematic approach prevents intense deformation (stretching and tilting) of the coherent structures that are active in the small domain simulation and leads to shorter run time to acquire a new stationary state for L0.

For L1, we first run a small domain simulation with the same parameters and grid resolution as the full domain simulation but with a different upper thermal condition $\partial\theta/\partial z = 0$ (adiabatic free slip wall at the top). This choice of upper thermal boundary condition was discussed in detail in Ref. [7, 8] and also in chapters 3 and 4. This first stage simulation is itself initialized with the small domain state used to initialize L0. After this first stage simulation reaches stationarity, we carry out the second stage of initialization (still on a small domain) where now the top boundary condition is the same as that used for L1 (free slip condition for velocity and $\theta = 0$). After this second stage simulation acquires stationarity, we carry out the third stage of initialization, which is copying stage two onto the full domain.

The first stage of initializing L2 is performed with a smaller domain simulation with adiabatic and free slip top boundary conditions, initialized with instantaneous data taken from the end of L1 in stage 1, at which TKE reaches its maximum. We then add uniformly distributed random noise to velocity components with an amplitude of 0.2. We then run the first stage of the initialization of L2 with this initial field. As the flow reaches stationarity, we then switch to the second stage, where we use the same boundary condition as L2 (free slip condition for velocity and $\theta = 0$) but still on a smaller domain until stationarity is reached. It should be pointed out that flow at this second stage becomes spatially intermittent but temporally stationary. At this point, although the flow becomes patchy, this patchiness persists in time and neither entirely collapse nor recovers from such a state.

Case	Ri	h/L_{MO}	t_{av}
L0	0	0	10.4
L1	1120	0.82	10.5
L2	1680	1.23	10.1

Table 5.2: Parameters that vary in different simulations

Now, the results of the second stages are then copied into the larger computational domain, and the last stage of initializing L2 is completed. It should be noted that skipping the first stage, and directly simulating the small domain simulation with the same boundary condition as L1 and L2, leads to full collapse due to the importance of the neutral OUL in recovery [7].

In this study, carefully initialized flow prevents near-wall turbulence from full collapse and stabilizing the OUL controls recovery from partial collapse leading to sustained patchiness of the flow in L2. Therefore, we can focus on the statistical characteristic of the flow at such strong stable stratification by having more samples and removing time dependency of the intermittent state.

5.4 Results

In this section, the results of the analysis using the formulation for energy density balance given in the section 5.2.2 are presented and discussed.

5.4.1 Horizontally averaged profiles

Prior to discussing the kinetic energy density in detail, we explore the main features of the different cases considered in this study. To do so, we consider vertical profiles of horizontally averaged first and second-order statistics of velocity and temperature (Fig. 5.1). The vertical profile of the streamwise mean velocity (Fig. 5.1a) shows the mean streamwise velocity increases with stratification. This is consistent with previous studies on smaller domains [52, 4, 130, 106, 46, 36, 8, 7] (see also chapters 3 and 4) and those with comparable domain size [50]. However, this increase in mean streamwise velocity is less pronounced in the inner layer part where $z/h \lesssim 0.15$ due to dominance of wall-generated shear over buoyancy [7]. Stable stratification caused by the flux of heat from the top boundary accentuates this increase in mean streamwise velocity moving upwards.

Profiles of streamwise velocity fluctuations in Fig. 5.1(d) suggest L0 and L1 have similar near-wall structures (e.g. streaks). The flow pattern in both cases is relatively similar in that spanwise homogeneity of turbulence is achieved. However, in L2, the flow consists of strips of active regions next to quiescent regions, as shown in Fig. 5.2. A similar flow structure is seen in the decay and early recovery phase of wall turbulence with surface cooling [7] (see also chapter 3). The difference between the patchiness of the flow in L2 and that in our previous studies is that in L2, the flow does not recover from such spanwise patchiness. This permanent intermittency of the flow in the spanwise direction is due to the balance between two simultaneous sources of stable stratification imposed from the wall and top boundary (Fig. 5.1c).

To show the strength of stratification, profiles of gradient Richardson number Ri_g are presented. The Ri_g is defined as

$$Ri_g = \frac{N^2}{S^2}, \tag{5.26}$$

where $N^2 = Ri\partial\overline{\theta}/\partial z$ is the buoyancy frequency and $S^2 = \left(\partial\overline{u}/\partial z\right)^2 + \left(\partial\overline{v}/\partial z\right)^2$. The profiles of Ri_g are shown in Fig. 5.1(b). As it can be seen, buoyancy become more significant over shear and the boundary layer become more stable moving upward and as Ri increases. In the OUL where $z/h \geq 0.8$, Ri_g acquires values close to the 0.25 stability criteria for both L1 and L2, which signifies strong effects of stratification in the OUL. In the near-wall region $z/h \leq 0.15$ shear dominates buoyancy and stratification has minimal effects [8] (see also chapter 4). Mean temperature is roughly constant when temperature is passive as in L0 (Fig. 5.1c). For L1 and L2, temperature contributes to the boundary layer dynamics as an active scalar. For both L1 and L2, a strong capping inversion can be seen near the upper boundary of the channel. The vertical gradient of temperature at the bottom wall increases as Ri increases.

The velocity variances $\overline{u'u'}$, $\overline{v'v'}$, and $\overline{w'w'}$ for L0, L1, and L2 at stationarity are shown in Fig. 5.1(d-f), respectively. In the near-wall region, these profiles are consistent with our earlier observation that, at stationarity, near-wall turbulence is governed mostly by wall-generated mean shear, and stratification plays a relatively minor role. The higher values for $\overline{u'u'}$ for L2 in the near-wall region where $z/h \lesssim 0.15$ (Fig. 5.1d) in comparison with cases L0 and L1 are due to spanwise patchiness of the flow rather than more intensive streamwise fluctuations (streaks) in the turbulent strips. The upper LGL (see Table 5.1 for the definition) in L2 is extended to $z/h \approx 0.4$ due to extensive boundary near-wall region growth and shrinking of the OUL part in L2 (Fig. 5.2 side contour plots) relative to L0 and L1. The profiles of $\overline{v'v'}$ and $\overline{w'w'}$ in L2 closely follow L1 in the OUL, where differences become more prominent between L0 and L2. The near-wall vortical structures

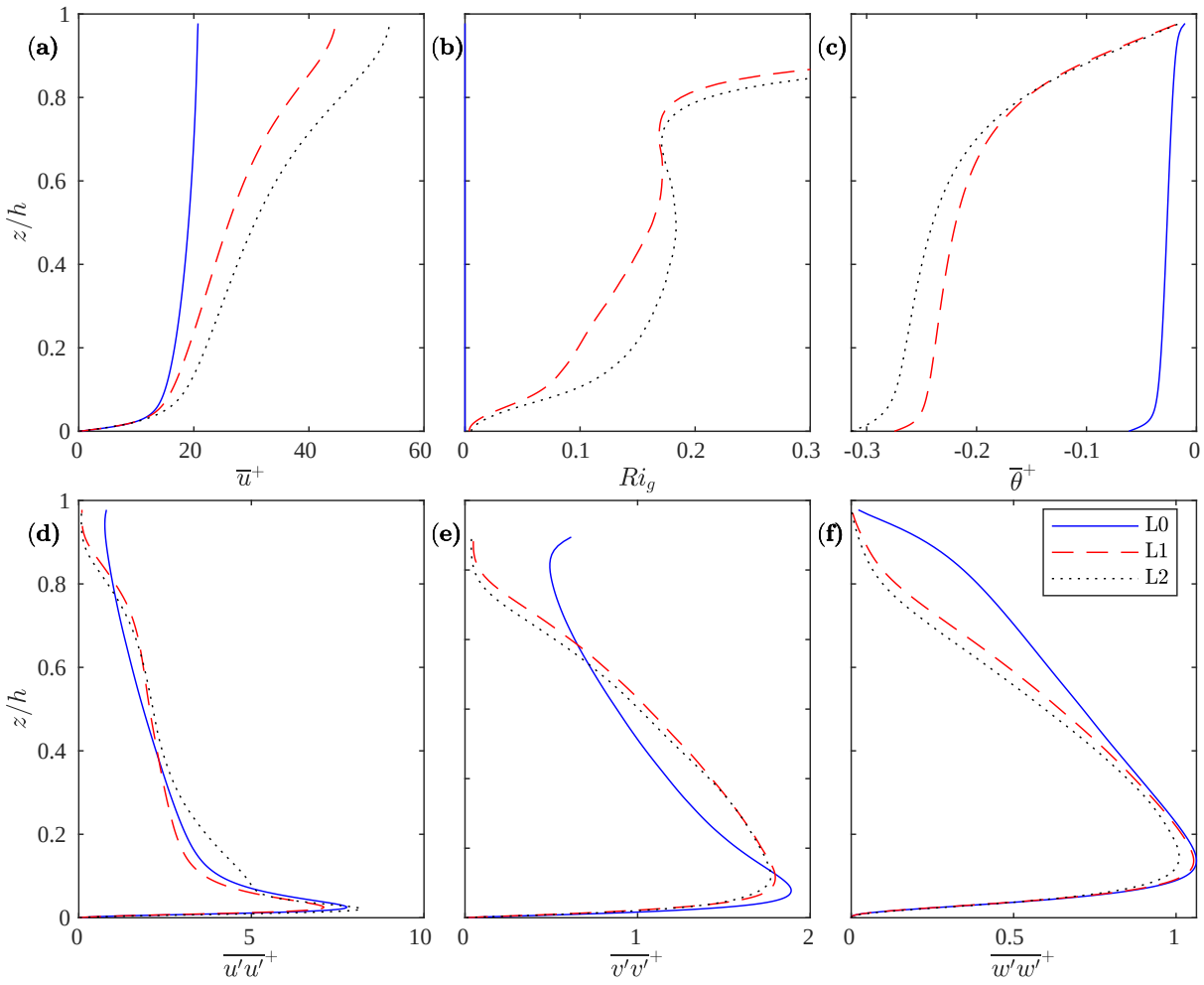

Figure 5.1: Vertical profiles of mean flow variables and velocity variances. (a) mean streamwise velocity, (b) gradient Richardson number, (c) mean temperature, (d) streamwise velocity variance, (e) spanwise velocity variance, and (f) wall-normal velocity variance

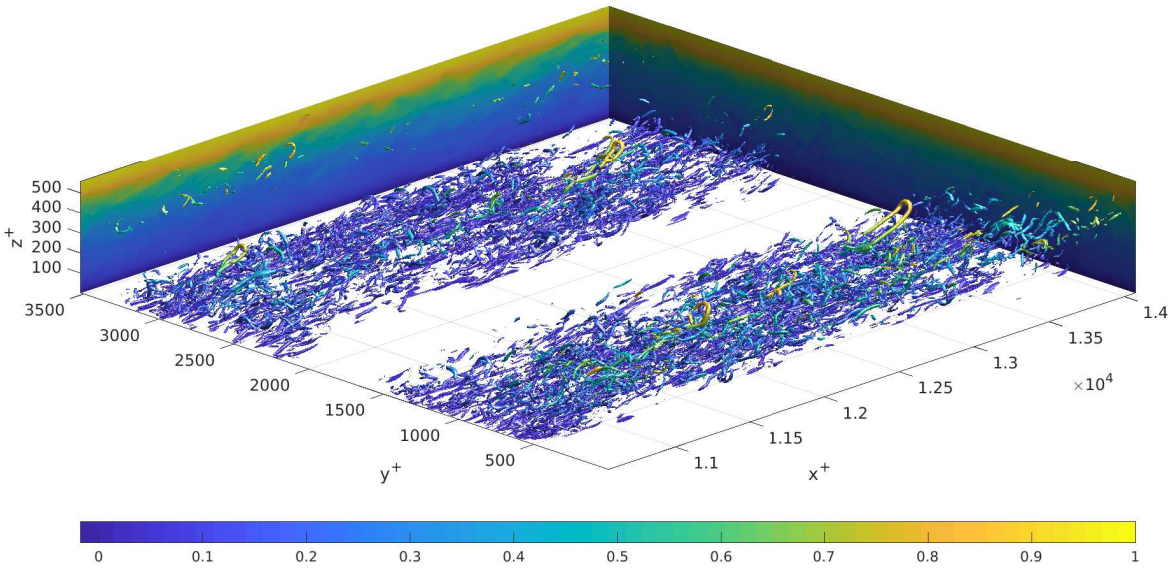

Figure 5.2: Isosurfaces of Q-criterion (second invariant of gradient tensor of fluctuating velocities) for L2 in the region where $6\pi \leq x/h \leq 8\pi$ and $0 \leq y/h \leq 2\pi$, which are colored by distance from the wall. In the cross-sectional slices, the kinetic energy in streamwise and spanwise planes are shown. The Q-criterion and total kinetic energy are normalized using their maximum values. The isosurfaces are plotted at the level of 0.01. The color bar illustrates values of normalized total kinetic energy.

are dominated by quasi-streamwise vortical structures rather than hairpin-like structures, as shown in Fig. 5.2 for L2 in the region where $6\pi \leq x/h \leq 8\pi$ and $0 \leq y/h \leq 2\pi$. Consistent with our previous observations in which smaller domain with spanwise domain of the size of π has one turbulent strip [7] (see also chapter 3), the full spanwise length has 6 strips suggesting that spanwise intermittencies has a repeating pattern in the spanwise direction at each π.

5.4.2 Hierarchy of flow structures

By looking at the energy cascade as a function of specific vertical length scales that are linked to known boundary layer processes, one may have a better understanding of the

impact of stable stratification on the energy cascade dynamics. These specific length scales are denoted by r_z, and in an energy cascade of wall turbulence can be categorized into four levels. The first level of the hierarchy is composed of structures with vertical sizes comparable to the height of the viscous sublayer (VSL), where $r_z^+ = 3$. The second level of the hierarchy is composed of flow structures with $r_z^+ = 15$ to account for BFL sized structures. Therefore, flow structures that are attached to the wall and belong to the second level of the hierarchy might form the BFL. On the other hand, the flow structures that belong to these first two levels and are detached from the wall are small enough to be affected by viscosity and may be involved in viscous effects further away from the wall. The third level of hierarchy is for structures of a size comparable to the height of the LGL where $r_z^+ = 0.14Re = 80$. Finally, the fourth level of hierarchy is composed of the flow structure of the size of the OUL where $r_z^+ = 0.75Re = 420$.

5.4.3 Kinetic energy

Let us now discuss kinetic energy, which allows us to include the effects of all horizontal modes in the kinetic energy cascade. Before we proceed, it is worth recalling that $\mathrm{ED}(\mathbf{k}, r_z, z)$ represents energy density for a vertical scale r_z and horizontal wavenumber vector $\mathbf{k}$. As we will see, the energy density in small r_z tends to be large, even though the kinetic energy integrated over small scales is relatively small. As a result, we will consider r_zED rather than ED, and similarly for terms in the budget, since it gives the energy per octave (or decade) of vertical scales [55]. Analogously , we premultiply spectra by horizontal wavenumbers, as is common [69, 70, 20, 8].

Fig. 5.3 shows the dependence of ED upon horizontal and vertical scales and also how energy distribution is changed by stratification. We first discuss dependence of energy density upon streamwise scales λ_x and height for different r_z and stratifications. To do so, ED (5.10) is summed over λ_y and contour plots of the result are shown in Fig. 5.3 (a,c,e) which correspond to L0, L1, and L2, respectively. In L0 and L1, ED is concentrated at larger λ_x as r_z increases (Fig. 5.3a,c). Moreover, by comparing Fig. 5.3(a,c) for $r_z^+ = 15$, one can say that the λ_x spectrum gets narrower by increasing stability of the boundary layer (increasing Ri). For example, the contour lines in L0 for $r_z^+ = 15$, which contain less than 0.15 of ED maximum, does not become closed for $\lambda_x \simeq L_x$. In L1 (for $r_z^+ = 15$), contour lines referring to 0.15 of ED maximum become closed for $\lambda_x \simeq L_x$. In L2, the most energetic streamwise scales ($\lambda_x/h \sim 1$) are suppressed and the largest λ_x become more active compared to L1.

In L0, for r_z of the size of the LGL with $r_z^+ = 80$ (Fig. 5.3a), the largest ED belongs to large structures [50] of the size in the range λ_x/h from 3 to 10. These structures reside

in the BFL and extend into the OUL, showing that structures with this vertical scale link viscous regions to the OUL. Thus, the third level of hierarchy bridges energy-containing scales of the size $\lambda_x/h \sim 1$ in the BFL to less energetic scales of the size $\lambda_x/h \sim L_x/h$ in the OUL. In contrast, such a link between streamwise scales in the inner and outer layers by vertical structures of the size of the height of the logarithmic layer (5.3a, inclined dashed blue contour lines) is suppressed in stratified cases L1 and L2 (Fig. 5.3d,f). In L2, ED resides mostly in the largest λ_x of the size of L_x. Moreover, in the most stratified case L2, the structures with a vertical size of $r_z^+ = 80$ do not reach the wall.

Now we discuss the dependence of energy density upon spanwise scales λ_y and height for different r_z and different simulations. To do so, ED is summed over λ_x, and contour plots of results are shown in Fig. 5.3(b,d,f) which correspond to L0, L1, and L2, respectively. The energy-containing spanwise scales are smaller than the energy-containing streamwise scales for all r_z. The dependence of energy-containing λ_y upon r_z is much weaker than streamwise scales. The energy density spectra as a function of λ_y and height shows symmetry around a line in the logarithmic region with $\lambda_y \sim z$. The linear dependence of λ_y on the distance from the wall signifies the role of the LGL in the formation of the attached eddies [20, 66]. The symmetry of spanwise scales around the line $\lambda_y \sim z$ is preserved for all energetic r_z suggesting that energy containing spanwise scales in the logarithmic layer are linearly dependant upon the distance from the wall. The similarity in behaviour of energy-containing spanwise scales upon height also suggests there is a self-similar process affecting all spanwise scales (i.e. self-sustaining process). All of the r_z scales are most energetic at $z^+ \approx 15$. In L2, there is a narrow band in which the size of energetic spanwise scales is almost constant with respect to height and for all r_z. This $\lambda_y/h \approx 3$ ($\lambda_y^+ \approx 1700$) associated with this band contains one turbulent strip and one quiescent region (Fig. 5.2). Moreover, energetic spanwise scales $\lambda_y/h \sim 0.2$ at $z^+ \in [10 - 100]$ for L2 are dominated by r_z of the size of the buffer layer and logarithmic layer height. These energetic scales are responsible for sustaining turbulence in the active regions (turbulent strips). The footprint of the OUL size structures in the BFL is not observed in L2 for energy containing spanwise scales. The presence of turbulent strips in the near-wall region without a footprint of $r_z^+ = 420$ size structures suggest that near-wall turbulence in a SBL can be autonomously sustained even without interacting with OUL size structures with vertical size comparable to h similar to unstratified cases [72].

The magnitude of premultiplied ED for all levels in the hierarchy is shown in Fig. 5.4 for a single stratification, L1. This case is chosen since stratification effects on turbulence are shown to be strong earlier in the surface cooling process [7, 8] (see also chapters 3 and 4), while spanwise homogeneity of turbulence is maintained. As shown, $r_z^+ = 15$ is the most energetic vertical scale among the r_z discussed here, which refer to structures of the

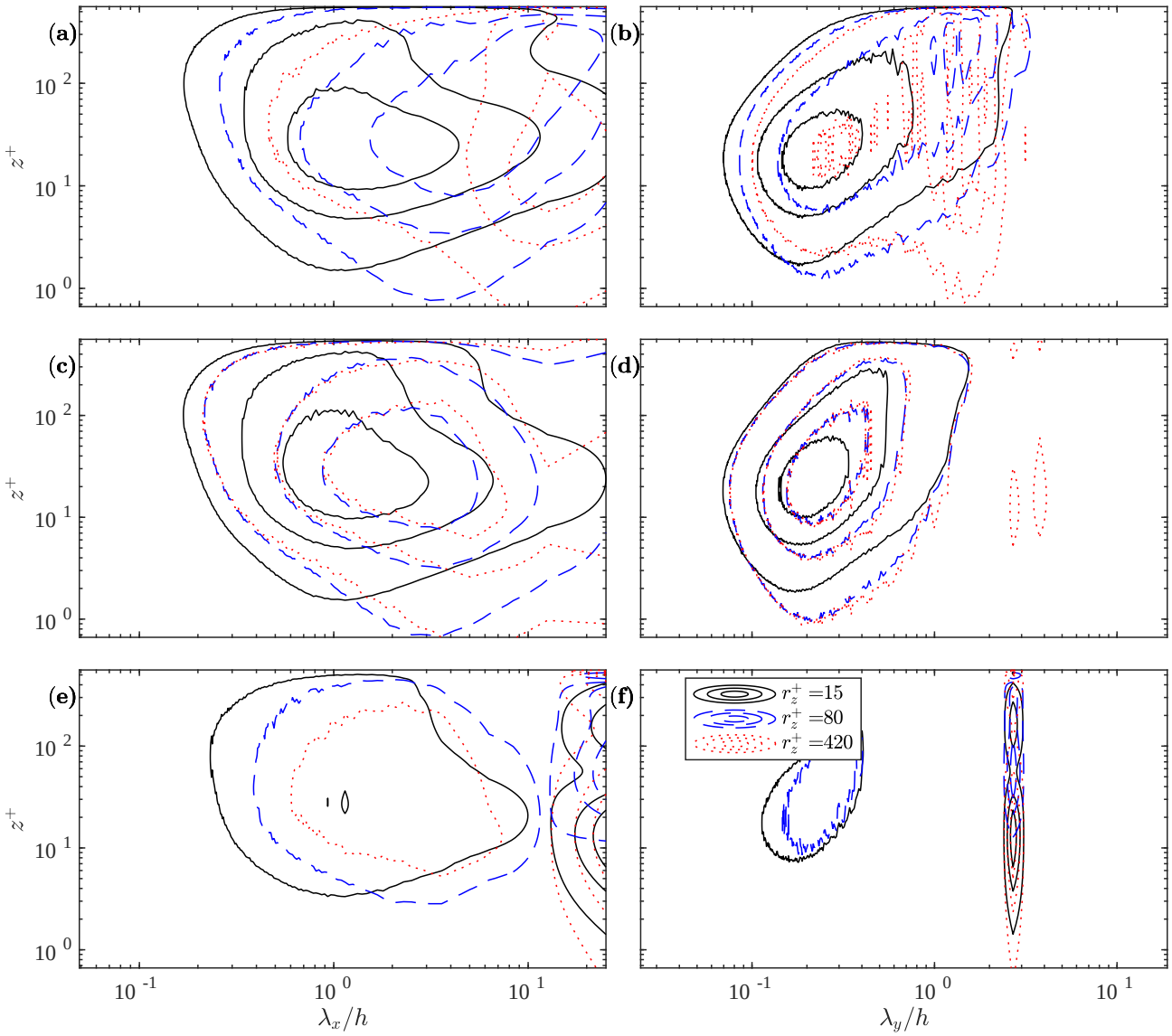

Figure 5.3: Premultiplied energy density (ED) for (a,c,e) streamwise ($r_z k_x \sum_{k_y}$ ED) and (b,d,f) spanwise ($r_z k_y \sum_{k_x}$ ED) wavelengths. Panels (a-b), (c-d), and (e-f) respectively refers to L0, L1, and L2. Contours are plotted at 0.15, 0.45, and 0.75 of the maximum of corresponding spectra.

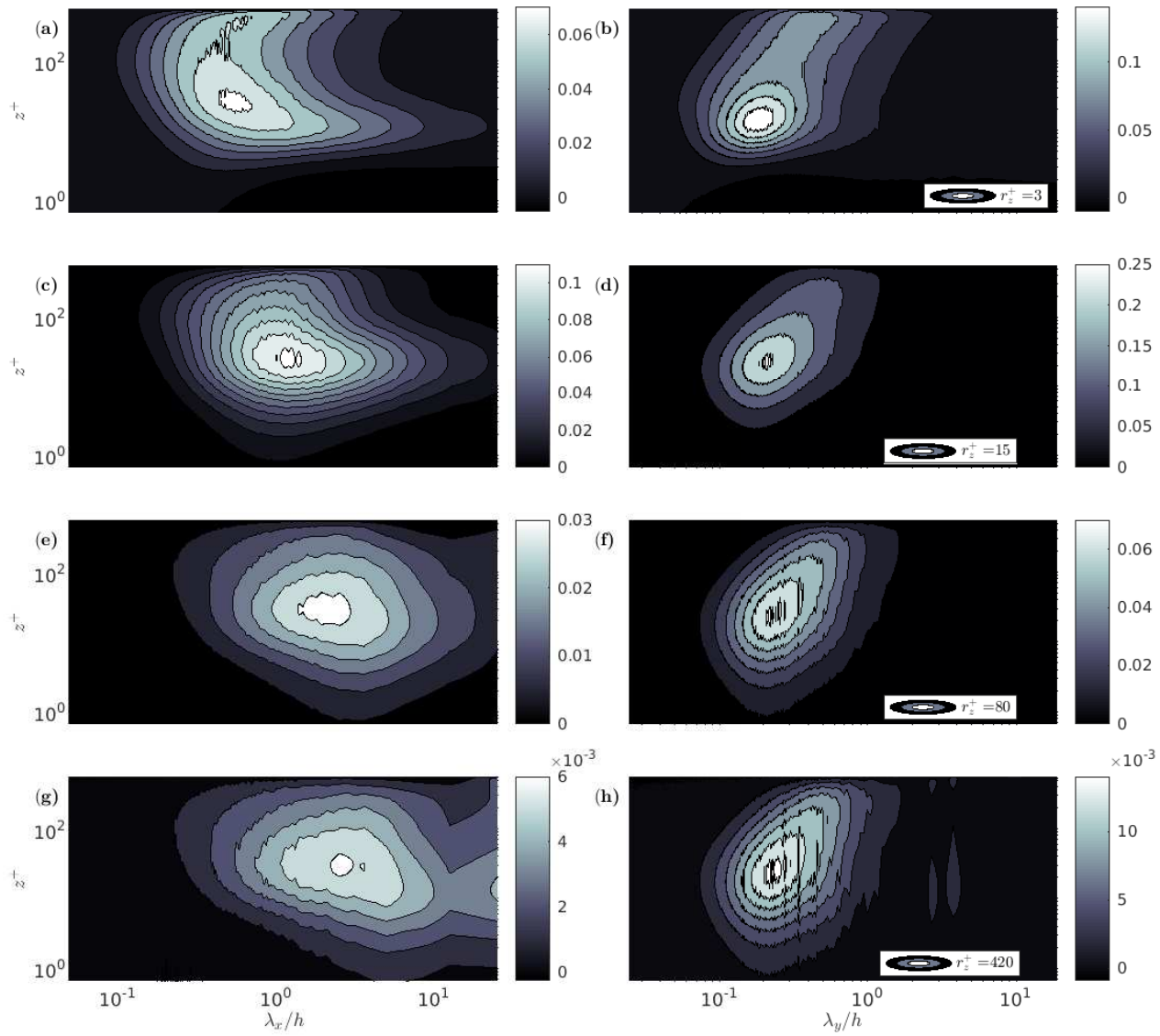

Figure 5.4: Premultiplied energy density for (a,c,e,g) streamwise ($r_z k_x \sum_{k_y} \mathrm{ED}$) and (b,d,f,h) spanwise ($r_z k_y \sum_{k_x} \mathrm{ED}$) wavelengths for L1. Panels (a-b), (c-d), (e-f), and (g-h) respectively refer to $r_z^+ = 3$, $r_z^+ = 15$, $r_z^+ = 80$, and $r_z^+ = 420$.

size of the BFL. The second, third, and fourth largest r_zED correspond to $r_z^+ = 3$, $r_z^+ = 80$, $r_z^+ = 420$, with the largest premultiplied ED in the OUL associated with the viscous scales, $r_z^+ = 3$.

5.4.4 Nonlinear energy transfer

In this section, the nonlinear transfer of ED is discussed. We start by analyzing the dependence of TR on r_z only by summing TR over all λ_x and λ_y as shown in Fig. 5.5. We also include the conventional horizontally averaged turbulence-transport T in the TKE budget [52, 4, 130, 61, 48, 7, 8] to show how closely TR at each r_z follows T.

TR summed over all horizontal wavelengths is mostly negative for large vertical scales $r_z^+ = 420$ and $r_z^+ = 80$ across the channel height, but the magnitude of premultiplied TR for $r_z^+ = 80$ is larger than for $r_z^+ = 420$. The TR term for $r_z^+ = 15$ is positive in the VSL and negative everywhere else, while TR for $r_z^+ = 3$ is positive across the channel height. The positiveness and negativeness in TR summed over all horizontal wavelengths refer to upward transport and downward transport, respectively. In the near-wall region, the upward and downward transfer corresponds to ejections and sweeps, respectively. By comparing profiles of premuliplied TR for different r_z with the TKE transport term T [8], it is clear that ejections in the lower part of the VSL are controlled by eddies with a vertical size comparable to the height of the VSL for different stratifications considered here. Thus, motions of larger eddies of the size of the buffer, logarithmic, and outer layers do not contribute to transport in the VSL. However, in the BFL and, above, all r_z contributes to TR.

The premultiplied spectra of TR are shown in Fig. 5.6 for L1. We first discuss dependence of TR upon λ_x and r_z as shown in Fig. 5.6(a,c,e,g). The small streamwise scales with $\lambda_x/h \sim 0.2$ contribute to the largest positive values of premultiplied TR for $r_z^+ = 3$ and 15. The vertical scales with $r_z^+ = 3$ contribute more to positive TR as also shown in Fig. 5.5. In the VSL and lower BFL, the streamwise scale λ_x/h from 0.2 to 3 are dominant in positive TR (Fig. 5.6a). In the BFL and aloft, the negative TR is associated with $1 \lesssim \lambda_x/h \lesssim 10$ (Fig. 5.6a, c, e, g).

Insights from nonlinear transfer for different vertical scales may improve our understanding of the inner and outer layer interactions. Fig. 5.6(a,c) suggest that for $r_z^+ = 3$ and $r_z^+ = 15$ in the VSL and lower part of the BFL, ED transfers into small streamwise scales ($\lambda_x/h < 1$) and out of larger streamwise scales ($\lambda_x/h > 1$) at the same height and aloft as shown in Fig. 5.6(a,b). For a given r_z, this energy transfer occurs from vertical scales greater than or equal to $r_z^+ = 80$, since for $r_z^+ = 420$ the transfer is mostly negative

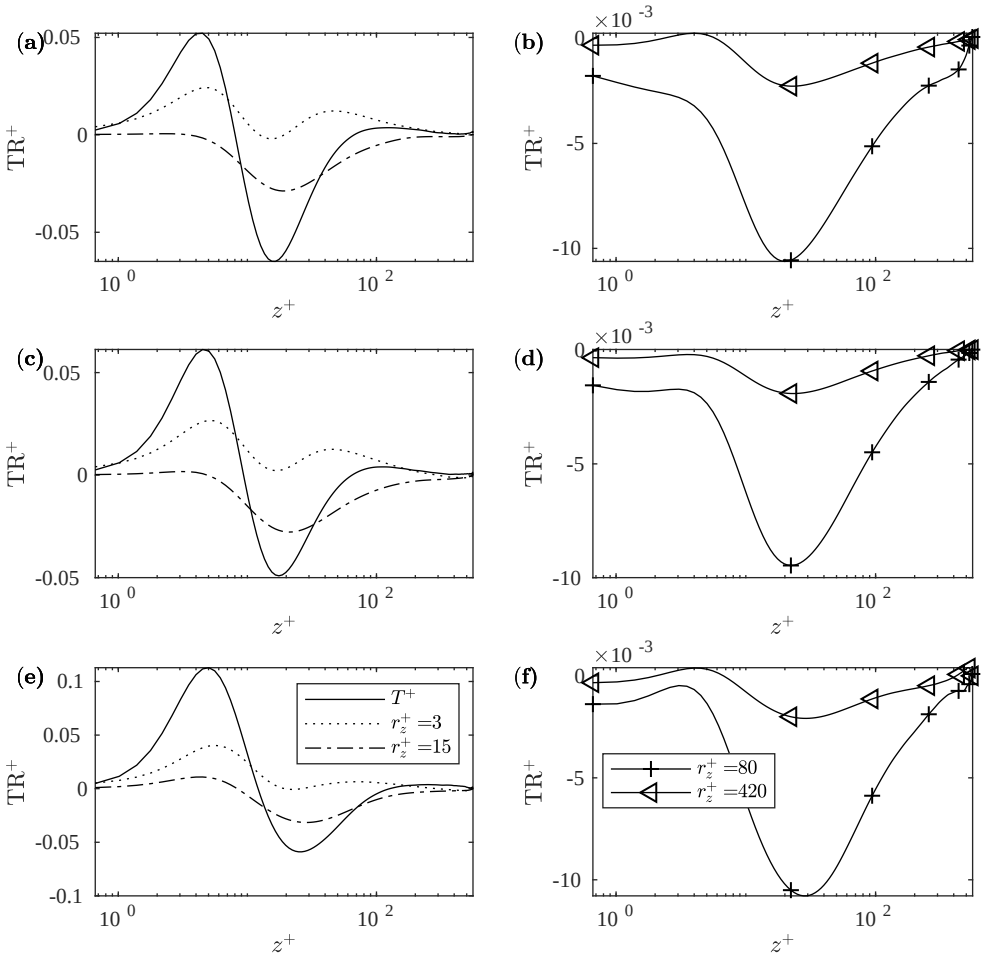

Figure 5.5: Premultiplied nonlinear transfer ($r_z \sum_{\mathbf{k}} \mathrm{TR}$) for different r_z, summed over all λ_x and λ_y, for (a-b) L0, (c-d) L1, and (e-f) L2. The T^+ refers to turbulence transport in horizontally averaged TKE budget [7, 8]. The plus sign for T and TR refers to normalization by Re. The transfer term for $r_z^+ = 80$ and $r_z^+ = 420$ are plotted separately in (b), (d), and (f) for L0, L1, and L2, respectively to make them distinguishable from corresponding profiles for $r_z^+ = 3$, and $r_z^+ = 15$ in (a), (c), and (e).

(Fig. 5.5b). For $r_z^+ = 80$ and $r_z^+ = 420$ (Fig. 5.6e,g) TR is primarily negative and thus TR mostly transfers ED into all λ_x and also into $\lambda_x/h \lesssim 1$ for smaller r_z. The large streamwise scales with $\lambda_x \sim L_x$ for OUL size vertical scales ($r_z^+ = 420$, Fig. 5.6g) contribute slightly to positive transfer, which penetrates down to the VSL. Large vertical scales with $r_z^+ = 420$ are tall enough ($r_z = 0.75h$) to influence the whole boundary layer, so they can contribute to the positive transfer of ED for the largest streamwise scales in the VSL. The negative transfer is more pronounced for $\lambda_x/h \sim 3$ regardless of r_z (and also stratification; not shown).

Now we discuss the dependence of TR upon λ_y and r_z as shown in Fig. 5.6(b,d,f,h). Generally, transfer takes place at spanwise scales that are an order of magnitude smaller than streamwise scales, consistent with studies of unstratified channel flows [20]. However, the maximum absolute values of transfer rate by spanwise scales are larger than those in streamwise scales. The largest values of positive and negative premultiplied TR are due to $r_z^+ = 3$ and $r_z^+ = 15$ respectively. Similar to the ED spectra in Fig. 5.4, TR is symmetric around a line ($\lambda_y \sim z$) in the logarithmic region for $r_z^+ > 3$, which strongly suggests that the LGL consists of self-similar attached eddies [65]. For $r_z^+ = 3$ (Fig. 5.6b) the VSL and lower BFL contain small spanwise scales with $\lambda_y/h \sim 0.2$ that contribute to largest positive TR. For $r_z^+ = 3$, the upper BFL and lower LGL contains negative transfer. Thus for $r_z^+ = 3$, the ED is transferred into $\lambda_y/h \sim 0.2$ in the upper VSL and lower BFL and out of slightly smaller scales in the upper BFL and lower LGL. For $r_z^+ > 3$ in Fig. 5.6(d,f,h) the ED is mostly transferred out of small spanwise scales with $\lambda_y/h \sim 0.2$ in the BFL and $\lambda_y \sim z$ in the LGL to other λ_y. For $r_z^+ = 80$ and 420, ED is transferred from $\lambda_y/h \lesssim 0.2$ even in the VSL.

Spectra of in-plane triad interactions are shown in Fig. 5.7. By comparing this and previous figures, one can say that nonlinear transfer for $r_z^+ > 3$ is dominated by in-plane triad interactions. In contrast, inter-plane interaction is more active in transferring ED among scales with $r_z^+ = 3$. Inter-plane interactions among streamwise scales transfer ED toward the largest λ_x close to the wall. Small positive transfer of ED among small streamwise scales as a result of TR_i for $r_z^+ = 80$ and $r_z^+ = 420$ is balanced by TR_o, so they are absent in the total nonlinear transfer.

5.4.5 Turbulence production

In this section, the production of ED is discussed. The spectra of turbulence production (SP) are shown in Fig. 5.8 for all simulations. The dependence of SP on streamwise scales, vertical scales, distance from the wall, and stratification are shown in Fig. 5.8(a,c,e). The

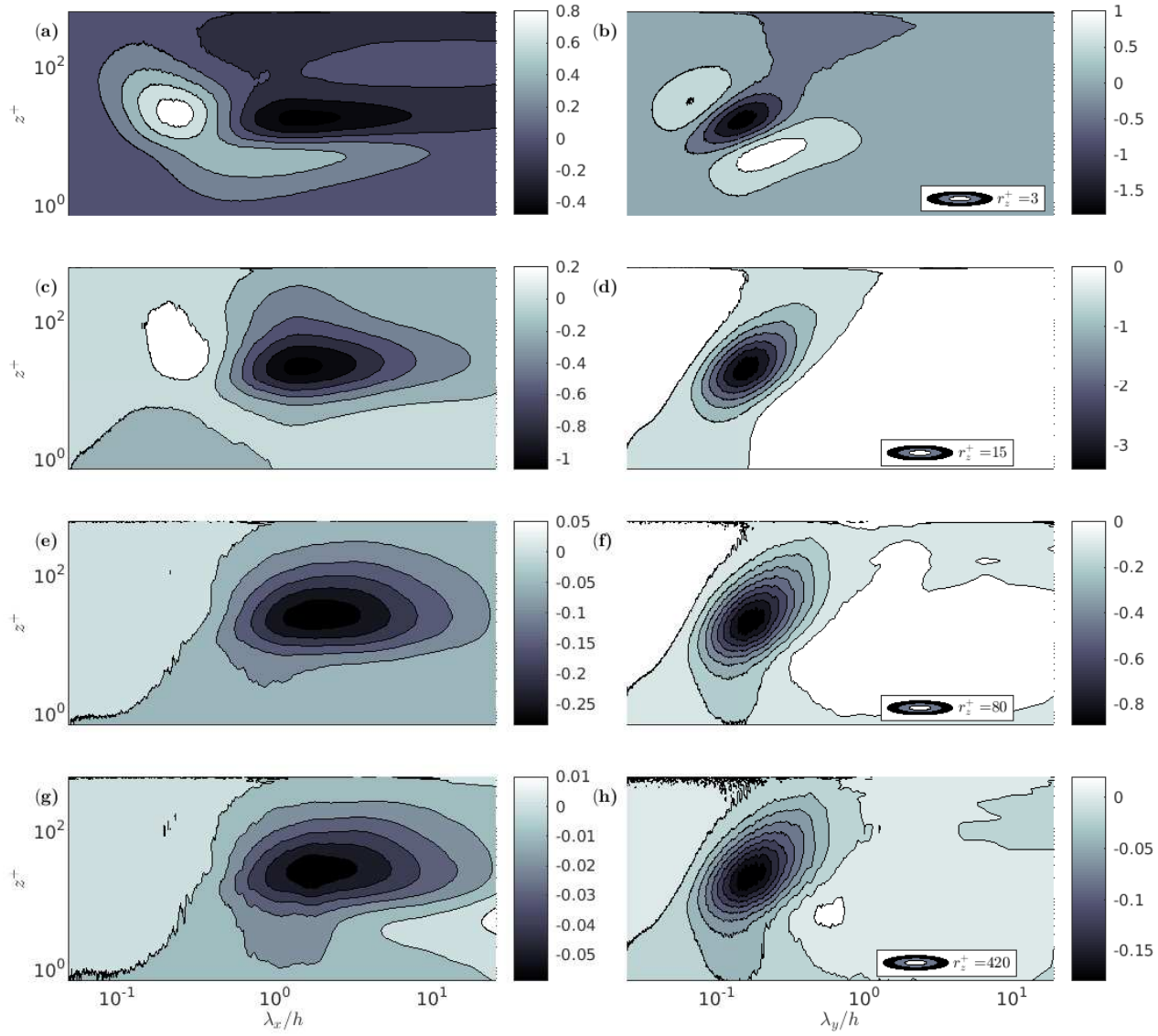

Figure 5.6: Premultiplied nonlinear transfer of energy density (TR) for (a,c,e,g) streamwise ($r_z k_x \sum_{k_y}$ TR) and (b,d,f,h) spanwise ($r_z k_y \sum_{k_x}$ TR) wavelengths for L1. Panels (a-b), (c-d), (e-f), and (g-h) respectively refer to $r_z^+ = 3$, $r_z^+ = 15$, $r_z^+ = 80$, and $r_z^+ = 420$.

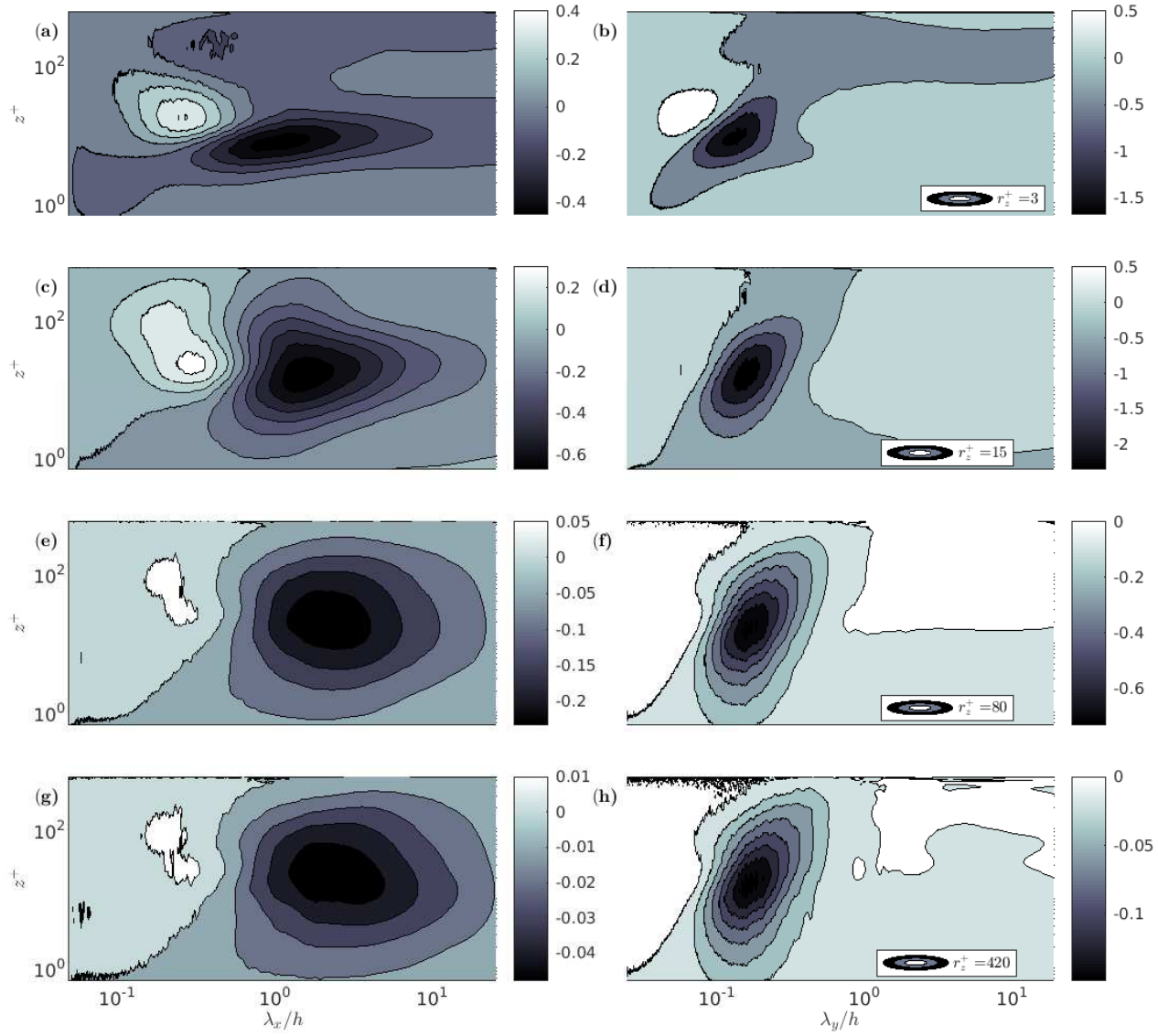

Figure 5.7: Premultiplied in-plane triad interactions (TR_i) for (a,c,e,g) streamwise ($r_z k_x \sum_{k_y} \mathrm{TR}_i$) and (b,d,f,h) spanwise ($r_z k_y \sum_{k_x} \mathrm{TR}_i$) wavelengths for L1. Panels (a-b), (c-d), (e-f), and (g-h) respectively refer to $r_z^+ = 3$, $r_z^+ = 15$, $r_z^+ = 80$, and $r_z^+ = 420$.

λ_x scales of the size of the channel height ($\lambda_x/h \approx 1$) centered at the BFL are the most productive scales for premultiplied ED. In L0 and L1, the less energetic streamwise scales carrying at least 0.1 of SP maxima become smaller with increasing Ri. By comparing Fig. 5.8(a,c,e) and Fig. 5.3, one can say that less energetic structures in the OUL of vertical size $r_z^+ = 80$ and $r_z^+ = 420$ are large with $\lambda_x/h \geq 10$ and penetrate the buffer region, suggesting they are inactive eddies as they only slightly contribute to production.

The dependence of SP on spanwise scales is shown in Fig. 5.8(b,d,f). The most productive spanwise scales for premultiplied ED in the BFL are of the size $\lambda_y/h \simeq 0.2$ ($\lambda_y^+ \simeq 100$) for all r_z and regardless of stratification. The scale $\lambda_y^+ \simeq 100$ is consistent with near-wall streak spacing for unstratified channels [71] and thus shows turbulence production in the near-wall region is strongly linked to near-wall streaks. Turbulence producing spanwise scales with vertical size of the logarithmic and outer layers are similar when SP is normalized using corresponding maximum values. Thus, turbulence producing spanwise scales with the vertical size of the logarithmic and outer layers are similar and stable stratification is in favor of making this coupling even stronger, so that contour lines in Fig. 5.8(d) for $r_z^+ = 80$ follows those for $r_z^+ = 420$ even more closely than in Fig. 5.8(b). In L2, $\lambda_y/h \approx 3$ are spanwise scales containing an active region next to a quiescent region at which production is slightly negative. The similarity between turbulence producing spanwise scales (λ_y in the SP) in L0, L1, and L2 can be seen in Fig. 5.8(b,d,f). Fig. 5.8(f) shows that in L2, the widest turbulence producing structure (active regions) is of spanwise size comparable to h. The least active spanwise scales of the size of the open-channel height in L2 explains why turbulent strips appear with a width comparable to h.

The magnitude of SP for all levels in the hierarchy is shown in Fig. 5.9 for a single stratification, L1. Turbulence production takes place at all r_z. The vertical scale $r_z^+ = 15$ (Fig. 5.9c) contributes to the premultiplied SP maximum, and the maximum premultiplied SP occurs in the BFL for all r_z considered here for L1. The vertical scale with $r_z^+ = 3$ (Fig. 5.9a), $r_z^+ = 80$ (Fig. 5.9e), and $r_z^+ = 420$ (Fig. 5.9g) contain other relatively large productions for streamwise scales, respectively. The largest value of SP associated with λ_y is three times larger (Fig. 5.9b,d,f,h) than the largest production associated with λ_x for all r_z (and for stratification regimes considered here). In fully developed cases (L0 and L1) and also in the active regions of L2 (results for L0 and L2 are not shown here), the SP in the BFL for horizontal and vertical scales shows a sustained kinetic energy injection associated with mean shear into all streamwise scales, all vertical scales, and spanwise scales between 0.1 and 1. This finding is consistent with a scale-by-scale budget of the structure function in Ref. [19] for unstratified shear layer turbulence.

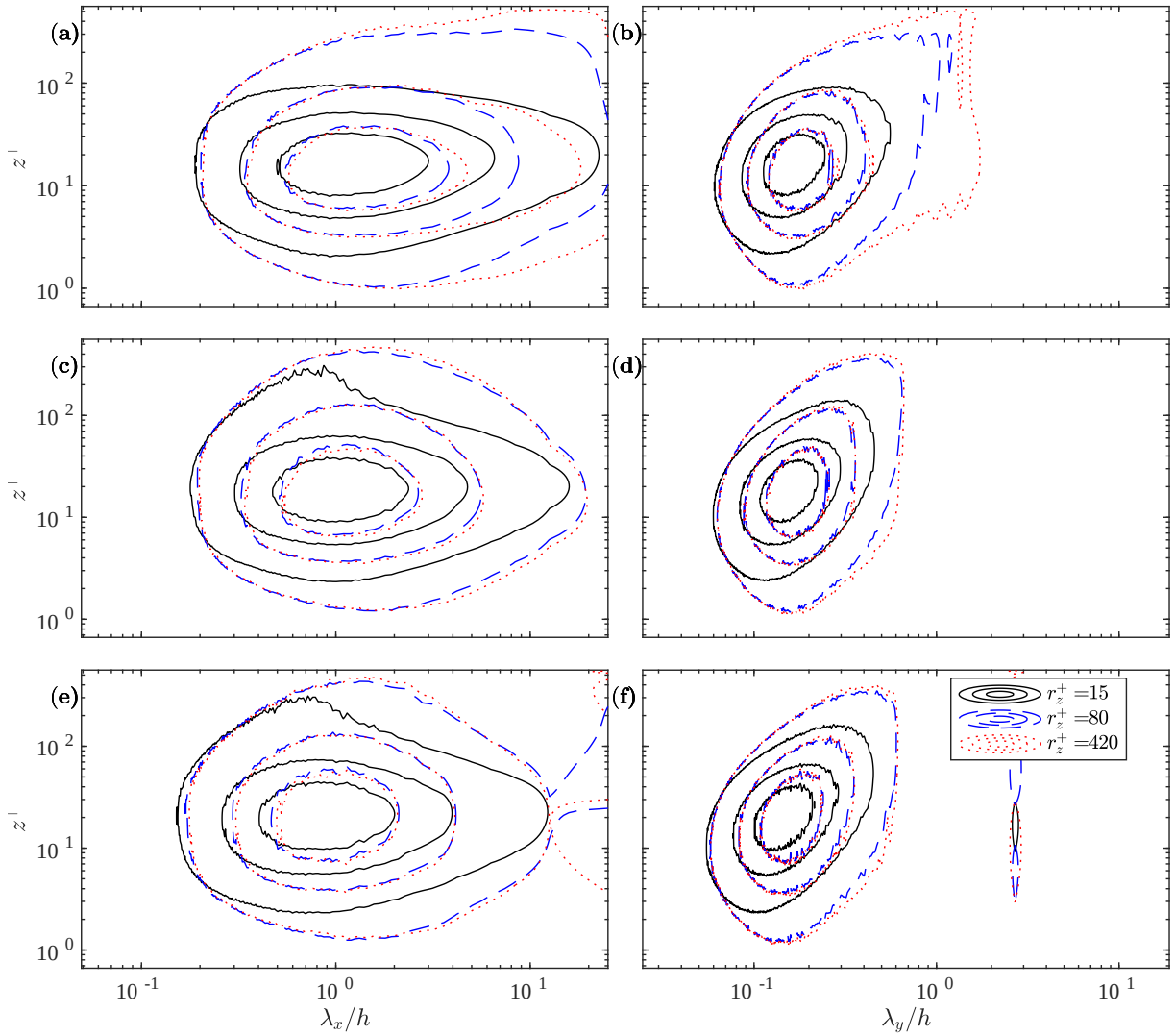

Figure 5.8: Premultiplied shear production (SP) for (a,c,e) streamwise ($r_z k_x \sum_{k_y}$ SP) and (b,d,f) spanwise ($r_z k_y \sum_{k_x}$ SP) wavelengths. Panels (a-b), (c-d), and (e-f) respectively refers to L0, L1, and L2. Profiles corresponding to each r_z are scaled using the maximum of corresponding spectra.

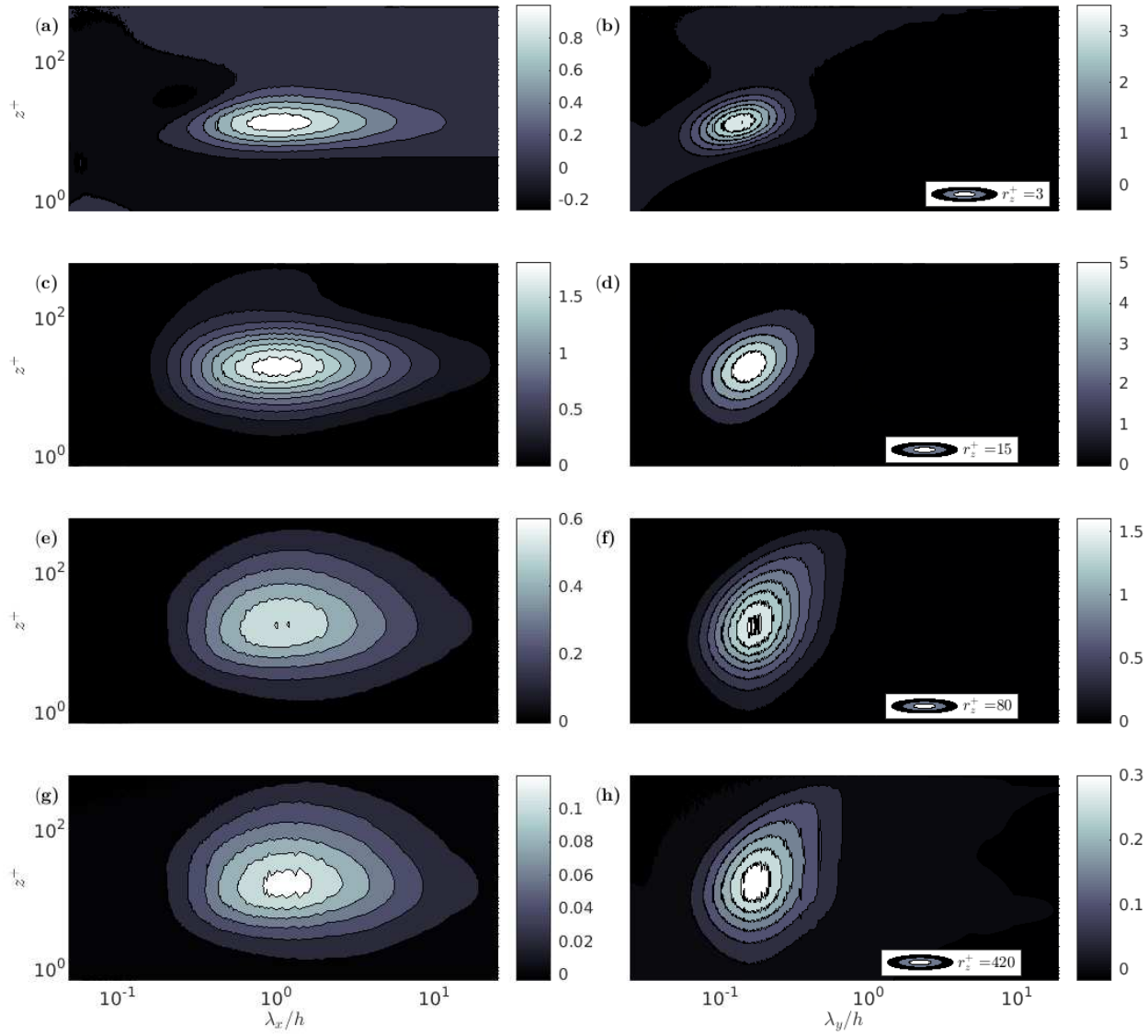

Figure 5.9: Premultiplied shear production (SP) for (a,c,e,g) streamwise ($r_z k_x \sum_{k_y}$ SP) and (b,d,f,h) spanwise ($r_z k_y \sum_{k_x}$ SP) wavelengths for L1. Panels (a-b), (c-d), (e-f), and (g-h) respectively refer to $r_z^+ = 3$, $r_z^+ = 15$, $r_z^+ = 80$, and $r_z^+ = 420$.

5.4.6 Viscous effects

The premultiplied VD spectra are shown in Fig. 5.10 for L1. Generally, the vertical scale $r_z^+ = 3$ contains the maximum absolute values of viscous effects (premultiplied VD) among the r_z considered here. The dependence of VD on λ_x and r_z are shown in Fig. 5.10(a,c,e,g). The magnitude of the viscous term decreases with increasing vertical scale. The large values of VD (magnitude greater than 0.1) are negative in the near-wall region for $r_z^+ = 3$ and $r_z^+ = 15$ (Fig. 5.10a,b). This negative VD suggests that dissipation of ED in the near-wall region is associated with small r_z, as expected. As opposed to production (SP), the spectral distribution of viscous effects among different streamwise scales is more sensitive to r_z. The VD spectra for $r_z^+ = 3$ and $r_z^+ = 15$ are different than those with $r_z^+ = 80$ and $r_z^+ = 420$. Viscous effects take place at larger streamwise λ_x as r_z increases. Also, viscous effects spread out over a wider range of λ_x as r_z increases. The dependence of the viscous effects on spanwise scale are shown in Fig. 5.10(b,d,f,h). The most viscosity affected λ_y is much smaller than the corresponding λ_x. For $r_z^+ = 3$ and $r_z^+ = 15$ the VD is negative almost anywhere across channel height for all λ_y whereas for $r_z^+ = 80$ and $r_z^+ = 420$ the VD is positive in the VSL. By comparing both λ_x and λ_y contours, we see that the strongest viscous effects take place in the lower BFL. The viscous term VD for both λ_x and λ_y are similar for r_z of size comparable to the height of the LGL and OUL.

Viscous diffusion in the VSL is positive in the horizontally averaged TKE budget, as discussed in Ref. [8] (and also in chapter 4). The VD summed over wavelengths is shown in Fig. 5.11. As can be seen, the VD term corresponds to the summation of viscous dissipation and diffusion, which are total effects of viscosity in a horizontally averaged TKE budget. Thus, positive VD for $r_z^+ = 80$ and $r_z^+ = 420$ in the VSL is associated with viscous diffusion since dissipation is negative.

Note positive values of VD comes from inter-plane viscous effects since VD_i is directly related to (-ED) which is negative (equation 5.22). For r_z of the size of the LGL and OUL, VD becomes positive at small wavelengths, signifying dominance of inter-plane viscous effects at such scales. These positive VD occur in the lower part of the VSL, suggesting that the role of such tall vertical structures is to actually intensify ED. This intensification of ED in lower part of the VSL takes place at $\lambda_x/h \approx 1$ and $\lambda_y/h \approx 0.2$, which correspond to the scales contributing to maximum SP. Thus, part of the ED generation in the lower part of the VSL is a result of inter-plane viscous effects. We will discuss importance of the positive VD shortly.

Spectra of in-plane viscous effects are shown in Fig. 5.12. By comparing Fig. 5.10 and Fig. 5.12 one can say that the VD is primarily controlled by inter-plane viscous effects, and the role of in-plane viscous effects is secondary as the magnitude of the VD_i is much smaller

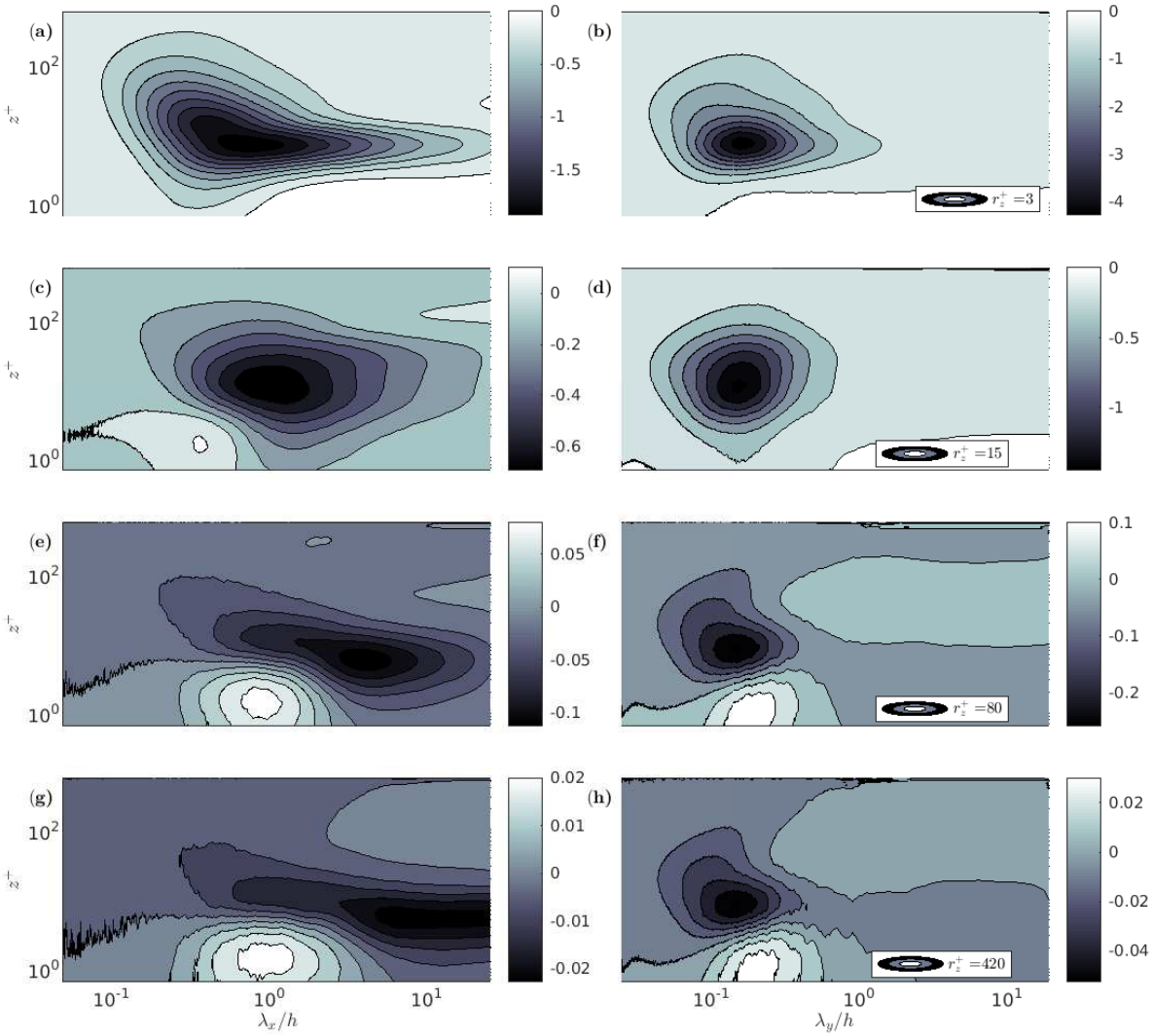

Figure 5.10: Premultiplied viscous effects (VD) for (a,c,e,g) streamwise ($r_z k_x \sum_{k_y}$ VD) and (b,d,f,h) spanwise ($r_z k_y \sum_{k_x}$ VD) wavelengths for L1. Panels (a-b), (c-d), (e-f), and (g-h) respectively refer to $r_z^+ = 3$, $r_z^+ = 15$, $r_z^+ = 80$, and $r_z^+ = 420$.

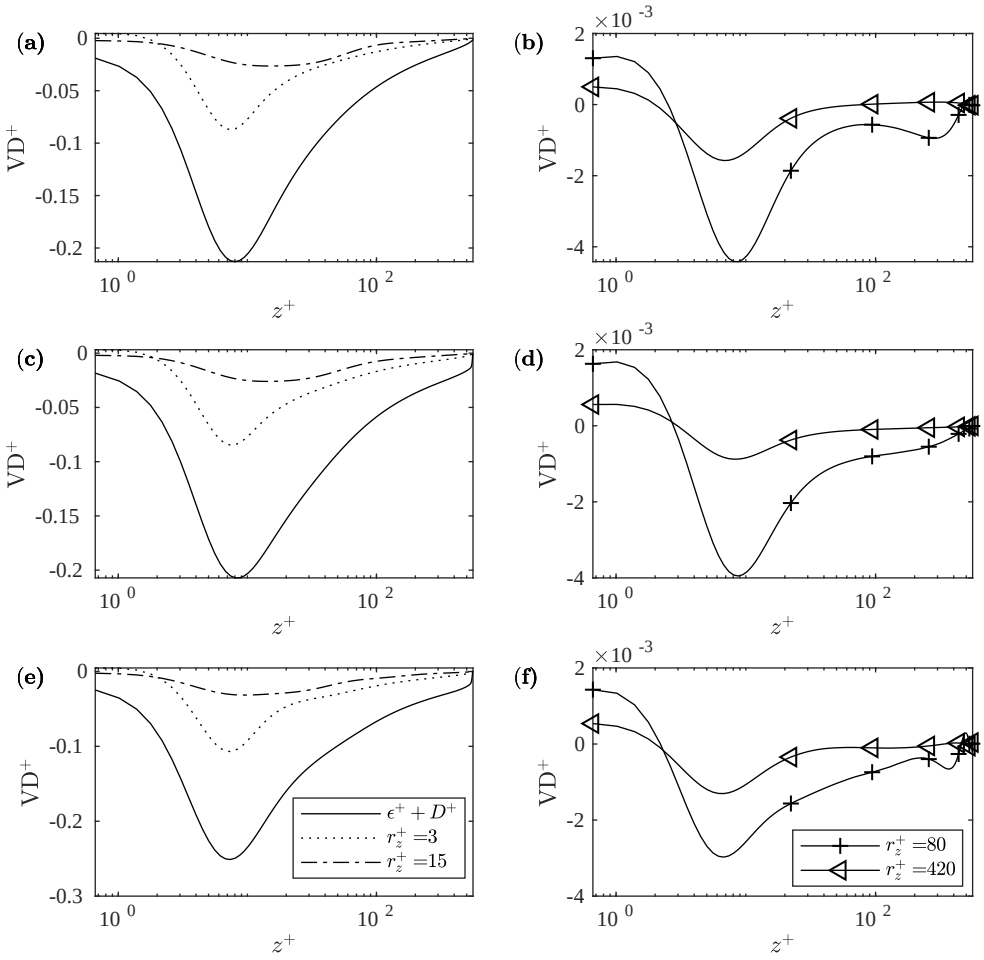

Figure 5.11: Premultiplied viscous term ($r_z \sum_{\mathbf{k}} \mathrm{VD}$) for different r_z, summed over all λ_x and λ_y, for (a-b) L0, (c-d) L1, and (e-f) L2. The viscous term for vertical sales $r_z^+ = 80$, and $r_z^+ = 420$ are shown in (b), (d), and (e) for L0, L1, and L2, respectively. The ϵ^+ and D^+ refers to turbulence dissipation and diffusion, respectively in horizontally averaged TKE budget normalized by Re [7, 8].

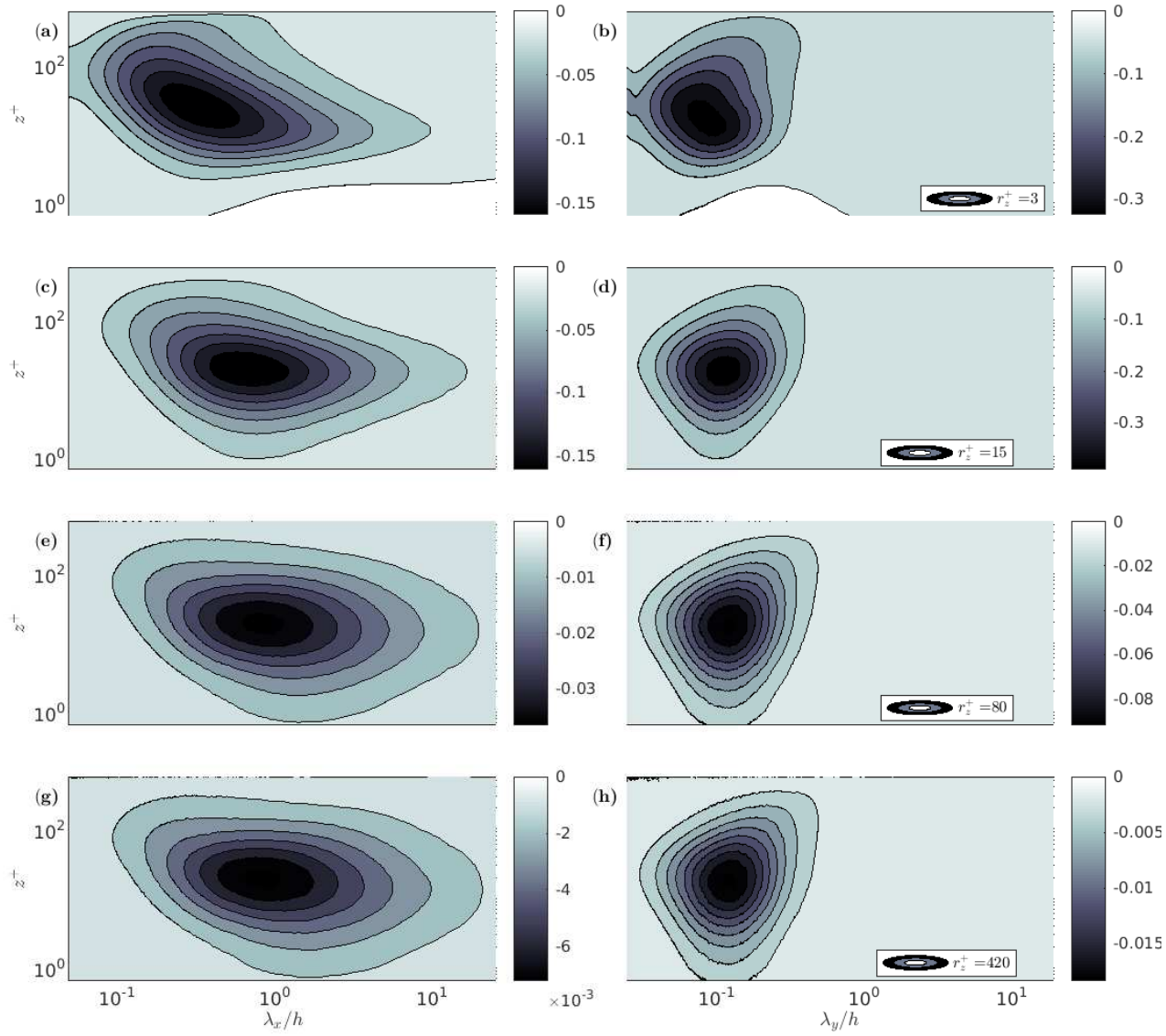

Figure 5.12: Premultiplied in-plane viscous effects (VD_i) for (a,c,e,g) streamwise ($r_z k_x \sum_{k_y} \mathrm{VD}_i$) and (b,d,f,h) spanwise ($r_z k_y \sum_{k_x} \mathrm{VD}_i$) wavelengths for L1. Panels (a-b), (c-d), (e-f), and (g-h) respectively refer to $r_z^+ = 3$, $r_z^+ = 15$, $r_z^+ = 80$, and $r_z^+ = 420$.

than VD at all scales. The shape of the spectra for in-plane viscous effects are similar for different r_z regardless of stratification (not shown for L0 and L2). The dependence of VD_i on spanwise scales is shown in Fig. 5.12(b,d,f,h). The λ_y of greatest VD in the logarithmic layer is linearly dependant upon height ($\lambda_y \sim z$) for $r_z^+ \geq 15$.

Now we discuss the importance of positive VD. It has been discussed in Ref. [8] (and also in chapter 4) that pressure-work, similar to unstratified channel flows, is a crucial mechanism for transporting turbulence from the lower VSL, where the transport term in the horizontally averaged TKE budget is small. However, pressure-work requires sustainable velocity fluctuation to actively transfer TKE to the upper VSL, where transfer terms can distribute TKE to the rest of the channel. An important question is which mechanism in the viscous region, where production is also small due to wall impermeability, can provide sustainable velocity fluctuations? As discussed, inter-plane viscous interactions among scales of the size of the LGL and OUL seems to be a plausible answer. The nonlinear transfer, production, and buoyancy (discussed below) terms are small compared to viscous effects in the lower VSL, similar to unstratified channel flows [67, 11, 8] .

5.4.7 Buoyancy destruction

Buoyancy is not a dominant mechanism in the budget of horizontally averaged TKE for the SBL [103, 6, 135, 119, 8]. Similarly, it is not a dominant mechanism in the budget of ED. However, to identify the range of scales that are most affected by buoyancy, we discuss BD spectra in this section for L1.

The dependence of BD on λ_x is shown in Fig. 5.13(a,c,e,g). The premultipled BD is concentrated in the LGL and is dominated by $r_z^+ = 15$. As r_z increases, BD effects extend deeper down in the boundary layer and involves larger λ_x. The range of buoyancy affected λ_x/h extends from 0.1 to 10 for $r_z^+ = 15$. As r_z^+ increases to 420, the range of buoyancy affected λ_x/h extend from 1 to L_x. The dependence of BD on λ_y is shown in Fig. 5.13(b,d,f,h). The λ_y spectra are narrower than the λ_x spectra, similar to other terms in ED budget discussed so far. As r_z increases, BD involves larger λ_y. The range of buoyancy affected λ_y/h scales extend from 0.2 to 1 for $r_z^+ = 15$ and from 0.2 to 10 for $r_z^+ = 420$.

By comparing BD and SP spectra for L1 (Fig. 5.13 and Fig. 5.9), one might say that the range of scales that are affected by buoyancy includes all scales that contribute to turbulence production. This range of buoyancy affected scales is expected since part of the kinetic energy injected by SP is converted to potential energy by BD. But there are large

scale $\lambda_x/h \sim L_x/h$ and $\lambda_y/h \gtrsim 1$ for all r_z that contribute to BD but not SP. Also, the maximum of BD for streamwise scales is centered farther from the wall compared to SP.

Although buoyancy is not a dominant mechanism in the energy budget for reasons explained below, it imposes an additional restriction on the computational domain size. As can be seen in Fig. 5.13 for $r_z^+ = 420$, buoyancy activates large spanwise scales that contribute to BD more than for SP. The stable stratification is in favor of suppressing large non-productive vertical scales by widening their corresponding spanwise λ_y and elongating their λ_x (Fig. 5.13).

5.4.8 Pressure-work

The pressure-work term summed over horizontal wavelengths are shown in Fig. 5.14. Consistent with our previous findings [7, 8], the largest values of pressure-work occur in the lower VSL and above the VSL the contribution of PW is small. However, the vertical scales of the size of VSL and BFL are dominant in the lower VSL for premultiplied PW among vertical scales considered here. Since pressure-work term is small in most of channel height (except in the VSL), we will not further discuss dependence of PW on horizontal wave lengths.

5.5 Discussion

From the results presented in analyzing the budget of energy density, it was shown that the overall balance is between SP, TR, and VD. The scale dependence of this balance will be discussed in this section. By comparing Fig. 5.6, Fig. 5.9, and 5.10, one can say that SP correlates with negative TR for all r_z. The net output of the production and nonlinear transfer approximately balance VD. Thus ED generated by SP at $\lambda_y/h \gtrsim 1$ is transferred by negative TR and dissipated by VD. The kinetic energy of vertical scales are mainly altered by three different mechanisms: 1) mean flow production, 2) draining energy from inter-scales interactions by in-plane triads, and, 3) receiving from inter-scales by inter-plane interactions. As stated, the viscous effect dissipates the net of energy production and transfer. Thus, due to the small contribution of buoyancy destruction, the net of transport and production is approximately balanced by viscous effects consistent with unstratified cases [96]. Moreover the positive TR for $r_z^+ = 3$ and $r_z^+ = 15$ at $\lambda_x/h < 1$ and $\lambda_y/h \sim 1$, that are inactive in SP (merely due to wall-generated inhomogeneity), are directly connects TR and VD.

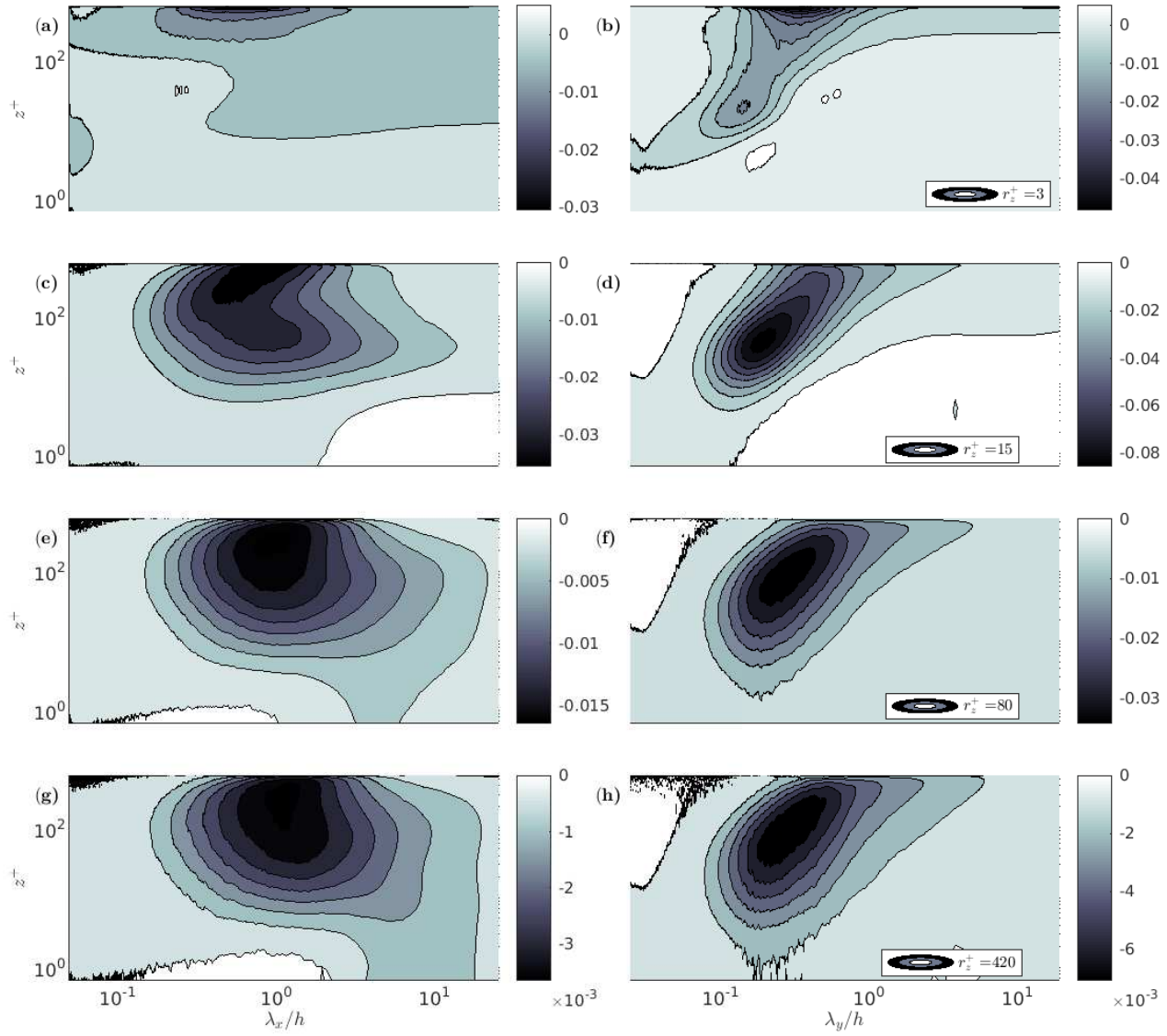

Figure 5.13: Premultiplied buoyancy term (BD) for (a,c,e,g) streamwise ($r_z k_x \sum_{k_y}$ BD) and (b,d,f,h) spanwise ($r_z k_y \sum_{k_x}$ BD) wavelengths for L1. Panels (a-b), (c-d), (e-f), and (g-h) respectively refer to $r_z^+ = 3$, $r_z^+ = 15$, $r_z^+ = 80$, and $r_z^+ = 420$.

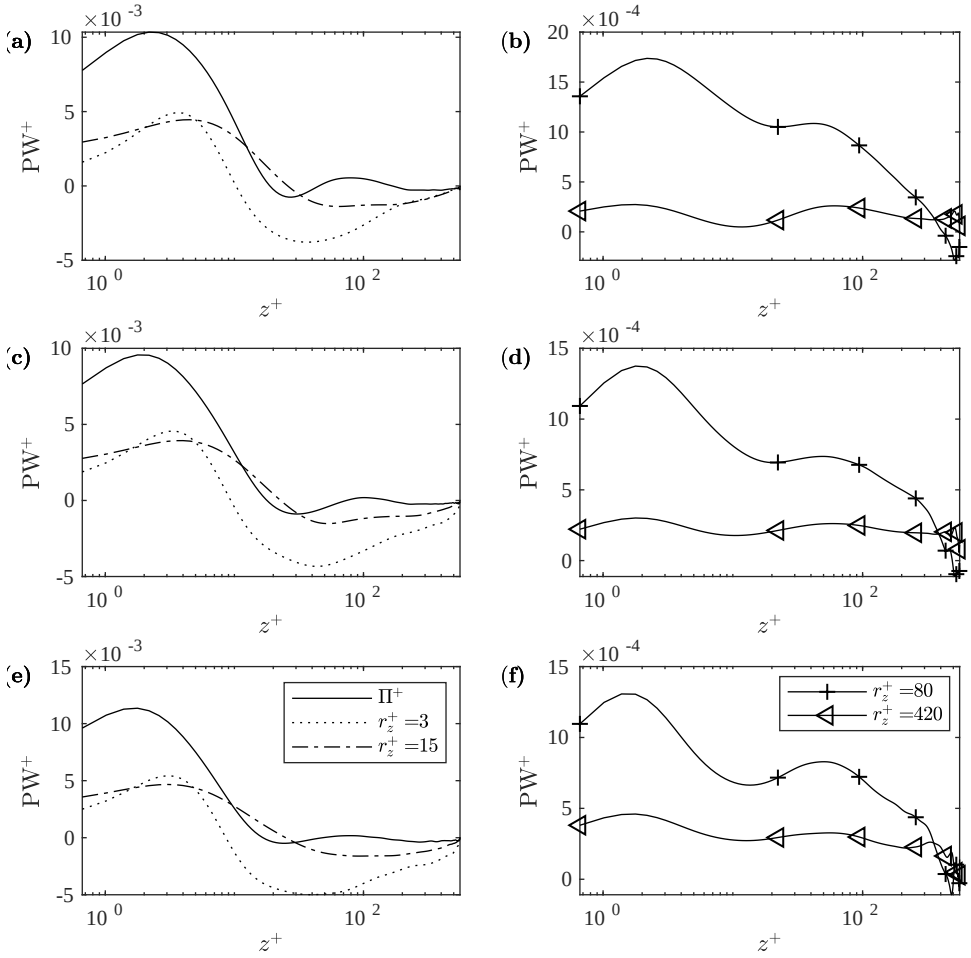

Figure 5.14: Premultiplied pressure-work term ($r_z \sum_{\mathbf{k}} \mathrm{PW}$) for different r_z, summed over all λ_x and λ_y, for (a-b) L0, (c-d) L1, and (e-f) L2. The pressure-work term for $r_z^+ = 80$ and $r_z^+ = 420$ are plotted separately in (b), (d), and (f) for L0, L1, and L2, respectively to make them distinguishable from corresponding profiles for $r_z^+ = 3$, and $r_z^+ = 15$ in (a), (c), and (e). The Π^+ refers to pressure-work term in horizontally averaged TKE budget [7, 8]. The plus sign for Π and PW refers to normalization by Re.

Although BD affects all ED producing scales (dominant range of scales in the production term), the centre of action for buoyancy (in the LGL) and production (in the BFL) are different. For both BD and SP, $r_z^+ = 15$ is the dominant vertical scale. Thus, λ_x and λ_y for $r_z^+ = 15$ in the BFL (maximum SP; Fig. 5.8a,b) are not significantly affected by buoyancy destruction. The difference in the heights for centre of action of buoyancy and shear production is a direct result of wall-impermeability and the no-slip condition. This condition on the wall (and also on the top boundary) imposes that vertical fluctuations can not occur in the viscous region or the OUL close to the top boundary. For a similar reason, the maximum tangential Reynolds stress is not located in the viscous region. However, strong wall-generated shear with a maximum at the wall shifts the centre of action for shear production further down close to the wall. Starting from the decay phase [7], the wall-generated shear becomes weaker as a result of and skin friction is reduced [8]. Thus, the near-wall viscous region grows due to reduced mean shear. This growth of the near-wall viscous region shifts the centre of action for production. Thus turbulence collapse in an SSBL may be a process in which the production centre of action locates above the buoyancy centre of the action. In this situation, the near-wall production is hindered by buoyancy destruction as it suppresses vertical velocity fluctuations.

5.6 Conclusions

In this chapter, we studied the mechanisms that are involved in the kinetic energy cascade in a stably stratified open-channel flow using a mathematical framework introduced to analyze kinetic energy density in spectral-scale space. We categorized flow structures into a hierarchy with four different levels based on the vertical scales of the viscous sublayer, buffer layer, logarithmic layer, and outer layer.

We considered an unstratified case (L0) as well as two strongly stable cases (L1 and L2). For the unstratified case, for vertical scales of the size of logarithmic layer ($r_z^+ = 80$), which corresponds to the third level in the hierarchy, the range of streamwise scales (λ_x/h) from 3 to 10 are most energetic. These energetic streamwise scales reside in the BFL and extend into the OUL, showing that the third level in the hierarchy of vertical scales links viscous regions to the OUL. Such a link is suppressed in stratified cases. For the case with the strongest stratification (L2), the flow evolved into a state with alternating strips of turbulent and quiescent regions. In L2, for which flow becomes intermittent, the energy density in streamwise scales with $\lambda_x/h \approx 1$ is suppressed, and ED is mainly found in the largest streamwise scales of size of L_x.

It was found that in all cases considered in this work, energetic λ_x become larger as r_z

increases. The large λ_x are reduced with increasing Ri for all r_z. Energetic spanwise scales are smaller than streamwise scales for all r_z and the dependence of λ_y spectra upon r_z is much weaker compared to the λ_x spectra dependence upon r_z regardless of Ri. The $\lambda_y \sim z$ relation for the energetic scales in the logarithmic region for all r_z shows the self-similarity of eddies in the LGL. All of the r_z scales are most energetic at $z^+ \approx 15$ for all Ri considered here.

By analysing nonlinear energy transfer it was found that among r_z considered here, the upward transport in lower part of the viscous sublayer is controlled by small vertical scales of size comparable to the height of the viscous sublayer ($r_z^+ = 3$) regardless of stratification (choice of Ri). The largest nonlinear transfer rate by spanwise scales is larger than that by streamwise scales. Nonlinear transfer for streamwise scales is dominated by in-plane triad interactions, and inter-plane interactions are more active in transferring energy density among spanwise scales. The most energy productive streamwise scales are comparable to channel height ($\lambda_x/h \approx 1$) regardless of the given vertical scale and stratification (Ri). These energy productive streamwise scales are centered in the BFL. Turbulence production take place at all vertical scales. Turbulence producing spanwise scales with vertical size comparable to the height of the logarithmic layer ($r_z^+ = 80$) and outer layer ($r_z^+ = 420$) are similar. The range of scales that are affected by buoyancy includes all energy producing scales. However, there are scales $\lambda_x/h \sim L_x$ and $\lambda_y/h \gtrsim 1$ for all r_z (buoyancy dominated scales) that are active in buoyancy destruction (BD) and are inactive in production (SP). These scales that are activated as a result of buoyancy destruction imposes extra demands for larger computational domain size to simulate strongly stable stratified boundary layers.

In this work we only considered four different vertical scales to simplify analysis of the kinetic energy cascade due to the significant computational expense that would be required to consider the full range of vertical scales for large domain simulations. An important unanswered question in our work, which requires study of the full range of vertical scales, is how the near-wall inverse cascade is impacted by stratification. This will be addressed in the future.

Chapter 6

Conclusions

6.1 Concluding remarks

In this thesis, the dynamics of turbulence in stably stratified boundary layers was studied using high-resolution DNS. In chapter 3, the response of wall turbulence to the introduction of stable stratification via bottom surface cooling was studied. It was shown that the cooling process could be categorized into different phases based on the values of the cooling rate that is imposed. The first phase is turbulence decay, regardless of the choice of cooling rate. The second phase is a recovery that is mostly dependant on the cooling rate where TKE may acquire values higher than those in the neutral case if the cooling rate is strong enough. For a strong cooling rate, turbulence may partially collapse as indicated by patchy turbulence, or totally collapse in the decay phase. The patchy turbulence is a consequence of a significant reduction in turbulence production and not an excessive amount of dissipation. In the case of the strongest cooling that is considered in this thesis, the inner layer turbulence is completely suppressed, and the outer layer turbulence decays subsequently. The flow in such cases contains flat structures in the near-wall region and pancake-like vortices in the outer layer.

Further analysis is focused on the cases in which the boundary layer is exposed to strong stable stratification. Our knowledge of such cases is still limited [94]. It was shown that in SSBLs, turbulence collapse initiates from the near-wall region and outer layer turbulence collapses subsequently. It was shown that near-wall turbulence in SSBLs could be autonomously sustained only if it is interacting with at least the lower part of the outer layer where $z^+ \leq 300$. In that sense, near-wall turbulence in SSBLs is partially autonomous, which suggests the difference of evolutionary SSBLs from unstratified cases

where near-wall turbulence is shown to be autonomous without interacting with outer-layer turbulence.

It has been thought for about two decades now that in SSBLs, turbulence and laminar regions coexist [4]. In this thesis, it was shown that regions that are called "laminar" in the literature are actually layers of viscously coupled stratified turbulence where the slope of the longitudinal spectra varies with height. In these regions $Re_B \ll 1$ and they contain layered vortices with suppressed vertical momentum flux where longitudinal spectra of streamwise velocity show consistency with viscously coupled stratified turbulence [140] in the buffer layer and in the logarithmic layer.

Donda *et. al* [36] showed that turbulence collapse is a transient phenomenon in which artificial enhancement of TKE may lead to full recovery. If one assumes near-wall turbulence collapse as the most severe effect of buoyancy destruction which can be transient, then one can conjecture that the near-wall effect of stable stratification on statistics up to any order is also transient if turbulence acquires spatial homogeneity and reaches quasi-stationarity. In chapter 4, characteristics of quasi-stationary near-wall turbulence under strong, stable stratification have been examined using DNS. To address the effects of stable stratification on the characteristics of near-wall turbulence, five different high-resolution cases are considered with different Richardson numbers ranging from the neutral to strongly stable stratified regime. It was found that the primary effects of stable stratification is actually transient. Nonetheless, in the near-wall region, where $z/h \lesssim 0.1$, stratification leads to a decrease in velocity variances, TKE, tangential Reynolds stress, and heat flux in the streamwise and wall-normal direction. Analysis of higher-order statistics shows that the tendency of positive streamwise velocity fluctuations is intensified as the surface cooling rate increases. Mean flow velocity above $z^+ \gtrsim 10$ is increased as Ri_τ increases as a direct effect of reduction in near-wall tangential Reynolds stress. Increasing Ri_τ intensifies buoyancy restoring force, which is strongest near the wall and becomes weaker as distance from the wall increases. However, the wall generated shear stress dominates these buoyancy forces.

An important question in boundary layer turbulence is how turbulence is maintained in the lower part of the viscous sublayer, where the damping effect of viscosity is strongest. Based on TKE budget analysis in chapter 4, it was shown that very near the wall where $z^+ \lesssim 1$, velocity fluctuations are small, and pressure-work term plays an important role in maintaining and transferring TKE to higher-momentum fluid farther away from the wall. It was shown that buoyancy has a remarkable effect on the budget of tangential Reynolds stress (even at stationarity) and hence on the evolution of turbulence production. It was shown that there are scales smaller than the Kolmogorov scale that may be important for wall-bounded stratified turbulence. Particularly in the VSL, the Corrsin scales are

smaller than Kolmogorov scales. Also, it was shown that Kolmogorov scales are not the smallest dissipative scales. Very near the wall where $z^+ \lesssim 1$, λ_z^w scales are also smaller than Kolmogorov scales. In the VSL, $l_C < \lambda_z^w$ in general.

The mechanisms that are involved in the kinetic energy cascade in a stably stratified open-channel flow were studied in chapter 5. We consider an unstratified case (L0) as well as two strongly stable cases (L1 and L2). For the unstratified case, for vertical scales of the size of the logarithmic layer ($r_z^+ = 80$) the range of streamwise scales (λ_x/h) from 3 to 10 are most energetic. These energetic streamwise scales reside in the BFL and extend into the OUL, linking viscous regions to the OUL. Such a link is suppressed in stratified cases. For the case with the strongest stratification with the highest Ri_τ (L2), the flow evolved into a state with alternating strips of turbulent and quiescent regions. In this case the energy density in streamwise scales with $\lambda_x/h \approx 1$ is suppressed, and ED is mainly found in the largest streamwise scales of size of L_x. It was found that in all cases considered in this work, energetic λ_x becomes larger as r_z increases. The large λ_x are reduced with increasing Ri_τ for all r_z. Energetic spanwise scales are smaller than streamwise scales for all r_z, and the dependence of λ_y spectra upon r_z is much weaker compared to the λ_x dependence upon r_z regardless of Ri_τ. The $\lambda_y \sim z$ relation for the energetic scales in the logarithmic region for all r_z shows the self-similarity of eddies in LGL. All of the r_z scales are most energetic at $z^+ \approx 15$ for all Ri_τ considered here.

By analyzing nonlinear energy transfer, it was found that among r_z considered here, the upward transport in the lower part of the viscous sublayer is controlled by small vertical scales of size comparable to the height of the viscous sublayer ($r_z^+ = 3$) regardless of stratification (choice of Ri_τ). The largest nonlinear transfer rate by spanwise scales is larger than that by streamwise scales. Nonlinear transfer for streamwise scales is dominated by in-plane triad interactions, and inter-plane interactions are more active in transferring energy density among spanwise scales. The most energy productive streamwise scales are of a size comparable to channel height ($\lambda_x/h \approx 1$) regardless of the given vertical scale and stratification (Ri_τ). These energy productive streamwise scales are centered in the BFL. Turbulence production takes place at all vertical scales.

Turbulence producing spanwise scales with a vertical size comparable to the height of the logarithmic layer ($r_z^+ = 80$) and the outer layer ($r_z^+ = 420$) are similar. The range of scales that are affected by buoyancy includes all energy-producing scales. However, there are $\lambda_x \sim L_x$ and $\lambda_y \gtrsim h$ for all r_z (buoyancy dominated scales) that are active in buoyancy destruction (BD) and are inactive in production (SP). These scales that are activated as a result of buoyancy destruction imposing extra demands for a larger computational domain size to simulate strongly stable stratified boundary layers.

6.2 Future work

The effects of higher Reynolds and Richardson numbers on the characteristics of the patchy state, the evolution of TKE and vorticity, and possible turbulence recovery can be the subject of future work. Such simulations can improve our understanding of the more realistic SBL, in particular, once turbulence becomes intermittent for strongly stable stratification.

The mechanisms that are involved in turbulence production and dissipation in a SBL, and which ones are dominant, could also be areas of future research. Particularly, how the dominant mechanisms are maintained in the presence of the stabilizing effects of buoyancy remains to be answered. Turbulence production and dissipation can be both studied via fluctuating vorticity dynamics. For example the dominant mechanisms in the evolution of streamwise vorticity fluctuations can provide insight on dominant mechanisms in the induction of wall-normal velocity fluctuations by streamwise vorticies and thus in turbulence production. Enstrophy on the other hand is directly related to dissipation. Therefore, studying the evolution of fluctuating vortex dynamics can shed light on both production and dissipation.

An important unanswered question in our work, which requires a study of the full range of vertical scales, is how the near-wall inverse cascade is impacted by stratification. This inverse cascade will also be addressed in the future. This inverse cascade of energy from smaller scales near the wall to larger scales aloft has been shown to be to be an essential factor in sustaining turbulence in unstratified boundary layers [56].

References

[1] M. Abkar and F. Port-Agel. The effect of free-atmosphere stratification on boundary-layer flow and power output from very large wind farms. *Energies*, 6(5):2338–2361, 2013.

[2] R. Adrian, D. O. Hessen, T. Blenckner, H. Hillebrand, S. Hilt, E. Jeppesen, D. M. Livingstone, D. Trolle, and F. Colijn. *Environmental Impacts—Lake Ecosystems*, pages 315–340. Springer International Publishing, Cham, 2016.

[3] R. J. Adrian. Hairpin vortex organization in wall turbulence. *Physics of Fluids*, 19(4):041301, 2007.

[4] V. Armenio and S. Sarkar. An investigation of stably stratified turbulent channel flow using large-eddy simulation. *Journal of Fluid Mechanics*, 459:142, 2002.

[5] V. Armenio and S. Sarkar. *Environmental Stratified Flows*, volume 479. Springer Science & Business Media, 2007.

[6] S. P. S. Arya. Buoyancy effects in a horizontal flat-plate boundary layer. *Journal of Fluid Mechanics*, 68(2):321343, 1975.

[7] A. Atoufi, K. A. Scott, and M. L. Waite. Wall turbulence response to surface cooling and formation of strongly stable stratified boundary layers. *Physics of Fluids*, 31(8):085114, 2019.

[8] A. Atoufi, K. A. Scott, and M. L. Waite. Characteristics of quasistationary near-wall turbulence subjected to strong stable stratification in open-channel flows. *Phys. Rev. Fluids*, 5:064603, Jun 2020.

[9] A. Atoufi, M. L. Waite, and K. A. Scott. Kinetic energy cascade in stably stratified open-channel flows. *Journal of Fluid Mechanics, submitted*, 2020.

[10] G. K. Batchelor. *The Theory of Homogeneous Turbulence*. Cambridge university press, 1953.

[11] M. Bernardini, S. Pirozzoli, and P. Orlandi. Velocity statistics in turbulent channel flow up to $Re_\tau = 4000$. *Journal of Fluid Mechanics*, 742:171191, 2014.

[12] T. R. Bewely. *Numerical Renaissance: Simulation, Optimization, and Control*. Renaissance Press, 1 edition, 2014.

[13] G. Blaisdell, E. Spyropoulos, and J. Qin. The effect of the formulation of nonlinear terms on aliasing errors in spectral methods. *Applied Numerical Mathematics*, 21(3):207 – 219, 1996.

[14] I. A. Bolotnov, R. T. Lahey, D. A. Drew, K. E. Jansen, and A. A. Oberai. Spectral analysis of turbulence based on the DNS of a channel flow. *Computers & Fluids*, 39(4):640 – 655, 2010.

[15] P. Bradshaw. "Inactive" motion and pressure fluctuations in turbulent boundary layers. *Journal of Fluid Mechanics*, 30(2):241258, 1967.

[16] G. Brethouwer, Y. Duguet, and P. Schlatter. Turbulent-laminar coexistence in wall flows with Coriolis, buoyancy or Lorentz forces. *Journal of Fluid Mechanics*, 704:137172, 2012.

[17] J. W. Brooke and T. J. Hanratty. Origin of turbulence-producing eddies in a channel flow. *Physics of Fluids A: Fluid Dynamics*, 5(4):1011–1022, 1993.

[18] C. Canuto, M. Y. Hussaini, A. Quarteroni, A. Thomas Jr, et al. *Spectral Methods in Fluid Dynamics*. Springer Science & Business Media, 1988.

[19] C. M. Casciola, P. Gualtieri, R. Benzi, and R. Piva. Scale-by-scale budget and similarity laws for shear turbulence. *Journal of Fluid Mechanics*, 476:105114, 2003.

[20] M. Cho, Y. Hwang, and H. Choi. Scale interactions and spectral energy transfer in turbulent channel flow. *Journal of Fluid Mechanics*, 854:474504, 2018.

[21] A. Cimarelli, E. De Angelis, J. Jiménez, and C. M. Casciola. Cascades and wall-normal fluxes in turbulent channel flows. *Journal of Fluid Mechanics*, 796:417436, 2016.

[22] J. Cloern. Temporal dynamics and ecological significance of salinity stratification in an estuary (South San-Francisco Bay, USA). *Oceanologica Acta*, 7(1):137–141, 1984.

[23] R. L. Coulter. A case study of turbulence in the stable nocturnal boundary layer. *Boundary-Layer Meteorology*, 52(1):75–91, Jul 1990.

[24] J. Cuxart, C. Yagüe, G. Morales, E. Terradellas, J. Orbe, J. Calvo, A. Fernández, M. R. Soler, C. Infante, P. Buenestado, A. Espinalt, H. E. Joergensen, J. M. Rees, J. Vilá, J. M. Redondo, I. R. Cantalapiedra, and L. Conangla. Stable atmospheric boundary-layer experiment in spain (SABLES 98): A report. *Boundary-Layer Meteorology*, 96(3):337–370, Sep 2000.

[25] P. Davidson, Y. Kaneda, and K. Sreenivasan. *Ten Chapters in Turbulence*. Cambridge University Press, 2012.

[26] P. A. Davidson. *Turbulence in Rotating, Stratified and Electrically Conducting Fluids*. Cambridge University Press, 2013.

[27] P. A. Davidson and B. R. Pearson. Identifying turbulent energy distributions in real, rather than Fourier, space. *Phys. Rev. Lett.*, 95:214501, Nov 2005.

[28] P. Davidson. *Turbulence: An Introduction for Scientists and Engineers*. Oxford University Press, USA, second edition, 2015.

[29] B. J. H. V. de Wiel, A. F. Moene, H. J. J. Jonker, P. Baas, S. Basu, J. M. M. Donda, J. Sun, and A. A. M. Holtslag. The minimum wind speed for sustainable turbulence in the nocturnal boundary layer. *Journal of the Atmospheric Sciences*, 69(11):3116–3127, 2012.

[30] B. J. H. V. de Wiel, E. Vignon, P. Baas, I. G. S. van Hooijdonk, S. J. A. van der Linden, J. A. van Hooft, F. C. Bosveld, S. R. de Roode, A. F. Moene, and C. Genthon. Regime transitions in near-surface temperature inversions: A conceptual model. *Journal of the Atmospheric Sciences*, 74(4):1057–1073, 2017.

[31] S. H. Derbyshire. Nieuwstadt's stable boundary layer revisited. *Quarterly Journal of the Royal Meteorological Society*, 116(491):127–158, 1990.

[32] E. Deusebio, P. Schlatter, G. Brethouwer, and E. Lindborg. Direct numerical simulations of stratified open channel flows. *Journal of Physics: Conference Series*, 318(2):022009, 2011.

[33] T. M. Dillon. Vertical overturns: A comparison of Thorpe and Ozmidov length scales. *Journal of Geophysical Research: Oceans*, 87(C12):9601–9613, 1982.

[34] T. M. Dillon and D. R. Caldwell. The Batchelor spectrum and dissipation in the upper ocean. *Journal of Geophysical Research: Oceans*, 85(C4):1910–1916, 1980.

[35] A. J. Ding, T. Wang, V. Thouret, J.-P. Cammas, and P. Nédélec. Tropospheric ozone climatology over Beijing: analysis of aircraft data from the mozaic program. *Atmospheric Chemistry and Physics*, 8(1):1–13, 2008.

[36] J. M. M. Donda, I. G. S. van Hooijdonk, A. F. Moene, H. J. J. Jonker, G. J. F. van Heijst, H. J. H. Clercx, and B. J. H. van de Wiel. Collapse of turbulence in stably stratified channel flow: a transient phenomenon. *Quarterly Journal of the Royal Meteorological Society*, 141(691):2137–2147, 2015.

[37] J. M. M. Donda, I. G. S. van Hooijdonk, A. F. Moene, G. J. F. van Heijst, H. J. H. Clercx, and B. J. H. van de Wiel. The maximum sustainable heat flux in stably stratified channel flows. *Quarterly Journal of the Royal Meteorological Society*, 142(695):781–792, 2016.

[38] X. Dong, G. Dong, and C. Liu. Study on vorticity structures in late flow transition. *Physics of Fluids*, 30(10):104108, 2018.

[39] M. Drenkmper, B. Witha, G. Steinfeld, D. Heinemann, and M. Khn. The impact of stable atmospheric boundary layers on wind-turbine wakes within offshore wind farms. *Journal of Wind Engineering and Industrial Aerodynamics*, 144:146 – 153, 2015. Selected papers from the 6th International Symposium on Computational Wind Engineering CWE 2014.

[40] B. Dubrulle. Beyond Kolmogorov cascades. *Journal of Fluid Mechanics*, 867:P1, 2019.

[41] P. A. Durbin and B. P. Reif. *Statistical Theory and Modeling for Turbulent Flows*. John Wiley & Sons, 2011.

[42] D. R. Durran. *Numerical Methods for Fluid Dynamics: With Applications to Geophysics*, volume 32. Springer Science & Business Media, 2010.

[43] G. Eitel-Amor, R. rl, P. Schlatter, and O. Flores. Hairpin vortices in turbulent boundary layers. *Physics of Fluids*, 27(2):025108, 2015.

[44] T. H. Ellison. Turbulent transport of heat and momentum from an infinite rough plane. *Journal of Fluid Mechanics*, 2(5):456466, 1957.

[45] C. A. J. Fletcher. *Computational Techniques for Fluid Dynamics 2: Specific Techniques for Different Flow Categories*. Springer, 1991.

[46] O. Flores and J. J. Riley. Analysis of turbulence collapse in the stably stratified surface layer using direct numerical simulation. *Boundary-Layer Meteorology*, 139(2):241–259, May 2011.

[47] O. Flores and J. Jiménez. Hierarchy of minimal flow units in the logarithmic layer. *Physics of Fluids*, 22(7):071704, 2010.

[48] O. Flores and J. J. Riley. *Energy Balance in Stably-Stratified, Wall-Bounded Turbulence*, pages 89–99. Springer International Publishing, Cham, 2018.

[49] M. Frigo and S. G. Johnson. The design and implementation of FFTW3. *Proceedings of the IEEE*, 93(2):216–231, Feb 2005.

[50] M. García-Villalba and J. C. del Álamo. Turbulence modification by stable stratification in channel flow. *Physics of Fluids*, 23(4):045104, 2011.

[51] R. P. Garg, J. H. Ferziger, and S. G. Monismith. Hybrid spectral finite difference simulations of stratified turbulent flows on distributed memory architectures. *International Journal for Numerical Methods in Fluids*, 24(11):1129–1158, 1997.

[52] R. P. Garg, J. H. Ferziger, S. G. Monismith, and J. R. Koseff. Stably stratified turbulent channel flows. I. Stratification regimes and turbulence suppression mechanism. *Physics of Fluids*, 12(10):2569–2594, 2000.

[53] S. Genieys and M. Massot. From Navier-Stokes equations to Oberbeck-Boussinesq approximation : a unified approach. Paru comme un rapport interne de l'unité MAPLY (UMR 5585 - Lyon) en 2001 http://maply.univ-lyonl.fr/publis/publiv/2001/331/publi.ps.gz, April 2001.

[54] F. Hamba. Turbulent energy density and its transport equation in scale space. *Physics of Fluids*, 27(8):085108, 2015.

[55] F. Hamba. Turbulent energy density in scale space for inhomogeneous turbulence. *Journal of Fluid Mechanics*, 842:532553, 2018.

[56] F. Hamba. Inverse energy cascade and vortical structure in the near-wall region of turbulent channel flow. *Phys. Rev. Fluids*, 4:114609, Nov 2019.

[57] J. M. Hamilton, J. Kim, and F. Waleffe. Regeneration mechanisms of near-wall turbulence structures. *Journal of Fluid Mechanics*, 287:317348, 1995.

[58] P. He. A high order finite difference solver for massively parallel simulations of stably stratified turbulent channel flows. *Computers & Fluids*, 127:161 – 173, 2016.

[59] P. Holmes, J. L. Lumley, G. Berkooz, and C. W. Rowley. *Turbulence, Coherent Structures, Dynamical Systems and Symmetry*. Cambridge Monographs on Mechanics. Cambridge University Press, 2 edition, 2012.

[60] L. N. Howard. Note on a paper of John W. Miles. *Journal of Fluid Mechanics*, 10(4):509512, 1961.

[61] J. Huang and E. Bou-Zeid. Turbulence and Vertical Fluxes in the Stable Atmospheric Boundary Layer. Part I: A Large-Eddy Simulation Study. *Journal of the Atmospheric Sciences*, 70(6):1513–1527, 2013.

[62] J. C. R. Hunt, A. A. Wray, and P. Moin. Eddies, streams, and convergence zones in turbulent flows. *Studying Turbulence Using Numerical Simulation Databases*, pages 193–208, 1988.

[63] N. Hutchins and I. Marusic. Evidence of very long meandering features in the logarithmic region of turbulent boundary layers. *Journal of Fluid Mechanics*, 579:128, 2007.

[64] N. Hutchins and I. Marusic. Large-scale influences in near-wall turbulence. *Philosophical transactions. Series A, Mathematical, physical, and engineering sciences*, 365 1852:647–64, 2007.

[65] Y. Hwang. Statistical structure of self-sustaining attached eddies in turbulent channel flow. *Journal of Fluid Mechanics*, 767:254289, 2015.

[66] Y. Hwang and Y. Bengana. Self-sustaining process of minimal attached eddies in turbulent channel flow. *Journal of Fluid Mechanics*, 795:708738, 2016.

[67] J. Jiménez. The physics of wall turbulence. *Physica A: Statistical Mechanics and its Applications*, 263(1):252 – 262, 1999. Proceedings of the 20th IUPAP International Conference on Statistical Physics.

[68] J. Jiménez. Turbulence and vortex dynamics. *Notes for the Polytecnique course on turbulence*, 2004.

[69] J. Jiménez. Cascades in wall-bounded turbulence. *Annual Review of Fluid Mechanics*, 44(1):27–45, 2012.

[70] J. Jiménez. Near-wall turbulence. *Physics of Fluids*, 25(10):101302, 2013.

[71] J. Jiménez and P. Moin. The minimal flow unit in near-wall turbulence. *Journal of Fluid Mechanics*, 225:213240, 1991.

[72] J. Jiménez and A. Pinelli. The autonomous cycle of near-wall turbulence. *Journal of Fluid Mechanics*, 389:335359, 1999.

[73] S. Kara, M. C. Kara, T. Stoesser, and T. W. Sturm. Free-surface versus rigid-lid les computations for bridge-abutment flow. *Journal of Hydraulic Engineering*, 141(9):04015019, 2015.

[74] F. Karimpour and S. K. Venayagamoorthy. On turbulent mixing in stably stratified wall-bounded flows. *Physics of Fluids*, 27(4):046603, 2015.

[75] Khani, Sina. *Large eddy simulations and subgrid scale motions in stratified turbulence*. PhD thesis, University of Waterloo, 2015.

[76] J. Kim and P. Moin. Application of a fractional-step method to incompressible navier-stokes equations. *Journal of Computational Physics*, 59(2):308 – 323, 1985.

[77] M. P. Kirkpatrick, N. Williamson, S. W. Armfield, and V. Zecevic. Evolution of thermally stratified turbulent open channel flow after removal of the heat source. *Journal of Fluid Mechanics*, 876:356412, 2019.

[78] A. N. Kolmogorov. The local structure of turbulence in incompressible viscous fluid for very large Reynolds numbers. In *Dokl. Akad. Nauk SSSR*, volume 30, pages 299–303, 1941.

[79] S. Komori, R. Kurose, K. Iwano, T. Ukai, and N. Suzuki. Direct numerical simulation of wind-driven turbulence and scalar transfer at sheared gas–liquid interfaces. *Journal of Turbulence*, 11:N32, 2010.

[80] S. Komori, R. Nagaosa, Y. Murakami, S. Chiba, K. Ishii, and K. Kuwahara. Direct numerical simulation of three-dimensional open-channel flow with zero-shear gas–liquid interface. *Physics of Fluids A: Fluid Dynamics*, 5(1):115–125, 1993.

[81] P. K. Kundu, I. M. Cohen, and D. R. Dowling. *Fluid Mechanics*. Academic Press, Boston, sixth edition, 2016.

[82] C. J. Lang and M. L. Waite. Scale-dependent anisotropy in forced stratified turbulence. *Phys. Rev. Fluids*, 4:044801, 2019.

[83] J. Lee, J. Suh, H. J. Sung, and B. Pettersen. Structures of turbulent open-channel flow in the presence of an air–water interface. *Journal of Turbulence*, 13:N18, 2012.

[84] M. Lee and R. D. Moser. Direct numerical simulation of turbulent channel flow up to $Re_\tau \approx 5200$. *Journal of Fluid Mechanics*, 774:395415, 2015.

[85] M. Lesieur. *Turbulence in Fluids*. Springer, 4th edition, 2008.

[86] N. Li and S. Laizet. 2DECOMP & FFT—a highly scalable 2D decomposition library and FFT interface. In *Cray User Group 2010 conference*, pages 1–13, 2010.

[87] Z. Li, J. Guo, A. Ding, H. Liao, J. Liu, Y. Sun, T. Wang, H. Xue, H. Zhang, and B. Zhu. Aerosol and boundary-layer interactions and impact on air quality. *National Science Review*, 4(6):810–833, 2017.

[88] E. Lindborg. The energy cascade in a strongly stratified fluid. *Journal of Fluid Mechanics*, 550:207242, 2006.

[89] F. Lluesma-Rodríguez, S. Hoyas, and M. Perez-Quiles. Influence of the computational domain on DNS of turbulent heat transfer up to $Re_\tau = 2000$ for $Pr = 0.71$. *International Journal of Heat and Mass Transfer*, 122:983 – 992, 2018.

[90] E. N. Lorenz. Deterministic Nonperiodic Flow. *Journal of the Atmospheric Sciences*, 20(2):130–141, 03 1963.

[91] A. Lozano-Durn and J. Jiménez. Effect of the computational domain on direct simulations of turbulent channels up to $Re_\tau = 4200$. *Physics of Fluids*, 26(1):011702, 2014.

[92] A. Lozano-Durn and J. Jiménez. Time-resolved evolution of coherent structures in turbulent channels: characterization of eddies and cascades. *Journal of Fluid Mechanics*, 759:432471, 2014.

[93] J. L. Lumley. The spectrum of nearly inertial turbulence in a stably stratified fluid. *Journal of the Atmospheric Sciences*, 21(1):99–102, 1964.

[94] L. Mahrt. Stably stratified atmospheric boundary layers. *Annual Review of Fluid Mechanics*, 46:23–45, 2014.

[95] L. Mahrt. Microfronts in the nocturnal boundary layer. *Quarterly Journal of the Royal Meteorological Society*, 145(719):546–562, 2019.

[96] N. Marati, C. M. Casciola, and R. Piva. Energy cascade and spatial fluxes in wall turbulence. *Journal of Fluid Mechanics*, 521:191215, 2004.

[97] B. D. Mater, S. M. Schaad, and S. K. Venayagamoorthy. Relevance of the Thorpe length scale in stably stratified turbulence. *Physics of Fluids*, 25(7):076604, 2013.

[98] M. Metzger, B. McKeon, and H. Holmes. The near-neutral atmospheric surface layer: turbulence and non-stationarity. *Philosophical Transactions of the Royal Society A: Mathematical, Physical and Engineering Sciences*, 365(1852):859–876, 2007.

[99] J. W. Miles. On the stability of heterogeneous shear flows. *Journal of Fluid Mechanics*, 10(4):496508, 1961.

[100] P. Moin. *Fundamentals of Engineering Numerical Analysis*. Cambridge University Press, 2 edition, 2010.

[101] P. Moin and K. Mahesh. Direct numerical simulation: a tool in turbulence research. *Annual Review of Fluid Mechanics*, 30(1):539–578, 1998.

[102] R. D. Moser, J. Kim, and N. N. Mansour. Direct numerical simulation of turbulent channel flow up to $Re_\tau = 590$. *Physics of Fluids*, 11(4):943–945, 1999.

[103] C. I. H. Nicholl. Some dynamical effects of heat on a turbulent boundary layer. *Journal of Fluid Mechanics*, 40(2):361384, 1970.

[104] T. B. Nickels, I. Marusic, S. Hafez, and M. S. Chong. Evidence of the k_1^{-1} Law in a High-Reynolds-Number Turbulent Boundary Layer. *Phys. Rev. Lett.*, 95:074501, Aug 2005.

[105] F. T. M. Nieuwstadt. The turbulent structure of the stable, nocturnal boundary layer. *Journal of the Atmospheric Sciences*, 41(14):2202–2216, 1984.

[106] F. T. M. Nieuwstadt. Direct numerical simulation of stable channel flow at large stability. *Boundary-Layer Meteorology*, 116(2):277–299, Aug 2005.

[107] A. M. Obukhov. Turbulence in an atmosphere with a non-uniform temperature. *Boundary-Layer Meteorology*, 2(1):7–29, Mar 1971.

[108] Y. Ohya, D. E. Neff, and R. N. Meroney. Turbulence structure in a stratified boundary layer under stable conditions. *Boundary-Layer Meteorology*, 83(1):139–162, 1997.

[109] P. Orlandi. *Fluid Flow Phenomena: A Numerical Toolkit*, volume 55. Springer Science & Business Media, 2000.

[110] D. Pekurovsky. P3DFFT: A Framework for Parallel Computations of Fourier Transforms in Three Dimensions. *SIAM Journal on Scientific Computing*, 34(4):C192–C209, 2012.

[111] A. E. Perry, S. Henbest, and M. S. Chong. A theoretical and experimental study of wall turbulence. *Journal of Fluid Mechanics*, 165:163199, 1986.

[112] S. B. Pope. *Turbulent Flows*. Cambridge University Press, 2000.

[113] L. Quan, E. Ferrero, and F. Hu. Relating statistical moments and entropy in the stable boundary layer. *Physica A: Statistical Mechanics and its Applications*, 391(1):231 – 247, 2012.

[114] K. Rajagopal, M. Ruzicka, and A. Srinivasa. On the Oberbeck-Boussinesq approximation. *Mathematical Models and Methods in Applied Sciences*, 6(08):1157–1167, 1996.

[115] L. Ran, Z. Deng, X. Xu, P. Yan, W. Lin, Y. Wang, P. Tian, P. Wang, W. Pan, and D. Lu. Vertical profiles of black carbon measured by a micro-aethalometer in summer in the North China Plain. *Atmospheric Chemistry and Physics*, 16(16):10441–10454, 2016.

[116] L. F. Richardson. *Weather Prediction by Numerical Process*. Cambridge University Press, second edition, 2007.

[117] J. J. Riley and M.-P. Lelong. Fluid motions in the presence of strong stable stratification. *Annual Review of Fluid Mechanics*, 32(1):613–657, 2000.

[118] J. J. Riley and E. Lindborg. Stratified turbulence: A possible interpretation of some geophysical turbulence measurements. *Journal of the Atmospheric Sciences*, 65(7):2416–2424, 2008.

[119] S. Shah and E. Bou-Zeid. Rate of decay of turbulent kinetic energy in abruptly stabilized Ekman boundary layers. *Phys. Rev. Fluids*, 4:074602, Jul 2019.

[120] Z. Sorbjan. Gradient-based scales and similarity laws in the stable boundary layer. *Quarterly Journal of the Royal Meteorological Society*, 136(650):1243–1254, 2010.

[121] Z. Sorbjan. Local structure of turbulence in stably stratified boundary layers. *Journal of the Atmospheric Sciences*, 63(5):1526–1537, 2006.

[122] E. Spiegel and G. Veronis. On the Boussinesq approximation for a compressible fluid. *The Astrophysical Journal*, 131:442, 1960.

[123] R. Stewart. The problem of diffusion in a stratified fluid. In H. Landsberg and J. V. Mieghem, editors, *Advances in Geophysics*, volume 6, pages 303 – 311. Elsevier, 1959.

[124] S. H. Strogatz. *Nonlinear dynamics and chaos with applications to physics, biology, chemistry, and engineering*. CRC press, 2018.

[125] R. B. Stull. *An Introduction to Boundary Layer Meteorology*, volume 13. Springer Science & Business Media, 2012.

[126] N. E. Sujovolsky, P. D. Mininni, and A. Pouquet. Generation of turbulence through frontogenesis in sheared stratified flows. *Physics of Fluids*, 30(8):086601, 2018.

[127] M. Tabib, A. Rasheed, and T. Kvamsdal. Investigation of the impact of wakes and stratification on the performance of an onshore wind farm. *Energy Procedia*, 80:302 – 311, 2015.

[128] T. Tatsumi and G. I. Taylor. The theory of decay process of incompressible isotropic turbulence. *Proceedings of the Royal Society of London. Series A. Mathematical and Physical Sciences*, 239(1216):16–45, 1957.

[129] J. R. Taylor. *Numerical simulations of the stratified oceanic bottom boundary layer*. PhD thesis, University of California San Diego, 2008.

[130] J. R. Taylor, S. Sarkar, and V. Armenio. Large eddy simulation of stably stratified open channel flow. *Physics of Fluids*, 17(11):116602, 2005.

[131] H. Tennekes and J. L. Lumley. *A First Course in Turbulence*. MIT press, 1972.

[132] P. A. Thompson. *Compressible-Fluid Dynamic*. McGraw-Hill, 1971.

[133] A. A. Townsend. Equilibrium layers and wall turbulence. *Journal of Fluid Mechanics*, 11(1):97120, 1961.

[134] A. A. Townsend. *The Structure of Turbulent Shear Flow*. Cambridge University Press, 1976.

[135] T. Van Buren, O. Williams, and A. J. Smits. Turbulent boundary layer response to the introduction of stable stratification. *Journal of Fluid Mechanics*, 811:569581, 2017.

[136] I. G. S. van Hooijdonk, A. F. Moene, M. Scheffer, H. J. H. Clercx, and B. J. H. van de Wiel. Early warning signals for regime transition in the stable boundary layer: A model study. *Boundary-Layer Meteorology*, 162(2):283–306, Feb 2017.

[137] I. G. S. van Hooijdonk, J. M. M. Donda, H. J. H. Clercx, F. C. Bosveld, and B. J. H. van de Wiel. Shear capacity as prognostic for nocturnal boundary layer regimes. *Journal of the Atmospheric Sciences*, 72(4):1518–1532, 2015.

[138] P. Vedula, R. D. Moser, and P. S. Zandonade. Validity of quasinormal approximation in turbulent channel flow. *Physics of Fluids*, 17(5):055106, 2005.

[139] A. W. Vreman and J. G. M. Kuerten. Statistics of spatial derivatives of velocity and pressure in turbulent channel flow. *Physics of Fluids*, 26(8):085103, 2014.

[140] M. L. Waite. Direct numerical simulations of laboratory-scale stratified turbulence. In T. von Larcher and P. Williams, editors, *Modeling Atmospheric and Oceanic Flows*, chapter 8, pages 159–175. American Geophysical Union (AGU), 2014.

[141] M. L. Waite and P. Bartello. Stratified turbulence dominated by vortical motion. *Journal of Fluid Mechanics*, 517:281308, 2004.

[142] O. Williams, T. Hohman, T. Van Buren, E. Bou-Zeid, and A. J. Smits. The effect of stable thermal stratification on turbulent boundary layer statistics. *Journal of Fluid Mechanics*, 812:10391075, 2017.

[143] J. C. Wyngaard. *Turbulence in the Atmosphere*. Cambridge University Press, 2010.

[144] O. Zeman and J. L. Lumley. Modeling buoyancy driven mixed layers. *Journal of the Atmospheric Sciences*, 33(10):1974–1988, 1976.

[145] F. Zonta and A. Soldati. Stably Stratified Wall-Bounded Turbulence. *Applied Mechanics Reviews*, 70(4), 08 2018. 040801.

APPENDICES

Appendix A

Reynolds stress and TKE evolution in SBLs

A.1 TKE budget

The evolution of TKE in the SBL is governed by [52]

$$\frac{\partial k}{\partial t} + \overline{u}_j \frac{\partial k}{\partial x_j} = P + T + \Pi + D + \epsilon + B \tag{A.1}$$

where

$$P = -\overline{u_i' u_j'} \frac{\partial \overline{u}_i}{\partial x_j},\ T = -\frac{\partial \overline{u_i' u_i' u_j'}}{\partial x_j},\ \Pi = -\frac{\partial \overline{p' u_i'}}{\partial x_i},\ D = \frac{1}{Re} \frac{\partial^2 k}{\partial x_j \partial x_j}, \tag{A.2}$$
$$\epsilon = -\frac{2}{Re} \overline{\frac{\partial u_i'}{\partial x_j} \frac{\partial u_i'}{\partial x_j}},\ B = Ri\ \overline{u_i' \theta'} \delta_{i3},$$

are production, turbulent transport, pressure-transport (pressure work), viscous diffusion, viscous dissipation, and buoyant destruction, respectively.

A.2 Reynolds stresses transport equations

The budget of Reynolds stresses are governed by :

$$\frac{\partial}{\partial t} \overline{u_i' u_j'} + \overline{u_k} \frac{\partial}{\partial x_k} \overline{u_i' u_j'} = \mathrm{P_{ij}} + \mathrm{T_{ij}} + \Phi_{\mathrm{ij}} + \mathrm{D_{ij}} + \epsilon_{\mathrm{ij}} + \mathrm{B_{ij}}, \tag{A.3}$$

where

$$\mathrm{P_{ij}} = -\left(\overline{u_i'u_k'}\frac{\partial \overline{u_j}}{\partial x_k} + \overline{u_j'u_k'}\frac{\partial \overline{u_i}}{\partial x_k}\right),\ \mathrm{T_{ij}} = -\frac{\partial \overline{u_i'u_j'u_k'}}{\partial x_k}, \tag{A.4}$$
$$\Pi_{\mathrm{ij}} = -\left(\frac{\partial \overline{p'u_i'}}{\partial x_j} + \frac{\partial \overline{p'u_j'}}{\partial x_i}\right),\ \Phi_{\mathrm{ij}} = \overline{\left(p'\frac{\partial u_i'}{\partial x_j} + p'\frac{\partial u_j'}{\partial x_i}\right)},$$

are production, turbulent transport, pressure-transport, pressure-strain, and

$$\mathrm{D_{ij}} = \frac{1}{Re_\tau}\frac{\partial^2 \overline{u_i'u_j'}}{\partial x_k \partial x_k},\ \epsilon_{\mathrm{ij}} = -\frac{2}{Re_\tau}\overline{\frac{\partial u_i'}{\partial x_k}\frac{\partial u_j'}{\partial x_k}},\ \mathrm{B_{ij}} = Ri_\tau\left(\overline{u_i'\theta'}\delta_{j3} + \overline{u_j'\theta'}\delta_{i3}\right), \tag{A.5}$$

are viscous diffusion, viscous dissipation, and buoyancy. The buoyancy terms are called buoyancy destruction if they are negative. The budget equation for TKE is similar to (A.3) with $i = j$. Note that, in the TKE budget, we refer to B as buoyant destruction, since it is generally negative.